Resolving geometrically necessary dislocations and application in copper.

Kerr, David

Resolving Geometrically Necessary Dislocations and Application in Copper

Prifysgol Abertawe
Swansea University

David Kerr

College of Engineering

Swansea University

A thesis submitted for the degree of

Doctor of Philosophy

May 2013

Abstract

The use of Electron Back-Scatter Diffraction (EBSD) as a tool for strain measurement is not a new application. The band contrast within a captured Kikuchi pattern has been shown to decrease in regions with high plastic strain. Recently, however, highly accurate EBSD orientation maps have been used to recover dislocation content by directly relating lattice curvature, measured as point-to-point misorientation differences, to the crystal structure of the material using minimization techniques to recover the dislocation content determined to be geometrically necessary. This dislocation content is termed the Geometrically-Necessary Dislocations (GND) content.

High resolution EBSD techniques exist which are able to index Kikuchi patterns much more accurately than the more widely used Hough transformation; however, the Hough transformation shows advantages of low computational cost and fast data acquistion times. As a result, larger data sets are theoretically possible using a Hough transformation, however with a lower indexing accuracy. The main aims of this work are to determine the optimal settings for data acquisition by EBSD for the purposes of strain mapping, to write code to create a strain map, and to use that code and mapping settings for an investigation into the microstructural development of bent samples of copper. Three sets of samples, each receiving varying applied strains and heat-treatments were created and statistics concerning the strain around key features, such as $\Sigma 3$ and $\Sigma 3^n$ boundaries which are important for the mechanical performance of the material, were determined.

The results of the investigation into the optimal settings for the purpose of strain mapping by Hough transformation and EBSD showed

that a higher Kikuchi pattern resolution can be sacrificed to decrease mapping time and increase the size of data set possible. External time constraints, such as the microscope filament life span, limit the longest mapping time possible and so must be considered where large data sets are desirable. The accuracy of indexing by band centres and band edges was shown to be similar, however with greatly differing noise profiles. A portion of the noise of indexing by band edges was shown to be normally distributed and a noise reduction algorithm to remove normally distributed noise is suggested. It is also shown that the fraction of total dislocation content recoverable as GNDs changes as the structure of GNDs changes, which makes strain analysis based on the value of the GND content calculated ineffective. Instead, analysis of the GND structure itself is shown to correlate better with the restorative state of a material. A method of quantifying the connectedness of GND content is created and is suggested for future use.

The investigation of bent samples of copper showed the effect of strain on the development of the copper microstructure after heat-treatment. Different GND structures were observed at different stages of restoration, including a secondary recovery stage after deformation is left behind mobile boundaries. Conversely, observation of the GND structure was then shown to determine the restoration stage, which aided the conclusion that the compressive end of the samples was restoring faster than the tensile side. This is believed to be because the neutral plane, at which the strain changes from tensile to compressive in nature, is located closer to the tensile end of the sample due to strain hardening effects during bending. The larger strain in the compressive region acts as a higher driving force for restoration than the tensile end. The strain around boundaries was also measured based on the boundary character. $\Sigma 3$ boundaries were shown to shield the grain bulk from deformation under applied strain compared to non-$\Sigma 3$ boundaries.

DECLARATION

This work has not previously been accepted in substance for any degree and is not being concurrently submitted in candidature for any degree.

Signed ..... (candidate)

Date 18/10/13

STATEMENT 1

This thesis is the result of my own investigations, except where otherwise stated. Where correction services have been used, the extent and nature of the correction is clearly marked in a footnote(s).

Other sources are acknowledged by footnotes giving explicit references. A bibliography is appended.

Signed ..... (candidate)

Date 18/10/13

STATEMENT 2

I hereby give consent for my thesis, if accepted, to be available for photocopying and for inter-library loan, and for the title and summary to be made available to outside organisations.

Signed ..... (candidate)

Date 18/10/13

NB: *Candidates on whose behalf a bar on access has been approved by the University (see Note 7), should use the following version of Statement 2:*

I hereby give consent for my thesis, if accepted, to be available for photocopying and for inter-library loans **after expiry of a bar on access approved by the Swansea University.**

Signed Not Applicable ..... (candidate)

Date .....

For Aneurin and Appa, even though he bit me.

Acknowledgements

I would like to sincerely thank Prof. Valerie Randle for her encouragement and guidance throughout the course of this project. I would also like to thank Dr. Mark Coleman and Peter Davies for their technical help and support, and also my colleagues Lisa Hill and Mike Waterton for the helpful discussions and social working environment.

I am grateful for the opportunity to complete this work at Swansea University and use the excellent research facilities provided by Prof. Valerie Randle.

I would also like to thank Dr. Ben Spencer for the opportunity for collaboration. Lastly, I would like to acknowledge the Micromechanics group of Oxford University for kindly providing a map created using XCF.

Contents

List of Figures

Chapter 1

Introduction

1.1 Introduction

EBSD is a technique based within a Scanning Electron Microscope (SEM) and is used to determine the orientation of a crystal at a point. Two dimensional orientation maps can be produced after sampling points in a grid which highlight the size and orientation of grains, boundaries, triple junctions and other key microstructural features. This is typically accomplished using a point-to-point step size as coarse as possible such that the shape of features is retained but map creation time is minimized.

Recently, a considerable amount of research has been dedicated to the application of EBSD for the measurement of elastic and plastic strain. It may be possible to determine elastic strain directly by comparison of a strained and unstrained Kikuchi pattern [1], while plastic strain is determined from comparison of Kikuchi patterns from points separated by a small distance [2]. A small difference in orientation between neighbouring points infers a lattice curvature which represents a minimum length of dislocations which must be present in the material to create the observed lattice curvature [3]. This minimum length of dislocations is termed the GND content. The GND content is calculated using the measured lattice curvature and the system of dislocations known from the crystal structure present in the material. A Statistically Stored Dislocations (SSD) content, which has no net effect on the lattice curvature may also be present in the material but

is not recoverable by this method, and hence the definition of GND content as a minimum.

Indexing of Kikuchi patterns is accomplished using automatic methods. High resolution EBSD systems index Kikuchi patterns using a Cross-Correlation Function (XCF), by identifying changes in regions of interest from a strain free reference pattern. This method can achieve a misorientation resolution of +/- 0.01° [4]. The more widely used Hough transformation indexes Kikuchi patterns by transforming Kikuchi patterns into Hough space and identifying peaks. The misorientation resolution of the Hough transformation is much larger than that of XCF, +/- 0.5°, but mapping times are greatly reduced by the Hough transformation being less computationally expensive and Kikuchi pattern time being reduced by the lack of high quality Kikuchi patterns being required. As a result, the Hough transformation presents an opportunity for larger data sets to be created, while also having the advantage of being in more widespread use.

The measurement of strain by EBSD is desirable for investigations which require knowledge of deformation around microstructural features. Orientation maps created by EBSD map the features in question, and subsequent GND maps provide strain information. This has been applied to compare dislocation substructures within macro and non-macrozone regions of Ti6Al4V [5] and to identify the source of lower elastic yield limit and higher yield strength in ultra-fine grained dual-phase steels when the martensitic particle volume fraction is increased [6]. Additionally, orientation mapping in conjunction with strain mapping may prove useful in characterizing the development of deformed microstructures and twin boundaries for materials which are given Grain Boundary Engineering (GBE) treatment regimens. GBE aims to design and optimize a microstructure via thermomechanical processing to alter the grain boundary character distribution in a material. This is typically accomplished in FCC materials by promoting the formation of twinned boundaries and twinned boundary connectors [7].

1.2 Project Objectives

The aims of the present work is divided into two parts. The first part involves determining appropriate methodology for the measurement of GNDs by EBSD and

then optimizing that methodology. This includes optimizing the conditions for data acquisition by EBSD and also the writing of code for subsequent calculation of GNDs. The effectiveness of strain measurement using a Hough transformation indexing method and optimized settings will be explored. Possible post-processing techniques will also be explored and their effectiveness determined.

The second part involves the use of the GND code and optimized settings of the first part in an investigation into the development of the microstructure of bent samples of copper. The bending and subsequent heat-treatment allows for direct comparisons of microstructures developed under tension and compression. The samples will be given regimen similar to a GBE regimens so the effect of strain around key microstructural features, especially $\Sigma 3$ and $\Sigma 3^n$ boundaries which are important for the mechanical performance of the material, can be observed. The strength of the Hough transformation lies in the low computational cost and fast data acquisition times, however with a lower indexing accuracy than other techniques. In an attempt to minimize the effect of the lowered indexing accuracy, the largest data sets possible will be created and statistics from those maps around key microstructural features gathered and interpreted.

Chapter 2

Microstructure of Copper and Measurement Using EBSD

2.1 Introduction

The aim of materials science is to further our understanding of the behaviour of materials and to use this information to engineer materials with properties more suitable to their desired functions. The study of metallic materials at the microscopic level has shown that the structure of grain boundaries have a significant effect on the bulk properties of the material. The ability to manipulate grain boundary structures may lead beneficial bulk properties in materials.

Grain boundaries may form in low energy configurations based on the geometry and crystallography at the interface, giving rise to beneficial properties. The geometry of a grain boundary interface is fully described by five macroscopic and three microscopic degrees of freedom. A common axis and a rotation angle, termed the misorientation, is typically used to describe the lattice change across a grain boundary. The misorientation scheme may also be used to determine the Coincidence-Site Lattice (CSL) classification, designated using a Σ number representing the reciprocal density of coinciding lattice points of the two crystal orientations. The misorientation describes three of the five macroscopic degrees of freedom, with the remaining two describing the orientation of the boundary plane. Conventional EBSD analysis of a sample surface does not allow for analysis of the boundary

plane (however, destructive techniques such as Focussed Ion Beam (FIB) milling or other stereological techniques may be used), and as a result the misorientation or CSL designation alone may be used as a kind of short hand to classify a boundary. Grain boundary structure and methods of description are further explained in Section 2.3.

Low Σ number CSL boundaries have been associated with low energy beneficial boundaries. However, as the actual boundary orientation is not considered by the misorientation scheme used to classify a CSL, and hence only the lattice coincidence and not the boundary coincidence is measured, the CSL alone has been shown to be insufficient in predicting the existence of beneficial properties of a boundary. The CSL classification is still, however, useful as a tool to indicate possible beneficial boundary properties. It is described further in Section 2.3.2.

Low stacking fault energy materials, such as copper, readily form low energy annealing twin ($\Sigma 3$) boundaries. Immobile coherent $\Sigma 3$ boundaries may interact with mobile incoherent $\Sigma 3$ boundaries during annealing to form additional $\Sigma 3n$ boundaries. Attempts to incorporate large fractions of these beneficial boundaries in materials, termed grain boundary engineering, has been the subject of much research. This is typically accomplished by either single or multi-step regimes of straining and annealing to promote the formation of or adjusting of existing boundaries into low energy formations [7]. The exact mechanism of formation of annealing twins is still relatively recondite, with both energy and kinetic based models predicting their formation. The magnitude and direction of the strain also effects the type of $\Sigma 3$ variant formed during processing.

The plastic deformation caused during straining the material activates the motion and interaction of a vast system of dislocations in the material. At grain boundaries, dislocation slip may be transferred across the boundary based on the availability of slip systems in the receiving grain in relation to the incoming dislocation. As a result, the grain boundary geometry plays a key role in the dislocation mechanics of the material, and hence the flow stress and other bulk properties.

2.2 Copper

Copper, chemical symbol Cu, has atomic number 29 and atomic weight $63.546\frac{g}{mol}$. In pure form, it is known for its high ductility, electrical and thermal conductivity, leading to its frequent application in electrical wiring. Copper atoms arrange in Face-Centred Cubic (FCC) crystals.

2.2.1 FCC Crystal Structure

Metallic crystals may take many forms. These structures include triclinic, hexagonal, tetragonal and cubic. The arrangement of atoms in a cubic system generally come in three categories; simple cubic, Body-Centred Cubic (BCC), or FCC, shown in Fig. 2.1.

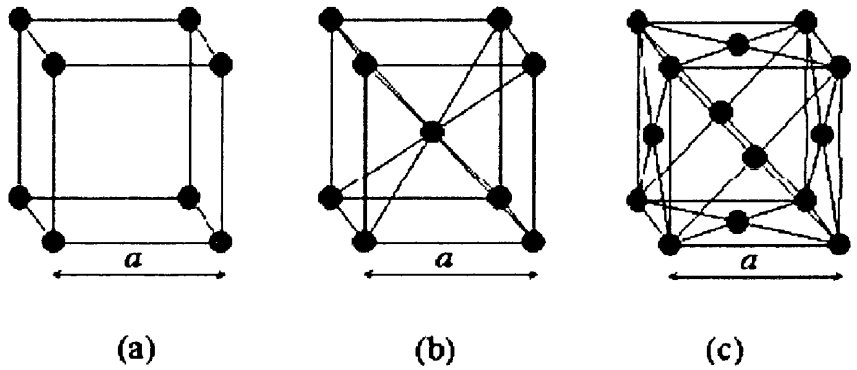

Figure 2.1: (a) Simple Cubic (b) Boby-Centred Cubic (c) Face-Centred Cubic

The lattice parameter, a, indicates the width of the unit cell. Atoms in the FCC crystal structure are closest along <110> directions and are most dense on {111} planes. These are termed the close-packed direction and close-packed plane.

2.2.2 Crystal Defects

Crystal structures in real materials contain many defects. These may be point defects (vacancy or interstitial atoms), or volume effects such as dislocations. Dislocations are important for overall materials properties, such as ductility and tensile

strength, and will be explained further in this report as a precursor to dislocation content measurement in a polycrystal.

There are two main categories of dislocations; edge and screw. Edge dislocations may be imagined as an extra half plane of atoms inserted into a crystal lattice such that the lattice becomes distorted in the region around the dislocation. A screw dislocation may be imagined by the bonds on a half plan of atoms being broken and displaced in the space of the plane. An example of a pure edge and pure screw dislocation is shown in Fig. 2.2.

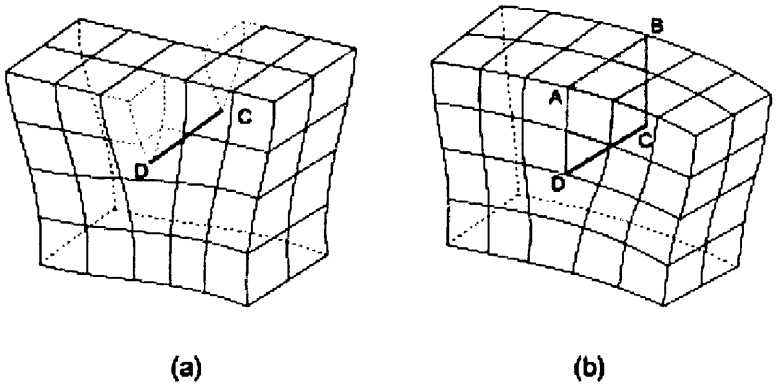

Figure 2.2: (a) Pure screw dislocation (b) Pure edge dislocation [8]

Definition of these dislocations is most useful when given in terms of a Burgers vector of a Burgers circuit. A Burgers circuit is created by an atom to atom path around a dislocation feature, creating a closed loop. If the same atom to atom path is taken in a perfect crystal, the difference in the start and end point is termed the Burgers vector, shown in Fig. 2.3.

The Burgers vector leads to the definition of dislocations as positive or negative. Equivalent dislocations with Burgers vectors in opposite directions are opposite in character of each other. By definition, the edge dislocation in Fig. 2.2 is a positive edge dislocation, while a dislocation with an additional plane below ABCD would be a negative dislocation. Dislocation interactions often lead dislocations of opposite sign annihilating each other.

In practice, dislocations may come together creating a line of dislocation with mixed edge and screw character. Where the Burgers vector is perpendicular to

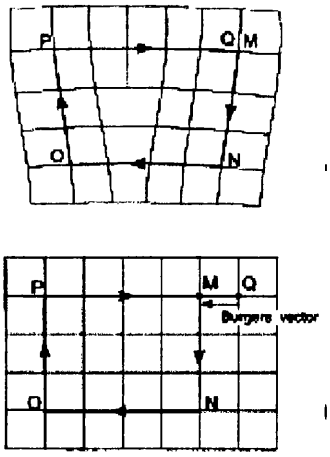

Figure 2.3: A Burgers circuit around a crystal defect, and the resulting Burgers vector when compared to a perfect crystal [8]

the dislocation line, the dislocation segment is pure edge in character, and when they are parallel is it pure screw in character.

Dislocations may move through a material by either climb or slip. Dislocation slip involves the breaking of the atomic bonds below the dislocation and a relatively small position change, shown in Fig. 2.4.

Slip allows dislocations to move at small applied stresses. The plane of the slip is defined as the plane containing both the Burgers vector and the dislocation line direction. This combination of slip plane and vector are called a slip system. In FCC materials, these slip systems are the combination of close-packed planes and close-packed directions, <110>{111}.

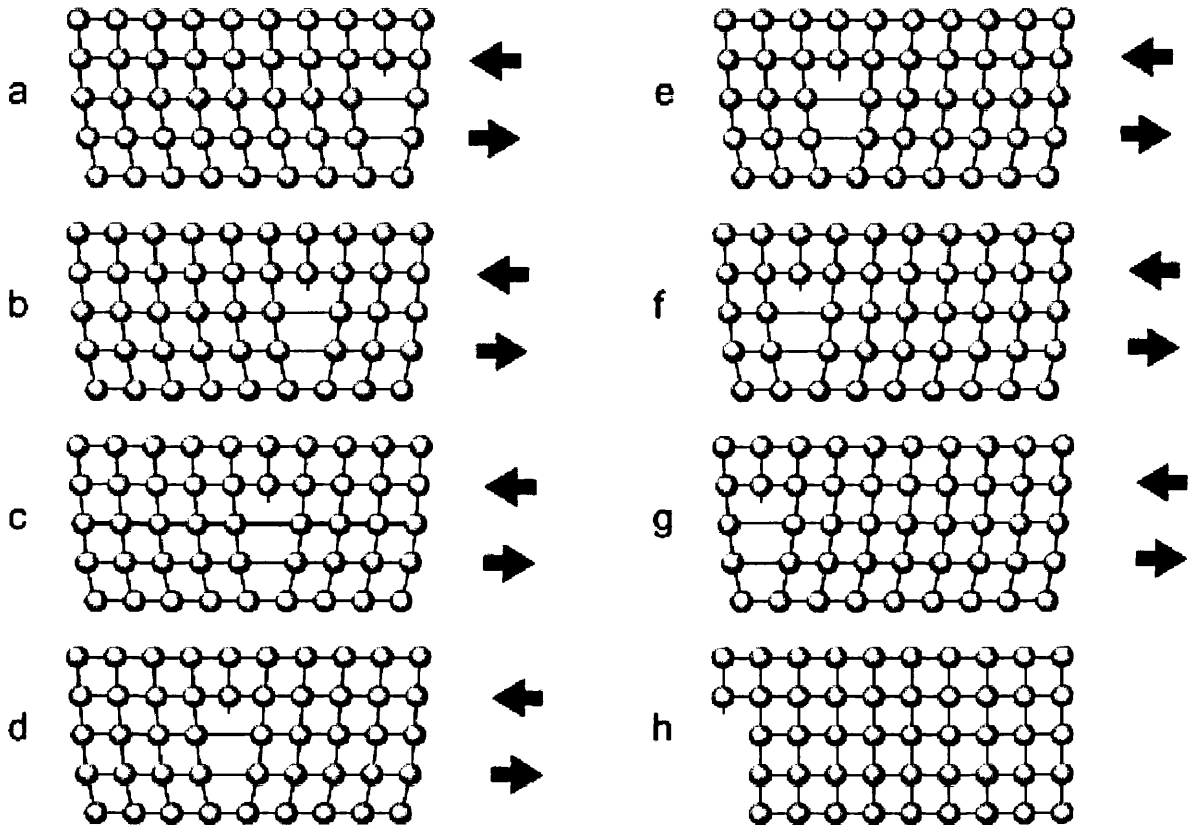

Figure 2.4: Schematic of dislocation movement by slip in a crystal

2.3 Grain Boundaries

There are three main types of interfaces. Depending on the location of the interface being embedded in a bulk material on both sides, one side, or not at all, interfaces can be categorized as bulk, semi-bulk, or thin film respectively [9]. An interface with the same material on either side is referred to as a grain boundary. As previously mentioned, grain boundaries are a topic of major research due to their effect on the overall material properties. The length of grain boundaries present in a material affects the strength and toughness by the well known Hall-Petch effect.

This section aims to provide a review of the theory of grain boundaries in polycrystals. A grain boundary is a type of interface, defined as the region between two grains of differing orientation. Grain boundaries have been a subject of much research due to the beneficial properties shown by certain boundary types. Certain boundaries have been shown to have low energy and free volume, as well as improved solute segregation, diffusion, mobility, sliding, fracture, cavitation, hardening, resistivity, and corrosion properties [10]. In order to describe grain boundaries, five degrees of freedom are required. Systems of grain boundary description and the five degrees of freedom are detailed in Section 2.3.1.

Certain grain boundaries have been found to possess special properties, such as corrosion and cracking resistance. Studies have shown a correlation between boundaries possessing these special properties, and a geometric relationship based on the misorientation of the two grains, termed the coincidence-site lattice. The CSL classifies boundaries based on the reciprocal density of coinciding lattice points, termed the Σ number, between two grain orientations, shown in Section 2.3.2. Some low-Σ CSL boundaries have been associated with special properties. However, not all boundaries categorized to be special using the CSL model have special properties. The CSL model defines the lattice coincidence of two grain orientations, however the boundary plane orientation is not defined by the CSL model and hence the actual boundary coincidence is not defined. The role of the grain boundary plane and its importance is shown in Section 2.3.3.

FCC materials readily form $\Sigma 3$ boundaries, and are of particular importance due to their low energy and beneficial properties. The formation of $\Sigma 3$ boundaries is a subject of much research and is shown in Section 2.3.4. Thermomechanical

treatments can influence the grain boundary character of a polycrystal by promoting the formation of $\Sigma 3$ boundaries and multiple twinning by $\Sigma 3^n$ boundary interactions. This practice is known as grain boundary engineering and further methods are found in Section 2.3.5.

2.3.1 Grain Boundary Description

A grain boundary is the interface region of two grains of differing orientations. The geometry of the boundary requires eight degrees of freedom for a full description; five macroscopic and three translational (microscopic). Many grain boundaries in real materials are not planar and are observed to be curved. Three of the macroscopic degrees of freedom fully characterize the orientation between the two grains, while the remaining two characterize the boundary plane [9]. The interface-plane scheme of boundary description uses two degrees of freedom each to describe the normal of each boundary surface. A disorientation angle about the common normal of the two planes provides the fifth degree of macroscopic freedom.

The common normal of the two planes provides a sub section of boundaries; twist, tilt, and general. Pure tilt boundaries have a rotation axis parallel to the boundary plane, while pure twist boundaries have a rotation axis perpendicular to the boundary plane, and a general boundary has both tilt and twist components.

Two types of tilt boundaries also exist; symmetrical and asymmetrical. If the two boundary surface normals, n_1 and n_2, are equal and the rotation angle >0, then the boundary is of pure twist character, as shown in Fig. 2.5. For tilt boundaries, if the tilt axis is plane on either side of the boundary is from the same family it is termed a symmetrical tilt boundary, and if the planes are different it is an asymmetrical tilt boundary. A schematic of a pure twist boundary described using the interface-plane scheme is shown in Fig. 2.5.

Another grain boundary description method disregards the orientation of the boundary plane and instead describes the three degrees of freedom of the geometric relationship of orientations of neighbouring grains. This method is the misorientation scheme.

In the misorientation scheme, the relative rotation between two lattice orientations is described by an angle of rotation about an axis, UVW, common to both

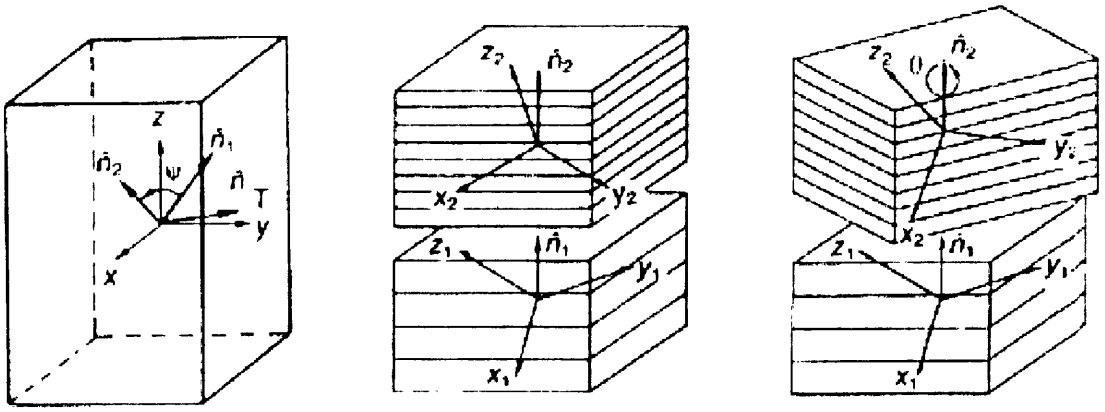

Figure 2.5: Schematic of a twist type boundary using the interface plane scheme for boundary description [9]

lattices. These are often termed the angle/axis pair [11], and is shown in Fig. 2.6

Due to crystal symmetry operations, there may be many equivalent angle/axis pairs which describe the same relative rotation; however, by convention, the pair which provides the smallest rotation, or misorientation angle, is used [12].

Small misorientations found in a real material may not necessarily be grain boundaries, but instead low angle boundaries. Low angle boundaries are not the interfaces of separate grains, but instead are internal boundaries within a grain. Dislocations configured in a low energy stable uniform array may create internal divisions inside a grain which are represented by these low misorientation angles [8], shown in Fig. 2.7.

Fig. 2.7 shows and random arrangement of dislocations moving by glide and climb to a lower energy arrangement of a symmetrical tilt boundary. Since glide and climb of the dislocations is involved, the process of low angle boundary formation is therefore a thermally activated process. The reduction in energy of the tilt boundary formation of the dislocations is accomplished by the reduction of a long range stress field. The strain, instead of being distributed into a curve throughout the material, is localized around the dislocations.

The misorientation scheme's angle/axis pairs are helpful for description of commonly found boundaries. However, for mathematical calculations a misorientation matrix may be more efficient. A misorientation matrix is essentially a transformation matrix multiplied by one grain's orientation matrix in order to produce the

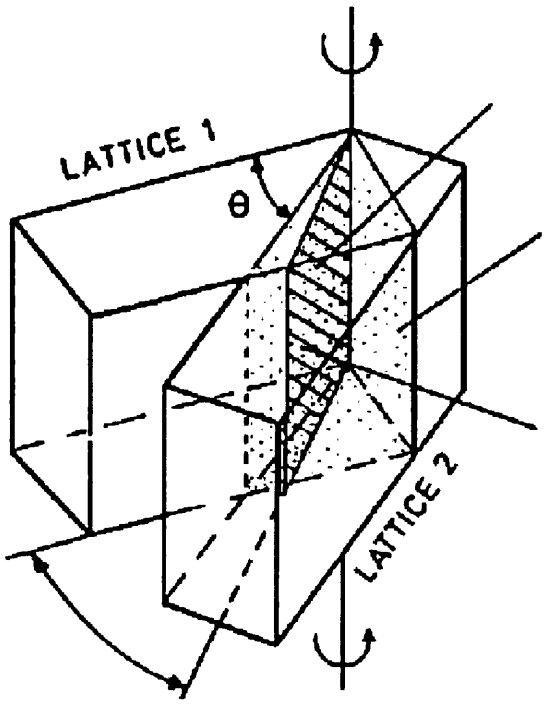

Figure 2.6: Misorientation angle, θ, between lattice 1 and lattice 2 [11]

desired end orientation. It can be calculated as follows:

$$M_{12} = g_1^{-1} g_2 \tag{2.1}$$

where g_1 and g_2 are orientation matrices consisting of the direction cosines of grain 1 and grain 2, respectively, from a reference orientation, and M_{12} is the misorientation matrix [13][14].

The most common representation of misorientation data is using the angle of rotation on its own. It is only one of three macroscopic variables representing the orientation relationship at a grain boundary, however in some cases it is a suitable approximation [15].

The five macroscopic degrees of freedom of an interface have previously been described. The remaining three microscopic (or translational) degrees of freedom involve rigid body translations parallel and perpendicular to the interface plane. The microscopic degrees of freedom account for volume expansion at the interface and hence are related to the free energy. The difficulty of measuring the

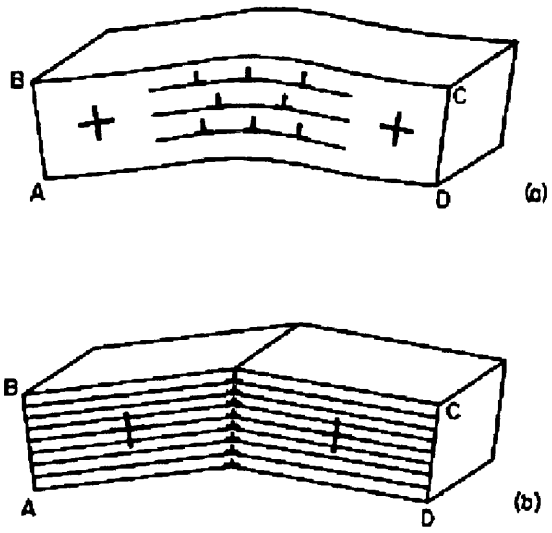

Figure 2.7: (a) A random array of dislocations with the net effect of creating a curved lattice and (b) dislocation alignment by slip and climb into a low angle symmetrical tilt boundary [8]

microscopic degrees of freedom means that they are neglected in studies of grain boundary interfaces.

A coherent interface is one with corresponding atom planes and lines continuous across the interface. If this long-range order is not present, and one to one atom matching is not present locally, then the interface is referred to as incoherent. A semi-coherent interface may be created where one to one atom matching, as well as continuity of lattice planes and lines is maintained only locally at the interface by elastic and plastic strains. Dislocations and elastic strain will combine to create short range order at the interface of an otherwise incoherent boundary.

Commensurability is a further measure of this order. An interface is commensurate if a periodic unit cell can be defined for the system. Coherent boundaries are by definition also commensurate, however semi-coherent and incoherent boundaries may be commensurate or incommensurate. The commensurability of semi-coherent boundaries depends on the periodic nature of the dislocations and elastic strains at the interface [9].

2.3.2 Coincidence Site Lattice Model

The idea of lattice coincidence was first proposed in 1949 [16]. Since then the CSL model has become the standard boundary classification model. This is due to its ease of calculation and data acquisition using modern automated EBSD set ups.

The CSL model is a geometrical relation describing the lattice coincidence of two independent crystal orientations. A sigma number is assigned to classify boundaries based on the reciprocal number of coinciding lattice points. For example, a $\Sigma 7$ boundary will have 1 in 7 lattice points coinciding. An example of a $\Sigma 7$ superlattice can be seen in an FCC bicrystal with a misorientation of 38° about a 111 axis, or -22° about the same axis however rotated in the opposite direction, shown in Fig. 2.8.

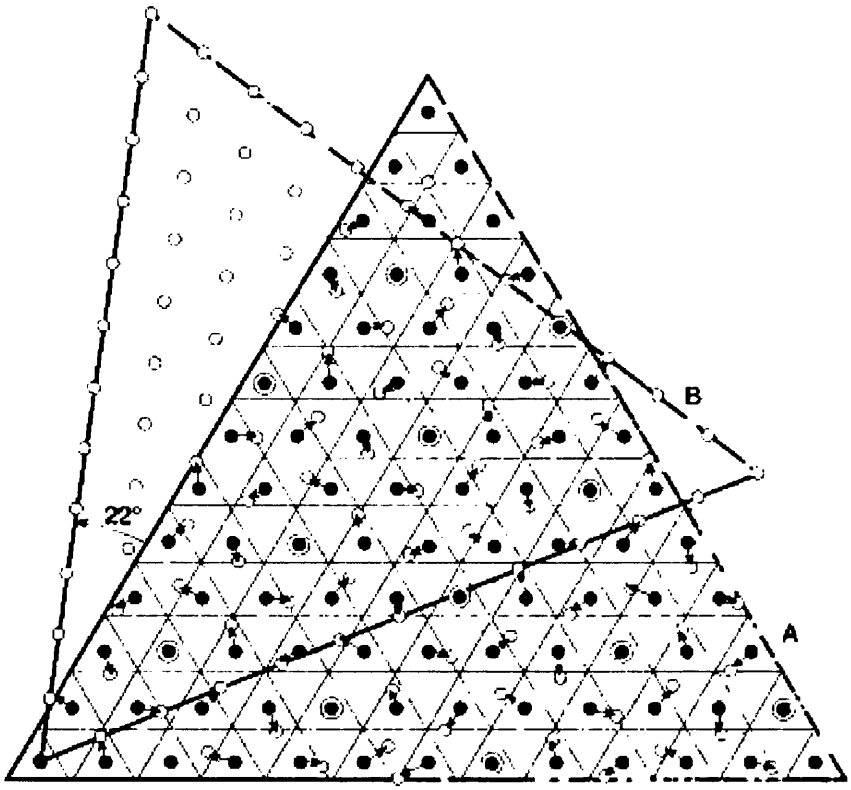

Figure 2.8: Two FCC 111 planes related by -22° or 38°. 1 in 7 atom points coincide.

The Σ value of the CSL can be generated from the axis and angle of misorien-

tation;

$$\Sigma = x^2 + Ny^2 \tag{2.2}$$

where x and y are integers, and

$$N = U^2 + V^2 + W^2 \tag{2.3}$$

from the axis of rotation [13][14]. The relation to the misorientation angle is then given by;

$$\theta = 2\tan^{-1}\frac{y}{x}\sqrt{N} \tag{2.4}$$

The actual grain boundary plane is a plane through this CSL. The best fit planes will be those oriented with the highest density of coinciding lattice points. Deviations from this best fit plane orientation result in a stepped structure at the boundary, which are believed to be dislocation arrays accommodated at the boundary [17]. These dislocation arrays manifest as a deviation in misorientation from the exact CSL, as such a criterion for the allowed deviation from exact CSL is used for Σ designation. The most commonly quoted is the Brandon criterion [18] given as;

$$\delta\sigma \leq \frac{v_o}{\Sigma^{1/2}} \tag{2.5}$$

where v_o is the proportionality constant based on the angular lower limit for grain boundaries, usually quoted at 15°. More restrictive criterions have been proposed due to the designation of CSL boundaries using the Brandon criterion which do not exhibit special properties. Another criterion proposed by Palumbo-Aust based is given as [19];

$$\delta\sigma \leq \frac{v_o}{\Sigma^{5/6}} \tag{2.6}$$

This criterion has been shown to be more adequate for predicting low-Σ special boundaries resistant to sensitization and intergranular corrosion in Alloy 800 [20].

Interest in the CSL model was mainly due to its link with CSL boundaries hav-

ing special advantageous properties (resistance to intergranular corrosion cracking, segregation, and precipitation) compared to random non-CSL boundaries [15]. A study on Pb with low concentrations of Sn showed that non-CSL boundaries became pinned or had reduced migration due to the Sn addition, while low Σ boundaries were relatively unaffected [21]. This was believed to be due to a lower free volume at the CSL boundaries corresponding to a better fit boundary. In this same respect, low-Σ boundaries in a study on 304 Stainless Steel were found to have lower energy than random boundaries and were less susceptible to intergranular corrosion [22].

Grain boundary energies have been studied as a function of misorientation angle in samples of Au and Al [23]. The correlation between interfacial energy and misorientation angle for [110] tilt boundaries is shown in Fig. 2.9.

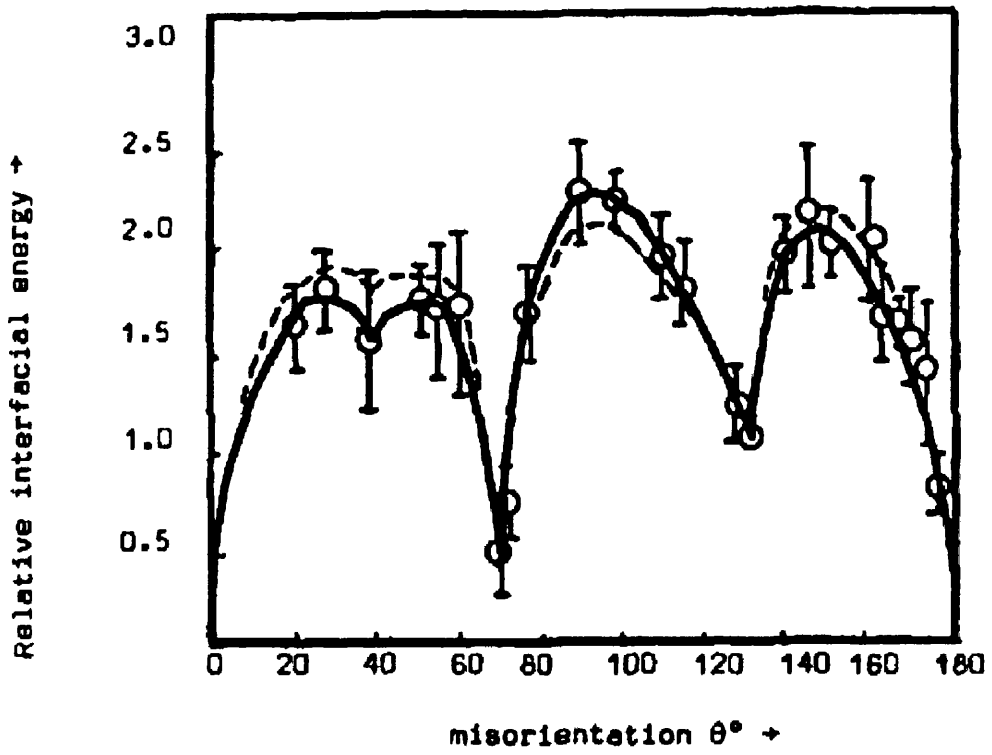

Figure 2.9: Relative interfacial energy vs misorientation angle of [110] tilt boundaries in aluminum [23]

The deep energy cusps correspond to the (111) and (311) $\Sigma 3$ boundaries re-

spectively. The Σ3 boundary is of particular importance in FCC materials due to in twin relation which will be explained in the next section.

Recent studies on the free volume and energy of CSL boundaries in FCC materials have shown the basis for some CSL boundary special properties, but have also highlighted the shortcomings of the CSL model in classifying special boundaries.

A study on grain boundary energy by Olmsted et al., however, has shown the deficiencies of the CSL model. The grain boundary energies of Ni and Al samples were collected using embedded-atom interatomic potentials, and compared to parameters such as disorientation angle, Σ number, and excess free volume [24]. The results are shown in Fig. 2.10.

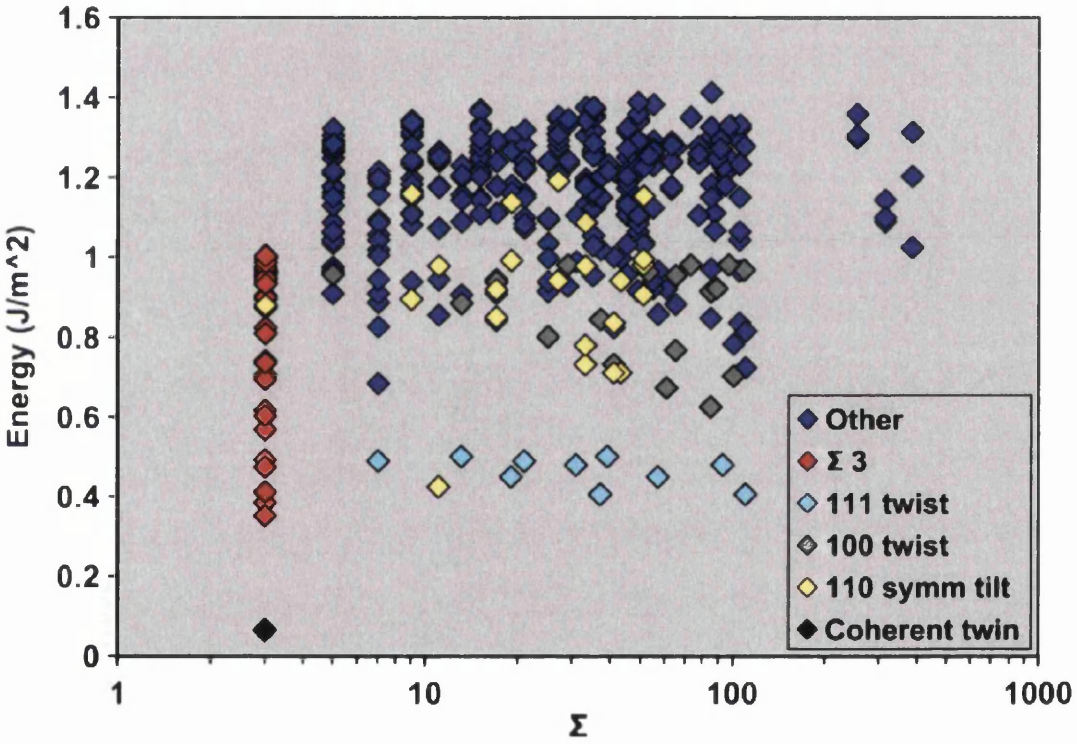

Figure 2.10: Grain boundary energy as a function of Σ number in Ni [24].

Coherent Σ3 boundaries were found to have the lowest energy of the boundaries measured. However, incoherent Σ3 boundaries, or Σ3s which do not lie on the 111 boundary plane, were found to have variable energy. These results were similar to the excess free volume measurements shown in Fig. 2.11.

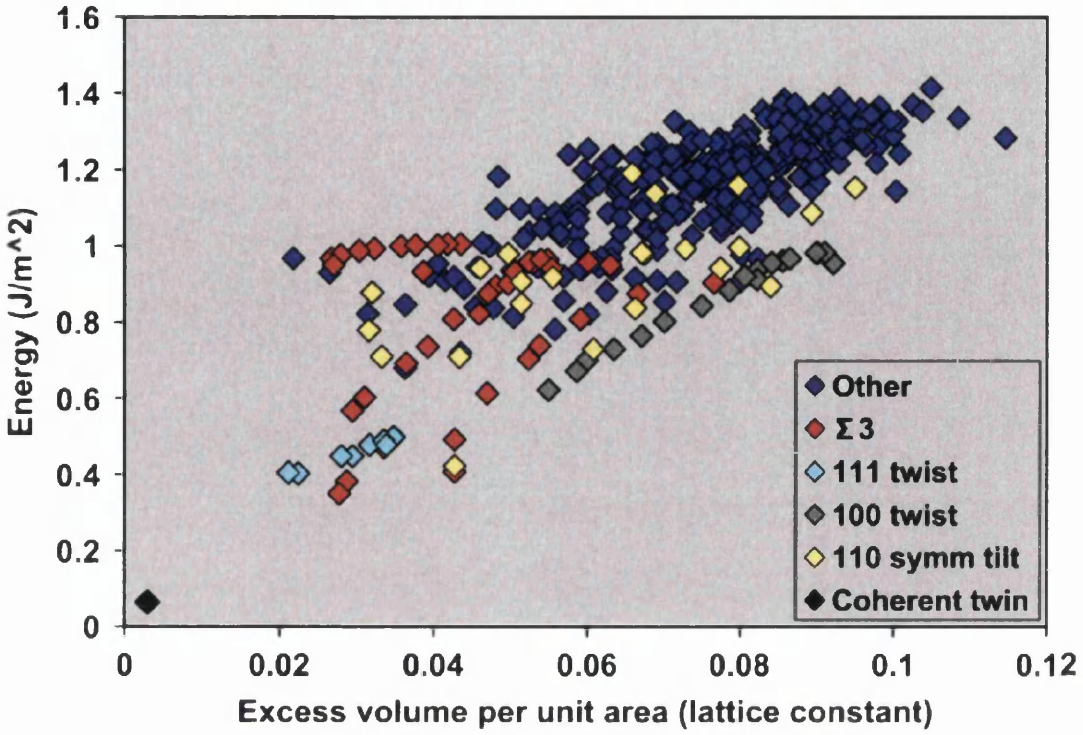

Figure 2.11: Grain boundary energy as a function of free volume in Ni [24]

Again, coherent Σ3 boundaries were found to have the lowest excess free volume and energy, but the free volume of incoherent Σ3 boundaries was variable and in some cases higher than random boundaries. Similar studies have been also been reported [25][26][27][28][29][30].

The variability of excess free volume and energy measurements of Σ3 boundaries in Fig.2.10 shows the shortcoming of the CSL model in predicting boundaries with special properties. The CSL model is merely a geometric model based on the orientations of neighbouring grains and does not consider the boundary plane. The boundary plane has been shown to be very important to predicting special property behaviour of boundaries. Early papers concerning the CSL model themselves stressed the importance of the boundary plane occupying a position which minimizes the free energy as well as the importance of boundary coincidence instead of lattice coincidence. However, due to the simplicity in experimental data acquisition, the CSL model is still useful as a preliminary characterization tool

[15].

The CSL model also applies at triple junctions. A triple junction is a line where three grains and three distinct boundary sections meet. A lattice of common sites can be formed not only for a system of two crystals, but also for three or possibly multiple crystals. Given three separate crystal orientations meeting in a triple junction, it follows that there are three rotation matrices giving the relation between the three crystal orientations one after the other.

$$R_3 = R_1 R_2^{-1} \tag{2.7}$$

In this respect, if two of the above rotations are CSLs, it follows that the third rotation must be a CSL [31]. This relation is shown as;

$$\Sigma_{3^n} = \frac{\Sigma_1 \Sigma_2}{\alpha} \tag{2.8}$$

where α is the greatest common divisor of the components of the integer matrix $(\Sigma_1 R_1 * \Sigma_2 R_2)$ [32][33]. A superlattice of the three separate crystal orientations meeting at the triple junction could then be defined in terms of a CSL.

$$\Sigma_{TJ} = \frac{\Sigma_1 \Sigma_2 \Sigma_3}{2} \tag{2.9}$$

where Σ_{TJ} is the Σ number of the triple junction. Special cases of CSLs at triple junctions involve heavily twinned materials. An annealing twin has a $\Sigma 3$ misorientation and a 111 grain boundary plane, also known as a coherent twin. An incoherent twin is a boundary with a $\Sigma 3$ misorientation but not lying on the 111 plane, but instead typically on the 112 family of planes. While coherent $\Sigma 3$s have a low free volume, incoherent $\Sigma 3$s may have tilt or twist type on rational or irrational planes. $\Sigma 3$ boundaries interact with each other at triple junctions, leading to multiple twinning.

These $\Sigma 3$ interactions are governed by the following equations;

$$\begin{aligned} \Sigma_A + \Sigma_B &\rightarrow \Sigma_{A \times B} \textbf{ or} \\ \Sigma_A + \Sigma_B &\rightarrow \Sigma_{\frac{A}{B}} \end{aligned} \tag{2.10}$$

where A/B is an integer and $A > B$ in the second relationship. For example, a $\Sigma 3$ and a $\Sigma 9$ meeting at a triple junction may result in either of the following interactions [34].

$$\begin{aligned} \Sigma 3 + \Sigma 9 &\rightarrow \Sigma 27 \textbf{ or} \\ \Sigma 3 + \Sigma 9 &\rightarrow \Sigma 3 \end{aligned} \tag{2.11}$$

Multiple twinning like this is a major contributor to high populations of $\Sigma 3$ boundaries in grain boundary engineered materials.

2.3.3 Grain Boundary Plane

The role of the grain boundary plane is important in determining the special properties of boundaries. The CSL model is helpful due to its simplicity in calculation, however it is not able to accurately predict boundaries with special properties, which mainly rely of the excess free volume and free energy of the boundary. These parameters are determined by the orientation of the boundary plane in conjunction with the CSL geometry [35].

The interface-plane scheme is an adequate method for describing CSL boundaries based on tilt or twist character, which are thought to have lower excess free volume and free energy than random high angle boundaries. There are four main classes of these boundaries:

Symmetrical tilt boundaries -

$$\begin{aligned} \phi &= 0 \\ \{h_1 k_1 l_1\} &= \{h_2 k_2 l_2\} \end{aligned} \tag{2.12}$$

The tilt axis is parallel to the axis of misorientation. A symmetrical tilt boundary has planes of the same family on either side of the interface. The twist angle, Φ=0.

Asymmetrical tilt boundaries -

$$\begin{aligned} \phi &= 0 \\ \{h_1 k_1 l_1\} &\neq \{h_2 k_2 l_2\} \end{aligned} \tag{2.13}$$

The tilt axis is parallel to the misorientation axis, but the twist angle Φ=0. The family of planes on either side of the interface is different but commensurate, such that $(h_{12} + k_{12} + l_{12})/(h_{22} + k_{22} + l_{22})$ is an integer.

Twist boundaries -

$$\begin{aligned} \phi &\neq 0 \\ \{h_1 k_1 l_1\} &= \{h_2 k_2 l_2\} \end{aligned} \tag{2.14}$$

Identical planes on either side of the interface are rotated by a non-zero twist angle, Φ.

General boundaries -

$$\begin{aligned} \phi &\neq 0 \\ \{h_1 k_1 l_1\} &\neq \{h_2 k_2 l_2\} \end{aligned} \tag{2.15}$$

Have both tilt and twist character. These are random high angle boundaries, however some may be classified as CSLs [9][35] depending on lattice coincidence shown in Section 2.3.2.

Analysis of the interfacial geometry of a boundary, and hence an ability to predict its physical properties, requires determination of all five macroscopic degrees of freedom. If the material is a polycrystal, two methods of grain boundary plane determination may be used.

Direct measurement of the grain boundary plane can be accomplished by serial sectioning of the material. The three available degrees of freedom of the misorientation are initially measured, as well as the initial boundary plane inclination, or the fourth degree of freedom. The fifth degree of freedom is measured by a destructive process of removing layers of the material, typically by FIB, until the

boundary plane tilt is measured as a difference between the initial boundary position and the position after milling [36].

A stereological method may also be employed. After the grain boundary character distribution is measured, the grain boundaries connecting two triple junctions are joined by line segments, essentially breaking each boundary into planar segments. The direction of the trace determines the fourth degree of freedom. After a sufficient data set has been collected, the probability of certain boundary planes appearing in the material can be ascertained, and is given as a multiple of a random distribution [37][38]. This method has been used to determine the five-parameter grain boundary distributions, and how grain boundary engineering regimes affect the grain boundary planes.

A study using this technique by Rohrer et al. using alpha-brass found that there was a high tendency for boundaries to terminate on $\{111\}$ planes, even when $\Sigma 3$ boundaries are removed from the distribution, suggesting that special boundaries terminate on low index planes [39]. Another study by Randle et al. using Nickel and Copper also found a preference for low planes which were asymmetrical tilts near at least one low-index plane, after thermo mechanical processing [40].

2.3.4 Twinning

A twin is a special boundary with CSL designation $\Sigma 3$. It is formed by deformation or annealing. Low stacking fault energy FCC materials readily form annealing twins and can have large twinned grain boundary populations. A twin boundary refers to interfaces with adjacent crystals being mirror images of each other, as show in Fig. 2.12.

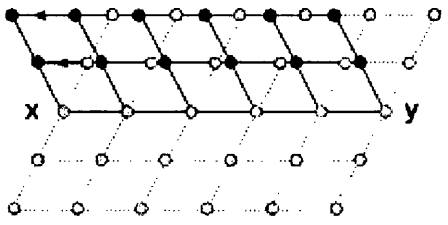

Figure 2.12: Arrangement of atoms at a twin interface represented by dark spheres [8]

The open circles represent the position of atoms in the original crystal, while the black circles represent the atom positions of a twinned boundary. In FCC materials, this formation often occurs as stacking faults on 111 closed packed planes. A stacking fault refers to a miss-ordering of planes in a crystal, typically the 111 family of planes in FCC as shown in Fig. 2.13.

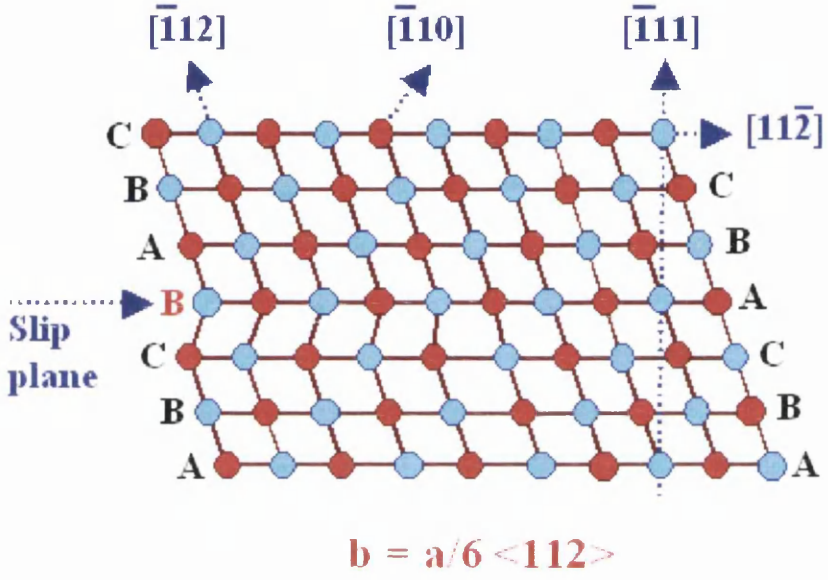

Figure 2.13: Schematic of a partial dislocation resulting in a stacking fault in an FCC crystal

The 111 planes of an FCC crystal are shown in Fig. 2.13. The order of these planes repeats (ABCABCABC) as the crystal extends, however if the order changes (ABCBCABCA), a stacking fault is created. Physically, when a stacking fault ends inside a crystal, this defect separating the faulted region from the non-faulted region is a Shockley partial dislocation. A diagram representing this case is also shown in Fig. 2.13.

The plane of the diagram is the (10-1) plane. Blue circles are positions of atoms in the (10-1) plane of the paper, while the red circles are atoms in the (10-1) planes immediately above and below the paper. The (111) planes are at 90° to this diagram. The right of the diagram represents a perfect crystal where the order of the (111) planes can be seen, while the left contains a partial dislocation along

[1-21] changing the order of the (111) planes. In this case, the Burgers vector is;

$$b = \frac{a}{6}[1\bar{2}1] \tag{2.16}$$

The magnitude of the Burgers vector is less than that for an edge or screw dislocation, and hence this defect type is termed a partial dislocation [8].

The stacking fault energy of the material is known to have a large effect on the population of twins in the grain boundary network. Low to medium stacking fault energy materials, such as copper or nickel, twin readily while higher stacking fault energy materials, such as aluminum, are not observed to have high twin populations [11].

Twins are frequently found in FCC metals after deformation and annealing. Deformation and annealing twins are physically identical, however the mechanism of formation for each these twin types are different. Deformation twins are formed by the glide of Shockley partials during deformation. The formation of annealing twins has been the subject of much interest. Annealing twins formed during annealing may take on four main morphologies shown in Fig. 2.14.

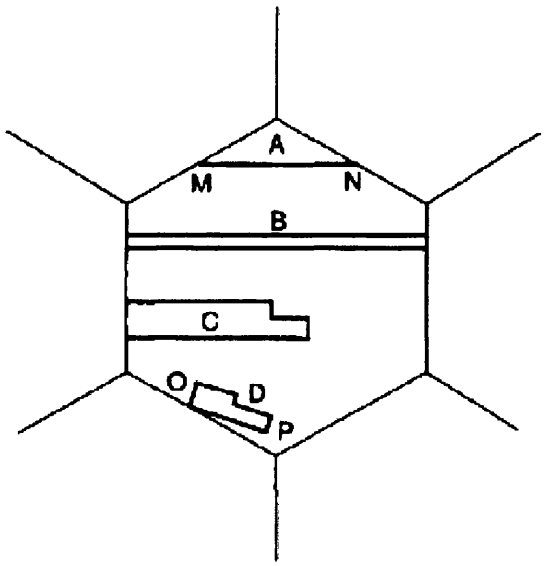

Figure 2.14: Four main annealing twin morphologies [41]

Twin A is a corner twin, producing the boundary trace MN in the parent grain.

Twin B is an example of a thin twin spanning the width of the parent grain. Twin C is an example of a twin starting at the edge and terminating within the parent grain. Finally, twin D producing trace OP is inclined towards a grain boundary [41]. However, these morphologies represent twin boundaries in a two-dimensional view and their structure in the material normal to sample surface is not determined. When looking in the sample normal direction, a twin such as B may not span the grain length and appear with jogs such as twin C. Recrystallized structures also form clusters of $\Sigma 3^n$ related regions. Outer boundaries of the cluster are all random high angle boundaries, while inner boundaries are $\Sigma 3^n$ related. These are complex $\Sigma 3^n$ related structures and not simply grains with interior twins. They are formed by a number of twinning events of ultimately a single orientation [33].

The models for the mechanisms of formation of annealing twins can be classified into two main types; energy based models with the nucleation of twins by stacking faults or fault packets, and kinetic models which require growth accidents during boundary migration.

An early twinning model by Fullman and Fisher in 1951 proposed that annealing twins form during grain growth when the free energy between a grains neighbours and its twin would be less than that of the grain itself. The twin boundary would then continue to extend as a twin of the original crystal [42]. However, this model lacks mechanistic details and it would be hard to explain the presence of twin types C and D from the previous figure.

The early stages of annealing twin formation were then initially observed by Dash and Brown in 1963 [43]. Their work showed that twins consisted of stacking fault packets with a complicated morphology. This work was then expanded by Myers and Murr in 1978 using similar techniques. Their work resulted in the pop out model of annealing twin formation. Stacking faults were proposed to pop out at grain boundary ledges, with the noncoherent portion would then grow into the grain [44].

Models involving the migration of the high angle boundary were then created to explain the formation of twins during grain boundary migration. Gindraux and Form showed that annealing twin formation required the movement of newly formed boundaries, and that already existing boundaries in a deformed matrix did not move to allow twin formation [45]. Also, annealing twins formed during

recrystallization of a deformed matrix, the driving force for recrystallization of such is the dislocation energy of the cold-worked state. It follows that twin boundaries must reduce the total energy of the new system. An energy balance was presented by Gindraux and Form as follows;

$$\Delta E_{rec} = \Delta E_{el} + (\Delta E_{gb})_o + (\Delta E_{tb})_o - (\Delta E_{gb})_n - (\Delta E_{tb})_n \qquad (2.17)$$

where ΔE_{rec} is recrystallization energy, ΔE_{el} is the stored elastic energy, ΔE_{gb} is the grain boundary energy, and ΔE_{tb} is the twin boundary energy.

Growth accident models based on the formation of annealing twins during boundary migration followed this work, the first of which was by Gleiter et al., who considered twins to be the results of growth accidents leading to stacking faults [46]. One such model is that proposed by Mahajan et al. This model proposes that Shockley partial dislocation loops nucleate on 111 steps of a migrating curved boundary [41]. This model assumes that a curved boundary may contain facets on 111 planes. At high boundary migration rates, and in turn high driving forces for boundary migration, growth accidents may cause stacking faults on these 111 facets. If stacking faults continue to form during the migration of this boundary step, a twin boundary can be formed.

The factors determining twinning frequency during grain growth are [47]:

1. Grain size
2. Temperature and time of annealing
3. Velocity of grain boundary migration
4. Grain boundary energy
5. Stacking fault energy of the material

Pande et al. found that the formation of twins is caused by boundary migration, and their density is proportional to the driving force for boundary migration (the driving force for boundary migration being related to the above criteria)[48]. This has been shown experimentally by small additions of boron in samples of nickel. Boron poisons grain boundaries in nickel, pinning them in place and stunting

boundary migration. Recrystallized samples of nickel containing boron are found to have considerably less twin density than pure samples [41][47].

In contrast to this, twin formation at very low driving forces for boundary migration were studied by Field et al., who used in situ heating during EBSD to observe twin formation. Varying temperatures for recrystallization were used to vary the driving force for boundary migration. Low driving forces for boundary migrations were associated with low temperature anneals creating lower boundary migration velocities and longer times to full recrystallization. An inverse relationship was found between twin density and the driving force for boundary migration at low temperature regions. This was thought to be because the annealing twins played a part in the recrystallization kinetics. When grain growth appeared to become stagnant, annealing twin formation allowed grain growth to continue [49].

At high boundary migration rates, growth accidents seem to result in twinning formation. However, as shown by Field et al., at low boundary migration rates twinning may be an energetic necessity to allow grain growth to continue. It is conceivable that a plot of boundary velocity vs twin density would result in a negative slope for very low boundary velocities up to a critical value where growth accidents may occur, resulting in a positive slope where twin density is proportional to the boundary velocity.

The nature of the force causing deformation before annealing and subsequent recrystallization may also have an effect on twin formation. Shear stresses tend to promote twin formation, but do not determine the twin variant formed. Recrystallized samples of copper deformed with high shear stresses tend to form more twin boundaries than samples deformed without an imposed shear force [50]. However, the sheer force and the Schmid factor of the parent grain may not determine the twin variant formed. In a study of twin formation in a copper tricrystal, the selection of the twin plane was found to be dependent on the direction of the boundary migration and the geometry of the grain boundaries. The twin variant with plane normal closest to the direction of boundary migration would be the variant which would form, regardless of the slip plane activity or the Schmid factors of the parent grain [51].

2.3.5 Grain Boundary Engineering

Grain boundary engineering refers to grain boundary design and control using thermo-mechanical processes to promote the formation of favourable boundaries and improve bulk properties, such as intergranular fracture and degradation [52]. Initially, successes were attributed to the formation of low Σ CSL boundaries. Fig. 2.15 shows an inverse linear relationship between low sigma boundary fraction, nearly all of which measured were $\Sigma 3^n$ and the corrosion rate in high performance nickel-based alloys [34].

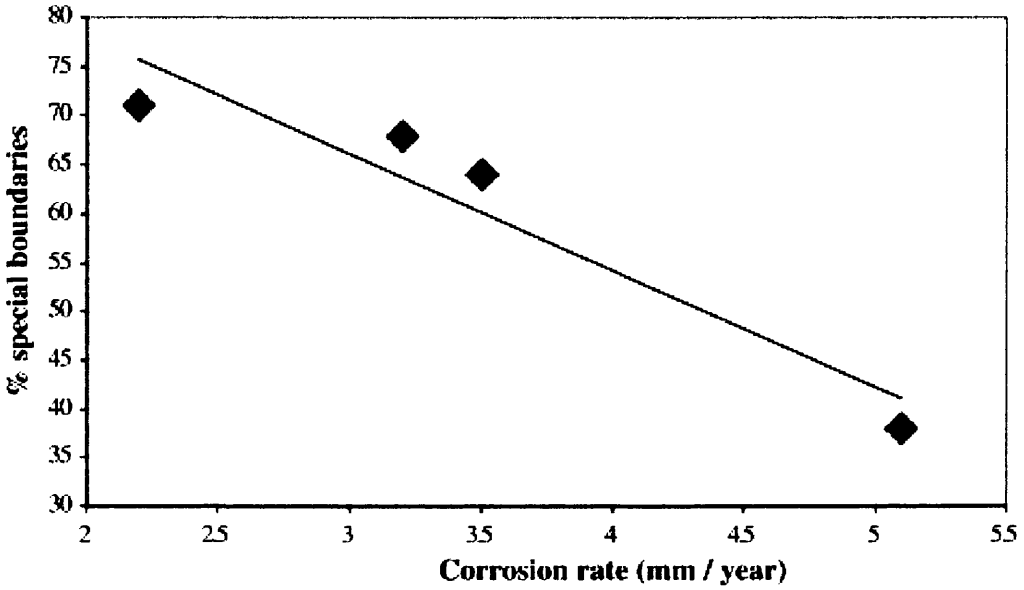

Figure 2.15: Proportion of special boundaries ($\Sigma \leq 29$) in high performance nickel based alloy as a function of corrosion rate [34] adapted from [53]

In early studies of grain boundary engineering, any low Σ boundary was considered to be a special boundary. However, not all low Σ boundaries have special properties, and even certain Σ which usually have special properties have properties dependent on the grain boundary plane [15]. Grain boundary engineering is found in practice to be restricted to low stacking fault FCC materials which readily form $\Sigma 3$ boundaries. The formation of $\Sigma 3$ boundaries and $\Sigma 3^n$ boundaries through multiple twinning are critical to the bulk property improvements found in grain boundary engineering. The formation of coherent twin boundaries does not

imply bulk property improvements since they are not incorporated into the grain boundary network and are instead contained within a parent grain. Their effect on bulk properties is instead indirect, by interacting with mobile $\Sigma 3$ boundaries to incorporate more of these boundaries into the microstructure [7].

Multiple twinning refers to interactions between mobile and immobile $\Sigma 3$ and $\Sigma 3^n$ boundaries at triple junctions to form additional $\Sigma 3$ boundaries. Coherent $\Sigma 3$ boundaries lie on 111 planes and are immobile, while incoherent $\Sigma 3$ boundaries lie on 112 or other low index tilt or twist planes. Coherent $\Sigma 3$ boundaries have particularly low free volume and boundary energy, while incoherent $\Sigma 3$ boundaries have a higher free volume at the boundary interface, but still generally lower than random high angle boundaries hence both should have special properties. Coherent $\Sigma 3$ boundaries are immobile, while incoherent $\Sigma 3$ boundaries have a high boundary migration rate and are immune to boundary pinning by additions at the boundary. Incoherent $\Sigma 3$ may meet coherent $\Sigma 3$s or other incoherent $\Sigma 3$ boundaries during boundary migration. The interaction is governed by the rules of CSL boundary interactions called the $\Sigma 3$ regeneration mechanism, leading to multiple twinning [54]. Multiple twinning leads to a theoretically twin-limited microstructure, with a grain boundary character distribution composed entirely of special boundaries and hence is resistant to intergranular corrosion and degradation.

There are two methodologies of grain boundary engineering; strain annealing and strain recrystallization.

2.3.5.1 Strain Annealing

Strain annealing grain boundary engineering processes involve low levels of strain followed by a long term anneal [34]. Low levels of strain, typically 5-10%, are used and a low temperature annealing which is low enough to prevent the re-crystallization of the microstructure for times from one to several hours. This is to provide sufficient driving force for formation of new low Σ boundaries without complete recrystallization of the microstructure. The mechanism of special boundary formation in strain annealing processes lies in the deformation. The induced strain causes grains to subdivide and form random high angle boundaries. As a result, initially after deformation the special boundary fraction is reduced due to

the added random high angle boundaries [55]. Upon annealing, the deformation provides the driving force for the formation of special boundaries from the random high angle boundaries. Dislocations formed during strain are annealed out by climb and boundary migration [56]. For this reason, the amount of deformation and the annealing temperature are of critical importance. Too much deformation or an annealing temperature which is too high will cause complete recrystallization of the microstructure instead of the relief of the stress by low energy boundary formation.

The deviation from exact CSL misorientation is also seen to reduce in $\Sigma 3^n$ boundaries after strain annealing. This fine tuning is not observed in CSL boundaries other than $\Sigma 3^n$ boundaries [57].

Strain annealing investigations on copper and nickel using 6-7% strain and anneal treatments of 0.38-0.4Tm for 6-14 hours found that the special boundary fraction increased to above 0.8 for most samples [58][59]. Single step processes on nickel involving 6% strain, annealed for 10 minutes at 900°C increases in special boundary fractions from 36.5% to 74.7% [55]. While the special boundary fraction increased, detrimental grain size increases also occurred. Grain size control can be a problem with strain annealing processes. Additionally, the energy and time intensive multi-hour anneals are factors which can prevent strain annealing production processes.

2.3.5.2 Strain Recrystallization

Strain recrystallization processes differ from strain annealing by the amount of strain, annealing temperature and time, and the mechanism of special boundary formation. Typically, strain recrystallization processes involve higher strains ranging from 20-30%. The annealing temperature used is also higher than strain annealing, typically 0.6-0.8Tm but always high enough to cause recrystallization. The annealing time is on the order of minutes instead of hours as with strain annealing [34]. The number of iterations used also differs, with strain annealing usually involving less than 3 iterations and more for strain recrystallization.

The effect of each iteration on the grain boundary character distribution varies in strain recrystallization. The initial iterations may result in a reduction of CSL

fraction, as shown in Fig. 2.16 [34].

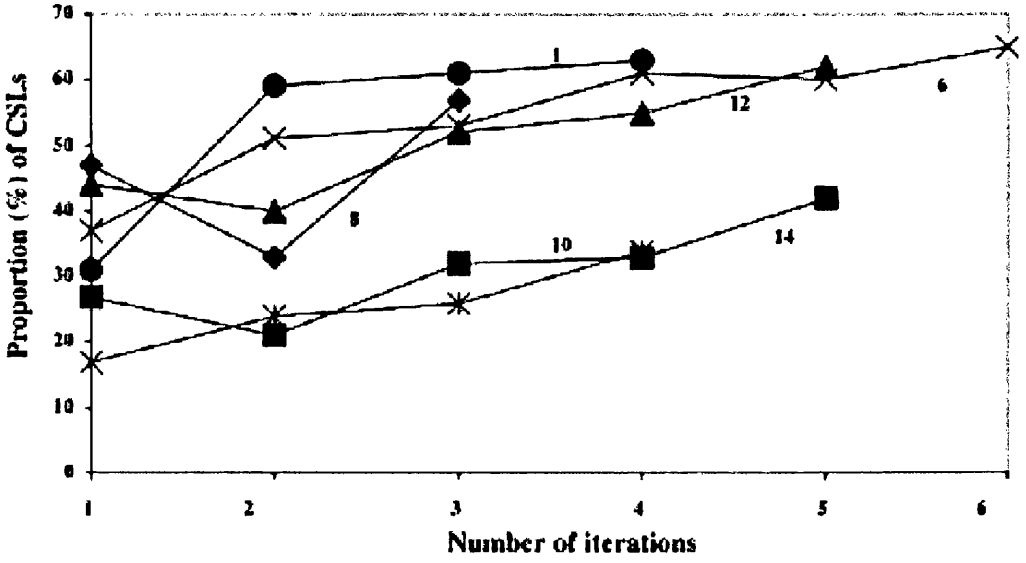

Figure 2.16: Proportion of CSL boundaries as a function of iteration number [34]

This erratic behaviour may be explained as a retained strain in the form of dislocation pile-ups at twin boundaries in the first strain iteration, increasing the driving force for recrystallization. Mobile boundaries then move through the microstructure, which may wipe out $\Sigma 3$ boundaries, depending on the initial microstructure, resulting in a drop in CSL boundaries. After the initially high build-ups of dislocations are relaxed, boundary migration velocities reduce to speeds which are more optimal for the formation of annealing twins [60].

A comparison of low strain and medium strain processing routes was undertaken in 2009. The microstructural parameters for low strain annealed samples was found to be more erratic than medium strain samples. More $\Sigma 9$ and $\Sigma 27$ boundaries were also found in the medium strain samples, although a higher percentage of $\Sigma 9$ boundaries lying on special planes were found in the low strain samples [61].

2.3.5.3 Effectiveness of Grain Boundary Engineering

The most commonly quoted statistic concerning the effectiveness of a grain boundary engineering method is the low Σ CSL boundary fraction, either by length or

by number. This does give a good indication of a materials resistance to intergranular corrosion and degradation, however special boundaries incorporated into the boundary network break up the connectedness of random boundaries, increasing resistance to intergranular cracking. As shown by Watanabe, cracks only propagate on random high angle boundaries and may be arrested at triple junctions containing two special boundaries [62]. Therefore, a measure of the break-up of the random boundary network may be more appropriate for the effectiveness of a grain boundary engineering method [34].

A higher proportion of low Σ CSL boundaries would imply a more broken up random boundary network, however not all low Σ CSL boundaries are incorporated into the boundary network [63]. $\Sigma 3$ twins may form on the interior of grains, and though they play an important role in multiple twinning, do not directly affect the grain boundary network connectivity. Therefore, special boundary fraction alone does not give a good indication of the effectiveness.

Statistics of triple junction character have been proposed to gauge effectiveness. A triple junction may be comprised of zero to three special boundaries. Triple junctions consisting of two special boundaries may arrest crack propagation, while triple junctions consisting of three boundaries indicate less random boundary population. Higher fractions of these types of triple junctions may indicate more effective grain boundary engineering [64][65][66]. However, the length scale of random boundary connectivity is not given by this method.

Random boundary percolation models give a length scale to the random boundary network. Percolation models categorize boundaries as either special or non-special. Connected boundaries of like-type are then grouped into clusters. Properties of these clusters can then be statistically calculated, such as cluster mass distribution, average radius of gyration, connectivity length and strength of the percolating cluster, which may give a better representation of the effectiveness of grain boundary engineering [65][67][68][69][70][71][72][73].

2.4 Geometrically Necessary Dislocations

The interaction of dislocations in a material is a very complicated system with a great effect on the bulk properties of the material. Dislocation slip may be trans-

ferred across grain boundaries or build up at the interface, thus grain boundary properties can also be affected by dislocation content. Some dislocation content, so called geometrically necessary dislocation content, can be recovered from orientation measurements obtained by EBSD. The use of automated EBSD makes the measurement of this dislocation content a relatively fast process compared to similar dislocation measurement methods.

A review of the theoretical development of GNDs is given in this chapter. Dislocations may be separated into two groups, GNDs which impose geometrical constraints on a crystal lattice, and SSDs whose geometric effect on the crystal lattice is cancelled out due to redundancies and crystal symmetry [74].

The basis for GND calculations comes from work by Nye, who developed a dislocation density tensor which related Burgers vectors and line vectors of dislocations in a reference volume. The dislocation density tensor is also shown by Nye to be related to a lattice curvature tensor [3].

Motivation for the study of GNDs has mainly been concerned with local plasticity models. Traditional multiple-slip Taylor plasticity models are size dependent and are not adequate for explaining plasticity at micron size scales. GNDs have been included as a way to create local and non-local plasticity models which accurately predict behaviour at small size scales [75].

Recent developments have included the calculation of local GND densities by means of EBSD measurements. An overview of the EBSD technique and methodology can be found in Section 3.1. By solving local orientations using EBSD, orientation gradients may be calculated and resolved into the lattice curvature tensor described by Nye. An in depth explanation of Nye's tensor can be found in Section 2.4, and a how it is applied to EBSD results in Section 2.4.2.1. The dislocation density tensor may then be calculated and a minimum length of dislocation can be determined based on the active slip systems of the specific material. In this way, the dislocation content of a material can be analyzed using EBSD and automated OIM without the time consuming use of Transmission Electron Microscope (TEM). The exact method of calculation and orientation collection greatly affects the final GND calculation. Their effect on the accuracy of the results is shown in Section 4.

2.4.1 Crystal Plasticity

One main focus for GND research has been in their role in local plasticity. Traditional Taylor based plasticity models possess no internal length scale [76], and are found to be ineffective at determining materials parameters at micron lengths. Predictions from these classic plasticity models for non-uniform deformation do not exhibit size dependence.

Microstructural grain size effects are caused by grain boundaries, related by the well known Hall-Petch effect, and particle reinforcements. These cause strain gradients, which strain gradient plasticity models generally attribute to hardening by geometrically necessary dislocations [74]. Deformation causes dislocations to be generated. They accumulate in the material either by random trappings of dislocations (SSDs) or by a geometric need to conform to the deformation (GNDs). Uniform strain is associated with the statistically stored dislocations, while the strain gradients are associated with the geometrically necessary dislocations [77]. Strain gradient plasticity models aim to predict the effects of this uniform strain component and its gradient.

Two main models exist which combine the strain component and its gradient. The Nix and Gao model shows a relation between the square of flow stress and the strain gradient GND content [78][79]. Another model by Fleck and Hutchinson considers the contribution of SSDs and GNDs to be separate to the plasticity [80]. An assessment and comparison of the models was completed by Evans and Hutchinson [75].

2.4.2 Dislocation Density Tensor

The basis for GND calculations comes from theoretical framework developed by Nye [3]. Considering a reference volume of a crystal large enough for the effects of the dislocations contained within to be averaged, Nye proposed a relation between the Burgers vectors and the line vectors of the dislocations in the volume called the dislocation density tensor. The dislocation density tensor was then related to resulting lattice curvature by a tensor called the lattice curvature tensor.

Nyes original definition of the dislocation density tensor considers dislocations to be continuously distributed and described by a number density of lines inter-

secting an arbitrarily oriented plane. A definition of the tensor as a length of dislocation in a volume, which is easier for calculation and minimization for non simple cubic systems, was later presented by Arsenlis and Parks [81]. Nye started by showing that a Burgers circuit of unit area normal to unit vector l_j with Burgers vector B_i can be described by:

$$B_i = \alpha_{ij} l_j \tag{2.18}$$

The second rank tensor, α_{ij}, relates the Burgers vector to the line vector of a dislocation. It is referred to as the dislocation density tensor and specifies the state of dislocation in the region. A proof of this equation is provided by Nye in his original paper.

Calculation of the components of α_{ij} can be accomplished as follows. Considering all dislocations in the reference volume, suppose there are dislocations with a portion of length parallel to unit vector r and with Burgers vector b. If there are n number of these dislocations crossing unit area normal to r, then the number crossing unit area normal to l in $nr \bullet l$. The associated Burgers vector is;

$$B_i = b_i(nr_j l_j) \tag{2.19}$$

Substituting this into the previous equation, we obtain;

$$\alpha_{ij} = nb_i r_j \tag{2.20}$$

The total α_{ij} is obtained by a summation of $nb_i r_j$ for all sets of dislocations. In order to specify the curvatures resulting from the state of dislocations described by α_{ij}, let $\mathrm{d}\Phi_i$ be the lattice rotations about each primary axes and $\mathrm{d}x_j$ be a displacement vector. The relation between these two vectors can be described by;

$$\mathrm{d}\Phi_i = \kappa_{ij} \mathrm{d}x_j \tag{2.21}$$

where κ_{ij} is a second rank tensor which describes the curvature of the lattice. The dislocation tensor is related to this lattice curvature tensor by the equation;

$$\alpha_{ij} = \kappa_{ji} - \delta_{ij}\kappa_{kk} \tag{2.22}$$

where δ is the kronecker delta ($\delta_{ij} = 1$ for $i=j$, and $\delta_{ij} = 0$ for $i \neq j$). This provides a link between dislocations and the resulting lattice effects. However, both plastic and elastic stresses may exist in a real material, and as this model does not incorporate the elastic stress state which changes according to the plastic stress, simply measuring the lattice curvatures cannot be resolved into the dislocation state [82]. Modifications to the equation are needed. Refinements by Kroner [82][83] and Ashby [74], attempted to create a combined theory of plasticity and residual stress. As shown by Kroner, with the addition of an elastic distortion tensor, the previous equation becomes

$$\alpha_{ik} = \kappa_{ki} - \delta_{ki}\kappa_{mm} - \epsilon_{klj}\mathrm{d}e_{ij}(\frac{e_l}{\mathrm{d}x_l}) \tag{2.23}$$

These equations define dislocation density as a number density of lines intersecting an arbitrarily oriented plane, however it can be simpler to describe the tensor as a line length in a reference volume.

The effect of dislocation line segments on the tensor can be calculated by

$$\alpha_{ij} \equiv \frac{1}{V}L\int Lb_i t_j \mathrm{d}s \tag{2.24}$$

which is essentially an integration of the properties of each dislocation line segment ds, over the entire length of dislocations L, in the reference volume V. If each dislocation segment is considered separately, the integral can be rewritten as a summation.

$$\alpha_{ij} \equiv \frac{1}{V}\sum \xi b_i^{\xi}\int lt_j^{\xi}\mathrm{d}s^{\xi} \tag{2.25}$$

The effect of dislocation lines on the dislocation tensor are now more apparent. For example, Fig. 2.17 shows a dislocation line starting at x^- and ending at x^+.

In this case, Nyes tensor in the previous equation can be rewritten as;

$$\alpha_{ij} = \frac{1}{V}b_i(x_j^+ - x_j^-) \tag{2.26}$$

The geometric effects on the volume by the dislocation line segments can be simplified to a single dislocation with the same constant Burgers vector and a tangent line vector from the dislocation start point to the end point (the average

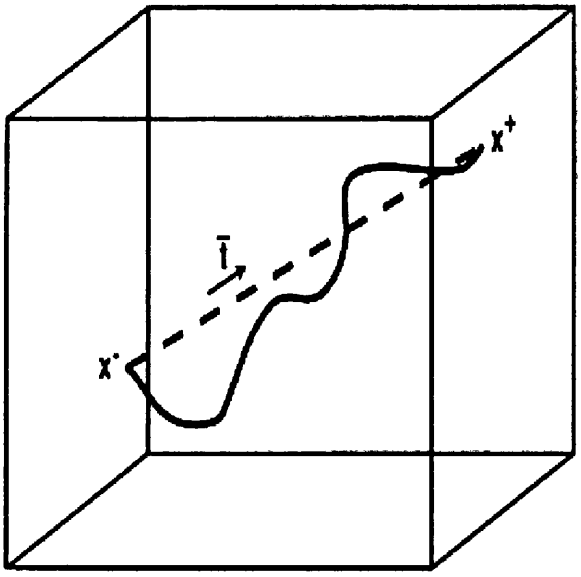

Figure 2.17: A dislocation line threading through a reference volume and it's equivalent net effect on the dislocation density tensor, $\bar{t}$ [81]

tangent line vector). The length of this simplified dislocation would be the GND component, while any excess line length in the original dislocation would be the SSD component. In this same respect, closed dislocation loops contained entirely within the reference volume are completely statistically stored and have no effect on the dislocation tensor as their average tangent line vector resolves to zero.

This substitution of the average tangent line vector for the entire dislocation line length can be rewritten in the previous equation as

$$\alpha_{ij} = \frac{1}{V} \sum \xi \bar{l^{\xi}} b_i^{\xi} \bar{t_j^{\xi}} \tag{2.27}$$

where l is the secant length. Another substitution can be made by defining the dislocation density as a line length in a volume, or l/V.

$$\alpha_{ij} = \sum \xi \rho_{GND}^{\xi} b_i^{\xi} \bar{t_j^{\xi}} \tag{2.28}$$

$\rho GN\xi$ is the geometrically necessary dislocation density of dislocation type ξ. It is the total length of dislocation type ξ in the reference volume which contributes

a geometric effect [81].

2.4.2.1 Calculating the Dislocation Density Tensor Using EBSD

As previously shown by Nye, and in Section 2.4, the state of dislocations in a material affects the lattice curvature in a measurable way. In this way, measuring GND density is perfectly suited for EBSD as the lattice curvature can be calculated using orientation gradients taken from microtexture measurements using EBSD.

Sun et al. [84][85][86] were the first to apply Nyes tensor to recover GND content from EBSD measurements. Sun et al. used a method similar to Randle et al. [87], however connecting the misorientation measurements to Nyes dislocation framework. Field et al. later used this same method to analyze the GND distribution on the microscale in compressed aluminum single crystals [88].

Pantleon later showed that these previous studies used too approximate a treatment for the lattice rotation vectors, and proposed refinements to further restrict the dislocation density tensor [2].

Pantleons method is as follows. The previous lattice curvature equation can be described for two points separated by Δx. In sample coordinates, the lattice curvature vector can be described as follows;

$$\kappa_{kl} = \frac{\mathrm{d}\theta_k}{\mathrm{d}x_l} \approx \frac{\Delta\theta_k}{\Delta x_l} \tag{2.29}$$

where Δx_l is the distance between the two points (commonly the step size used in the EBSD), and θ_k is the lattice rotation vector, and is calculated as;

$$\Delta\theta_k = -\epsilon_{kil} \tag{2.30}$$

In this equation, Δg is a second rank tensor and is calculated as the misorientation between the two points ($\Delta g = {g_A}^{-1} g_B$), $\Delta\theta$ is the angle between corresponding axis of the two points ($\Delta\theta$ = arccos (Δg_{ii}-1)/2), and is the Levi-Civita permutation symbol. This equation then becomes an implied summation over the values of κ_{ij}, with only two non-trivial elements.

At each point, the elements of the lattice curvature tensor can be solved for by using the neighbouring orientations in all directions. The values of the lattice

curvature tensor can then be used to solve for the elements of the dislocation tensor. However, because EBSD only creates maps in two dimensions, orientation gradients in the sample normal direction are not known, and hence unless a 3D-EBSD technique is used lattice curvature tensors i3 are unknown and some of the elements of the dislocation tensor which require these to be determined remain unknown [2]. However, the accuracy of 3D- EBSD techniques, such as serial sectioning, may not be suitable for GND calculations [86].

For a two dimensional orientation map, the elements of the dislocation tensor which can be determined are

$$\alpha_{13} = \kappa_{31}$$

$$\alpha_{21} = \kappa_{12}$$

$$\alpha_{23} = \kappa_{32}$$

$$\alpha_{33} = -\kappa_{11} - \kappa_{22}$$

and the remaining elements are

$$\alpha_{22} = -\kappa_{11} - \kappa_{33}$$

$$\alpha_{31} = \kappa_{13}$$

$$\alpha_{32} = \kappa_{23}$$

As pointed out by Pantleon, one difference is also available

$$\alpha_{11} - \alpha_{22} = \kappa_{11} - \kappa_{22}$$

However, this difference is valid based on the assumption that the elastic strain gradient is zero or negligible. In a study by Wilkinson and Randman, this assumption was shown to be valid [89]. Elastic strains were shown to be significantly smaller than lattice rotations around a Berkovich indent in Fe. The addition of the elastic strain gradients as corrections to the lattice curvatures calculated from the rotation field resulted in only small modifications and only small changes to the estimated GND content.

These dislocation tensor components, as previously mentioned, only specify the state of dislocations in the material. Due to crystal symmetry, these geometric constraints specified by the dislocation tensor may be satisfied by infinitely many configurations of dislocations due to crystal redundancies. However, due to the definition of, and derivation of, the dislocation tensor as a geometric property, a minimization of the dislocation density is implied [81].

2.4.2.2 Minimization Techniques

It should be noted that when the exact number and formation of dislocations in the material is known, the dislocation tensor may be calculated and the resulting lattice curvature predicted; however, the inverse is not true. If the lattice curvature is measured and the dislocation tensor calculated, the exact number and formation of dislocations cannot be unambiguously predicted. Due to crystal symmetries and dislocation redundancies, there are infinitely many combinations of dislocations which may result in a measured lattice curvature. The definition of GNDs implies a minimum of dislocations, and so minimization techniques are employed to resolve the dislocation tensor into a set of dislocation densities. It is reasonable to consider only pure edge and pure screw type dislocations for minimization. Face-centred cubic materials with {111} slip planes and <110> slip directions have a total of 18 different dislocation types, 12 edge and 6 screw. Using FCC as an example, the 9 dislocation density tensor elements create 9 equations with 18 dislocation density variables, which a unique solution is obviously not possible for and hence minimization techniques are used. The 18 dislocation densities and their line variable are given in Fig. 2.18.

However, due to the opacity of crystalline materials, orientation gradients normal to the sample surface are not normally measurable, and hence only 5 of the 9 dislocation density tensor elements can be known. This means that minimization techniques need to be undertaken with 5 equations of 18 dislocation density variables (6 equations are available if elastic strain is negated using the difference shown by Pantleon). In specific cases where the orientation gradients in the sample normal direction are known to be zero, or if other data acquisition methods are used (such as FIB), all 9 sets of equations may be used.

Density	t	s	n
ρ_1	$\frac{1}{\sqrt{6}}[\bar{1}\bar{1}2]$	$\frac{1}{\sqrt{2}}[\bar{1}10]$	$\frac{1}{\sqrt{3}}[111]$
ρ_2	$\frac{1}{\sqrt{6}}[\bar{1}2\bar{1}]$	$\frac{1}{\sqrt{2}}[10\bar{1}]$	$\frac{1}{\sqrt{3}}[111]$
ρ_3	$\frac{1}{\sqrt{6}}[2\bar{1}\bar{1}]$	$\frac{1}{\sqrt{2}}[0\bar{1}1]$	$\frac{1}{\sqrt{3}}[111]$
ρ_4	$\frac{1}{\sqrt{6}}[\bar{1}\bar{1}\bar{2}$	$\frac{1}{\sqrt{2}}[\bar{1}\bar{1}0]$	$\frac{1}{\sqrt{3}}[1\bar{1}\bar{1}]$
ρ_5	$\frac{1}{\sqrt{6}}[\bar{1}21]$	$\frac{1}{\sqrt{2}}[101]$	$\frac{1}{\sqrt{3}}[1\bar{1}\bar{1}]$
ρ_6	$\frac{1}{\sqrt{6}}[211]$	$\frac{1}{\sqrt{2}}[01\bar{1}]$	$\frac{1}{\sqrt{3}}[1\bar{1}\bar{1}]$
ρ_7	$\frac{1}{\sqrt{6}}[1\bar{1}2]$	$\frac{1}{\sqrt{2}}[110]$	$\frac{1}{\sqrt{3}}[\bar{1}1\bar{1}]$
ρ_8	$\frac{1}{\sqrt{6}}[121]$	$\frac{1}{\sqrt{2}}[\bar{1}01]$	$\frac{1}{\sqrt{3}}[\bar{1}1\bar{1}]$
ρ_9	$\frac{1}{\sqrt{6}}[\bar{2}11]$	$\frac{1}{\sqrt{2}}[0\bar{1}1]$	$\frac{1}{\sqrt{3}}[\bar{1}1\bar{1}]$
ρ_{10}	$\frac{1}{\sqrt{6}}[112]$	$\frac{1}{\sqrt{2}}[1\bar{1}0]$	$\frac{1}{\sqrt{3}}[\bar{1}11]$
ρ_{11}	$\frac{1}{\sqrt{6}}[1\bar{2}1]$	$\frac{1}{\sqrt{2}}[\bar{1}01]$	$\frac{1}{\sqrt{3}}[\bar{1}11]$
ρ_{12}	$\frac{1}{\sqrt{6}}[\bar{2}1\bar{1}]$	$\frac{1}{\sqrt{2}}[011]$	$\frac{1}{\sqrt{3}}[\bar{1}11]$
ρ_{13}	$\frac{1}{\sqrt{2}}[110]$	$\frac{1}{\sqrt{2}}[110]$	$\frac{1}{\sqrt{3}}[1\bar{1}\bar{1}]$ or $\frac{1}{\sqrt{3}}[\bar{1}1\bar{1}]$
ρ_{14}	$\frac{1}{\sqrt{2}}[101]$	$\frac{1}{\sqrt{2}}[101]$	$\frac{1}{\sqrt{3}}[1\bar{1}\bar{1}]$ or $\frac{1}{\sqrt{3}}[\bar{1}11]$
ρ_{15}	$\frac{1}{\sqrt{2}}[011]$	$\frac{1}{\sqrt{2}}[011]$	$\frac{1}{\sqrt{3}}[\bar{1}1\bar{1}]$ or $\frac{1}{\sqrt{3}}[11\bar{1}]$
ρ_{16}	$\frac{1}{\sqrt{2}}[\bar{1}10]$	$\frac{1}{\sqrt{2}}[\bar{1}10]$	$\frac{1}{\sqrt{3}}[111]$ or $\frac{1}{\sqrt{3}}[\bar{1}\bar{1}1]$
ρ_{17}	$\frac{1}{\sqrt{2}}[10\bar{1}]$	$\frac{1}{\sqrt{2}}[10\bar{1}]$	$\frac{1}{\sqrt{3}}[111]$ or $\frac{1}{\sqrt{3}}[\bar{1}1\bar{1}]$
ρ_{18}	$\frac{1}{\sqrt{2}}[0\bar{1}1]$	$\frac{1}{\sqrt{2}}[0\bar{1}1]$	$\frac{1}{\sqrt{3}}[111]$ or $\frac{1}{\sqrt{3}}[1\bar{1}\bar{1}]$

Figure 2.18: The 18 basic dislocation densities and their line variables for an FCC crystal structure [81].

The first minimization technique is the L2 method or least squares method. The sum of the squares of the dislocation densities is minimized subject to satisfy the dislocation tensor equations. This method is preferable because it is easily computable due to matrix relations, but there is no real physical argument to expect a solution which minimizes the sum of squares of the dislocation densities.

The density of each dislocation type and the dislocation density tensor can be rewritten as;

$$A\rho = \mathrm{A} \tag{2.31}$$

where the dislocation tensor is represented by a nine-dimensional column vector A, ρ is an n-dimensional vector representing the density of each dislocation type, and A is a linear operator made up of the combination of Burgers vectors line vectors acting on ρ. A singular value decomposition then takes the form

$$\rho_{GND} = (ATA)^{-1}ATA = BA \tag{2.32}$$

where B is a Moore-Penrose pseudo-inverse of A. For an FCC crystal system, this matrix is shown in Fig 2.19.

$$\begin{bmatrix} \rho_1 \\ \rho_2 \\ \rho_3 \\ \rho_4 \\ \rho_5 \\ \rho_6 \\ \rho_7 \\ \rho_8 \\ \rho_9 \\ \rho_{10} \\ \rho_{11} \\ \rho_{12} \\ \rho_{13} \\ \rho_{14} \\ \rho_{15} \\ \rho_{16} \\ \rho_{17} \\ \rho_{18} \end{bmatrix} b = \begin{bmatrix} a & 7c & -13c & -7c & -a & 13c & c & -c & 0 \\ -a & 13c & -7c & -c & 0 & c & 7c & -13c & a \\ 0 & c & -c & -13c & a & 7c & 13c & -7c & -a \\ a & -7c & 13c & 7c & -a & 13c & -c & -c & 0 \\ -a & -13c & 7c & c & 0 & c & -7c & -13c & a \\ 0 & -c & c & 13c & a & 7c & -13c & -7c & -a \\ a & -7c & -13c & 7c & -a & -13c & c & c & 0 \\ -a & -13c & -7c & c & 0 & -c & 7c & 13c & a \\ 0 & -c & -c & 13c & a & -7c & 13c & 7c & -a \\ a & 7c & 13c & -7c & -a & -13c & -c & c & 0 \\ -a & 13c & 7c & -c & 0 & -c & -7c & 13c & -a \\ 0 & c & c & -13c & a & -7c & -13c & 7c & -a \\ 5d & e & 0 & e & 5d & 0 & 0 & 0 & -d \\ 5d & 0 & e & 0 & -d & 0 & e & 0 & 5d \\ -d & 0 & 0 & 0 & 5d & e & 0 & e & 5d \\ 5d & -e & 0 & -e & 5d & 0 & 0 & 0 & -d \\ 5d & 0 & -e & 0 & -d & 0 & -e & 0 & 5d \\ -d & 0 & 0 & 0 & 5d & -e & 0 & -e & 5d \end{bmatrix} \begin{bmatrix} \alpha_{11} \\ \alpha_{12} \\ \alpha_{13} \\ \alpha_{21} \\ \alpha_{22} \\ \alpha_{23} \\ \alpha_{31} \\ \alpha_{32} \\ \alpha_{33} \end{bmatrix}$$

where $a = \frac{\sqrt{3}}{9}$ $c = \frac{\sqrt{3}}{84}$ $d = \frac{1}{18}$ $e = \frac{3}{14}$

Figure 2.19: Moore-Penrose Pseudo-inverse defining FCC dislocation line characteristics [81].

Since only a simple matrix multiplication is needed to complete this minimization technique, entire OIM maps can be resolved into GND content maps quickly and efficiently.

The second minimization technique is the L1 method, which attempts to minimize the dislocation line energy subject to the dislocation tensor equations. This method has a more physical reasoning for the minimization, however it can be

more computationally intensive. All dislocations have the same magnitude Burgers vector, so the only difference in energy between the different dislocation density types is the difference in energy between edge and screw dislocations.

$$\frac{E_{\mathbf{edge}}}{E_{\mathbf{screw}}} = \frac{1}{1-\mathrm{v}} \tag{2.33}$$

Optimization algorithms are then used to calculate the dislocation densities based on this energy minimization. These algorithms can be time intensive, and hence tend to only be used in studies which prefer their accuracy.

Comparisons of these two minimization techniques have been performed by Wilkinson and Randman [89]. The L2 minimization method generally returns a slightly higher estimation of the GND content that the L1 method, however the patterns produced by the two are similar. The authors point out that their preferred method of minimization is the L1.

Another method for calculating the GND density does not require a minimization technique or evaluation of the dislocation tensor. Following Kubin and Mortensen [90], Gao et al. [79], and employed by Calcagnotto et al. [6]

$$\rho_{GND} = \frac{2v}{ub} \tag{2.34}$$

which relates the GND density to the misorientation angle, v, the unit length u, and the magnitude of the Burgers vector b. Calcagnotto et al. [6] employed a Kernal Average Misorientation approach as a method for choosing v, which involved an average measurement of points of the nearest or next nearest neighbour. However, this may be an over-simplification of the GND calculation since the crystal system, the active slip systems, or any actual lattice curvatures are not involved.

2.4.2.3 Effect of Step Size on GND Calculations

Nyes tensor [3] incorporates a displacement vector when calculating the lattice curvature, and as shown by Pantleon [2], this is analogous to the step size parameter in an EBSD system. The step sized used in the EBSD and OIM maps can have great effects on the calculation of GNDs. If the step size is smaller than the dislocation spacing, then it is theoretically possible to resolve all of the dislocation

content in a material as GNDs; however, a step size which is significantly larger than the dislocation spacing will not detect lattice curvature changes between the measured points and less of the total dislocation content will be resolved as GNDs [86]. Therefore, small steps sizes are preferred. In practice, however, the spatial resolution of EBSD may not be adequate for such small step sizes.

At smaller step sizes, Electron Back-Scatter Diffraction Pattern (EBSP) indexing accuracy becomes much more important. Noise of fractions of a degree at very small step sizes will invalidate GND calculation. Wilkinson and Randman show that the expected noise on the GND measurements can be predicted by

$$\Delta\rho = \frac{\delta}{b\lambda} \tag{2.35}$$

where δ is the uncertainty of the orientation measurements in radians and λ is the step size [89]. With this equation it is clear that a reduction in step size while the orientation uncertainty remains unchanged will result in a higher GND noise. This can be a major problem if the orientation uncertainty is too high, as can be the case with Hough transformation methods. In these cases, small step sizes result in a GND noise which masks the actual GND distributions, but large step sizes miss much of the lattice curvature.

High resolution EBSD using a cross correlation method has been shown to be the most accurate in terms of angular resolution. The technique is described elsewhere [1][4]. Cross correlation methods have been shown to determine rotation tensors to +/- 7 x 10-4 or a misorientation resolution of +/- 0.01°, while typical Hough transformation resolutions tend to be about +/- 0.5°.

Calcagnotto and coworkers [6] attempted to overcome this issue by using a method of nearest neighbours to maintain a low step size/high spatial resolution while minimizing the effects of a low spatial resolution. Orientation measurements were taken with a low step size, but calculations for the lattice rotation tensor were taken as an average of the nearest or next nearest neighbours, excluding neighbours with a misorientation relative to the original point higher than a defined threshold (given as 2° in the report).

Chapter 3

Experimental Procedures and Calculation Methods

3.1 Electron Back-scatter Diffraction

EBSD is a technique using a SEM for measuring local crystal orientations. The SEM is itself a highly advanced tool for research of the microstructure of modern materials. The addition of EBSD capabilities provides an alternative to macroscopic texture measurements from X-ray techniques without the fine sample preparation required by TEM).

EBSD allows for determination of microtexture, or the local crystallographic orientation of single grains, by indexing of an EBSP more commonly known as a Kikuchi pattern. This is in comparison to texture studies which use X-ray techniques to obtain the texture of a volume of many grains. To obtain a good representation of texture, 1000 grains must be sampled by EBSD [91]. Data sets of this size are obtainable by fully automating the EBSD process. In addition, by lowering the point to point distance for orientation measurement, the shape of grain boundaries and triple junctions can be mapped. Orientation measurements across a boundary also allow for calculation of the misorientation and determination of the boundary character [60]. The analysis of grain boundary geometry by EBSD has been used in the study of recrystallization, intergranular corrosion and cracking, and the effect on mechanical properties of various materials.

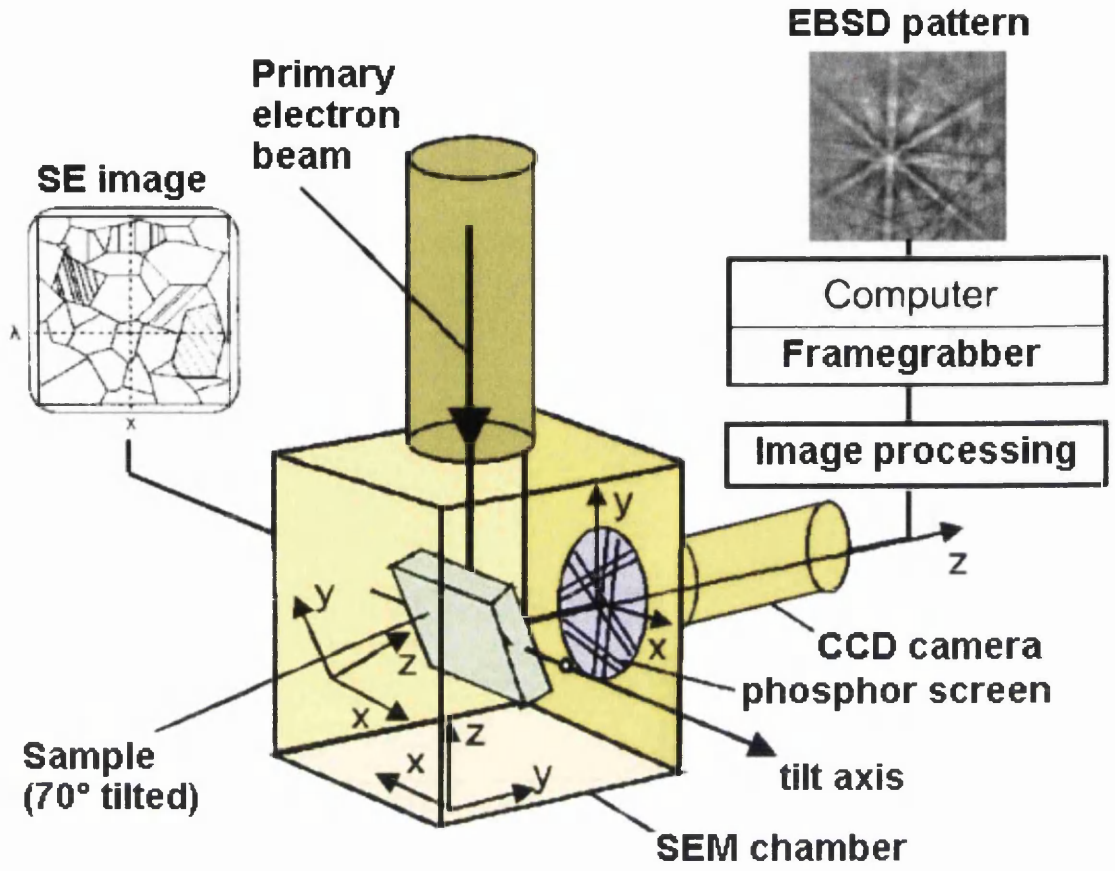

Figure 3.1: EBSD experimental set up within SEM [92]

The experimental set-up for EBSD is shown in Fig. 3.1. An incident electron beam from the SEM is focused on the sample, from which Back-Scattered Electron (BSE) are emitted. The BSEs become incident on the phosphor screen of the EBSD camera as an angular distribution representing conic sections, and seen as bright lines with a dark background. A typical EBSP is shown in Fig. 3.2. The depth of penetration into the sample by the electron beam is dependent on the operating voltage. A 20kV operating voltage was used in this study, equating to an interaction volume depth of 20nm. The sample to camera distance can also affect the angular resolution. BSEs from the interaction volume diffract on all lattice planes of the sample according to Bragg's Law in Eq. 3.1.

$$2d \sin\theta = n\lambda \tag{3.1}$$

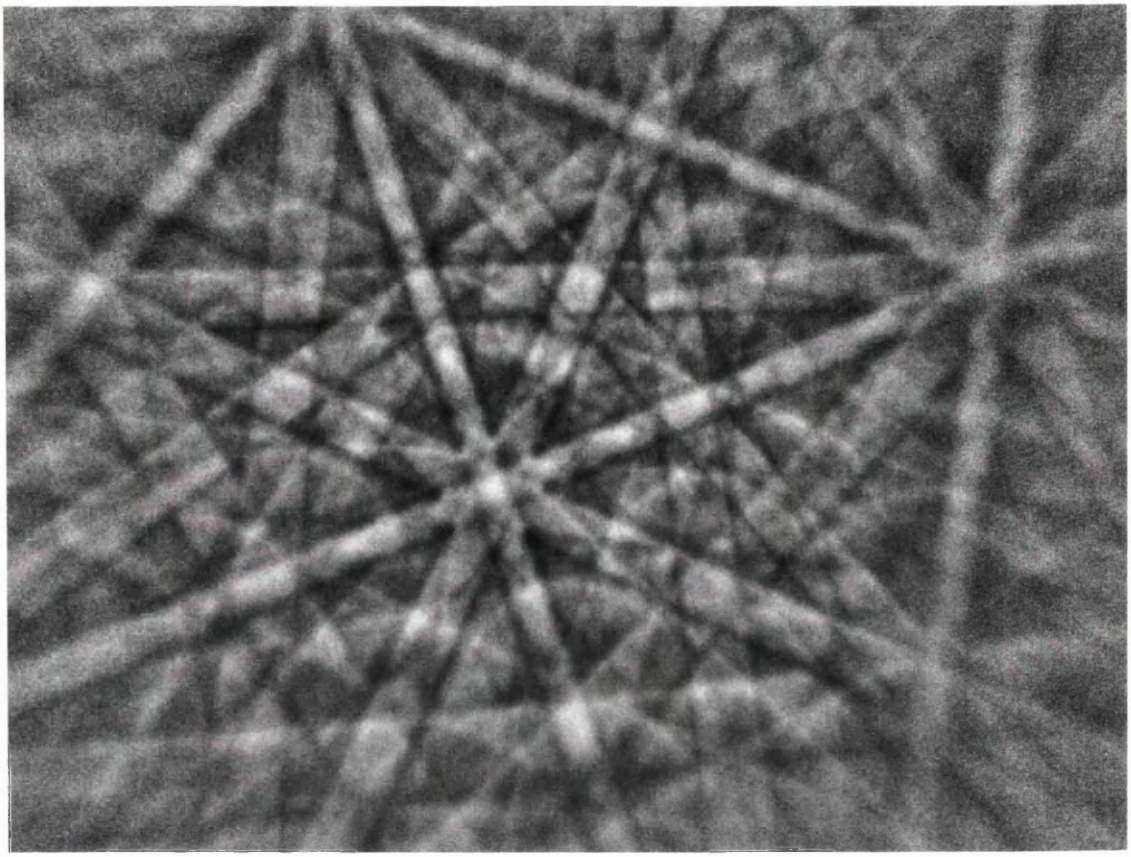

Figure 3.2: Typical EBSP obtained by EBSD from a sample of pure copper. The highest possible quality settings were used to obtain this pattern.

where d is the interplanar spacing of the family of planes, θ the Bragg angle, and λ the electron wavelength. The BSEs diffract elastically in a conic shape from every crystallographic plane. A small section of the conic shape is incident on the EBSD camera phosphor screen, making them appear linear. The sum of all BSEs diffracting from every plane creates the Kikuchi pattern.

Since the sample is tilted in relation to the electron beam, spatial resolutions differ in the axis parallel and perpendicular to the tilt axis. The spatial resolution parallel to the tilt axis is dependent on the width of the electron beam, which is itself determined by the lens aberrations and demagnification of the electron source. The beam width is generally small enough that it is not a limiting factor, and while adjustable, it is usually 50nm. The spatial resolution perpendicular to the tilt axis is dependent on the size of the volume of interaction of the elec-

tron beam in the sample (the penetration distance), which is itself dependent on the atomic number of the material and the accelerating voltage of the electron beam. Lighter materials have larger interaction volumes and hence worse spatial resolution. Decreasing the tilt angle will obviously also improve this resolution. A full study of the correlation between the spatial resolution and the operating conditions of the SEM was presented by Hjelen [93].

Determining the crystal orientation from an EBSP requires determination of the pattern centre and the distance to the source point of diffracted electrons. The pattern center is simply the point on the camera screen closest to the source point. The precision of these parameters will affect the precision of the orientation measurements. Calibration procedures for obtaining these parameters are available in the literature and an overview is presented in Randle 1992 [60].

The orientation of the crystal is described by a rotation matrix from a specimen coordinate system to the crystal coordinate system, and commonly denoted g. The axes of the specimen coordinate system are chosen based on the external shape of the sample, such as the direction of rolling or tension, and denoted RD (rolling direction), TD (transverse direction, perpendicular to RD on the sample surface), and ND (normal direction, perpendicular to the sample surface). To determine the g matrix, the position of two zone axes on the phosphor screen relative to the pattern centre (x_1,y_1 and x_2,y_2) and their crystallographic directions ([u_1,v_1,w_1] and [u_2,v_2,w_2]) are determined by indexing of the Kikuchi pattern. A third direction is then calculated from the cross product of [u_1,v_1,w_1] and [u_2,v_2,w_2] and its screen position determined from the cross product of (x_1,y_1,z) and (x_2,y_2,z); where z is the distance from the point source on the sample to the pattern centre. The crystallographic direction [h_c,k_c,l_c] along the direction normal to the sample surface can then be determined by calculating the angles $_1$, $_2$, and $_3$ between (x_1,y_1,z), (x_2,y_2,z) and (x_3,y_3,z) by the scalar products [94];

$$
\begin{aligned}
u_1h_c + v_1k_c + w_1l_c &= \cos\gamma_1({u_1}^2 + {v_1}^2 + {w_1}^2)^{0.5} \\
u_2h_c + v_2k_c + w_2l_c &= \cos\gamma_2({u_2}^2 + {v_2}^2 + {w_2}^2)^{0.5} \\
u_3h_c + v_3k_c + w_3l_c &= \cos\gamma_3({u_3}^2 + {v_3}^2 + {w_3}^2)^{0.5}
\end{aligned}
\tag{3.2}
$$

Using the cross product of two zone axes as the third direction instead of a separate third zone axis allows this to be solvable, which would otherwise be prevented by error in the measurement of their positions and the position of the pattern centre.

3.1.1 Orientation Representations

3.1.1.1 Euler Angles

The orientation matrix, g, is a 3 X 3 rotation matrix from the specimen coordinate system to the crystal coordinate system consisting of the cosines of the angles between the specimen axes and the major crystal axis ([100], [010] and [001] for cubic), where C_c refers to the crystal coordinate system and C_s to the specimen coordinate system. It can be more convenient to express this rotation instead as three Euler angles. Euler angles break the orientation matrix into three separate rotations which net the same intended rotation, allowing only three key rotation angles to be used instead of a whole 3 X 3 matrix. From the specimen coordinate system, three rotations are applied;

1. 1 about the ND direction, transforming the TD to TD' and rolling direction to RD'.
2. about the new RD' axis, transforming the TD' to TD" and ND to ND".
3. 2 about the new ND" axis.

The Euler angles are often quoted as simply these three angles. Each rotation may be expressed in it's respective matrix form.

$$g_{\varphi_1} = \begin{pmatrix} \cos\varphi_1 & \sin\varphi_1 & 0 \\ -\sin\varphi_1 & \cos\varphi_1 & 0 \\ 0 & 0 & 1 \end{pmatrix}$$

$$g_{\Phi} = \begin{pmatrix} 1 & 0 & 0 \\ 0 & \cos\Phi & \sin\Phi \\ 0 & -\sin\Phi & \cos\Phi \end{pmatrix}$$

$$g_{\varphi_2} = \begin{pmatrix} \cos\varphi_2 & \sin\varphi_2 & 0 \\ -sin\varphi_2 & \cos\varphi_2 & 0 \\ 0 & 0 & 1 \end{pmatrix} \quad (3.3)$$

Multiplication of these matrices in order produces the orientation matrix.

$$g = g_{\varphi_2} g_{\Phi} g_{\varphi_1} \quad (3.4)$$

3.1.1.2 Pole and Inverse Pole Figures

Pole figures are used to plot multiple orientations, and if contoured, a pole figure can easily show macrotexture information comparable to that obtained by x-ray diffraction. A reference sphere is used with the specimen axes, RD, TD, and ND, onto which the crystal axes directions are projected. The points are then projected back onto the equatorial plane [95].

An inverse pole figure presents the same data as the pole figure instead with a single specimen axis projected onto a reference sphere of the crystal axes. The direction is represented by 48 equivalent points in each of the 48 unit triangles, and hence is graphically represented in a unit triangle.

3.2 Samples Used

Three sets of samples were created for this project. All samples were created from 99.9% pure copper with 3mm thickness, ordered from Goodfellow ltd. The first set of samples were created according to Fig. 3.3.

The samples were given a unique name shown in brackets. The second set of samples were created with much larger deformation in a folding machine with a variation of heat treatment times according to Fig. 3.4.

The folding machine held one end of the sample in place while the opposing end was folded to approximately 90° with a large lever, as shown in Fig. 3.5.

Finally, a third set of samples was created by varying the degree of bend and the temperature of the heat treatment according to Fig. 3.6.

The samples in this third set were named for their position on the following sample matrix.

	No Bend	23mm Radius Bend	16.5mm Radius Bend
No Additional Anneal	"00"	"10"	"20"
750°C for 30 min	"01"	"11"	"21"
820°C for 30 min	"02"	"12"	"22"

Bending was accomplished using a form and a vice. The sample was placed in a form with a steel ring either 23mm or 16.5mm radius on the opposing end. This set up was then placed in a vice and tightened until the inner curve of the sample matched the outer curve of the steel ring as pictured in Fig. 3.7.

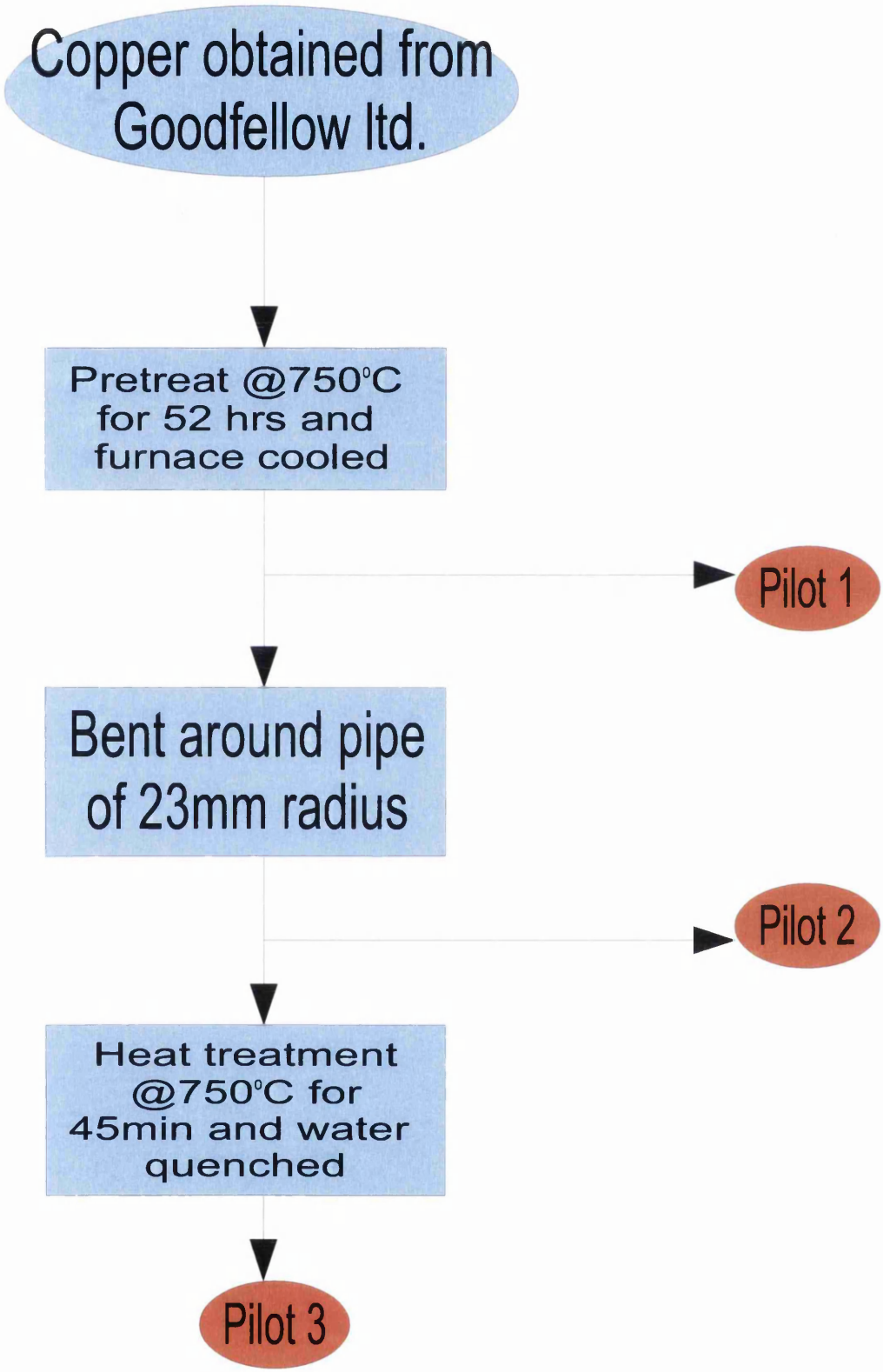

Figure 3.3: Method of creation of the first set of samples, termed the Pilot sample set. Samples are shown in orange with the sample name in brackets.

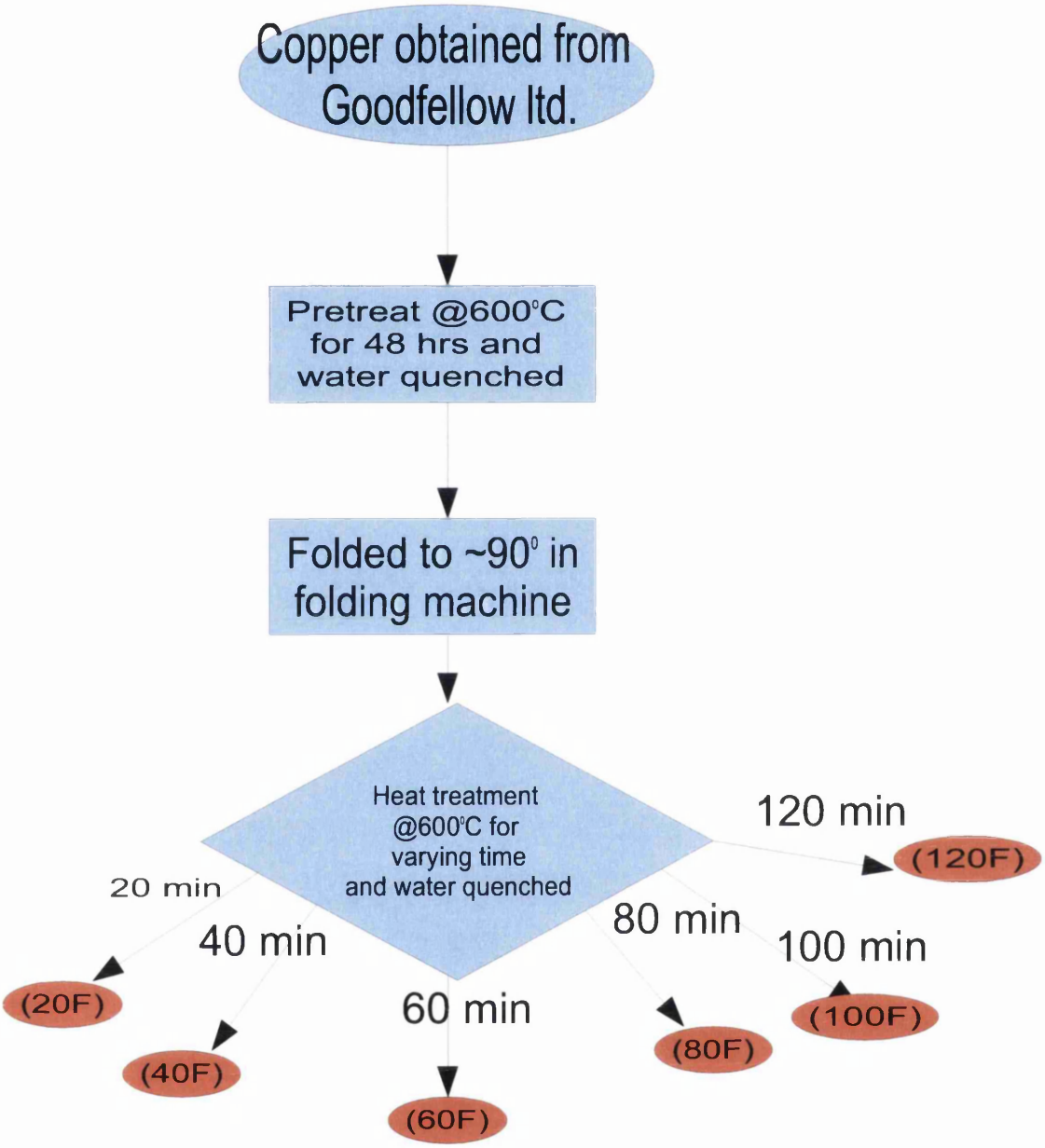

Figure 3.4: Method of creation of the second set of samples, termed the Folded sample set. Samples are shown in orange with the sample name in brackets.

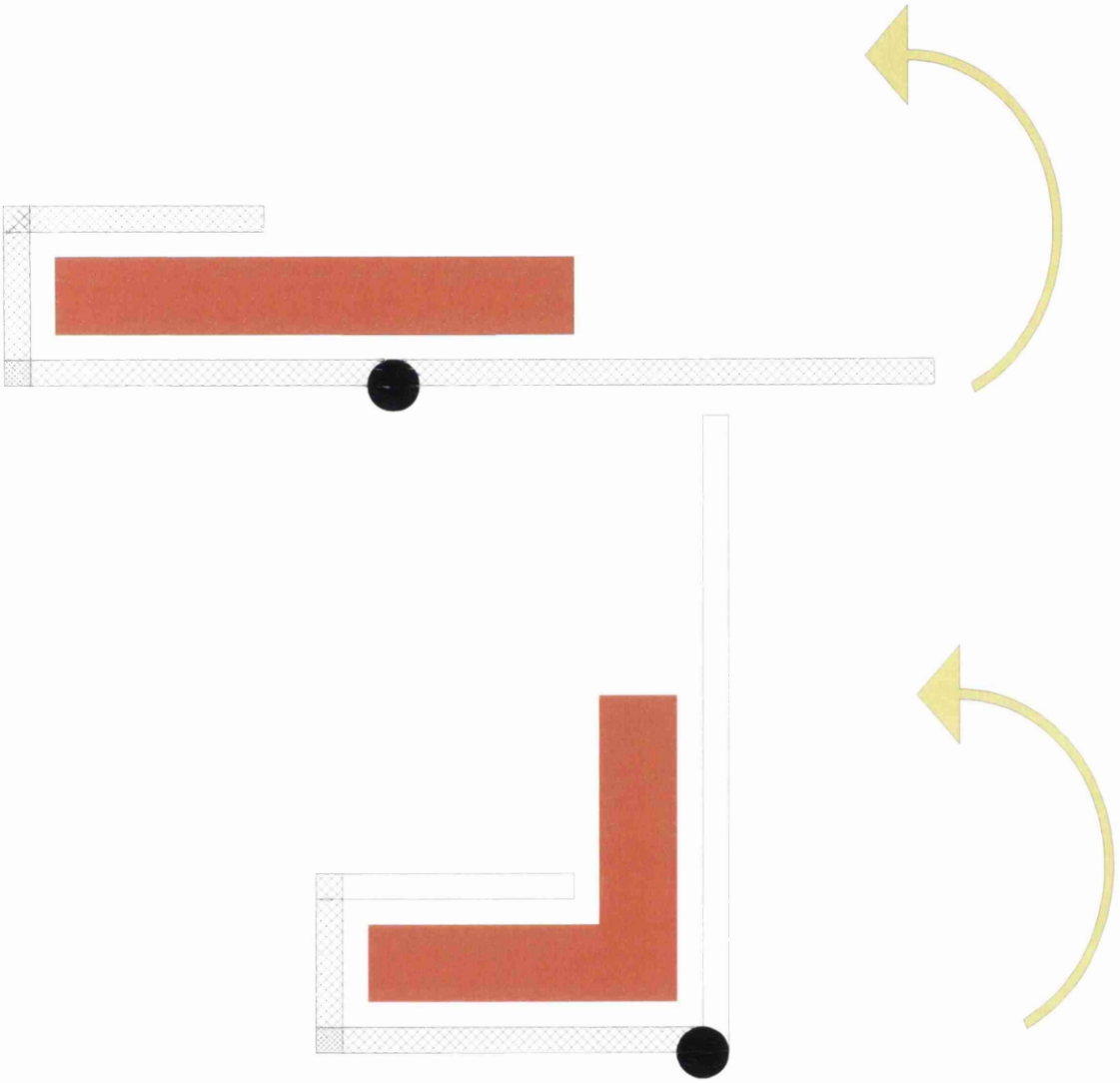

Figure 3.5: Mechanism of folding second set of samples.

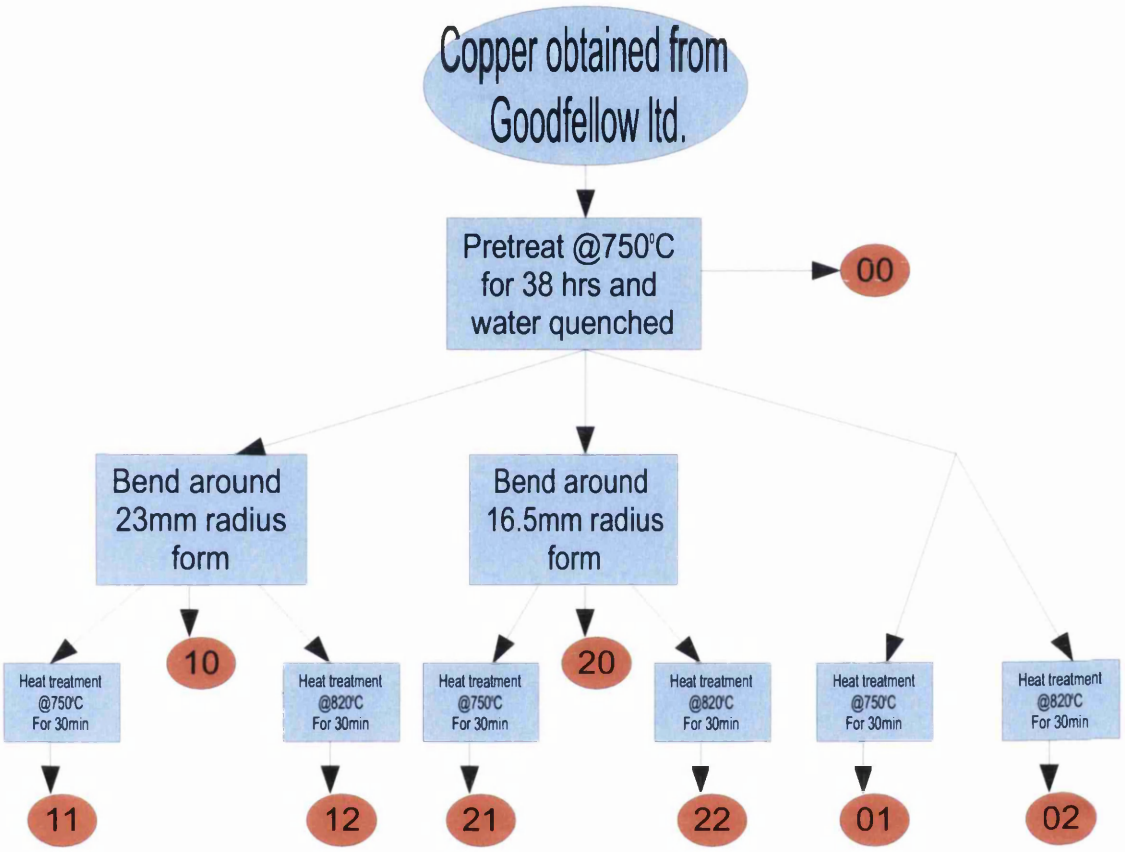

Figure 3.6: Method of creation of the third set of samples, termed the Matrix sample set. Samples are shown in orange with the sample name in brackets.

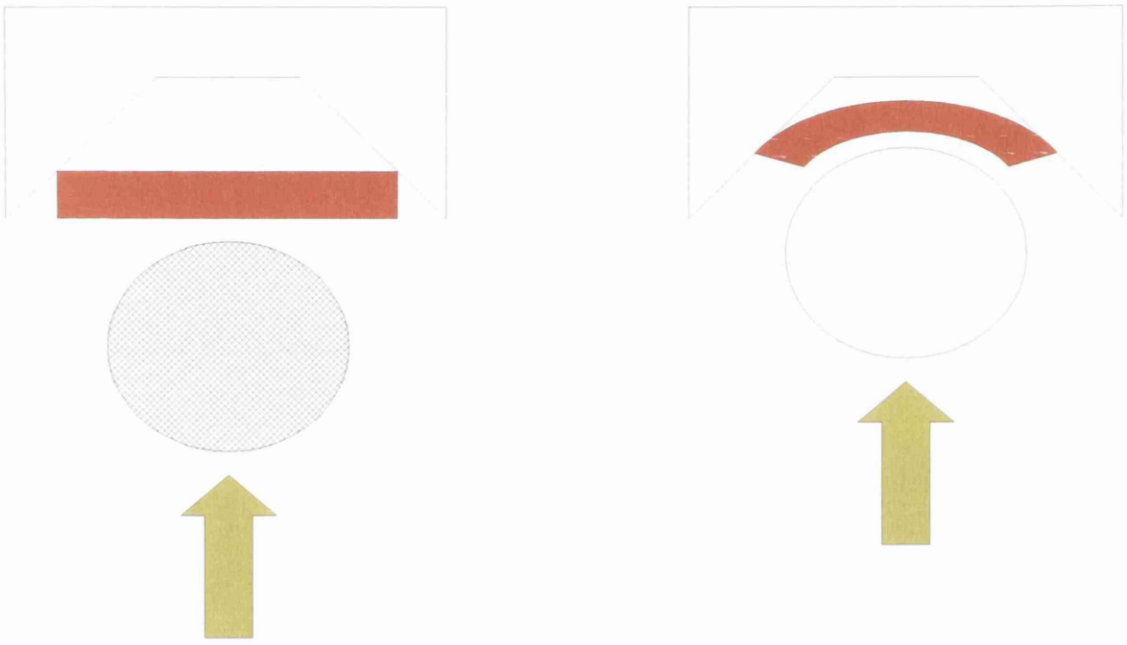

Figure 3.7: Mechanism of bending matrix samples.

Chapter 4

Orientation Mapping by EBSD for the Purpose of GND Calculation

4.1 Introduction

Crystal orientation maps can be created by EBSD for many purposes, and each may require different methods. For example, mapping for grain size determination would require mapping over large areas to gather a large sample size. The pattern indexing accuracy may be sacrificed for indexing speed as highly accurate microtexture information is not required. The step size should be kept to approximately 1/10th of the estimated grain size to ensure the size and shape of the grains measured is accurate while still maximizing for speed.

Mapping crystal orientations by EBSD for the purpose of GND measurement is another application which requires optimizing of EBSD parameters. The lattice curvature effect of a dislocation length is fractionally small, so accurate indexing of Kikuchi patterns is required to detect small amounts of dislocations. This requires that the Kikuchi pattern image is large enough and noise free enough for a robust Hough transformation. The step size should be small so as to resolve as much dislocation content as GNDs as possible, while not being too small such that the expected point-to-point misorientation is smaller than the indexing error. The

amount of time to complete a map must also be considered so a map can be completed in a reasonable time frame.

This section shows the effects of each of these factors on the resulting GND maps and suggests optimal settings. In addition, a noise reduction algorithm is suggested to correct for indexing inaccuracy.

4.2 Sample Preparation

This section is presented as a guide to the methods used to acquire experimental data for this project, and may be used as a starting point for further work. However, as there are many methods for sample preparation and newer automated systems available, the information contained in this section may not be optimal. Sample preparation for EBSD is a very complex system with many variables, usually culminating in a final silica polish; which itself is a very complex system with many variables (particle size of silica, wear on polishing pad, position and amount of downward pressure on sample, speed of pad rotation, etc). The goal of this experimental work is to obtain results from GND mapping and not to solve such a complex system. A preparation method was developed which often created adequate to good results and is in this section.

EBSD mapping for the purpose of GND analysis is the measurement of deformation in a sample, and as such is highly sensitive to any deformation caused during sample preparation. Slight changes to the preparation of a sample can produce vastly different results, often causing surface scratches which mask the underlying GND content.

The interaction volume of electrons producing an EBSP penetrates a distance into the surface of the sample dependent on the accelerating voltage of the beam. For an accelerating voltage of 20kV, this distance is approximately 200Å. This is a relatively small distance in comparison to the penetration depth of X-ray probes which reach approximately 2μm. A study by Field et al. showed that this low penetration depth can cause errors in the measurement of deformation as dislocation structures can relax approaching the free surface [96]. Additional surface structures caused by the surface preparation method can further complicate the matter, as evidenced by sample Pilot 3. The state of the sample surface must

then be a prime concern.

The preparation method suggested here was developed using only manual polishing machines. Automatic polishers may be a better alternative for future work as the results are possibly more consistent.

All samples were mounted in bakelite and ground down with various grades of sandpaper. As flat a surface as possible was created during these steps as it is believed that this may play a part in the results of the final silica polish.

The samples were then polished on a polishing wheel with a 6μm diamond paste and subsequent 1μm paste. The final steps were completed using a soft pad and fine silica polish. First, a silica polish at 300rpm with 0.06μm silica solution with moderate downward pressure on the sample was used. At this point, microtexture maps could be created with >98% indexing accuracy, but micro-scratches would be very prevalent at small step sizes. Next, polishing continued with a 0.02μm silica solution at approximately 200rpm with the sample simply held in place and no downward pressure applied. Maps created after this point would show only sporadic, harsh, micro-scratches. Finally, the sample was polished for a short period at 100rpm with the 0.02μm silica solution.

Lastly, samples were etched using a very mild etchant to soften any remaining scratches. Moderate to harsh etchants seemed to have the effect of burning in any remaining micro-scratches and make them more prevalent. In this case, 1% nital was used. The etchant appears to soften any remaining scratches and bring out the underlying GND structure. If needed, the sample was given another short period of polishing at 100rpm with the 0.02μm silica solution and re-etched. This was repeated, usually twice, until the sample surface was flat and scratch free.

A common problem encountered was surface contamination, seen as circular high GND regions in Fig. 4.1. These are not features of the dislocation structure as they often lie within grains or on grain boundaries and triple junctions with no discerning pattern. They are found when the surface preparation routine is carried out with a long wait before mapping, or if the time between the 1μm polish and fine silica polish is too long. They can be removed by going back to the 1μm polishing step and continuing as normal.

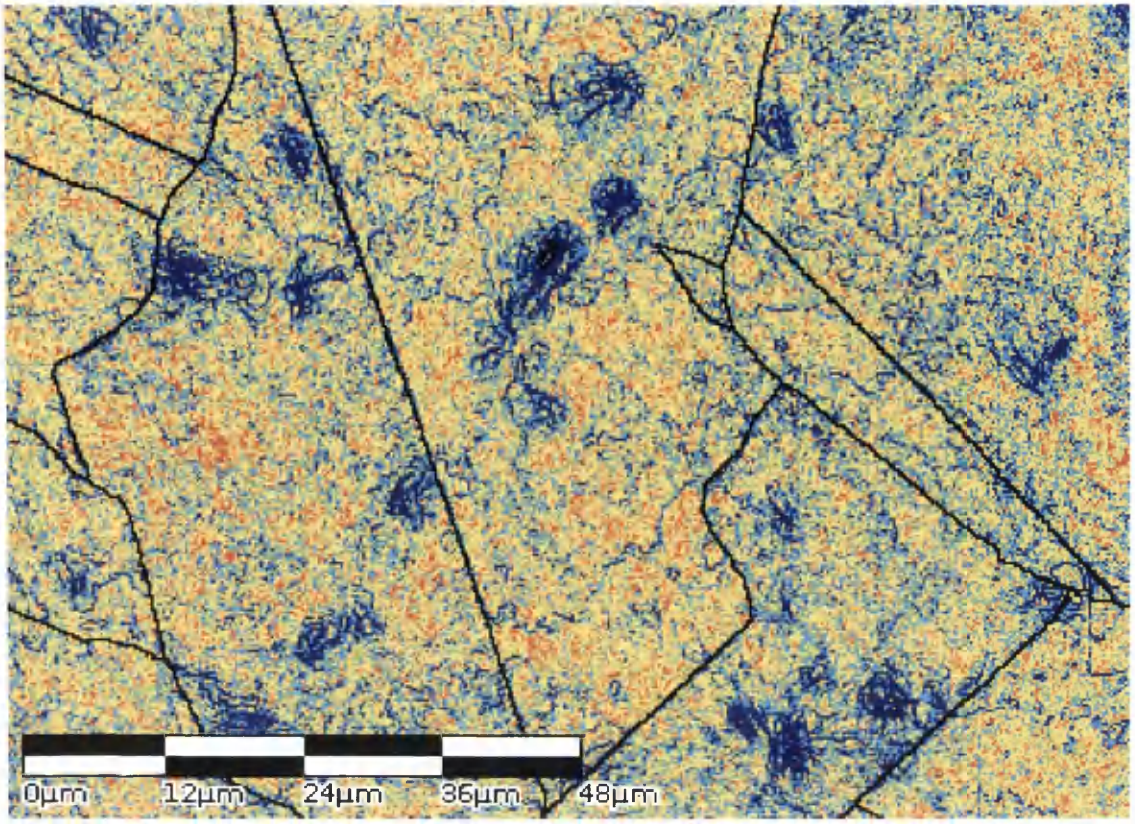

Figure 4.1: Example of surface prep affecting GND results. Map taken from a section of sample 11.

4.3 Optimizing EBSD Settings

4.3.1 Indexing By Hough Transformation

The Kikuchi pattern image space is essentially in three dimensions. The first two dimensions are the pixel positions (x,y) with the origin taken at the centre of the image. The third dimension may be considered to be the pixel intensity. Hough space also has three dimensions. The X and Y dimensions are replaced by θ and ρ, and the pixel intensity by the Hough space intensity. The image space has a discrete number of X Y pixels, as does the Hough space in the θ and ρ directions, $\Delta\theta$ $\Delta\rho$. The X and Y values are related to θ and ρ by Eq. 4.1 [97];

$$\rho = x_i \cos\theta_j + y_i \sin\theta_j \tag{4.1}$$

Solving this equation for a point in Hough space results in a line in the image space, while a point in image space results in a sinusoidal curve in Hough space with the Hough space intensity equal to the pixel intensity along the length of the curve (each point on the sine curve being a line in image space passing through the point) as shown in Fig. 4.2.

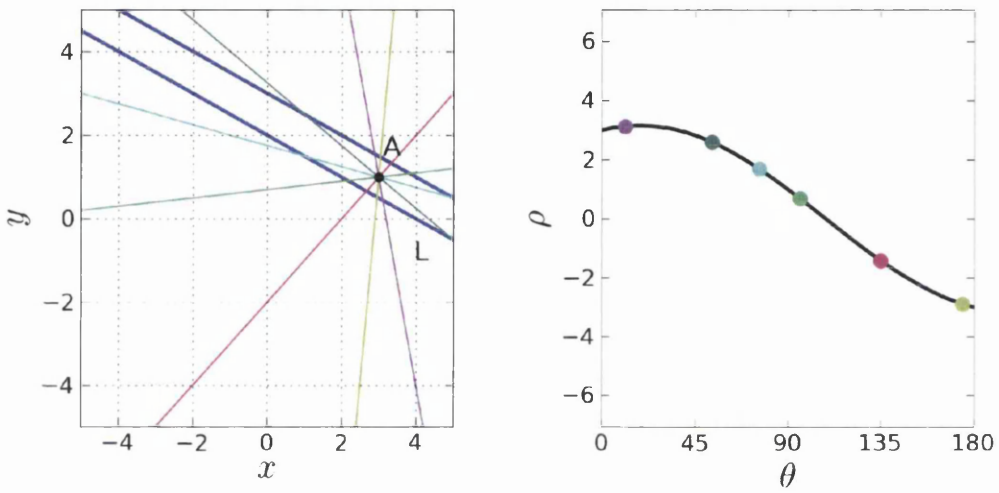

Figure 4.2: Point A within an imaginary Kikuchi band (interior of blue lines), and resulting Hough transform. All possible lines through A, L, create a point in Hough space resulting in a sinusoidal curve.

Adding more points to the image space creates more sine curves in the Hough space after transformation. Often these curves intersect. The value of the Hough space intensity at points of intersection are the sum of the intensities or, to prevent biasing effects, the average [98]. The line which joins points in image space is an intersection point of sinusoidal curves in Hough space, shown in Fig. 4.3.

Kikuchi bands with a thickness larger than 1px will appear as peaks in Hough space with the peak width corresponding to the band width. A 'butterfly' mask is used to enhance the contrast of the peaks in the Hough transform. This is a special convolution kernel (shaped like a butterfly) designed to match the shape of a typical Hough peak [99][100]. The size of the butterfly shape is dependent on the Hough space peak width, and hence the Kikuchi band width. The position of the peak centre or peak edges in Hough space is then used to index the crystal

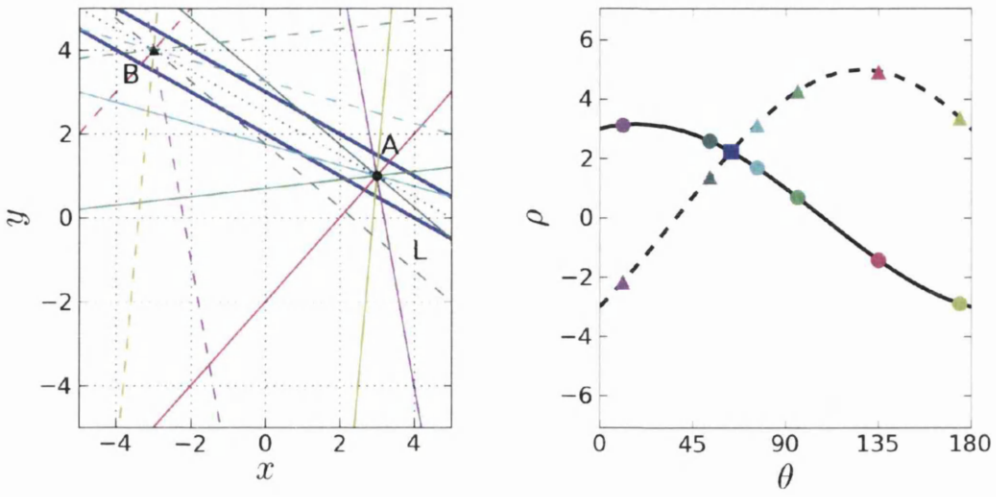

Figure 4.3: The line joining two points within a Kikuchi band in image space, B and A, is shown as the blue intersection point of their sinusoidal curves in Hough space.

orientation. Image noise can distort these peaks. Features in the image which are distorted by noise can result in a non-converging peak in Hough space.

The Hough space resolution becomes a factor in this case (a higher Hough space resolution refers to smaller $\Delta\theta$ and $\Delta\rho$, or more points in the Hough space). A high Hough space resolution would result in a spreading of the peak, complicating their detection. A low Hough space resolution would result in a higher more compact peak, making detection much easier. However, higher Hough space resolutions have more band position possibilities and hence in theory can index a pattern more accurately if the noise is sufficiently low and the image is sufficiently large. A higher Hough space resolution also requires more computational power, resulting in longer mapping times.

Traditionally, the Hough space resolution is kept as low as possible, to create large and compact peaks, but high enough such that the peak spread is not smaller than 1 for the bands with the smallest width. For the purpose of GND mapping, the highest Hough space resolution possible that achieves consistent indexing considering the pattern image size and noise level is more desirable to allow for detection of small angular changes.

The effect of changing the Hough space resolution on the resulting GND map is shown in Fig. 4.4. Lower Hough space resolutions result in a higher calculated GND content. The position of the peak in Hough space is more affected by the image noise at higher Hough space resolutions, however higher Hough space resolutions have the potential to index smaller misorientations than the lower Hough space resolution. The average resolved GND content decreases, and the GND map features change as the Hough space resolution increases, while the indexing rate was maintained >97%. The slight variation in indexing rate is less a result of the Hough space resolution change and more a product of the slight variation in the area being mapped. A map of the same sample area was attempted in each case, but can be seen to vary slightly. The indexing rate shows that the image size is sufficiently large for a robust high Hough resolution transformation. The decreases in average resolved GND content as the Hough space resolution increased shows that the indexing was becoming more accurate, and that the lower Hough resolution was not able to detect the smaller misorientations, which were possibly smaller than the $\Delta\theta$ and $\Delta\rho$ spacing at the lower Hough space resolution.

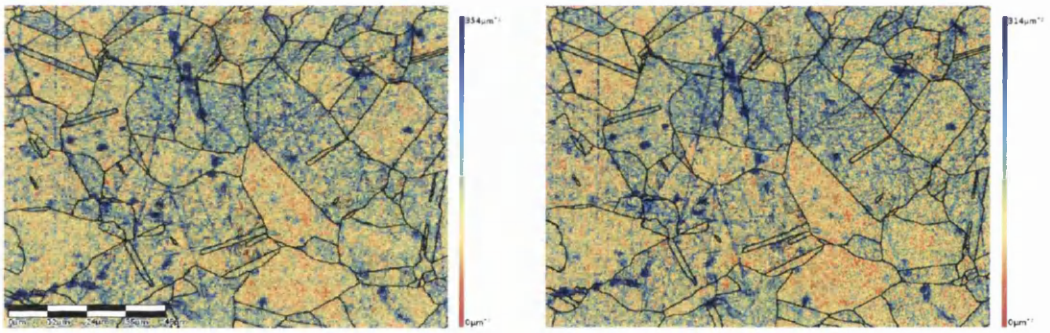

(a) Example GND map using 50 Hough setting

(b) Example GND map using 100 Hough setting

Figure 4.4: Comparison of GND mpas obtained with different Hough settings. A lower Hough setting has fewer possible band positions, increasing the smallest misorientations which are able to be resolved. This increases the average calculated GND content, shown by the change the scale bar between maps.

In practice, no real disadvantage was found for using a high Hough space resolution. Image sizes were sufficiently large with low enough image noise levels to allow for the most accurate indexing at the highest possible Hough space resolution

(125 for Flamenco software). Mapping time is increased at this Hough space resolution, but is not a major factor in the final map time (adding only a few hours to a multi-day map).

4.3.2 Step Size, Image Binning, Noise Reduction, and Method of Indexing

The step size chosen during orientation mapping has a significant effect on the resultant GND map. The step size must be of a size which reflects the measured lattice curvature, not being too small such that the noise of indexing camouflages the underlying GND structure, and not being too large such that GND structure features are missed. As a simple thought exercise, assuming a sample with a lattice curvature perfectly resembling a sinusoidal curve, the step size would be chosen to be fractionally smaller than the period of curvature. If the step size is larger than the period then the measured differences in orientation are not representative of the actual curvature, and if it is identical to the period then no curvature will be observed. If indexing were perfect, then as the step size was decreased the total dislocation content recovered as GNDs would increase up to a point where individual dislocations were being detected and the point-to-point misorientation tended towards zero. In practice, the effect of changing the step size is significant upon the fraction of dislocations resolved as GNDs, shown by the increase in the scale bar as the step size decreases in Fig. 4.5, but the underlying GND structure features are not significantly affected. The main concern when selecting a step size is the amount of area coverable in the time allotted by external constraints. A step size should be chosen which reflects the underlying structure of GND well without wasting time by over-mapping.

The step size must be chosen is conjunction with other mapping settings as the indexing accuracy can determine how small a step size is feasible. The quality of the EBSP image has a large effect on the resultant Hough transformation and the indexing accuracy of the EBSP. A large image is desirable as it creates a larger data set for the Hough transformation, but is also more computationally expensive. An accurate, noise free image, is also desirable.

Noise reduction is accomplished in two ways. Firstly, image binning reduces

the size of the image by dividing the image into non-overlapping neighbourhoods and replacing them with a single pixel with the average intensity. Neighbourhoods of 2x2, 4x4, or 8x8 are allowable in commercial Flamenco software. Image binning reduces image noise, but also reduces the image size and so gives a smaller data set for the Hough transformation. Secondly, multiple images may be taken and the average intensity at each pixel location used. This requires multiple images to be taken, and as such can result in significantly longer mapping times if the camera exposure time is a limiting factor.

A comparison of maps created with differing binning resolutions is presented in Fig. 4.6.

A large and low noise image creates a robust and accurate Hough transformation, making band detection and indexing easier and more accurate. As seen in Fig. 4.6 by the changing scale bars, while the fraction of dislocation content resolved as GNDs is slightly improved with increasing the EBSP image resolution, the features of the GND structure are highly affected. This is directly opposite to the effect of changing step size, where the GND structure features were retained by changing the step size but the fraction of dislocations resolved as GNDs was significantly affected. The 0 binning and 2x2 binning maps of Fig. 4.6 seem to be similar, however the 4x4 binning map shows significantly different features to the other two maps.

Once the EBSP has been captured using the chosen resolution and the Hough transformation has been created, the Kikuchi band edges (Hough peak gradients) or band centres (Hough peak centres) can be detected. Detecting the band edges or band centres in the Hough transformation are two separate tasks and can yield different results. A comparison of GND maps created by detecting Kikuchi band centres and band edges is shown in Fig. 4.7. Both maps produced $> 99\%$ indexing rates. The band edges map produced a higher average resolved GND content than the band centres map and the map features are starkly different between the two. The reasons for this are likely two fold.

The exact peak centre of a band can be hard to determine. Maximum pixel intensity would be expected across the band width, creating a flat peak which is a larger feature in Hough space. Imaging noise would then make this flat peak slightly rough, and the highest intensity point may not necessarily be the band

centre. In comparison, the band edges are smaller features. The position of smaller features in Hough space is more discrete in image space than larger ones, however as less image points contribute to smaller feature they are more affected by image noise. As a result, band edges can resolve smaller misorientations but result in more indexing noise. In addition, both methods would be differently affected by the constant size butterfly mask not exactly matching each peak width.

To illustrate this, a single point was indexed a sufficiently large number of times with varying settings and the orientation recorded (the full data set is included in Appendix A). The average misorientation from the average recorded orientation and the variance is shown in Fig. 4.8.

As expected, all indexing methods benefited from a 2 frame noise reduction. Settings which were similar always showed a reduction in average misorientation after an extra frame of noise reduction was added.

The differences shown between settings that differed only by high and low gain give an insight into the pattern quality and the effect of binning. Using high gain and band edges, moving from 0 binning to 2x2 binning reduced the average misorientation which subsequently increased again upon further reduction to 4x4 binning. This can be explained by the reduced noise on binning, but also the smaller image. Upon reduction to 2x2 binning, the average misorientation decreased because the image noise was decreased by pixel averaging. Increased binning to 4x4 may have improved the noise reduction further, but the image size was not large enough for the very fine Hough resolution to index the patterns reliably.

Using low gain settings and band edges, the average misorientation increased for band edges upon reduction to 2x2 binning. The noise level was low enough using low gain that there was no benefit to the pixel averaging of the image binning, and image the indexing suffered by having a smaller image for the Hough transformation.

Indexing by band centres shows more differences than band edges upon binning. Like indexing with band edges, there is always a benefit to the second frame of noise reduction. However, the benefits of image binning differ between the two indexing methods. Using high gain and band centres, the average misorientation appears to be maintained from 0 binning and 1 frame noise reduction, to 0 binning and 2

frames noise reduction, and through to 2x2 binning and 1 frame noise reduction. Only once 2x2 binning and 2 frames noise reduction is reached does the average misorientation finally decrease. It subsequently increases upon further binning to 4x4. It appears to show that reliable indexing is possible with band centres, but it is highly dependent on the image noise. This same trend is repeated for low gain.

The absolute lowest average misorientation values are found when 2x2 binning and 2 frames of noise reduction are used at low gain and indexing with band centres. However, the exposure times required when using low gain make the mapping times prohibitively long. The next lowest average misorientation value is found when 2x2 binning and 2 frames of noise reduction are used at high gain and indexing with band edges, although it is only marginally lower than indexing with band centres at the same settings. The mapping times for these settings are also not prohibitively large, again shown in Fig. 4.8.

It should be noted that the average misorientation values given represent only the precision of indexing and not accuracy, and hence show only a small portion of the indexing error. The accuracy of the system refers to the degree of closeness of measurements to the true value, while precision refers to the reproducibility of the measurements under unchanged conditions. The accuracy of the orientation measurements is very difficult to determine since the true values are unknown. In fact, a true orientation measurement by Hough transformation is not possible since Kikuchi lines are actually curved cones but being approximated to line segments to make indexing easier. The Hough transformation method of indexing also does not take into account elastic strains present in the crystal which would affect the Kikuchi pattern. Instead, the orientation of a perfect crystal which best fits the captured EBSP is substituted. Other indexing methods, such as using a XCF, have been shown to have a superior accuracy than the Hough transformation. The XCF compares regions of interest of the recorded EBSP to a reference pattern of an unstrained crystal. The changes between the regions of interest in the two patterns allow elastic strains and rotations to be accurately detected to a resolution of +/- 0.01° [1][4].

4.3.3 Noise Reduction

The noise of indexing consists of a combination of the accuracy noise and the precision noise. The accuracy noise is not knowable, but the nature of the precision noise can be determined.

The information in Appendix A was replotted to check for normality and determine the shape of the precision noise. The vertical axis contains the ordered values of the misorientation from the average orientation for each index, and the horizontal axis contains the normal order statistic medians. A theoretical normal distribution should then appear as a straight line when plotted. The results are shown in Fig. 4.9.

With the exception of a few outlying points in the 0 binned graphs, indexing by band edges does not rule out a normal distribution. The high gain 2x2 binning graphs especially appear to show this. The same can not be said for indexing by band centres, which appears have a heavily right skewed distribution when there is any distribution at all. Inspection of the values in Appendix A for band centres shows that for low image noise settings, indexing repeatedly returned the same values. With 0 binning and 2 noise reduction, only 2 unique orientations were returned over 50 separate indexes of the same point. Obviously, the precision noise for band edges and band centres are shaped differently.

The approximate normality of band edges is of interest because it is may be corrected. The field of image analysis contains hundreds of noise correction algorithms which can be adapted for this purpose. One such algorithm, a fast algorithm to remove Gaussian noise in digital images, uses a convolution mask to estimate the standard deviation of the noise, and then averages the value of points within a window which deviate less than the calculated noise standard deviation [101].

The algorithm assumes noise is modelled as additive white Gaussian noise, where in the value at pixel X_{ij} deviates from it's original value by a noise value which follows a Gaussian curve.

$$X_{ij} = O_{ij} + G_{ij} \tag{4.2}$$

Where O_{ij} is the original value and G_{ij} is the noise value. To find the standard

deviation of the noise for an image of size M x N, a convolution mask is used.

$$^{M,N}|X * MASK_{(i,j)}|$$

$$\text{MASK} = \begin{pmatrix} 1 & -2 & 1 \\ -2 & 4 & -2 \\ 1 & -2 & 1 \end{pmatrix} \text{ !(4.3)}$$

Where * denotes the convolution operation. This process is Immerkaer's fast method [102]. The original algorithm proposed by Vijaykumar is as follows:

1. The noisy image is taken as X.
2. The noise standard deviation (SD) is found out using Immerkaers fast method.
3. A 2-D filtering window S_{ij} of size 3x3 is selected from the noisy image and let the center pixel be X(i,j). In the window, subtract each element with the center pixel and the absolute value of the difference is calculated as AD = $|S_{ij}$ X(i,j)| .
4. If the absolute difference AD ¡ (SF*SD) (where SF is the smoothing factor and SD is the standard deviation), store the corresponding pixels in a one dimensional array as DA(x).
5. If the number of elements in the DA(x) is at least (2*W) -1 (where W is chosen to be 3 for a 3 x 3 window) then the mean of DA(x) is calculated and replaced it at the center pixel X(i,j) of the window.
6. Else the window size is increased and the same process is repeated.
7. Steps 3-6 are repeated until the processing is completed for the entire image.

This algorithm was developed for noisy images so only pixels within common features are averaged, retaining the features without blurring them. This can be further adapted for use on GND maps as there is further physical feature information known that would not be known for simple images. Grains and grain boundaries may be accounted for to further improve the algorithm for this application.

GND values should not be averaged across grain boundaries as the dislocation structures between the two do not interact as easily as within the grain. However, points near grain boundaries may not have enough neighbours to successfully apply the convolution mask, but must still be accounted for in the noise standard deviation calculation as they tend to be more deformed regions, and hence have a different indexing noise. Zero points, which occur when the dislocation density tensor can not be calculated typically at grain boundaries and unindexed points, should also be disregarded. Points a far distance apart should also not be averaged as they most likely belong to different dislocation structures. The indexing accuracy of the system can also be affected by the orientation of the crystal, so the standard deviation of noise may be recalculated for each grain. In practice this was seen to have negligible effect on the value of the calculated noise standard deviation and so was not included in the refined algorithm.

The previous algorithm was altered to account for these concerns and presented as follows:

1. The noisy image is taken as X.

2. The noise standard deviation (SD) is found out using Immerkaers fast method. The points used in the convolution mask are weighted for their position in the mask (4 for centre, -2 for adjacent points, 1 for diagonal points). Points which are not part of the same grain as the centre pixel and unindexed points are weighted zero. If the total weight is zero, the point is used in the noise calculation.

3. A 2-D filtering window S_{ij} of size 3x3 is selected from the noisy image and let the center pixel be X(i,j). In the window, subtract each element with the center pixel and the absolute value of the difference is calculated as AD = $|S_{ij}$ X(i,j)|. Zero points are disregarded.

4. If the absolute difference AD < (SF*SD) (where SF is the smoothing factor and SD is the standard deviation), store the corresponding pixels in a one dimensional array as DA(x).

5. If the number of elements in the DA(x) is at least (2*W) -1 (where W is

chosen to be 3 for a 3 x 3 window) then the mean of DA(x) is calculated and replaced it at the center pixel X(i,j) of the window.

The window size is not increased and the process not repeated so as not to average dislocation structures which are not related.

This algorithm is applied to the calculated GND values and not the measured orientations. If two points with identical orientation are separated by a point with a different orientation this indicates the presence of lattice curvature and hence dislocations. In this theoretical set up, the middle orientation may differ due to local plastic strain or error in the orientation determination. However, it is not possible to know the magnitude to which either factor contributes to the measured orientation. Replacing the middle point with an average of the three orientations merely lessens or removes the implied lattice curvature, which may have already been an over or underestimate due to error. Averaging only the orientations of points with a misorientation within a calculated noise standard deviation would also not be suitable since their orientations alone do not specify their link to the dislocation structure. Any attempt to average measured orientations would merely smooth the orientation gradients, which is not the desired outcome of noise reduction. The desired outcome is an increase in the contrast of the features of a GND map.

A noise reduction algorithm recently proposed by Kamaya appears to present this in error [103][104]. As the step size decreases, the misorientation tends towards zero. However, due to indexing error, the slope of an average misorientation vs step size plot will not show a zero intercept. The algorithm proposed by Kamaya replaced the centre orientation of a 3x3 window with the average orientation of all points within the window belonging to the same grain. It was shown that this decreased the intercept on the average misorientation vs step size plot and it was suggested that the error had been decreased. However, multiple steps of orientation averaging will result in all points converging on a single orientation, and the average misorientation tending towards zero. As such, the reduction in the intercept on an average misorientation vs step size plot would be expected, and not because of any reduction of error, but because all misorientations are tending towards zero.

4.4 GND Code

Once the orientation map has been created, the GND values at each point may be calculated and a map created. Since the orientations are only available in a 2-dimensional plane, only the change in orientation in the two dimensions are required. There are many ways of calculating these values, each with their own advantages and disadvantages.

The most obvious option is to use an L-shaped kernel, of which there are 4 variants. A point is taken, a neighbouring point in the X-direction is used for X-direction orientation changes, a neighbouring point in the Y-direction is taken for Y-direction orientation changes, and the GND value is plotted at the coordinates of the original point. An example of this kernel shape is shown in Fig. 4.10. This kernel shape has the advantage of maintaining the step size used for mapping as the x of the orientation change calculation. In addition, depending on the grain boundary shape and kernel variant used, this kernel may be fully satisfied as close to a grain boundary as possible which may be desired. However, this kernel only uses 3 unique orientations in the calculation, which may result in a less robust calculation.

The next option is the X-shaped kernel. The map is divided into non-overlapping 2x2 windows. The X and Y directions are taken as the diagonal directions of the window. The crystal coordinate system that the orientations are measured in must be rotated by 45° to match this new coordinate system, so each orientation is multiplied by at rotation matrix representing a 45° rotation before calculation. The calculated GND value is then plotted at the coordinates of the centre of the 2x2 window. An example of this kernel is shown in Fig. 4.10. Using this kernel, the Δx for orientation change calculation is $\sqrt{2}$ times the step size, however 4 unique orientations are used in the calculation.

Once the elements of the lattice curvature tensor are calculated, the GND value is then resolved. Five elements of the dislocation density tensor and one difference [2] are found using the six known elements of the lattice curvature tensor. An L2 minimization, minimizing the sum of the squares of each dislocation type, is completed using a Moore-Penrose pseudo-inverse method (this was previously explained in Section 2.4.2.2). For FCC, only the basic 12 edge and 6 screw

type dislocations were considered. The pseudo-inverse coefficient matrix from Section 2.4.2.2 can be altered to include the difference element, shown in Fig. 4.11. The total GND content is then the sum of each dislocation type, or the sum of the absolute value of the solutions to each the pseudo-inverse equations.

Code was written in the Java programming language and can found in Appendix B. An applet was created for ease of use and parameter selection, but is not essential. Points with only half of the lattice curvature tensor available are set to zero.

4.4.1 GND Map Image Creation

A map of the GND value is created using a linear colour scale. A true colour reference scale image provided in Appendix C is 3000 pixels tall. An upper bounds and a lower bounds are set, and then divided into 3000 equal bins representing each pixel colour in the reference scale. At each point, a colour is assigned based on the bin value of its GND content. This is repeated for every point until an imagine is built up. Zero points are set to black.

Typically, the upper bounds of the scale is set to twice the mean of all non-zero GND values and the lower bounds set to zero. However, this can be changed to better suit each map, and is specified with each picture.

4.4.2 Grain and Boundary Detection

In order to correlate GND content with texture and proximity to boundaries, a grain detection algorithm was written to group points into grains. A grain is defined as a closed section of points with orientation within a predefined threshold. The algorithm is as follows:

1. A point not yet assigned to a grain is found. A new grain is created and this point added. A list of the grain's outer points is also created and this point is added.

2. Points adjacent to the grain's outer points are checked to see if they have yet to be assigned to a grain. If they have not, it is checked if they belong to the same grain as the adjacent point which called it (this is done by checking if

the misorientation is below a user defined critical value) and it is added to the grain.

3. The points in the outer points list are replaced by a list containing the points added to the grain in step 2.

4. Steps 2 and 3 are repeated until no new points are added.

5. Steps 1, 2, 3, and 4 are repeated until all points belong to a grain.

A boundary detection algorithm was then added. For this purpose, a boundary is defined as a group of points within a user defined distance of the interface of two grains. The algorithm is as follows:

1. The first grain in the list is taken. The grain associations of points adjacent to the outer points are checked and a list of grain pairs created.

2. Step 1 is repeated for all grains, and all grain pairs added to the list.

3. The list of grain pairs is corrected for redundancy.

4. The first grain pair in the list is taken and a new boundary created. The outer points of each grain are added to the boundary if they are adjacent to an outer point in the opposing grain.

5. All points in each grain are then checked if they are within the boundary. This is done by finding the nearest point in the opposing grain and checking if the absolute distance is less than a critical value.

6. Steps 4 and 5 are repeated for all grain pairs.

Because a boundary is merely a group of points within a predefined distance of a feature, points may belong to more than one boundary. Points near triple junctions often belong to two boundaries.

4.5 Comparison With XCF

The XCF is a method of high resolution EBSD orientation determination. Regions of interest are highlighted in an EBSP and compared to a strain free pattern of known orientation. Small shifts in the position of regions of interest allow the elements of a rotation tensor from the reference pattern to be determined. A full explanation of the technique can be found in the literature [1][105].

For the purposes of a comparison, one map was created at Swansea University and the EBSPs were sent to Oxford University for XCF analysis. The map was taken from a section sample 20F, near the tip of the tensile deformed region of the fold. The results are presented in Fig. 4.12 to 4.16.

XCF is an image analysis technique and so requires the highest quality images possible to be most effective. Because of this, no image binning was used and the patterns were saved at the highest possible resolution with two frames averaged for noise reduction. The Hough transformation used a high Hough space resolution and indexed with band centres. As can be seen in Fig. 4.13, the overall pattern quality is very high. The GND map created using XCF used an energy L1 minimization compared to an L2 minimization for the Hough map. The XCF map shows peaks of high GND content which gradually decrease, and generally appears much less noisy than the Hough map. However, there is good feature retention between the two maps. Regions of high GND content, in front a boundary near the left and a triple junction near the top of the image, are retained from one method to the other.

While the Hough method results in a GND map with more noise, the underlying GND structure is still apparent and peaks match those from the XCF method.

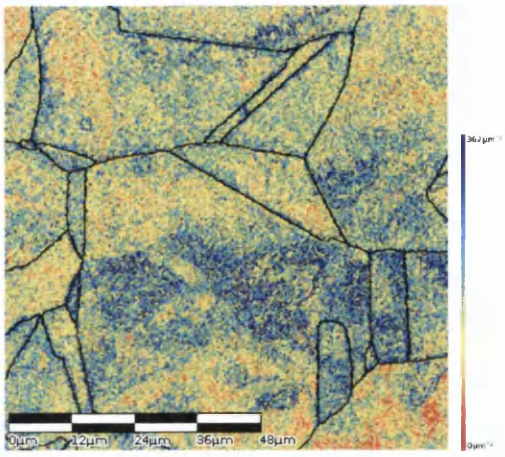

(a) 0.2μm step size

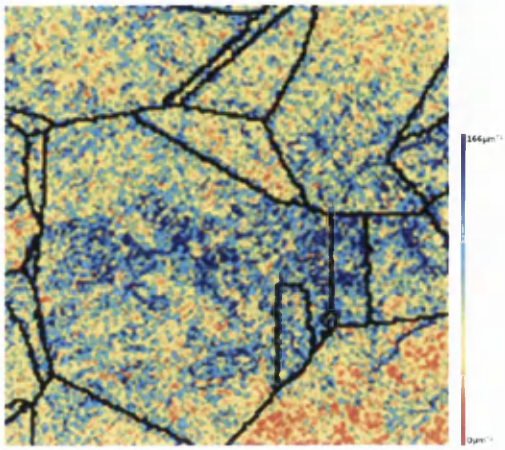

(b) 0.5μm step size

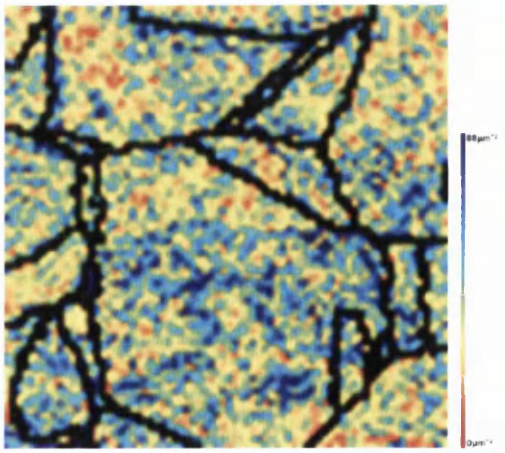

(c) 1μm step size

Figure 4.5: Effect of step size on resulting GND maps. All maps were created using 2x2 binning and 2 frames of noise reduction while indexing by band edges.

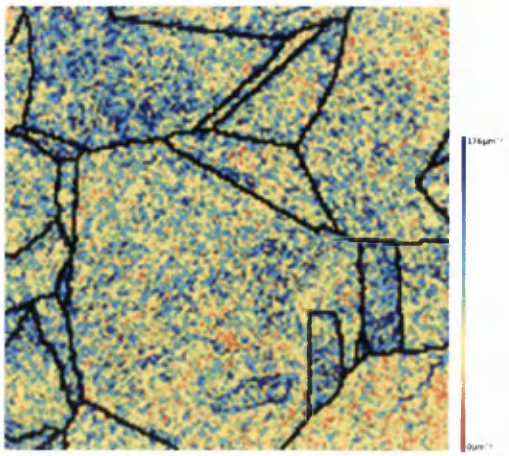

(a) 0 Binning

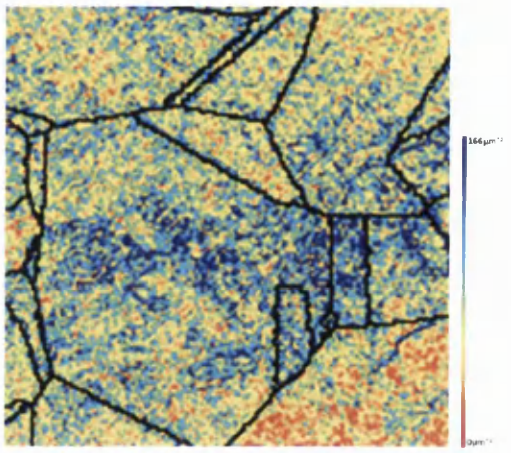

(b) 2x2 Binning

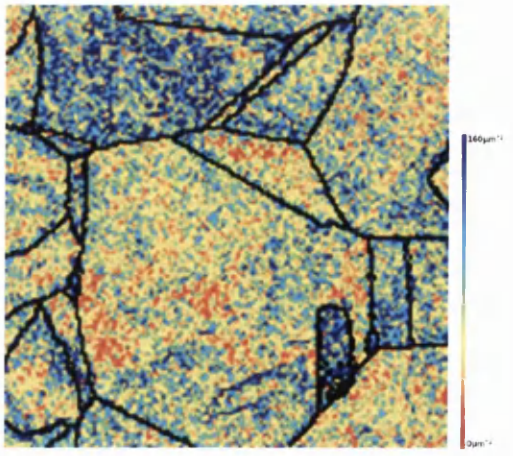

(c) 4x4 Binning

Figure 4.6: Effect of EBSP image resolution on resulting GND maps. All maps were created using a 0.5μm step size and 2 frames of noise reduction while indexing by band edges.

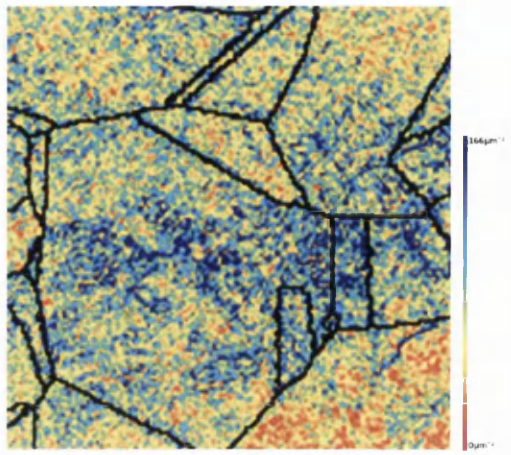

(a) Band Edges

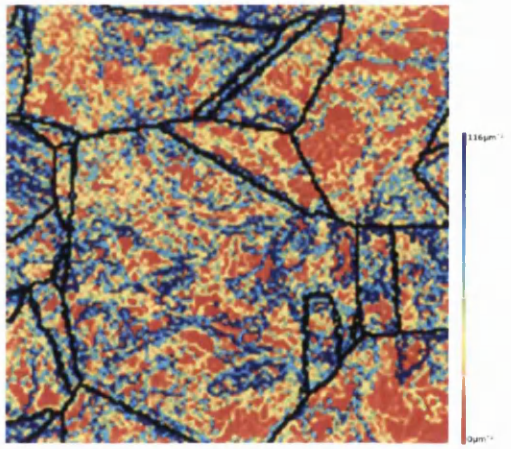

(b) Band Centres

Figure 4.7: Effect of method of indexing on resulting GND maps. Both maps were created using a 0.5μm step size, 2x2 binned EBSP patterns, and 2 frames of noise reduction.

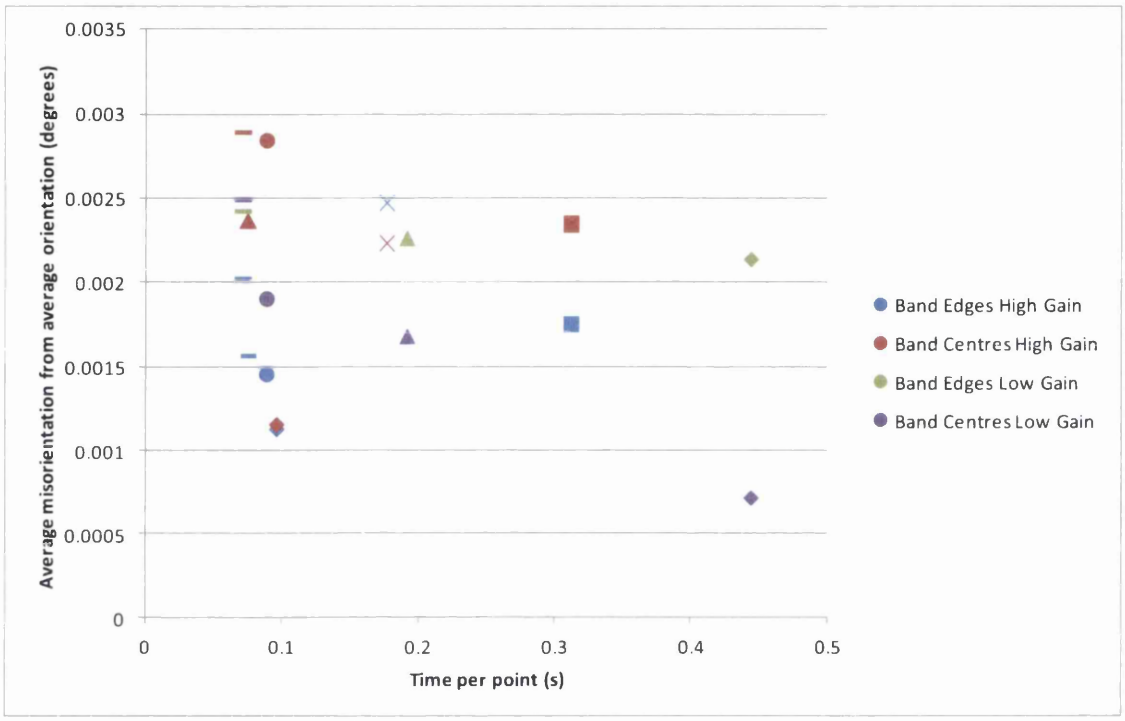

Figure 4.8: Average misorientation from the average orientation vs indexing time per point for points collected with various settings.
0 Bin 1 Noise = X shape
0 Bin 2 Noise = Square
2 Bin 1 Noise = Triangle
2 Bin 2 Noise = Diamond
4 Bin 1 Noise = Dash
4 Bin 2 Noise = Circle

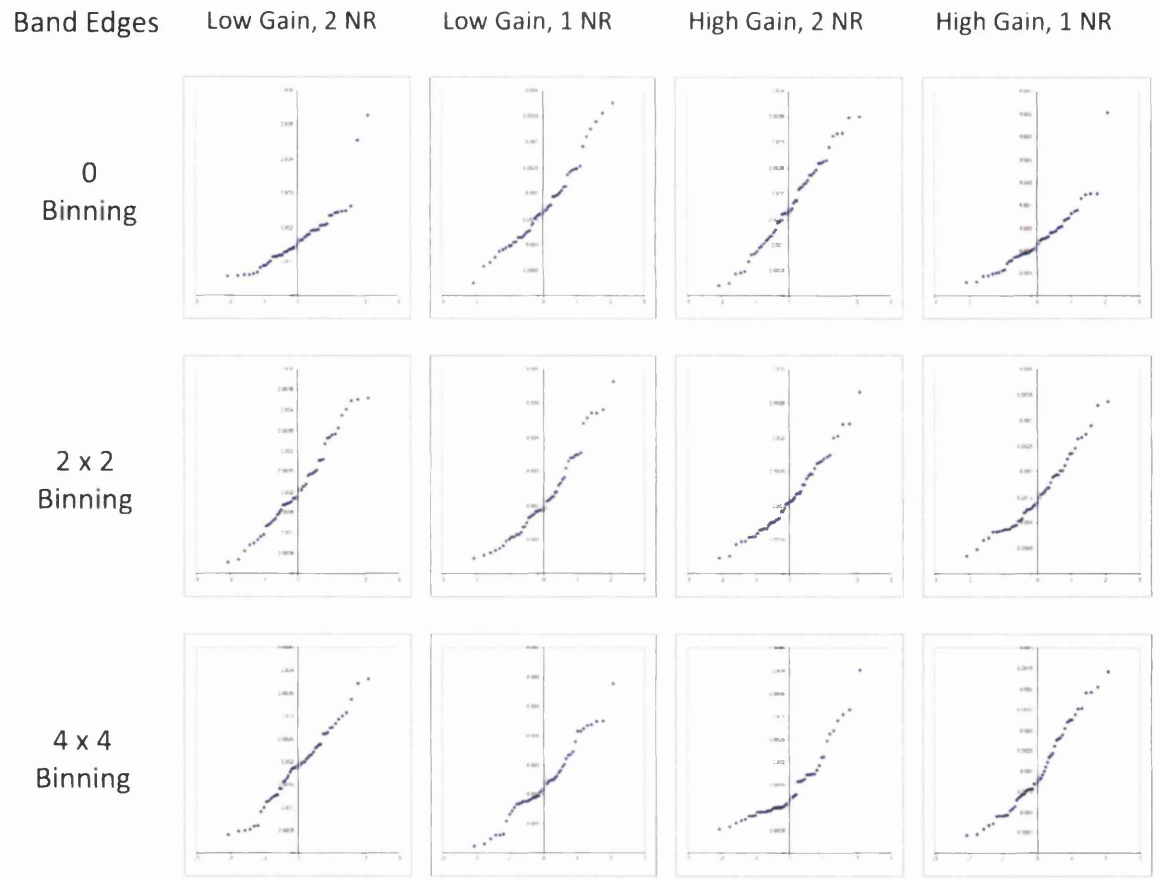

Figure 4.9: Normality check plots of various settings for indexing by band edges. The misorientation from average orientation values are ordered and plotted against the ordered expected values for a perfectly normal distribution. If the distribution is normal, it should be represented by a roughly linear plot with a slope of 1.

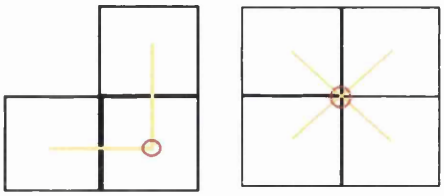

(a) L-Shaped Kernel (b) X-Shaped Kernel

Figure 4.10: Example of kernel shapes. Yellow lines show lattice curvature calculation and red circle shows point at which the GND content is plotted.

$$
\begin{bmatrix} \rho_1 \\ \rho_2 \\ \rho_3 \\ \rho_4 \\ \rho_5 \\ \rho_6 \\ \rho_7 \\ \rho_8 \\ \rho_9 \\ \rho_{10} \\ \rho_{11} \\ \rho_{12} \\ \rho_{13} \\ \rho_{14} \\ \rho_{15} \\ \rho_{16} \\ \rho_{17} \\ \rho_{18} \end{bmatrix} h = \begin{bmatrix} 7c & -13c & -7c & 13c & 0 & (a-0) \\ 13c & -7c & -c & c & a & (-a-a) \\ c & -c & -13c & 7c & -a & (0--a) \\ -7c & 13c & 7c & 13c & 0 & (a-0) \\ -13c & 7c & c & c & a & (-a-a) \\ -c & c & 13c & 7c & -a & (0--a) \\ -7c & -13c & 7c & -13c & 0 & (a-0) \\ -13c & -7c & c & -c & a & (-a-a) \\ -c & -c & 13c & -7c & -a & (0--a) \\ 7c & 13c & -7c & -13c & 0 & (a-0) \\ 13c & 7c & -c & -c & a & (-a-a) \\ c & c & -13c & -7c & -a & (0--a) \\ e & 0 & e & 0 & -d & (5d--d) \\ 0 & e & 0 & 0 & 5d & (5d-5d) \\ 0 & 0 & 0 & e & 5d & (-d-5d) \\ -e & 0 & -e & 0 & -d & (5d--d) \\ 0 & -e & 0 & 0 & 5d & (5d-5d) \\ 0 & 0 & 0 & -e & 5d & (-d-5d) \end{bmatrix} \begin{bmatrix} \\ \\ \\ \\ \\ \\ \\ \\ \\ \\ \\ \alpha_{12} \\ \alpha_{13} \\ \alpha_{21} \\ \alpha_{23} \\ \alpha_{33} \\ \alpha_{11} - \alpha_{22} \end{bmatrix}
$$

where $a = \frac{\sqrt{3}}{9}$ $c = \frac{\sqrt{3}}{84}$ $d = \frac{1}{18}$ $e = \frac{3}{14}$

Figure 4.11: A modified Moore-Penrose pseudo-inverse showing the available dislocation density tensor components and the one difference.

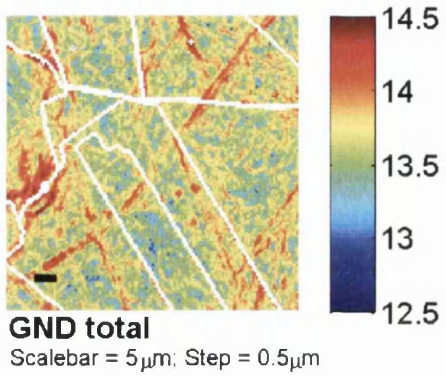

Figure 4.12: GND map created by indexing EBSPs by XCF method.

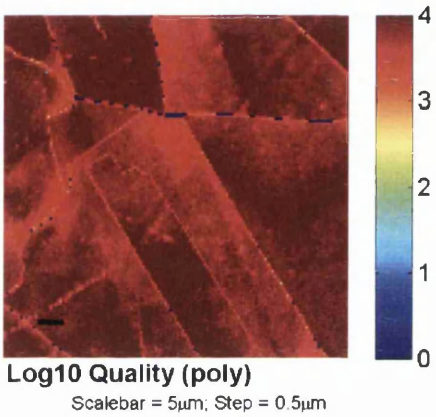

Figure 4.13: Map of quality of EBSPs used for GND map.

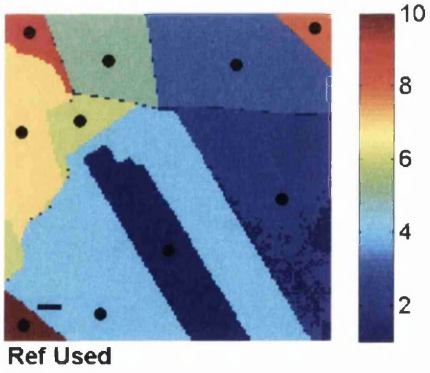

Figure 4.14: Map of pattern chosen as the strain free reference pattern for XCF analysis.

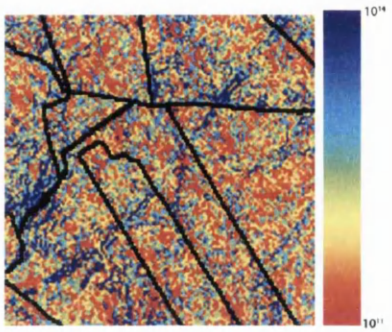

Figure 4.15: GND map created by indexing using a Hough transformation. The same EBSPs were used as with the previous XCF GND map.

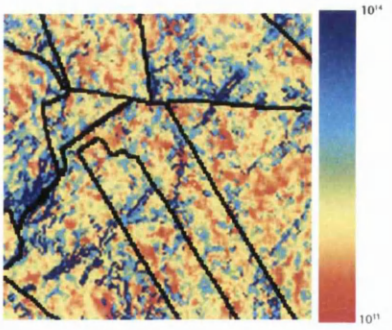

Figure 4.16: GND map created by indexing using a Hough transformation and de-noised. The same EBSPs were used as with the previous XCF GND map.

Chapter 5

Pilot Sample Set

The first set of samples were created and named according to Fig. 3.3 in Section 3.2. Samples of copper were cut from a 3mm thick piece of 99.9% pure copper obtained from Goodfellow Ltd. The samples were given an initial pre-treatment at 750°C to grow the grains and relieve some of the internal stresses in the material when received in the half hard state. A sample named Pilot 1 was set aside and the remaining two samples were bent around a pipe of 23mm radius. At this stage, one sample named Pilot 2 was set aside, and the remaining sample was given an additional heat treatment at 750°C for 45min. This final sample was named Pilot 3.

5.1 Microstructural Development of Pilot Samples After Bending and Annealing

The sample cross sections were mapped by EBSD, oriented according Fig. 5.1, with the red box representing the area shown in each map. The resulting maps are shown in Fig. 5.2 to 5.4.

The initial sample, Pilot 1, having received no deformation step shows equiaxed grains across the cross-sectional area. After bending, sample Pilot 2 shows slightly larger grains in front of smaller grains at the compressive end. To a lesser extent, the same is observed in the tensile region with slightly larger grains in front of smaller ones. The larger grains have been slightly elongated by the applied strain.

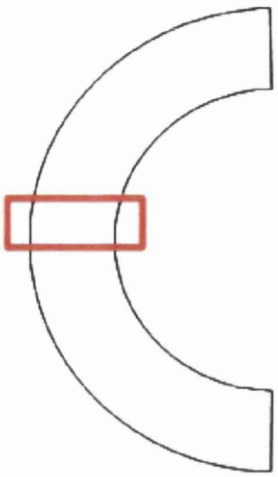

Figure 5.1: Pilot sample set cross-section map orientation. Maps were created across the width of the bend.

Upon heating, sample Pilot 3 shows noticeably larger grains in front of smaller ones at both ends of the sample in the tensile and compressive regions. These larger grains grow towards the centre of the sample, sandwiching larger grains in between them.

The samples appear to follow the grain growth patterns of folded samples of nickel in a study by Singh et al. [106]. Samples of nickel were folded to 90° and then heated. The high amount of strain resulted in elongated grains in the tensile and compressive regions, which were replaced by equiaxed grains upon heating. As recrystallization progressed, these grains did not grow, but larger grains formed in the region ahead of them. The trend continued until the centre, where the largest grains were found after sufficient heating times.

The pilot samples appear to follow the same trend as the samples of nickel, however differing in the amount of strain. The smaller amount of strain appears to create slightly elongated grains, but they are only significantly noticeable in the compressive region. Upon heating, larger grains appear in front of smaller grains at the absolute edges of the sample. These larger grains grow towards the centre of the sample, sandwiching smaller grains in between. Based on the folded nickel example, if the heat treatment were continued the larger grains would continue to form into the centre of the sample, resulting in the largest grains forming in the centre of the sample. The average grain sizes by area are shown in Fig. 5.5.

Figure 5.2: Cross-section of sample Pilot 1. Compressive end is pictured on the right. Average grain size was measured and is provided in Fig. 5.5.

Before and after bending, the average grain size slightly increases. The average grain size in the compressive region is larger than in the tensile region, which is consistent with the more elongated grains previously observed in the region. The centre region also shows a slightly higher grain size than the tensile region, which may indicate that the geometric centre of the sample may not be the exact centre of bending. Upon heating, the grains in the tensile and compressive end experience significant grain growth, while the centre section experiences grain growth to a lesser degree which is again consistent with the large grains at each end sandwiching smaller grains in Fig. 5.4.

A map of $\Sigma 3$ boundaries can be seen in Fig. 5.6 which shows a band contrast map of the sample with $\Sigma 3$, $\Sigma 9$, $\Sigma 27a$ and $\Sigma 27b$ highlighted in red, blue and yellow respectively. CSL boundaries were classified according to the Brandon criterion [18].

$\Sigma 3$ boundary fractions appear higher before the final anneal step, in the Pilot 1 and Pilot 2 samples. This is despite the tensile and compressive ends of sample Pilot 3 appearing significantly twinned. The strain ($\sim$6% at each end) and heat treatment temperature (750°C) are typical of strain annealing GBE regimens [107] used to promote twinning and break-up the random grain boundary network. Typical GBE regimens, however, apply iterations of strain and short time anneals (typically $\sim$3min) in order to control the final grain size. Instead, one long 45min anneal after strain was used to observe the formation of twins. As a result, each end of sample Pilot 3 is heavily twinned but with significantly larger grain size than the previous samples.

5.2 GND Analysis of Pilot 3

Using the orientation map shown in Fig. 5.4, a map of GND content of sample Pilot 3 was created according to the methods described in Section 4 in order to give insight into the formation of the twinned boundaries. The resulting GND map is shown in Fig. 5.7.

The map of Fig. 5.7 is very similar to the corresponding band contrast map, shown in Fig. 5.6. The similarities between the two maps are to be expected as the band contrast has been shown to be linked to the plastic strain level [108].

Electron diffraction is hindered by a more deformed crystal, resulting in lower band contrast. The point-to-point orientation changes caused by this plastic strain would then create a GND map with similar features to the band contrast map.

The band contrast is only an indicator of pattern quality, which can be linked to plastic strain if other factors such as surface condition are ruled out. A lowered band contrast could lead to a lower indexing accuracy due to lower EBSP pattern quality, which would cause the relation to high GND content. In this case, the lowered band contrast could be the cause of high GND content calculations without the region actually having high plastic strain.

This does not appear to be the case as areas of low band contrast do not always show high GND content. This indicates that the lowered band contrast does not significantly affect the indexing accuracy and directly cause high GND content readings. It also shows that the GND map gives insight into the plastic strain state of the material that would not be known using the band contrast map alone.

Inspection of the tensile and compressive regions shows high GND content (coloured blue) contained within certain grains. A zoomed in image of the tensile region, shown in Fig. 5.8 highlights this.

Certain grains appear to exhibit high GND content in each of the tensile, centre, and compressive regions of the sample. This implies a texture relation to GND content. The high content grains are likely caused by the twinning of a low content parent grain. As shown in Fig. 5.6, the high GND content grains of Fig. 5.8 are all twin related to a low GND content grain. Also, as seen in Fig. 5.9, grains within twin related domains in the tensile region alternate between high and low GND content.

The high GND content grains appear to be forming due to twinning, and can be explained using the preferential formation of recrystallization textures.

The deformation texture will determine the recrystallization texture upon annealing. For example, a copper type rolling texture ({112}<111>) would be expected to form a cube texture upon recrystallization ({001}<100>)[109]. This is due to the oriented growth of grains determined by the direction of strain. The strain energy release model (SERM) for recrystallization texture states that recrystallized grains will form such that the direction of the minimum Young's modulus will align with the direction of the maximum internal stress due to dislocations

formed during deformation [110]. The maximum internal stress direction may be obtained by the operating slip systems, which come from the deformation texture. It can be determined by the vector sum of activated slip systems, weighted by their contribution to slip. This alignment is shown in Fig. 5.10.

Grains with the minimum Young's modulus aligned with the direction of maximum internal stress grow preferentially so as to release as much internal stress as possible. As the grain grows, stacking faults occur, changing the direction of minimum Young's modulus and disallowing the maximum release of internal stress and causing plastic strain as the grain continues to grow. Alternatively, as obstacles to grain growth are encountered, a grain may form twins in order to continue growing. This would imply that the energy of the retained internal stress be lower than the energy of the barrier to grain growth and the energy of the twin boundary combined.

The Young's modulus in copper is at a minimum in the <100> directions at ~67 GPa, a maximum in the <111> directions at ~192 GPa, and approximately isotropic for polycrystalline copper at ~111 GPa [111]. The texture of the sample series is presented in Fig. 5.11 to investigate the texture of these directions.

Initially, sample Pilot 1 does not appear very textured. The material was obtained from Goodfellow Ltd. Half-hard, having been cold rolled. This cold rolling direction would be parallel to the direction currently set as the sample normal direction, and the normal direction of the cold rolling would be the direction currently set as the rolling direction. If these changes were applied, the pole figures of Fig. 5.11 for sample Pilot 1 and Pilot 2 exhibit a faint copper type rolling texture. However, the expected densities of these peaks are not significant.

The {100} plane normals appear to focus around the sample normal direction, at and between, the cubic directions. Accordingly, the {111} plane normals appear parallel to the sample normal direction and at the rolling direction poles. While {111} normals have peaks at each of the rolling, transverse, and normal directions in sample Pilot 1, after bending the transverse direction is not preferred.

Upon annealing, significant grain growth occurs in the tensile and compressive regions and high GND content grains appear in all three regions. Fig. 5.13 shows the texture in each region of sample Pilot 3. The texture measurement was repeated with high GND content grains removed from the subset. Texture mea-

surements of the tensile and centre regions appear to show that high GND content grains have a random texture. Removal of them from the subset strengthens the copper type rolling texture. The compressive region does not have enough grains to gather any significant texture measurements, although it appears it could follow the same trend if a larger area were measured.

Low GND content grains appear to have the low Young's modulus <100> directions preferred away from the sample normal direction. In the tensile region, and partially in the centre region, this is the direction of the compressive strain. Too few grains are sampled in the compressive region, although it appears that this same trend could be followed if a large sample size were taken.

Grains with low GND content and the preferred texture grow preferentially due to the internal stress energy released by this orientation. If the driving force for boundary migration is low, as the grain grows, barriers to grain growth are encountered. In order for the grain to continue growing, a twin may form. The twin may not have the preferred texture, and hence not be aligned for maximum release of internal stress, forming a high GND content grain. This is likely the mechanism causing twinning and perceived high GND content grains in the centre section of the sample, where the lower deformation provides a lower driving force for boundary migration.

Alternatively, if the driving force for grain growth is sufficiently high and boundary migration is sufficiently fast then stacking errors may occur during boundary migration. The new twinned orientation is, again, not properly aligned for maximum internal stress release and produces a high GND content grain. This is likely the mechanism causing twinning and high GND content grains in the deformed regions where the high deformation causes a driving force for boundary migration [49].

Certain grains in each region are difficult to classify using a binary definition of high or low GND content. It is likely that they are grains twin related to low GND content grains, but with a twinned orientation close to a low GND content orientation. This poses an interesting question for the selection of twin variant formed: if certain twin variants have an unfavourable texture, why are they formed in favour of twin variants with a texture which exhibits lower deformation?

This is likely due to the direction of boundary migration and the geometry

of the grain boundary. In a study of twin formations in a copper tri-crystal, it was found that the twin variant formed would be the one with a plane normal closest to the direct of grain boundary migration, regardless of the Schmid factors of the parent grain [51]. The twin variant formed is dependent on the direction of boundary migration and is formed either by growth accident or by a mechanism to allow the grain to continue growth. It is not the twin variant which would provide the lowest system energy.

5.2.1 Effect of Lowered Accuracy on Interpretation of GND Analysis of Sample Pilot 3

The texture relation to GND content is assumed based on the accuracy of the GND map. However, the accuracy of GND maps are dependent on the conditions of their creation. The map of Fig. 5.7 was created using a 2μm step size, 4x4 EBSP image binning, 2 frames of noise reduction, and 100 Hough space resolution. These settings are not the ideal for GND mapping determined in Section 4. The effects of the step size on this particular map are shown in Fig. 5.14.

As explained in Section 4.3, ideally the step size used for mapping would be on the order of a dislocation length. This is not possible due to spatial resolution and external mapping time restrictions, as well as the indexing accuracy not being sensitive enough to detect the small amount of dislocations characteristic with such step sizes. For these reasons, the step size is kept as small as possible to obtain an accurate map. However, the step size used to map sample Pilot 3, 2μm, can be so large that features of the dislocation content are hidden. Fig. 5.14 shows the results of lowering the step size on a section of the tensile region of sample Pilot 3. As the step size decreases, micro-scratches not visible at the 2μm step size become apparent. These micro-scratches are created during the surface polishing of the sample and may have affected the results. Investigation of the orientations of the grains from Fig. 5.8 reveal a possible explanation.

Grains shown in Fig. 5.8 to have high GND content are shown in Fig. 5.15 to have a <111> pole close to parallel with the sample normal. The family of {111} planes are close packed, and are more resistant to micro-scratching during polishing. Instead of a texture effect on GND content, the low GND measurements

for these grains may be as a result of them being more resistant to deformation during polishing and the step size being large enough to mask the presence of the scratches.

A subset of the tensile region of sample Pilot 3 was taken and an inverse pole figure of the sample surface normal created. This was repeated for the same area of the tensile region with grains of high GND content removed, and shown in Fig. 5.16.

Low GND content orientations show a preference for <111> directions at the sample surface normal, shown by the strengthening of the fibre texture after removal of high GND content grains. This, again, causes doubt as to the texture relation to GND content.

In order to test the apparent texture relation to GND content, a GND map would need to be created using ideal settings (recommended settings are given in Section 4.3). Unfortunately, a suitable surface condition was not possible for sample Pilot 3. Micro-scratches and surface contamination could not be removed by manual preparation methods (attempts at a map with recommended settings are shown in Appendix D). Further sample sets (folded and matrix samples) were created for this purpose.

Despite this, certain grains in the tensile and compressive end with a <111> direction parallel to the sample normal were still observed to have high GND content, so the texture relation to GND content can not be disregarded. This example serves to highlight that GND maps should be interpreted based on the methods used to create them.

Figure 5.3: Cross-section of sample Pilot 2. Compressive end is pictured on the right. Average grain size was measured and is provided in Fig. 5.5.

Figure 5.4: Cross-section of sample Pilot 3. Compressive end is pictured on the right. Average grain size was measured and is provided in Fig. 5.5.

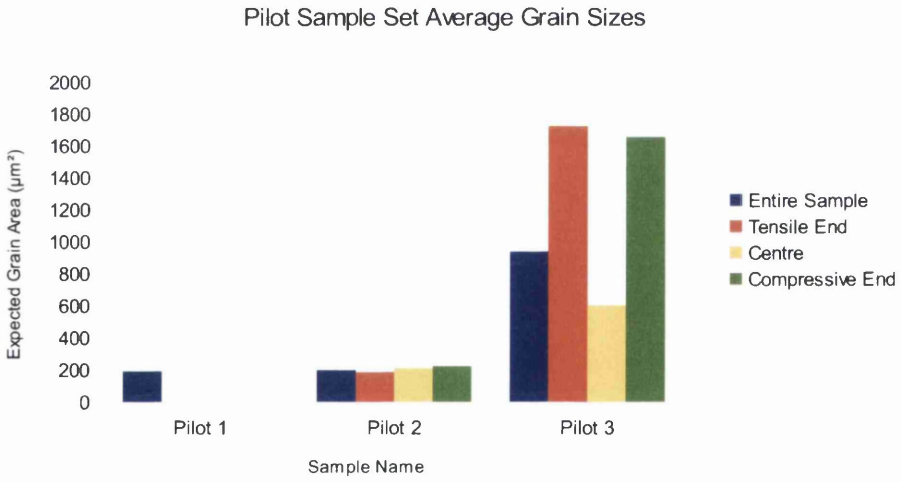

Figure 5.5: Pilot sample set average grain sizes. Average areas of grains in each sample, and each region within each region is plotted.

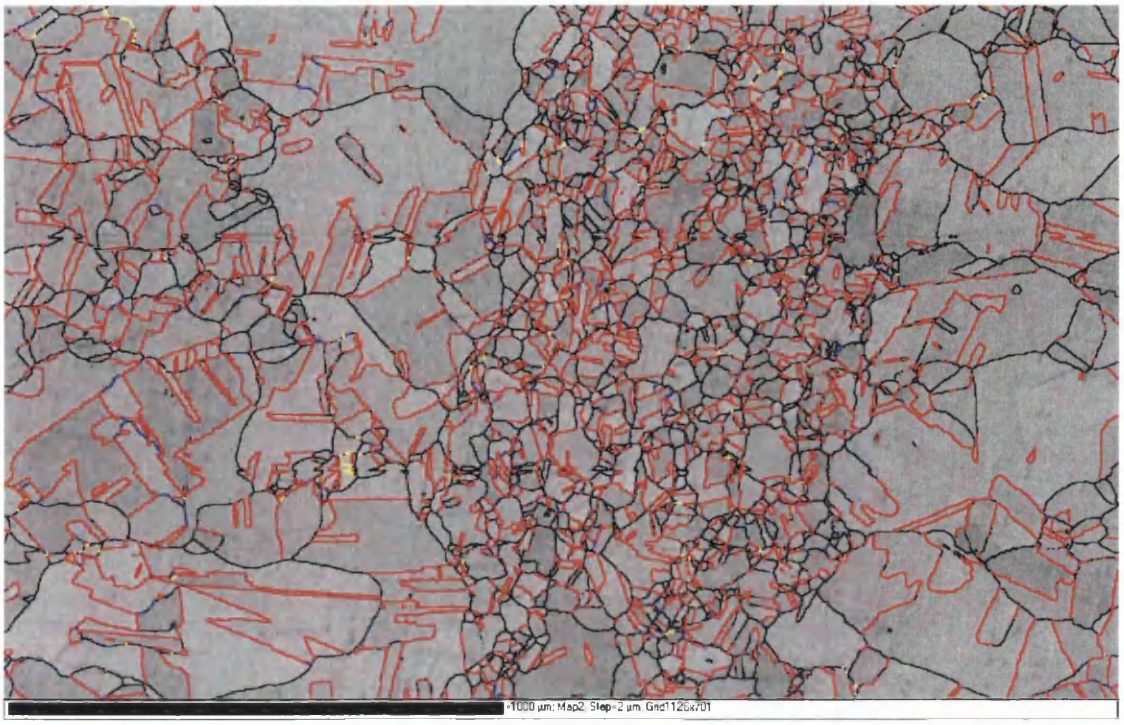

Figure 5.6: Cross section of sample Pilot 3. A grey-scale based on the band contrast is used, with Σ3 boundaries in red, Σ9 boundaries in blue and Σ27a and b in yellow.

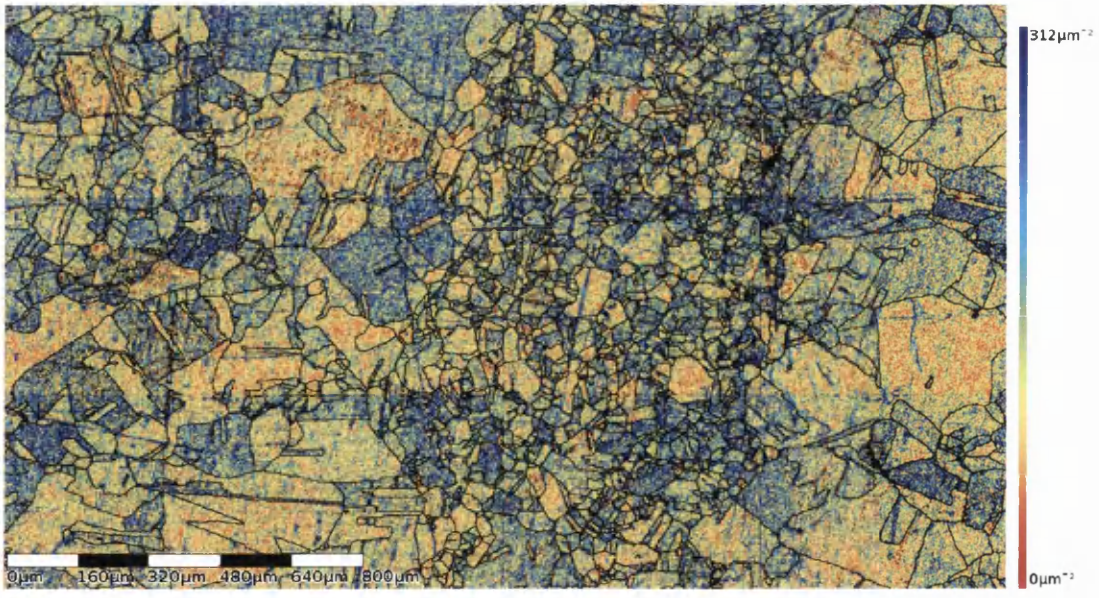

Figure 5.7: GND map of sample Pilot 3.

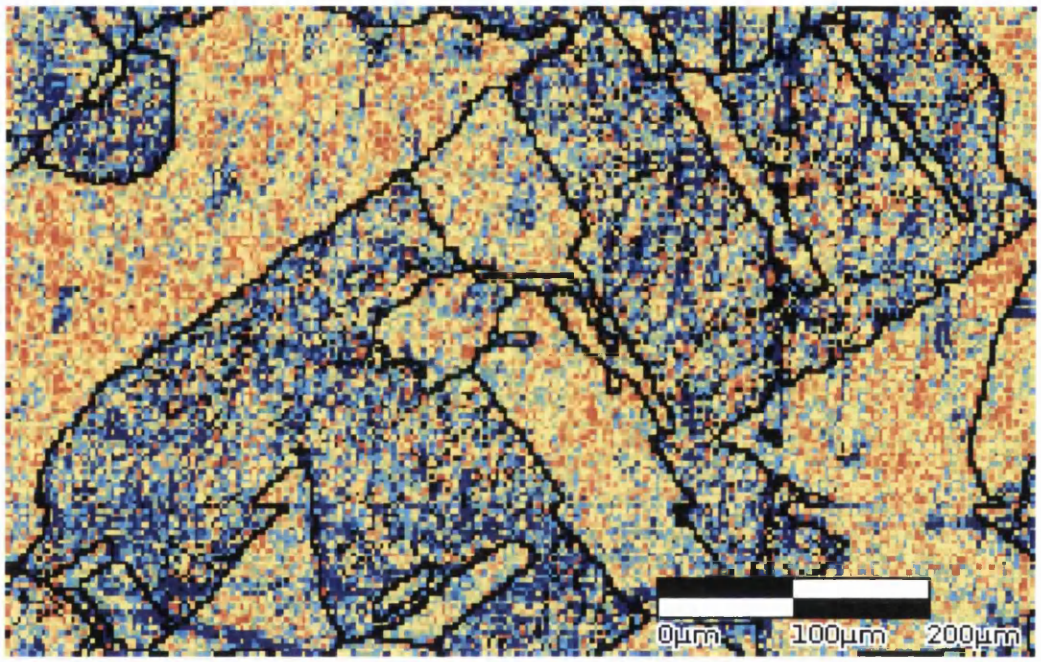

Figure 5.8: Small section of grains from sample Pilot 3 GND map in the tensile region. High GND content (coloured blue) appears preferred in certain grains.

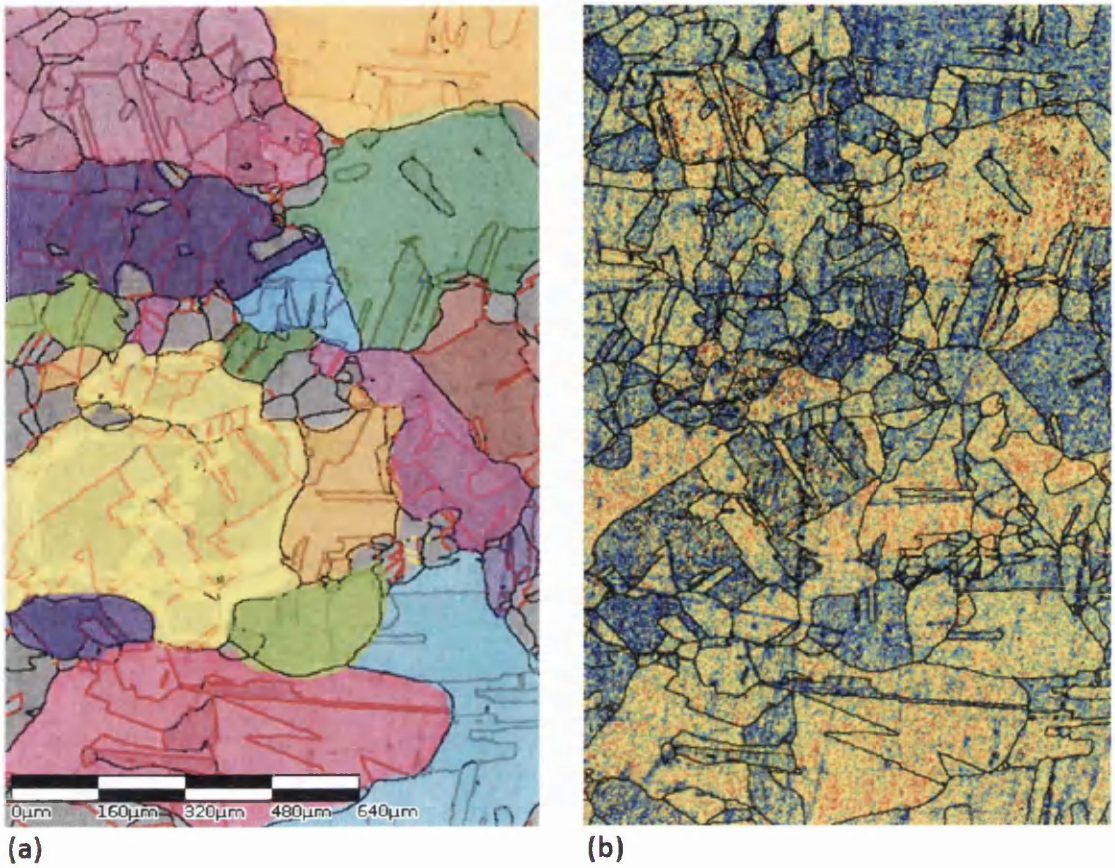

Figure 5.9: (A) Band contrast map of section from tensile of sample Pilot 3. Σ3 boundaries shown in red and Σ9 boundaries shown in blue. (B) GND map of same tensile section. High GND content shown in blue.

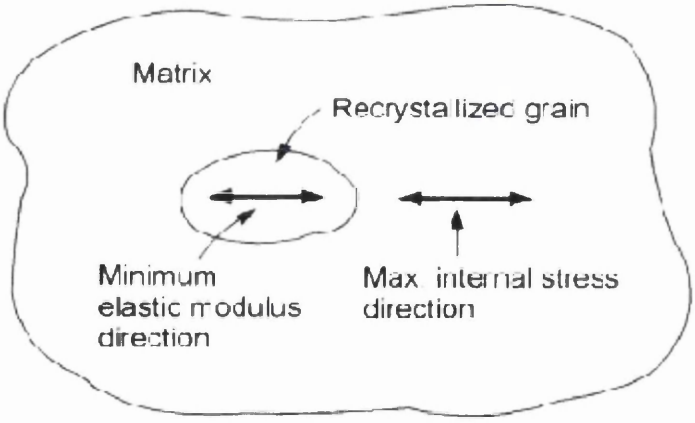

Figure 5.10: Alignment of recrystallized grains based on SERM model [110].

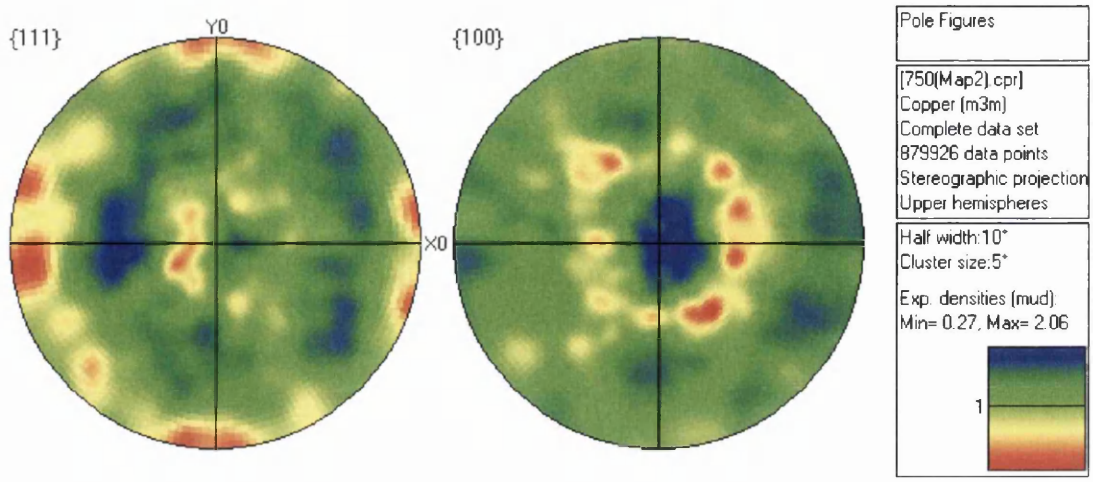

(a) Pilot 1

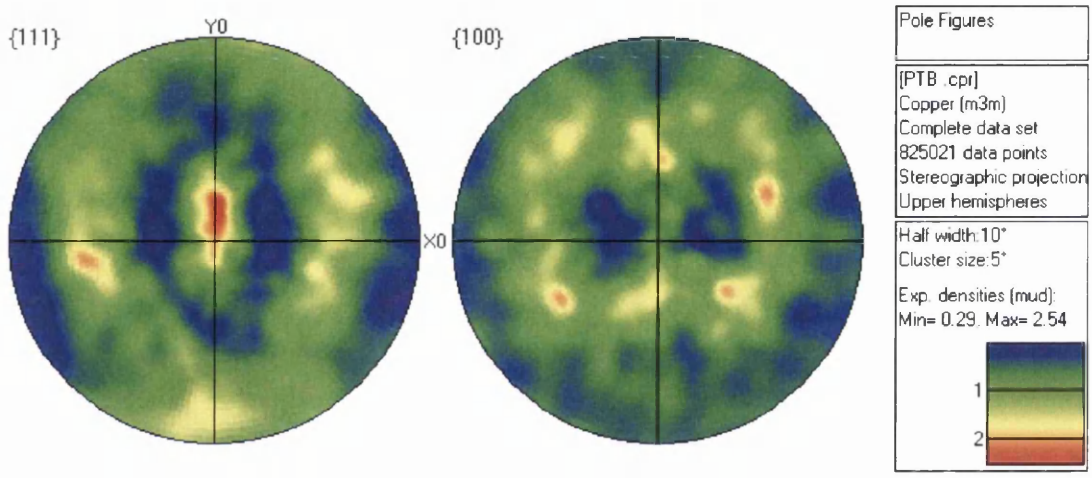

(b) Pilot 2

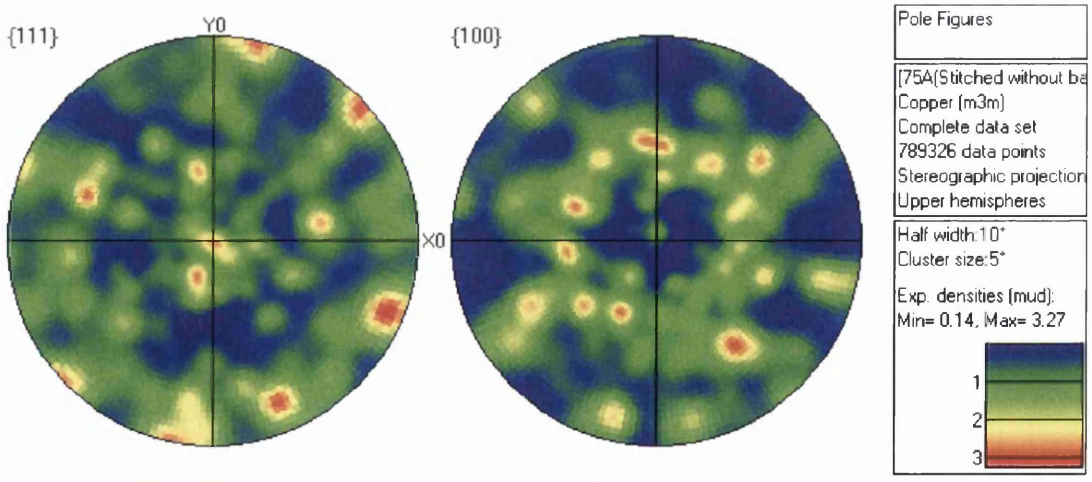

(c) Pilot 3

Figure 5.11: Pole figures of plane normals {111} and {100} for samples (A) Pilot 1, (B) Pilot 2, and (C) Pilot 3.

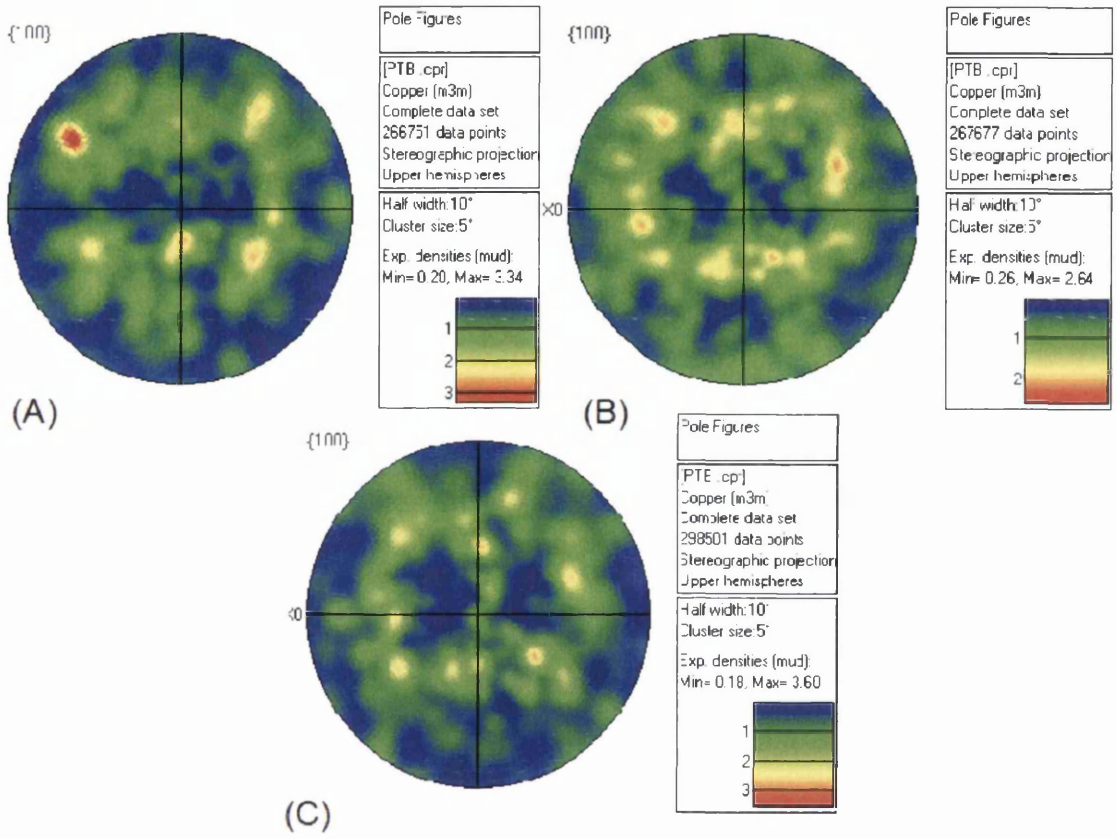

Figure 5.12: Pole figures of {100} normals in sample Pilot 2 in each of the (A) tensile region, (B) centre region, and (C) compressive region.

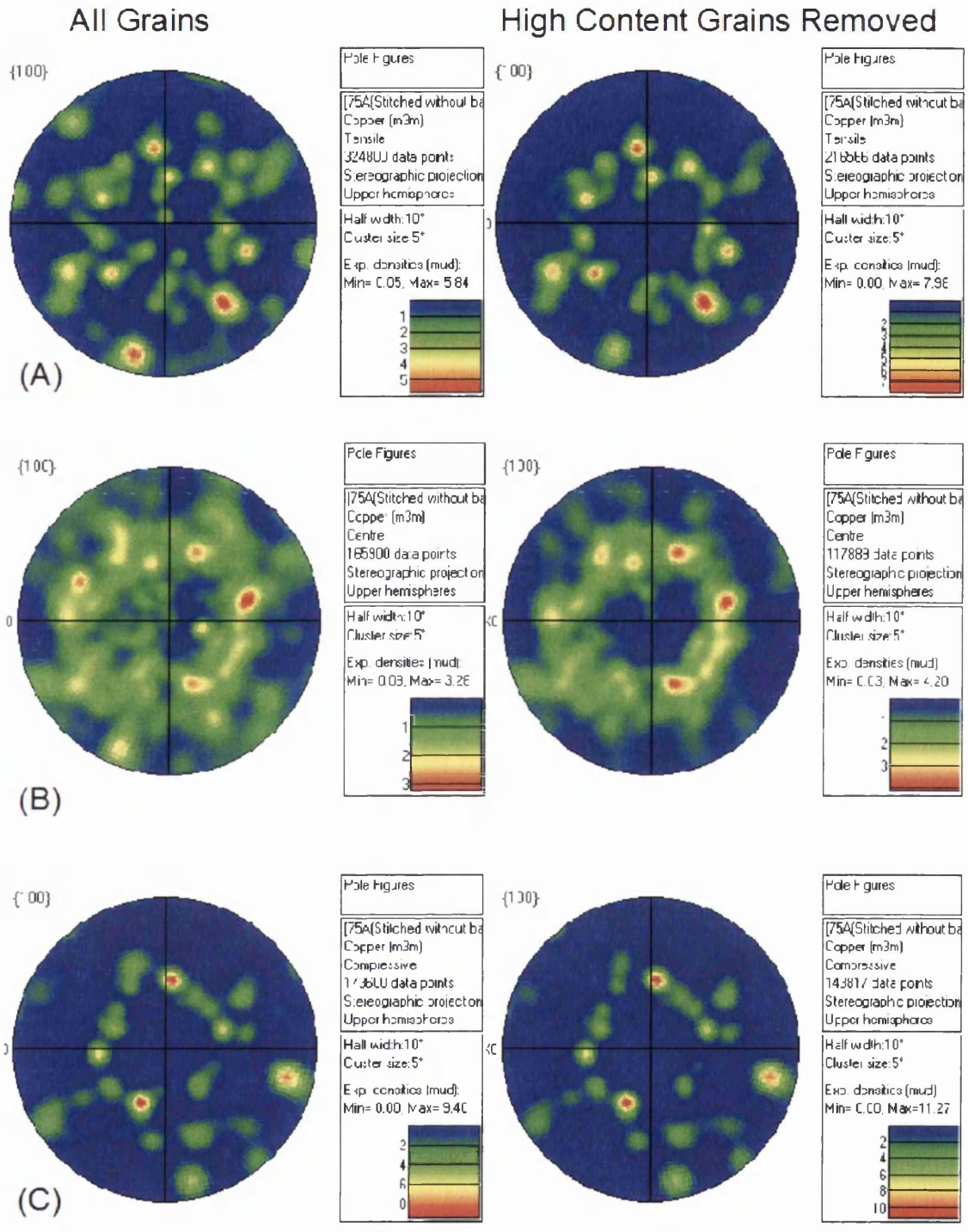

Figure 5.13: Pole figures of {100} normals of sample Pilot 3 with both all grains and high content grains removed. (A) Tensile region (B) Centre region (C) Compressive region.

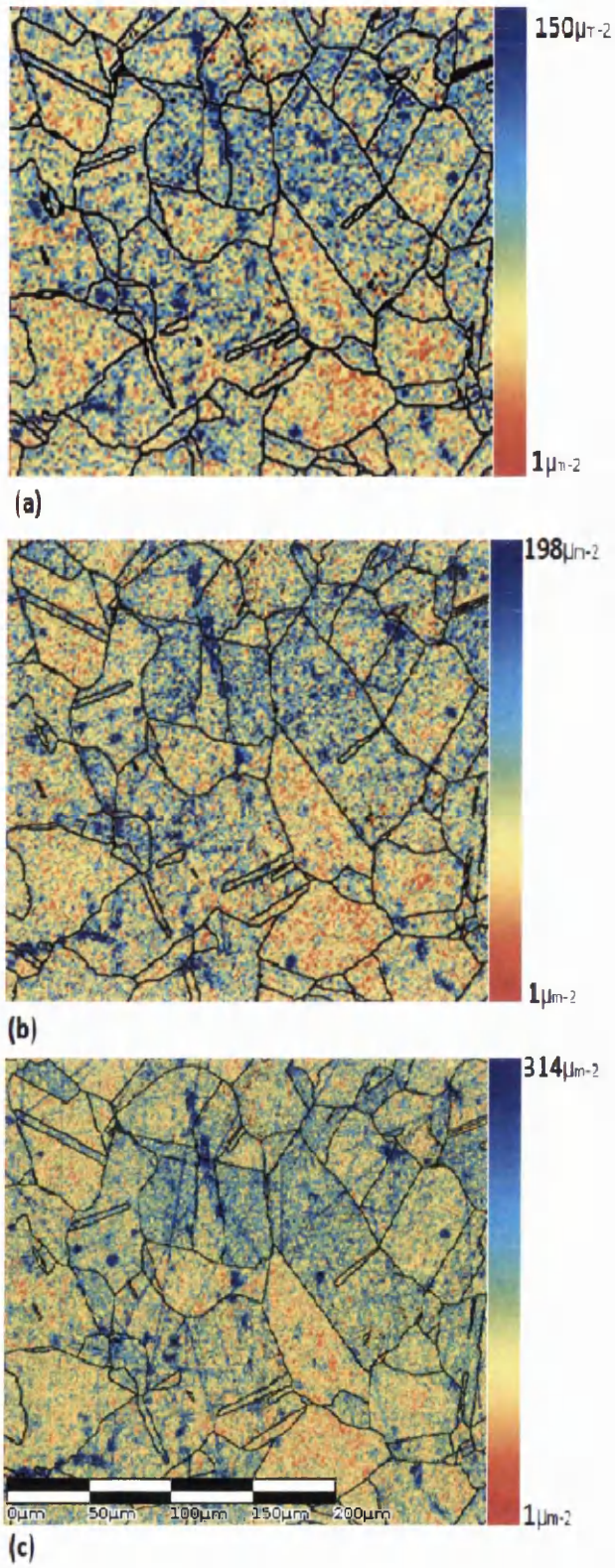

Figure 5.14: GND map of section from tensile end of sample Pilot 3 taken using step sizes of (a) 3μm, (b) 2μm, (c) 1μm.

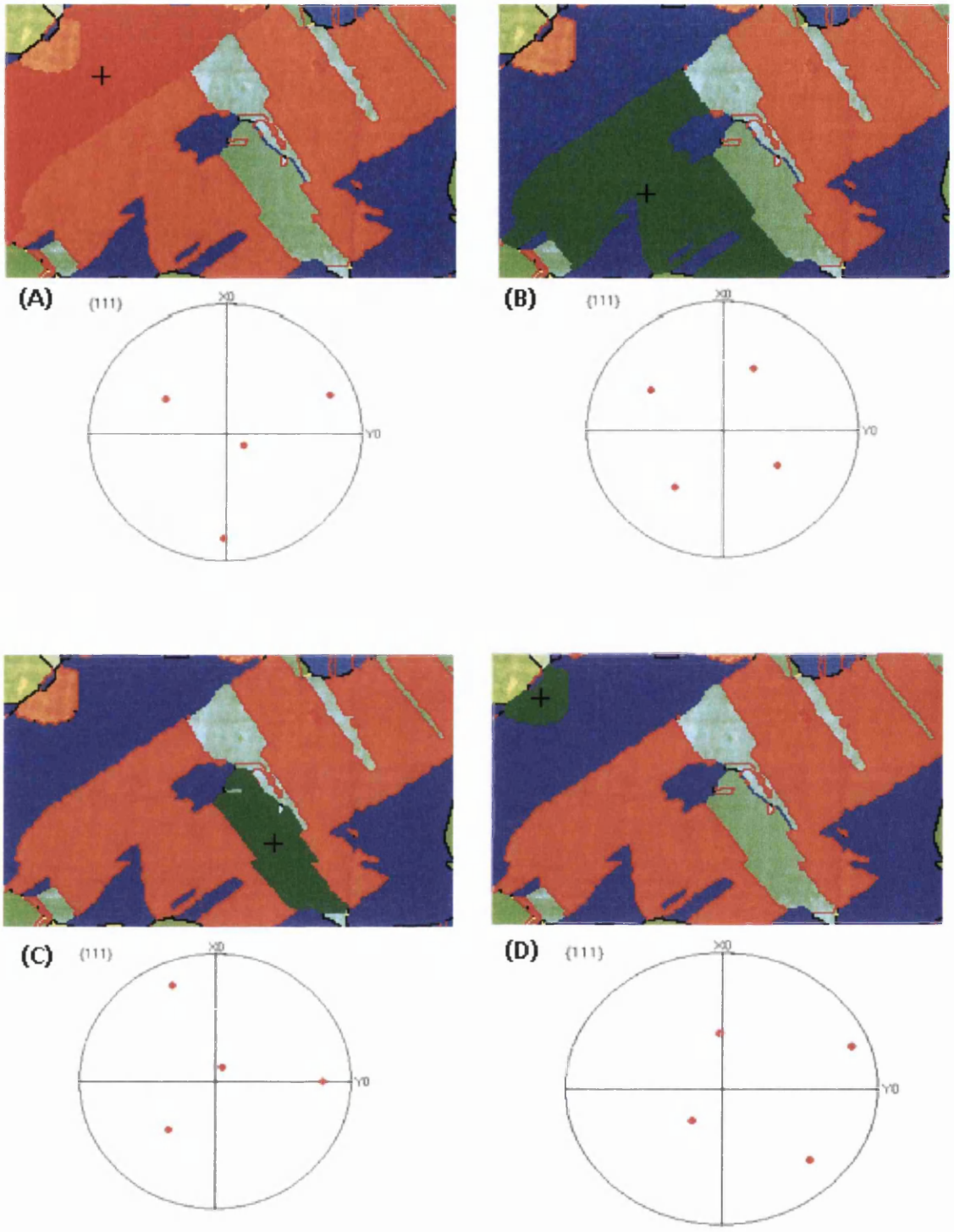

Figure 5.15: Orientation of key grains from Fig. 5.8 given using the {111} family of planes pole figure. Orientation below image corresponds to grain with black cross. Grains are coloured according to IPF colouring.

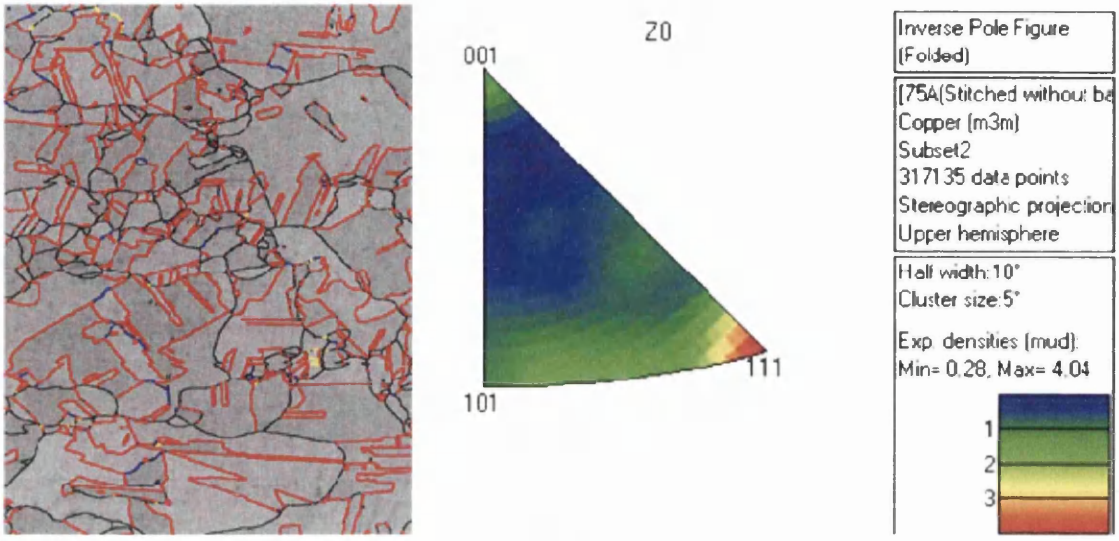

(a) Inverse pole figure of tensile region of sample Pilot 3

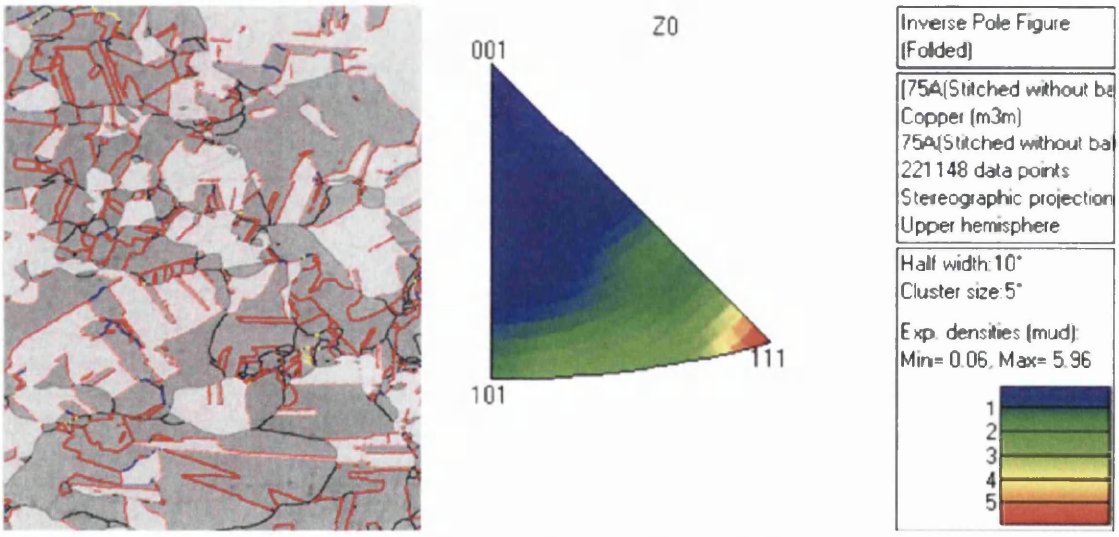

(b) Inverse pole figure of tensile region of sample Pilot 3 with high GND content grains removed

Figure 5.16: Area of sample Pilot 3 tensile region and corresponding sample normal direction inverse pole figure. (A) Entire tensile region, (B) Tensile region with high GND content grains removed.

Chapter 6

Folded Sample Set

Pure copper (99.9%) was obtained from Goodfellow Ltd half-hard. Samples were cut into 2.5cm x 1cm x 3mm thick pieces. All samples were initially given a furnace anneal at 600°C for 50.5hrs and water quenched to grow the grains and remove any residual strain. The samples were then folded in a folding machine to 90°, a schematic of which is shown in Fig. 3.5 in Section 3.2. The samples were then given an additional anneal at 600°C for varying times. Annealing times varied in 20min intervals. The samples were named for the second annealing time and a label 'F' added to distinguish them as being from the folded sample set and not similarly named samples presented in a later section. A fuller description of the creation of the samples can be found in Fig. 3.4 in Section 3.2.

6.1 Microstructural Development of Folded Samples After Folding and Annealing

The sample cross sections were mapped by EBSD, oriented according to Fig. 6.1, with the red box representing the area shown in each map. The resulting maps are shown in Fig. 6.2 to 6.7.

The 90° bend strains the sample much more than the Pilot sample set. Grain growth in the Pilot sample set starts in front of smaller, highly strained, grains at the edges of the sample and continues toward the centre of the sample. This growth front is visible in the folded sample set, likely due to the higher deformation.

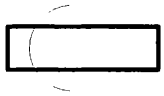

Figure 6.1: Folded sample set cross section map orientation. Maps were created at the apex of the fold.

There was difficulty in mapping the exact cross section from tensile to compressive deformation due to the small area of the compressive region. For this reason, grain size measurements are unreliable. Grains in the centre region of the samples appear to grow larger from samples 20F to 40F, and again from 40F to 60F. It would be expected that the grain sizes in the centre of samples would increase with increasing heating time, but this is not shown in sample 80F. The size of grains in the centre of sample 80F appear out of place as they are smaller than grains in the centre of samples 60F and 100F. Sample 120F also appears unusually small. This is likely caused by slight differences in the area being mapped in relation to the focus of deformation, or slight differences in the bending angle.

Certain samples also appear to show anomalous grain growth in the compression region. Fig. 6.3 and 6.6 show large grains in the compression region from samples 40F and 100F. Anomalously large grains were also found in the matrix sample set to be presented in Section 7, however the formation of the anomalous grains in each sample set seems to differ. The anomalous grains in the folded sample set appear to be formed by additional deformation in the compression region caused by indenting into the sample by the folding machine.

The folding process was not consistent enough for comparison between samples. In addition, the area of the compression region was too small to accurately find and map by EBSD. The range of grain sizes in the samples illustrates a sensitivity

Figure 6.2: Cross section of sample 20F. Compressive end is pictured at the top. Average grain size was measured and is provided in Fig.6.8.

Figure 6.3: Cross section of sample 40F. Compressive end is pictured at the top. Average grain size was measured and is provided in Fig.6.8.

Figure 6.4: Cross section of sample 60F. Compressive end is pictured at the top. Average grain size was measured and is provided in Fig.6.8.

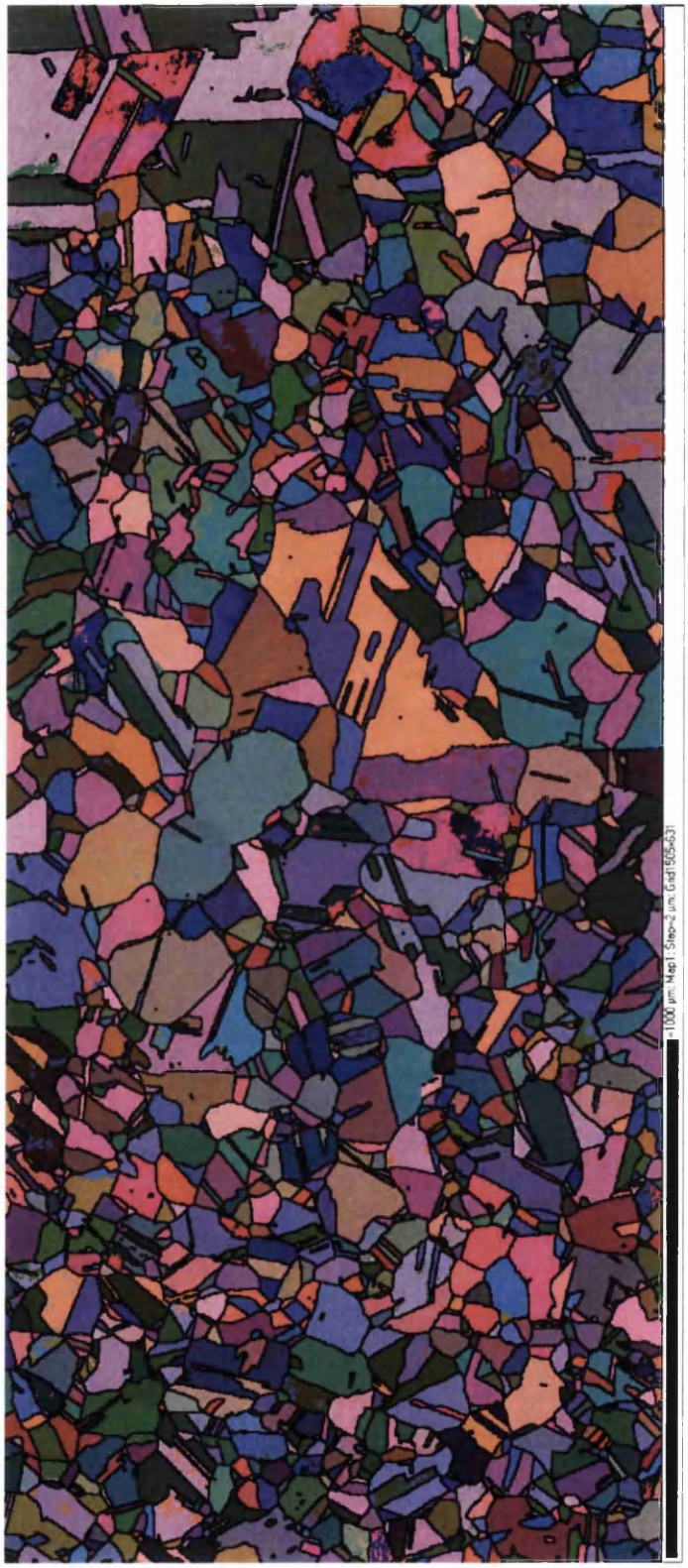

Figure 6.5: Cross section of sample 80F. Compressive end is pictured at the top. Average grain size was measured and is provided in Fig.6.8.

Figure 6.6: Cross section of sample 100F. Compressive end is pictured at the top. Average grain size was measured and is provided in Fig.6.8.

Figure 6.7: Cross section of sample 120F. Compressive end is pictured at the top. Average grain size was measured and is provided in Fig.6.8.

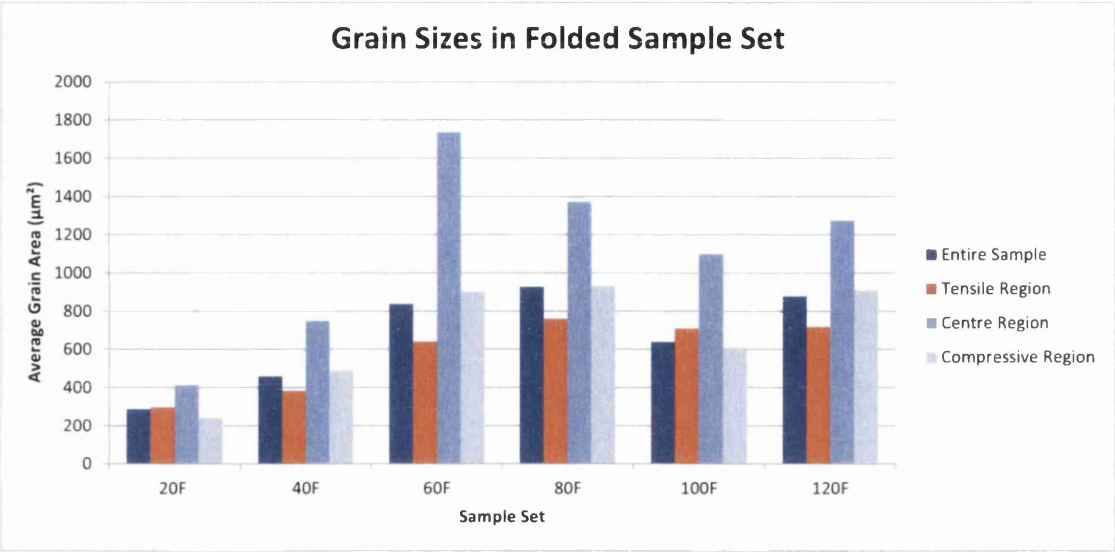

Figure 6.8: Grain sizes in each region of each sample in the folded sample set.

to slight changes in strain for high strain levels. The significant and unpredictable changes in grain sizes in the centre region of the samples is not seen in samples which experienced only a moderate strain step. Instead of comparing the complicated system of slight strain changes and grain sizes present in the sample set, one sample was chosen for GND analysis and comparisons between samples were disregarded. Sample 20F was chosen for this purpose.

6.2 GND Analysis of Sample 20F

A large GND map was created across the cross section of sample 20F in order to contrast the deformation levels in each region after annealing and is shown in Fig. 6.10. Fig. 6.10 was created using the ideal settings suggested in Section 4.3, however with the exception of indexing using band centres instead of band edges. Mapping by band centres results in less indexing noise than mapping by band edges when the EBSP pattern is of sufficiently high quality. The shape of the indexing noise differs to that of band edges, which shows a normal distribution, and as such is not suitable for the noise reduction algorithm suggested in Section 4.3.3 which averages GND content points within one standard deviation and some smoothing factor of each other.

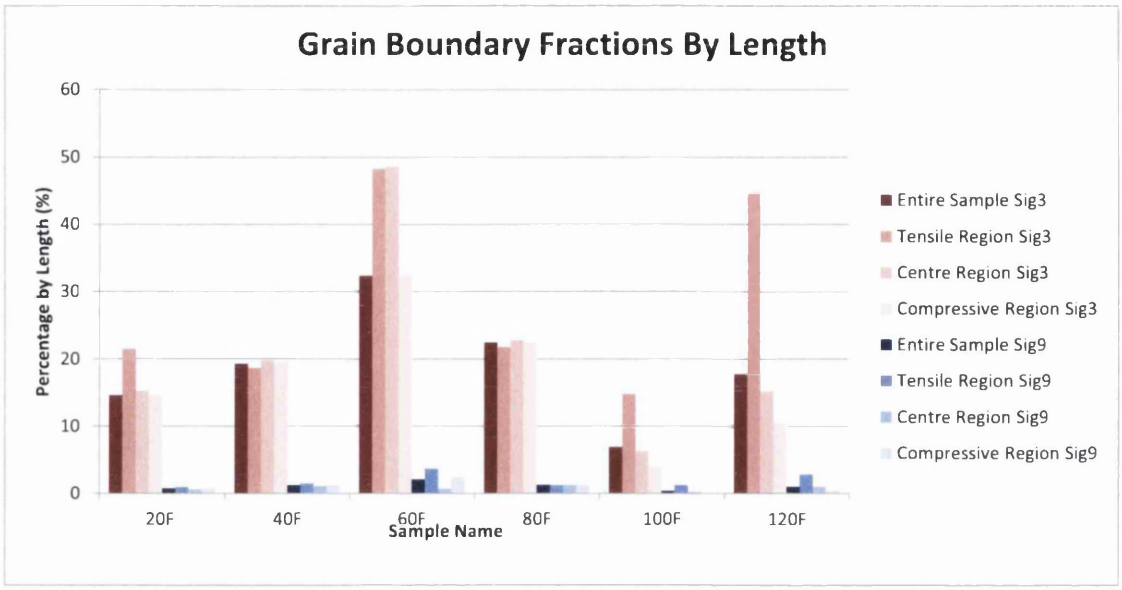

Figure 6.9: Σ3 and Σ9 boundary fractions in folded sample set. Fractions are presented as a percentage of total length of boundaries.

The GND structure in the tensile and compressive regions of the map differ greatly. The compressive region shows a high dislocation connectedness not seen in the tensile region. Dislocations appear to be interacting and forming tangles. These tangles emanate from certain microstructural features, such as sharp grain corners and steps, as well as triple junctions. Examples of GND tangles emanating from sharp grain corners and steps can be seen in Fig. 6.11.

Sharp corners and steps act as points on which stress would focus during deformation, creating dislocation sources. Corners and steps of boundaries also have a higher free volume than straight boundaries. As a result, the corners and steps are the likeliest places for dislocations to terminate upon annealing, causing dislocations to build up and form tangles at these areas. Excess dislocation content is unable to terminate at coherent or semi-coherent boundary interfaces, and so moves towards microstructural features with excess free volume.

As well as at sharp grain corners and steps, this can also be seen at the incoherent interface of twin boundaries, shown in Fig. 6.13.

Twin boundaries often have incoherent portions on the interior of the parent grain. The incoherent portion does not lie on the lowest energy planes, as the

Figure 6.10: GND map across cross-section of sample 20F. Compressive edge is pictured on the right.

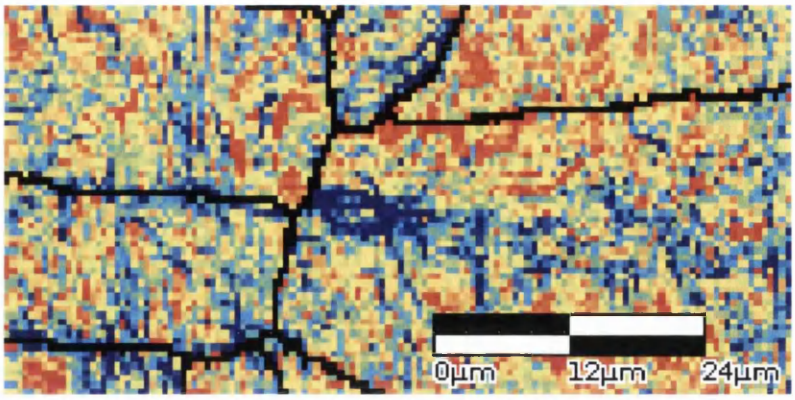

Figure 6.11: Portion of cross sectional GND map of sample 20F taken from the compressive region. GND content can be seen emanating from a triple junction.

coherent portion does, and so has a higher free volume. The higher free volume attracts mobile dislocations during annealing and forms a high dislocation content in front of the boundary. The incoherent boundary portion is also the mobile part of the twin boundary, growing into the parent grain.

The tensile region shows a much more diffuse dislocation structure than the compressive region, as seen in Fig. 6.10. High content dislocation tangles are not seen emanating from sharp grain corners and steps, or from triple junctions. There does, however, appear to be some light lower GND content connectedness.

The GND content profile is shown in Fig. 6.14. Points were averaged according to their distance from the tensile end in the map. Non-overlapping bins, 50 points wide, were taken across the map and the average content of each bin calculated and plotted against the distance from the tensile end.

A distinct peak is seen near the centre of the sample, about $1245\mu m$ from the left edge, which corresponds to a high content region shown in Fig. 6.10. The entire map is approximately 3285 μm, so this peak is considerably further towards the tensile end of the geometric centre. The tensile and compressive ends show a lower content than the peak due to the 20min anneal the sample has experienced. The anneal sufficiently relaxed the more severely deformed ends, while the centre region still shows retained strain. The position of the peak also indicates the centre of folding of the sample, which is closer to the tensile end of the sample.

The compressive region also shows a higher average GND content than the ten-

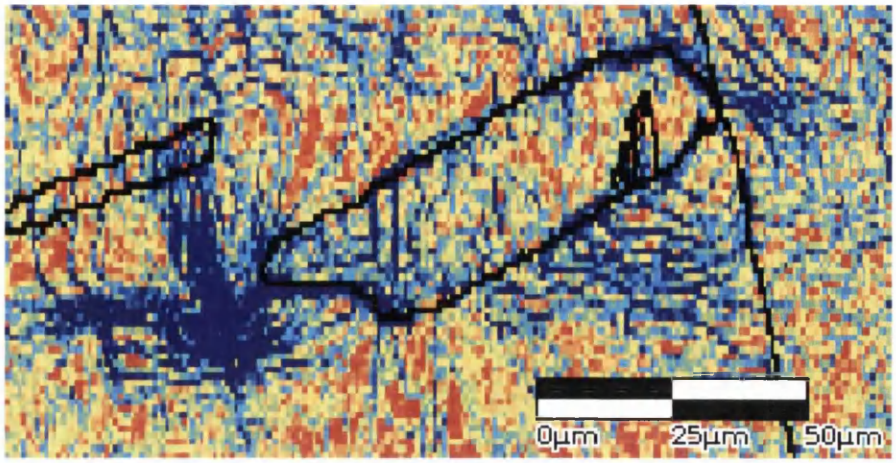

Figure 6.12: Portion of cross sectional GND map of sample 20F taken from the compressive region. GND content can be seen emanating from a sharp grain corner and triple junction.

sile region. When observing this result, the reader is reminded of the definition of a GND as those 'dislocations which are necessitated by observed lattice curvature' [3]. The compressive region shows a higher GND content, but it is unclear whether it has a higher absolute dislocation content.

The higher average GND content is due to the presence of the dislocation tangles in the compressive region. The accumulation of the dislocation content into tangles is more readily resolved as GND content due to the larger point-to-point misorientations than the diffuse dislocations of the tensile end. The larger point-to-point misorientations are more easily detected by Hough transformation as they are much larger than the indexing noise. Knowledge of the misorientation axis disappears as the misorientation angle decreases, and as such dislocation content with smaller misorientations is harder to resolve [4]. The finer dislocation structure in the tensile region may have a smaller period of curvature, causing a lower percentage of dislocations to be resolved as GNDs than in the compressive region, where the larger misorientations and larger curvature period of the tangles allow a higher percentage of resolved dislocations as GNDs. The absolute dislocation content in both regions may be comparable, or even higher in the tensile region, but since the SSD content of each region is unknown the absolute content cannot be compared. The GND structures of the two regions differ so much that a comparison

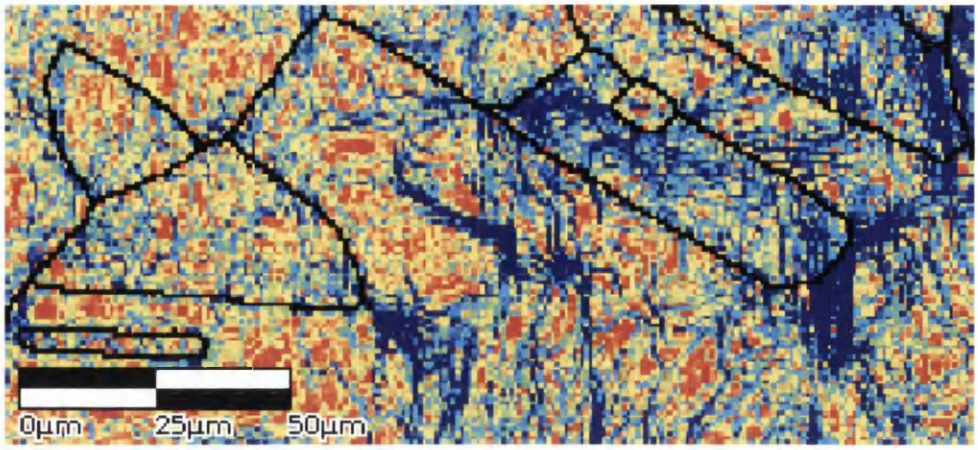

Figure 6.13: Portion of cross sectional GND map of sample 20F taken from the compressive region. GND content can be seen emanating from a grain tip and the incoherent portion of a twin boundary.

of the absolute content is not possible based on the GND information alone.

6.2.1 Qualitative GND Analysis of Deformed and Non-Deformed Regions in Sample 20F

In addition to the comparison of the GND content across the cross-section of the sample, a comparison of the GND content in the tensile region and the non-deformed region was investigated using sample 20F. Since the long ends of the sample experienced an identical annealing history to the sharp folded region but are far enough away from the fold that they did not experience deformation, they provide an ideal comparison for the development of GND content with and without strain.

High quality orientation maps were created at the tensile end of the folded region and in the middle of the long sample end away from the fold, as shown in Fig. 6.15. Two maps were created in each area, one using indexing by band centres and one indexing by band edges, with the rest of the mapping settings being the ideal settings recommended in Section 4.3 (with the exception of one map, which is later explained).

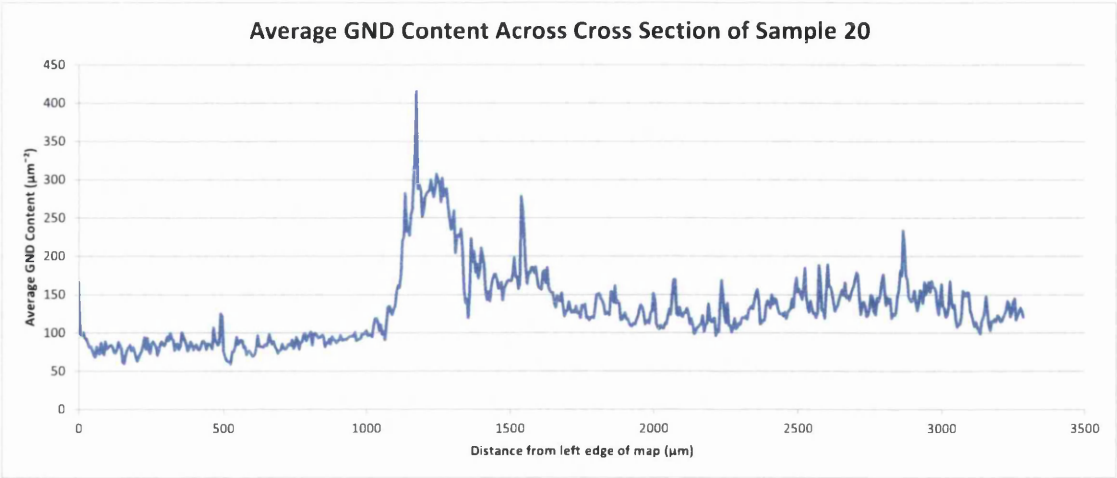

Figure 6.14: GND content profile of sample 20F cross section. Points were grouped into bins according to the distance from the left edge of the map. Bin sizes were 10 times the step size. The average GND content of each bin was calculated and plotted.

6.2.1.1 Deformed Region

The two orientation maps of the deformed region, one created indexing by band edges and one by band centres, are shown in Fig. 6.16 and 6.17. The GND maps are plotted on a linear scale from 0 to an upper bound calculated as 2 times the mean of all points. Only the map indexed by band edges was passed through the noise reduction algorithm, since it is the only one which shows part of the noise following a normal distribution, as explained in Section 4.3.3. The GND map created from the band centres indexed orientation map used a 100 Hough space resolution setting, while all other GND maps in this sample set were created using 120 Hough space resolution setting. For information on how this affects the results, see Section 4.3.1.

The map created using band edges indexing appears to show the same alternating between high and low GND content grains by twinning that was seen in sample Pilot 3. Both samples received a heat treatment after an applied tensile strain, however with differing temperature, time and amount of strain; furthermore, both samples appear to show an orientation relation to GND content. Examples of high and low GND content grains within twin related domains is shown is Fig. 6.18.

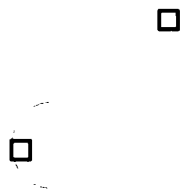

Figure 6.15: Areas of sample 20F used for comparison of development of GND content with and without strain. The deformed region map is highlighted in red near the tensile tip of the fold, and the non-deformed region map is also shown in red in the long end away from the fold.

The map created using band centres differs from the map created using band edges. Indexing by band centres is less sensitive to small orientation changes, but has a lower indexing noise, as explained in Section 4.3. As a result, larger orientation changes, and the resulting high GND content, are more clearly defined while small orientation changes are lost. This results in a more polarized GND map, with more values in the upper and lower regions and less in the mid.

The band centres map still shows the orientation relation to GND content as seen in the band edges map, however it is less obvious. A comparison is shown in Fig. 6.19.

The more polarized GND map created by band centres indexing appears to show GND content building up in front of certain boundaries and triple junctions. Examples of GND in front of boundaries can be seen in Fig. 6.20. The extent of the GND build up in front of the boundary may be related to the boundary character, as shown by the example in Fig. 6.20. GND content can be seen to be built up in front of the boundary between grain A and grain B, and not on the boundary section interrupted by grain C. The character of the boundary between grain A and B is constant, despite the interruption by grain C, and content can be seen to build up on either side of the interruption, indicating the boundary

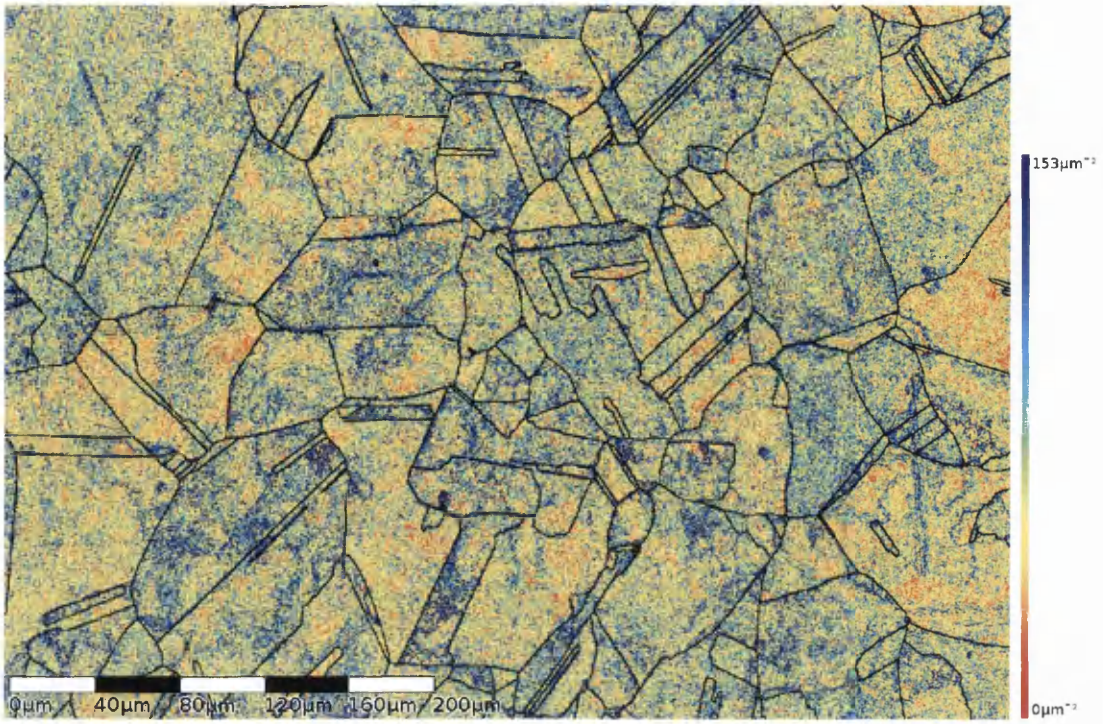

(a) GND map of deformed region of sample 20F mapped with band edges

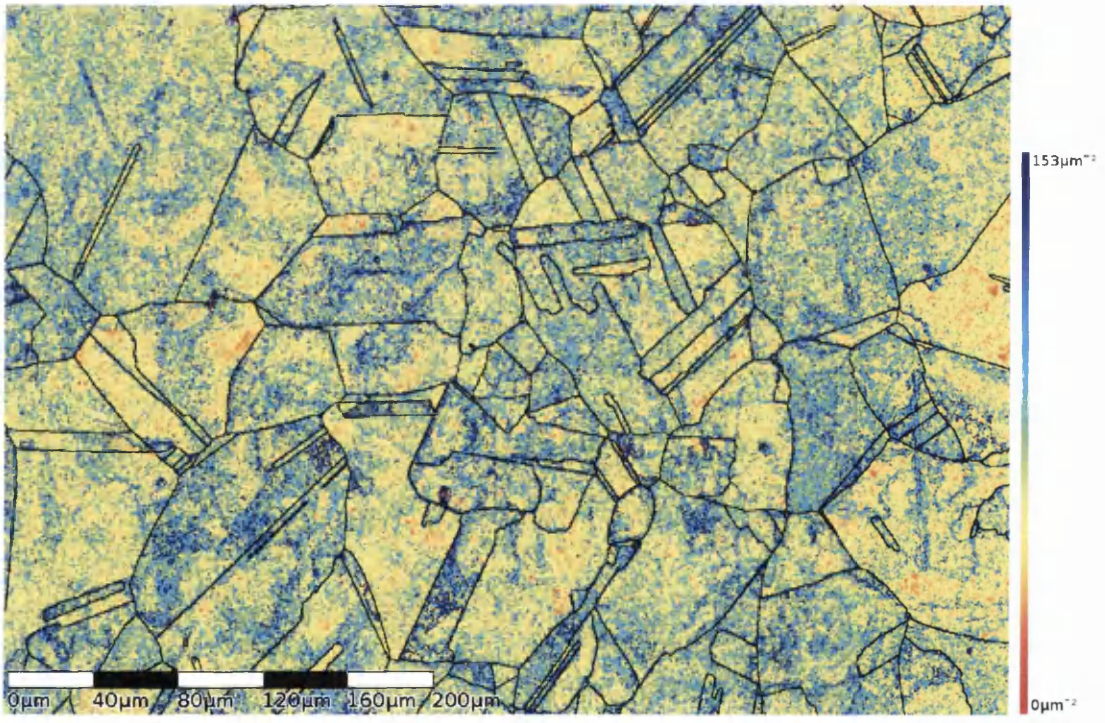

(b) GND map of deformed region of sample 20F mapped with band edges and de-noised

Figure 6.16: GND map of tensile region of sample 20F. Created from an orientation map indexed by band edges, (a) original data and (b) de-noised.

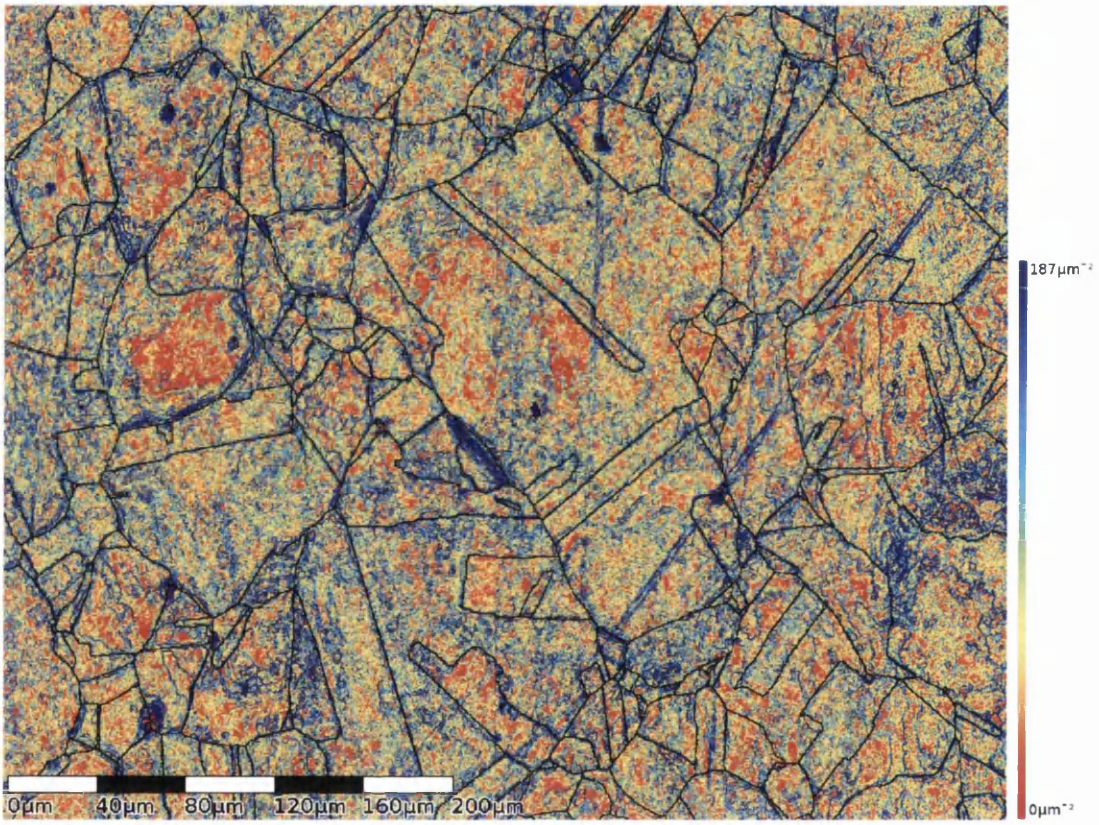

Figure 6.17: GND map of tensile region of sample 20F. Created from an orientation map indexed by band centres.

character relation.

GND content can also be seen emanating into grains from triple junctions, shown in Fig. 6.21. GND structures terminate at triple junctions likely due to the higher free volume of the junction which can more readily accommodate the deformation. The character of the triple junction may also influence the GND build up. The boundary opposite to the high GND build up in Fig. 6.21 is a $\Sigma 9$, which is known to act as connectors between $\Sigma 3$ boundaries. After heat treatments, the deviation from exact CSL misorientation of $\Sigma 9$ boundaries increases as they accommodate the orientation change needed for lower energy $\Sigma 3$ boundaries deviation from exact CSL misorientation to decrease [112].

6.2.1.2 Non-Deformed Region

Two GND maps, one coming from an orientation map indexed by band centres and one by band edges, are presented in Fig. 6.22 and 6.23. The maps are plotted in the same manner as the deformed region on a scale from 0 to twice the mean of all points, with only the band edges map being passed through the noise reduction algorithm.

Unlike the deformed region, the GND maps of the non-deformed region show no textural relation to GND content. GND structures appear throughout the microstructure and no single grain shows a higher content relative to its neighbours.

The GND structures in the non-deformed region are seen sparingly in the deformed region, but to a more advanced state in the non-deformed region. GND content forms tangles emanating from triple junctions, sharp grain corners and curved boundaries much like the compressive region of the sample. The tangles are very prominent in the more polarized band centres map but are also observed in the band edges map, as seen in examples in Fig. 6.24.

As a result of the GND tangles terminating at the higher free volume areas of triple junctions, boundary curves and corners, lower GND content is found in the interior of grains than in the areas nearer the boundaries. As with the deformed region, high GND content can be seen building up in front of certain boundaries. This may also be related to the boundary character. Boundaries with lower free volume may not allow dislocations to annihilate, and instead the deformation

builds up on the face of the boundary.

6.2.2 Quantitative GND Analysis of Deformed and Non-Deformed Regions in Sample 20F

A quantitative analysis was undertaken on each of the four GND maps of sample 20F in order to find any relationships between the GND content in front of a boundary and the grain boundary character, the shape of the boundary, the angle of the boundary in relation to the applied force, and also the position within the grain. Points with less than 10° misorientation were grouped into grains using the algorithm explained in Section 4.4.2. Boundaries were then detected as groups of points within a defined width of the interface of two adjacent grains. The algorithm for boundary detection is also provided in Section 4.4.2.

The output of the grain and boundary detection is shown in Fig. 6.26. Grains are shown in random colours, $\Sigma 3$ boundaries in red, $\Sigma 5$ boundaries in green, $\Sigma 7$ in purple, $\Sigma 9$ in blue, $\Sigma 27$ boundaries in bright yellow, and random boundaries in black. Triple junction points, used to calculate boundary angle and curvature, are shown as yellow points. The boundary thickness in the image serves as a guide for the points considered part of the boundary, and hence used in the boundary averages.

One map, the deformed region band centres map, was created with different settings from the other maps. It was created with a 100 Hough space resolution setting instead of the 120 suggested settings used in the other maps. The effect on the GND results due to this setting is explained in detail in Section 4.3.1, and will be taken into consideration and commented on further in this section when analyzing the quantitative results.

The shortest distance to a boundary interface was calculated for every point. Points were grouped into bins of three times the step size based on their distance to the nearest boundary, and an average was calculated. Only grains containing >50 points were included in the calculation. Grains smaller than 50 points were not large enough in relation to the step size to allow for accurate GND calculations in relation to position within the grain. The results are presented in Fig. 6.27.

In each of the band centres and band edges maps, the deformed and non-

deformed region show similar curve shapes. Both regions show higher content closer to the boundary, decreasing towards the bulk of the grain. The deformed region appears to plateau around $6\mu m$ from the boundary, while the non-deformed region shows a large drop off at the bulk of the grain. This confirms the previous qualitative results that appeared to show the GND content in the non-deformed region forming tangles near the outer parts of the grain and moving away from the grain bulk centre.

The band edges maps of the deformed and non-deformed regions shows higher average GND content in the non-deformed region. This may be counter-intuitive, as a higher plastic strain content is expected in the deformed region. The reason for this is due to the GND structure of each region, much like the difference between the tensile and compressive regions of the cross sectional GND map. The GNDs in the non-deformed region have accumulated together to form tangles, which are more readily resolved as GND content than the diffuse GND structures of the deformed region. The deformed region may have a higher absolute plastic strain content, but lower percentage of it is resolved as GND content than the non-deformed region.

The band centres maps of both deformed and non-deformed regions show a more distinct curve than the band edges maps. Because of the method of indexing, the band centres GND maps are more polarized, creating the larger difference in average content of each bin. Unlike the band edges maps, the deformed region with band centres shows a higher GND content than the non-deformed region with band centres. This is caused by the lower Hough setting used for the deformed region band centres map than that used for the non-deformed region band centres.

The exact number calculated as the average GND content for each bin has less significance than the shape of the curve plotted. Changes in surface preparation and also the underlying dislocation structure affect the fraction of total dislocations that are resolved as GNDs. While the fraction of dislocations resolved as GNDs can change at each point, within a map the conditions are similar enough that averages over the map and the shape of the curve plotted in Fig. 6.27, 6.29, and 6.30 are reliable; however, comparisons of the values of bins in different maps can not be compared.

In order to investigate the GND content across boundaries, the points belonging

to each boundary were grouped into bins in the same manner as with the previous grain content graphs. The side of the boundary containing higher content in the bin immediately in front of the boundary was classified as grain 'A', and the other side as grain 'B'.

The average for all grain 'A's and 'B's was taken based on the boundary character. Boundaries containing <50 points or using a grain <50 points in size were excluded from the calculations. The results are shown in Fig. 6.29.

The sidedness of the boundary, or the difference in the GND content peaks on either side of the boundary, is readily apparent using this method of plotting. A sharper slope across the boundary indicates a more sided boundary, either because the boundary is acting as a source of dislocations or as a barrier to dislocation movement.

The initial appearance of the graphs indicate an erratic pattern for $\Sigma 9$ boundaries. Examples were observed in the qualitative analysis of GND content stemming from triple junctions containing $\Sigma 9$ boundaries, so $\Sigma 9$ boundaries may have a higher sidedness. However, the erratic results for these boundaries is likely due to the small sample size. This is especially evident in the one-sided boundary plots of Fig. 6.30, where maps of the same area do not show consistent patterns for $\Sigma 9$ boundaries but do for $\Sigma 3$ and non-CSL boundaries. The number of each boundary type in each map is as high as 29 and as low as 8 for $\Sigma 9$ boundaries, while the number of boundaries used in the $\Sigma 3$ and non-CSL boundary calculations is typically >200.

The band centres maps offer a comparison of the GND content across $\Sigma 3$ boundaries in the deformed and non-deformed regions since they are both of sufficient size. The lower Hough space resolution setting of the deformed region band centres map, as expected, shows higher average content, however the curves and the relations between curves on the same graph are preserved.

Both sides of the boundary are combined and plotted for one-sided boundary GND content in Fig. 6.30. The GND content farther away from $\Sigma 3$ boundaries is shown to be lower than non-CSL boundaries, but increases to higher than non-CSL boundaries directly in front of the boundary. This difference between $\Sigma 3$ and non-CSL boundaries is seen in the deformed and non-deformed regions, however a larger difference is seen in the deformed region band centres map than in the

non-deformed region band centres map. The band centres maps contained the most boundary samples contributing to the average, so a larger difference in these maps is more significant.

Comparison of these maps to the two-sided boundary content maps provides additional insight into the deformation behaviour of the boundaries. In each case, the GND content is lower on both sides of Σ3 boundaries than non-CSL boundaries far away from the boundary interface. Close to the boundary interface, in the deformed region the peaks of Σ3 and non-CSL boundaries for grain B is similar but larger for grain A. The non-deformed region shows a larger peak for grain A and grain B for Σ3 boundaries.

The peaks for Σ3 boundaries and non-CSL boundaries are similar in the deformed region band edges graph. The non-deformed region band edges map does not repeat the higher Σ3 boundary peak seen in the band centres graph, however the non-deformed region band edges map does not include enough boundaries to form a reliable result. It represents a smaller area of the sample, and less than a third of the number of boundaries are used for the calculation than in the other graphs.

6.3 Folded Sample Set Summary

Samples of pure copper were folded to ~90° and given varying heat treatments. Significant grain growth is found at the centre region of each sample, with the grains in the tensile and compressive regions coarsening to a much lesser degree. This is in contrast to sample Pilot 3, which experienced a much smaller strain step, and showed grain growth starting in the grains in front of the tensile and compressive regions and moving inwards, sandwiching smaller grains in the centre region. Grains experiencing a key strain level are likely preferred for growth. This will be explored in a later discussion section.

The cross section of sample 20F was mapped for GND content. A diffuse GND structure was found in the tensile region and a tangled GND structure found in the compressive region. The highest content region was found near the centre. While the compressive region showed a higher average GND content than the tensile region, the difference in the GND structures of the two regions means that the

absolute dislocation contents of the two are not comparable using the GND values alone.

A larger section of the tensile deformed region, and a non-deformed region away from the fold were mapped for GND content. The non-deformed region showed a similar tangled GND structure to the compressive region of the sample. The diffuse GND structure of the tensile deformed region showed a texture relation to GND content within twin related domains similar to that shown in the tensile region of sample 75A.

The quantitative approach was used to analyze the GND content in front of boundaries based on the boundary character. The tensile deformed region showed no relation to boundary GND content and character, but the non-deformed region showed a peak for $\Sigma 3$ for a large map indexed by band centres.

Using a similar quantitative approach, the GND content was analyzed based on the position within the grain. It was shown that the GND content in the non-deformed region moved outwards towards the edges of the grains, with a drop off in the GND content for points in the bulk centre of the grain that is not seen in the tensile deformed region.

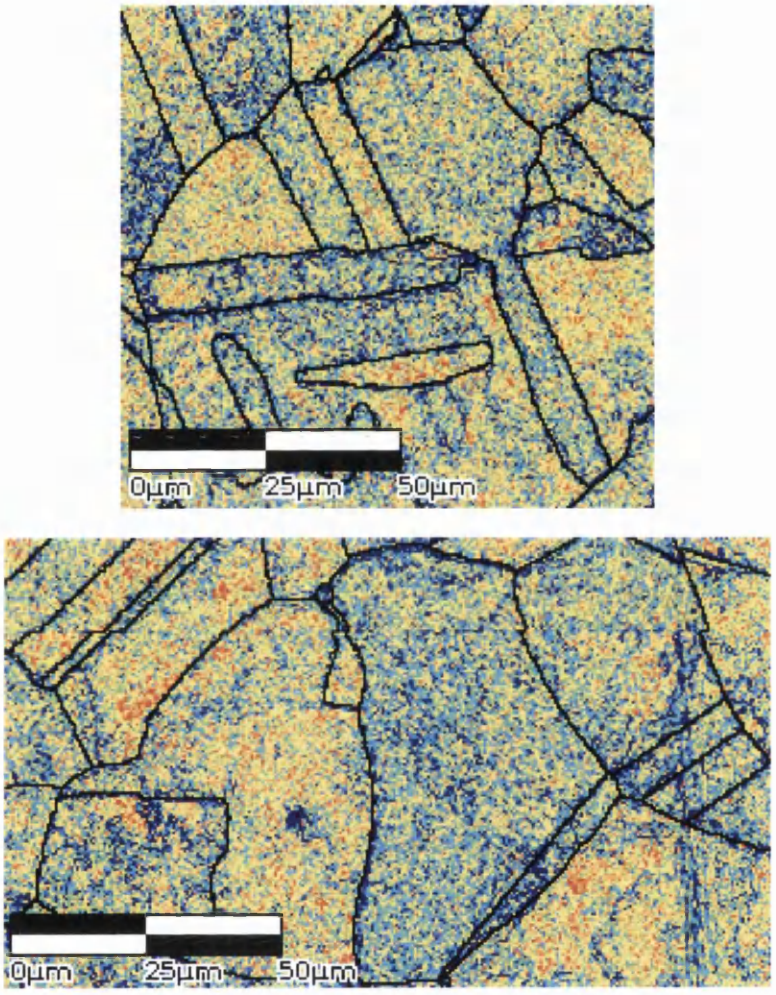

(b) Alternating high and low GND content grains in deformed region of sample 20F

Figure 6.18: Example of alternating high and low GND content grains within a twin related domain. Taken from a GND map of the deformed region indexed by band edges.

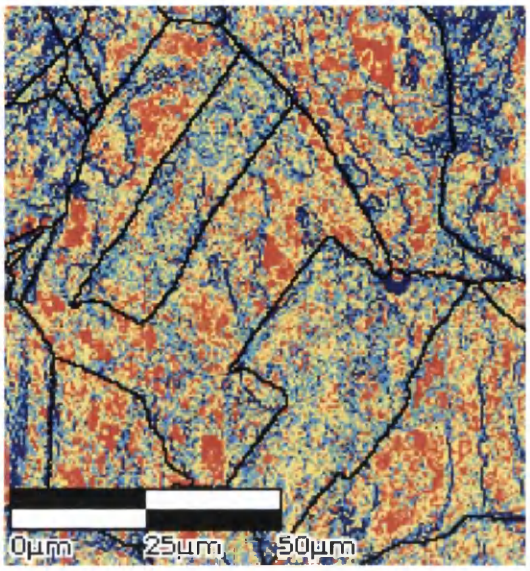

Figure 6.19: Example of alternating high and low GND content grains within a twin related domain. Taken from GND map of deformed region indexed by band centres.

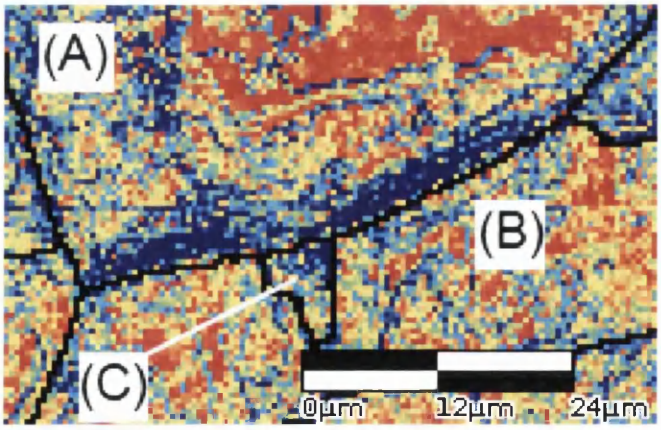

Figure 6.20: Example of GND content build up in front of a boundary taken from map of deformed region indexed by band centres. The GND content appears higher in the interface between grain A and grain B, and lower at the interface between grain A and grain C.

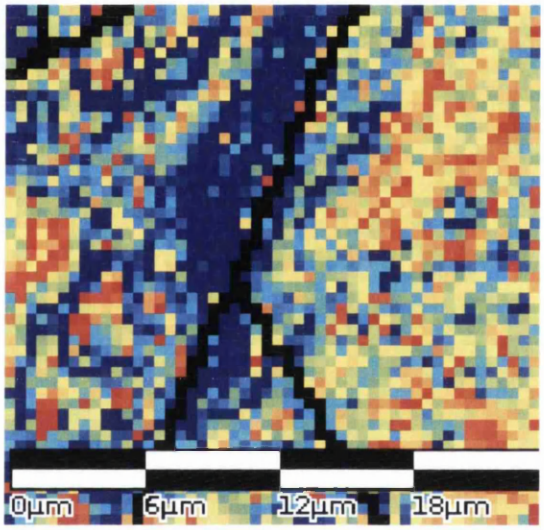

Figure 6.21: Example of GND content at a triple junction taken from deformed region of sample 20F map indexed by band centres. Upper boundary is Σ9 in character.

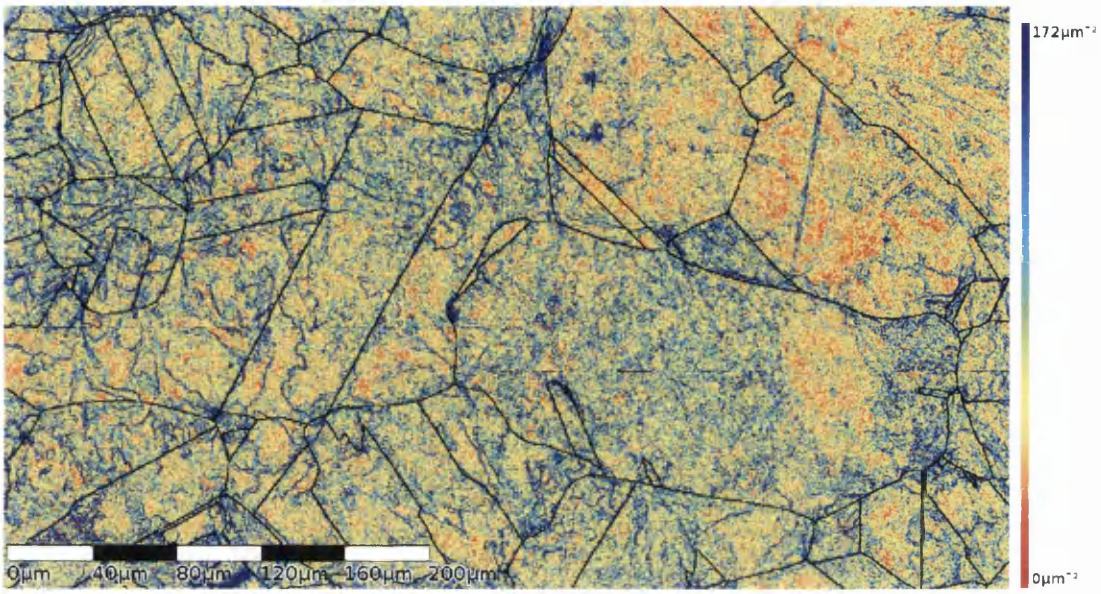

(a) GND map of non-deformed region of sample 20F mapped with band edges

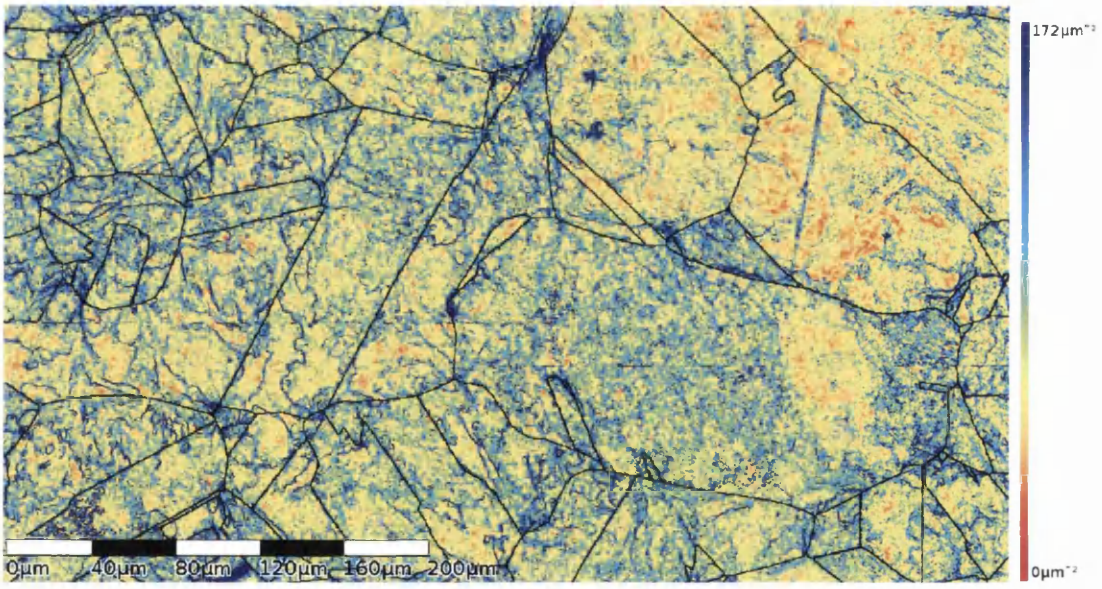

(b) GND map of non-deformed region of sample 20F mapped with band edges and de-noised

Figure 6.22: GND map of non-deformed region of sample 20F mapped with band edges (A) original data and (B) de-noised.

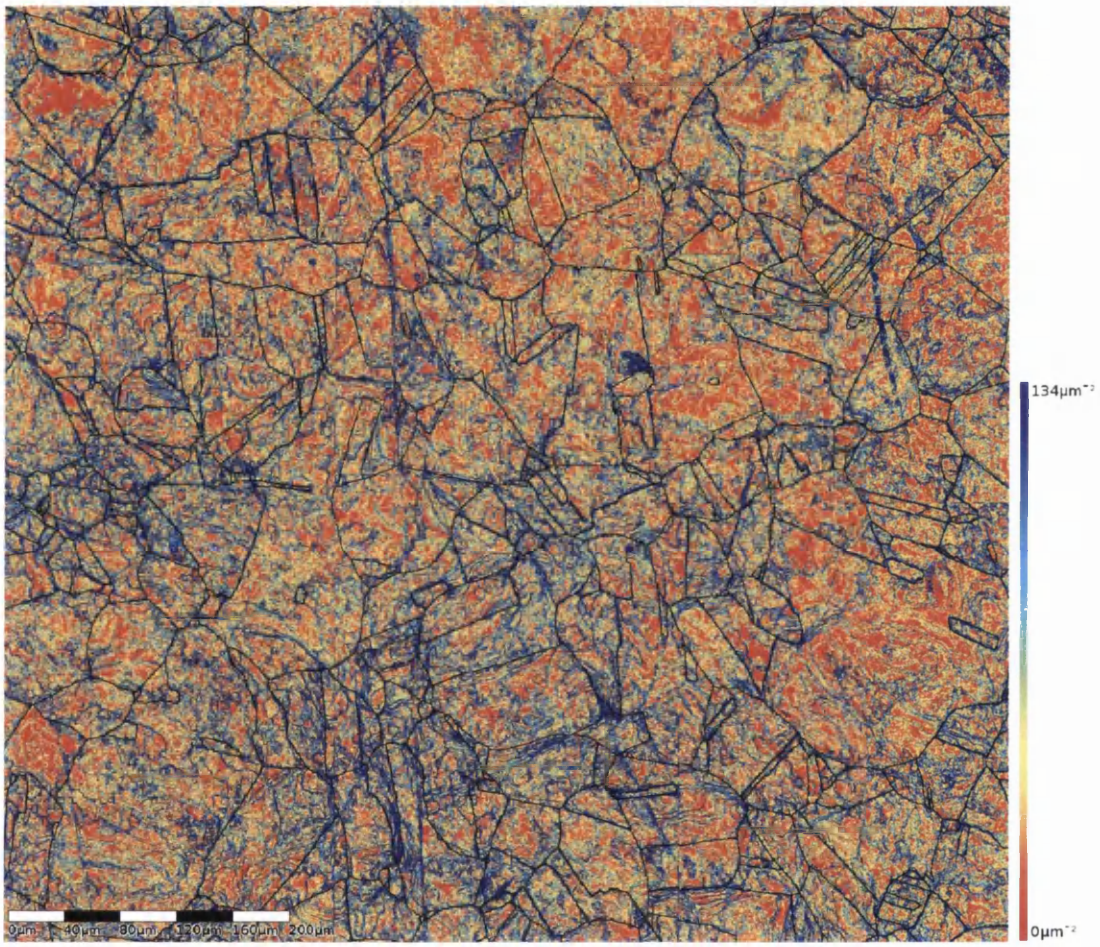

Figure 6.23: GND map of non-deformed region of sample 20F. Created from orientation map index by band centres.

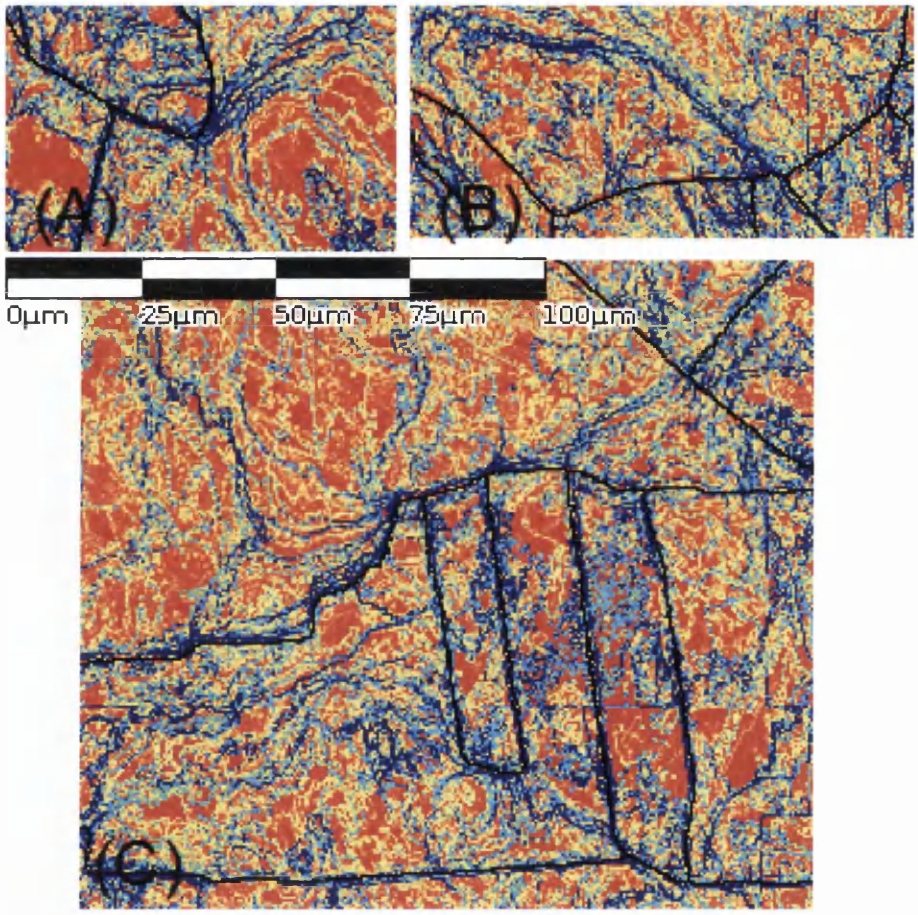

Figure 6.24: Examples of GND tangles emanating from grain corners and triple junctions. Taken from GND map of the non-deformed region of sample 20F created using indexing by band centres.

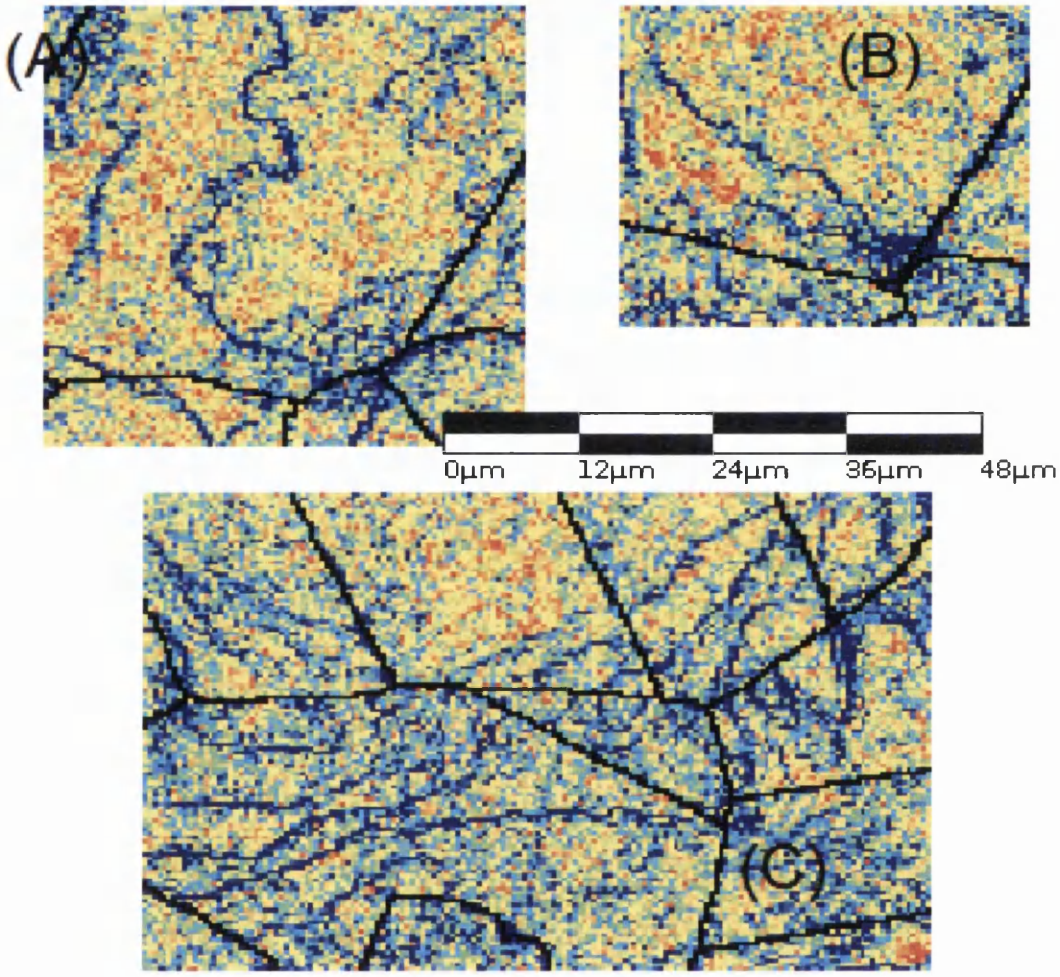

Figure 6.25: Examples of GND tangles emanating from grain corners and triple junctions. Taken from GND map of the non-deformed region of sample 20F created using indexing by band edges.

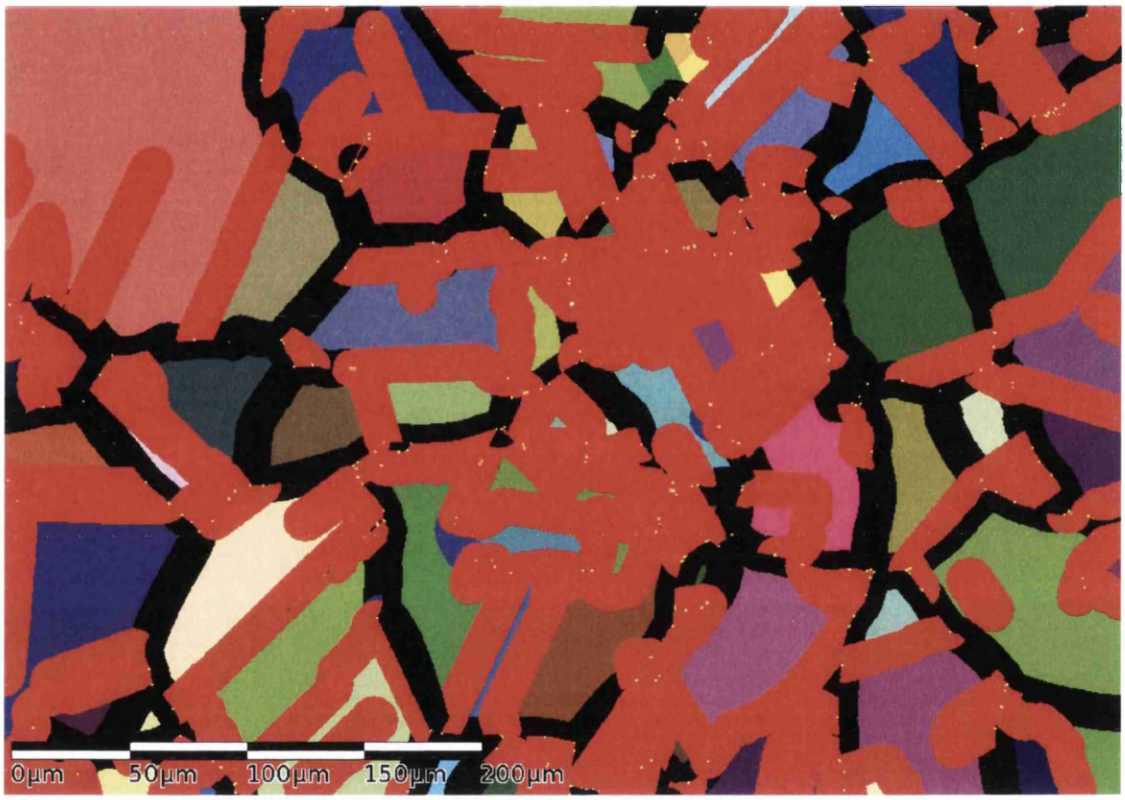

Figure 6.26: Map of detected grains and boundaries in the deformed region of sample 20F. Grains are shown in random colours. Σ3 boundaries are shown in red, Σ9 boundaries in blue and random boundaries in black. Yellow points are detected triple junctions.

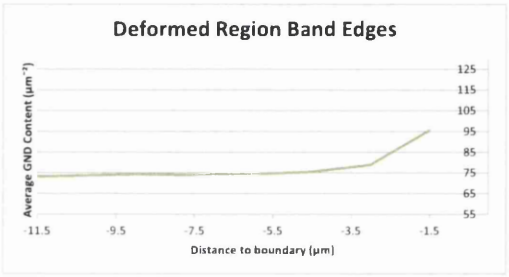

(a) Deformed Region Band Edges

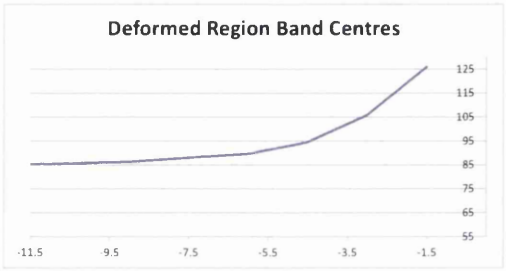

(b) Deformed Region Band Centres

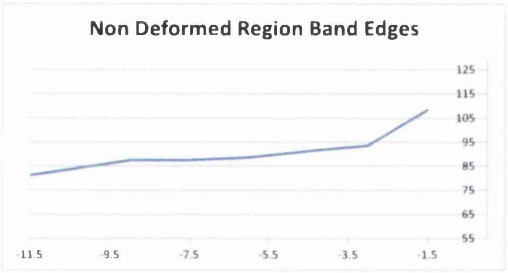

(c) Non-Deformed Region Band Edges

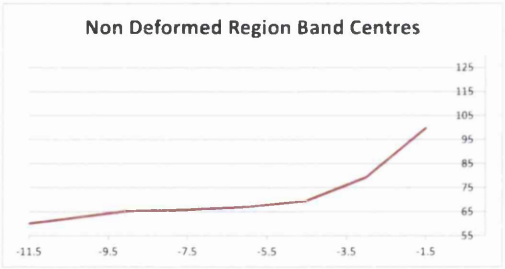

(d) Non-Deformed Region Band Centres

Figure 6.27: Average GND content from grain bulk to nearest boundary for each map.

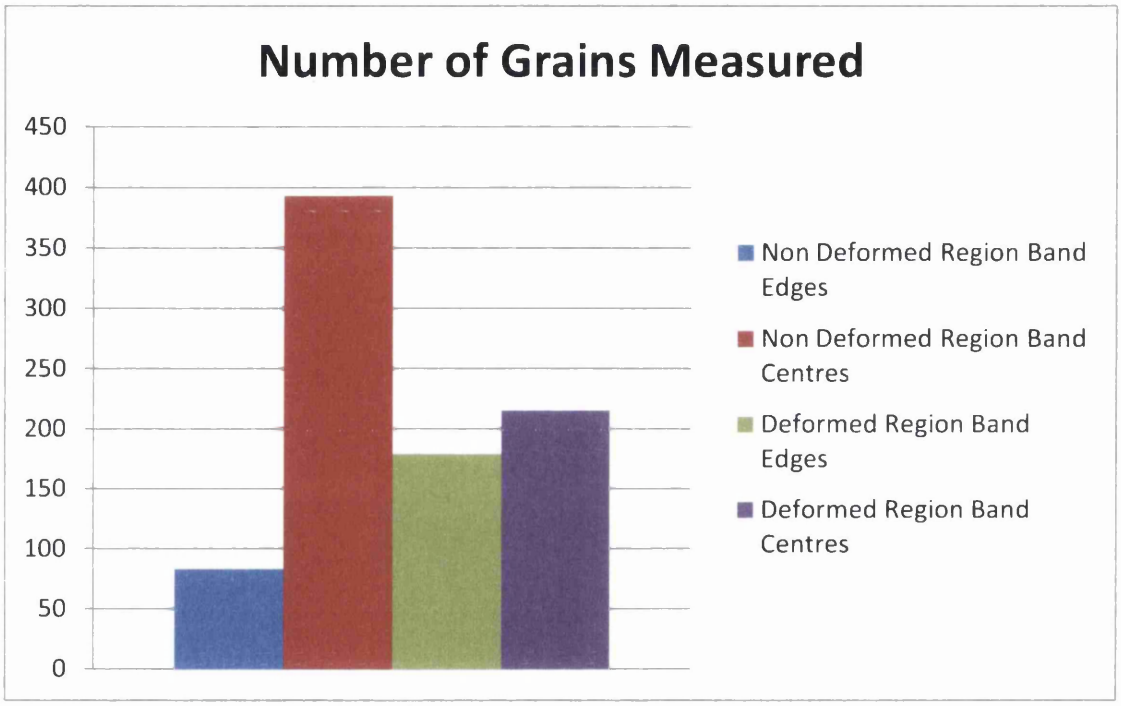

Figure 6.28: Number of grains measured in each GND map of sample 20F.

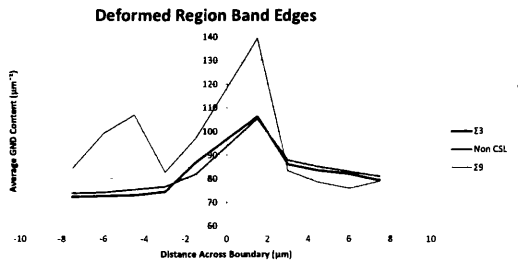

(a) Deformed region mapped by band edges

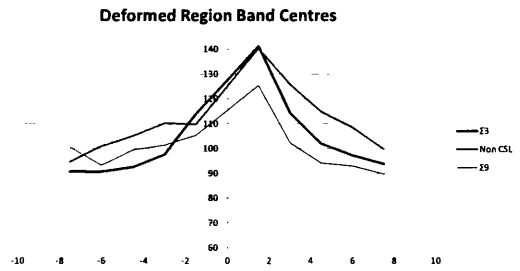

(b) Deformed region mapped by band centres

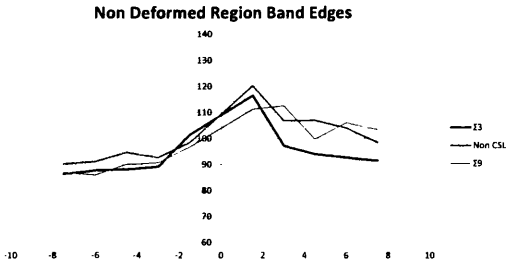

(c) Non-deformed region mapped by band edges

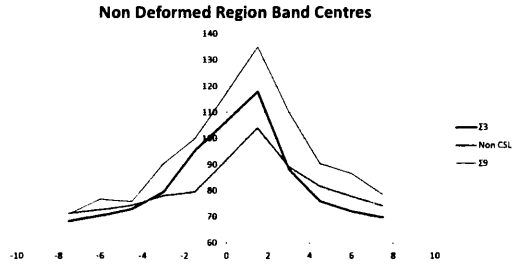

(d) Non-deformed region mapped by band centres

Figure 6.29: Two-sided GND boundary content in sample 20F. The average GND content for points in front of boundaries was taken based on proximity to the boundary. Points were averages in bins of 3 times the step size. The sides of the boundary with the lowest and highest GND content were termed grain 'A' and 'B' respectively. The average content for all grain 'A' is plotted on the left side of the axis.

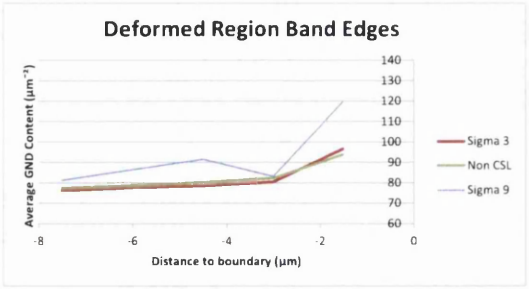

(a) Deformed region mapped by band edges

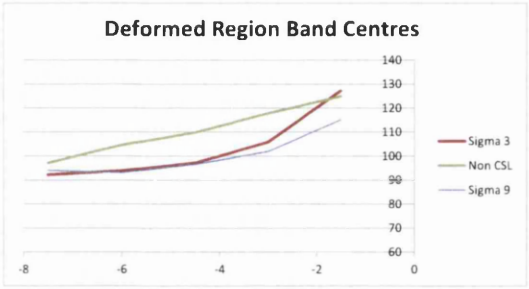

(b) Deformed region mapped by band centres

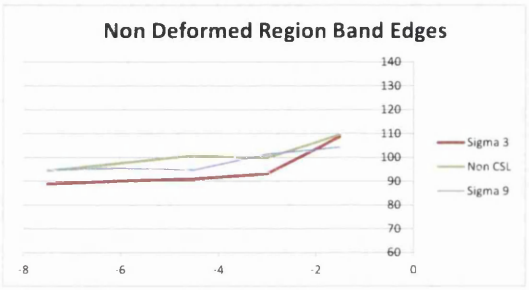

(c) Non-deformed region mapped by band edges

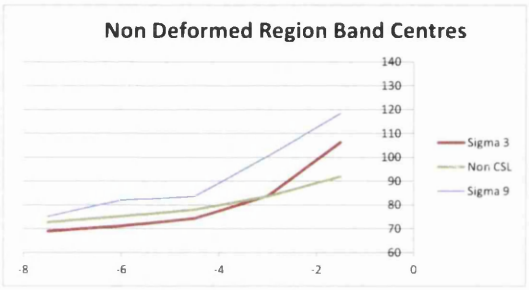

(d) Non-deformed region mapped by band centres

Figure 6.30: One-sided GND boundary content in sample 20F. The same data as in Fig. 6.29 was replotted with both sides of the boundary combined.

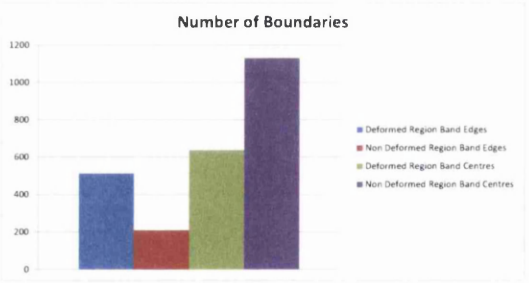

(a) Number of boundaries measured

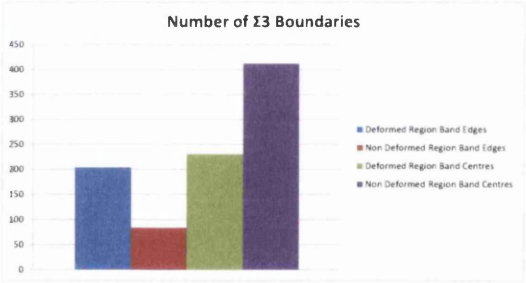

(b) Number of Σ3 boundaries measured

Figure 6.31: Number of boundaries and number of Σ3 boundaries measured in sample 20F.

Chapter 7

Matrix Sample Set

The folded sample set, presented in chapter 6 showed interesting results when comparing the GND structures in a tensile deformed region and a compressive deformed region. Different structures were also seen in an area of the sample which did not experience any deformation. However, the GND maps created were of different areas and one used a lower hough space resolution setting than the others.

Another sample was created to analyse the formation of the orientation relation to GND content seen in the tensile region of sample Pilot 3 and sample 20F, which was observed as high GND content wholly contained within certain grains, and the dislocation tangles seen in the non-deformed region and compressive region of sample 20F, with standardized settings used for creation of the GND maps to allow for easier comparison.

Unlike the GND results presented for sample 20F of section 6, after each deformation or annealing step a new sample was taken. Because more than one sample is used for comparison, inconsistencies and differences in surface preparation occur and must be considered when looking at results.

Samples were created according to Fig. 3.6 in Section 3.2. Pure copper (99.9%) was obtained from Goodfellow Ltd half-hard. Samples were cut into 2.5cm x 1cm x 3mm thick pieces. All samples were initially given a furnace anneal at 750°C for 38hrs and water quenched to grow the grains and remove any residual strain.

Two different radii were used for bending, 16.5mm and 23mm. Two different

temperatures were also used for a subsequent 30min anneal, 750°C and 820°C (~0.7Tm and ~0.75Tm respectively). Samples were named according to their position in a two-dimensional matrix containing combinations of these bending radii and annealing temperatures, seen in Table ?? in Section 3.2.

The sample cross sections were mapped by EBSD, oriented according to Fig. 7.1, with the red box representing the area shown in each map. The resulting maps are shown in Fig. 7.2 to 7.10.

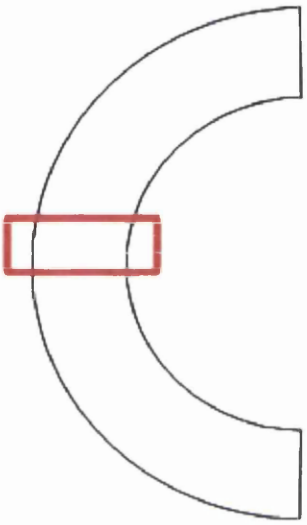

Figure 7.1: Matrix sample set cross section map orientation

The average grain areas of each sample and each region of the sample is reported in Fig. 7.11. In each sample, with the exception of sample 11 which showed significant anomalous grain growth, the grain size in the compressive region is smaller than in the tensile region. This can be an indication that there was more deformation in the compressive region of the samples. Also, interestingly the samples heat treated at 820°C show a smaller grain size than those heat treated at 750°C.

The boundary fraction of $\Sigma 3$ and $\Sigma 9$ boundaries for each sample is presented in Fig. 7.12. Again, a significant peak is seen for sample 11, which showed the largest grains. With the exception of sample 11, in each case the fraction of $\Sigma 3$ and $\Sigma 9$ boundaries actually decreases.

Figure 7.2: Cross section of sample 00. Average grain size was measured and is provided in Fig. 7.11.

Figure 7.3: Cross section of sample 01. Average grain size was measured and is provided in Fig. 7.11.

Figure 7.4: Cross section of sample 02. Average grain size was measured and is provided in Fig. 7.11.

Figure 7.5: Cross section of sample 10. Compressive end is pictured at the top of the page. Average grain size was measured and is provided in Fig. 7.11.

Figure 7.6: Cross section of sample 11. Compressive end is pictured at the top of the page. Average grain size was measured and is provided in Fig. 7.11.

Figure 7.7: Cross section of sample 12. Compressive end is pictured at the top of the page. Average grain size was measured and is provided in Fig. 7.11.

Figure 7.8: Cross section of sample 20. Compressive end is pictured at the top of the page. Average grain size was measured and is provided in Fig. 7.11.

Figure 7.9: Cross section of sample 21. Compressive end is pictured at the top of the page. Average grain size was measured and is provided in Fig. 7.11.

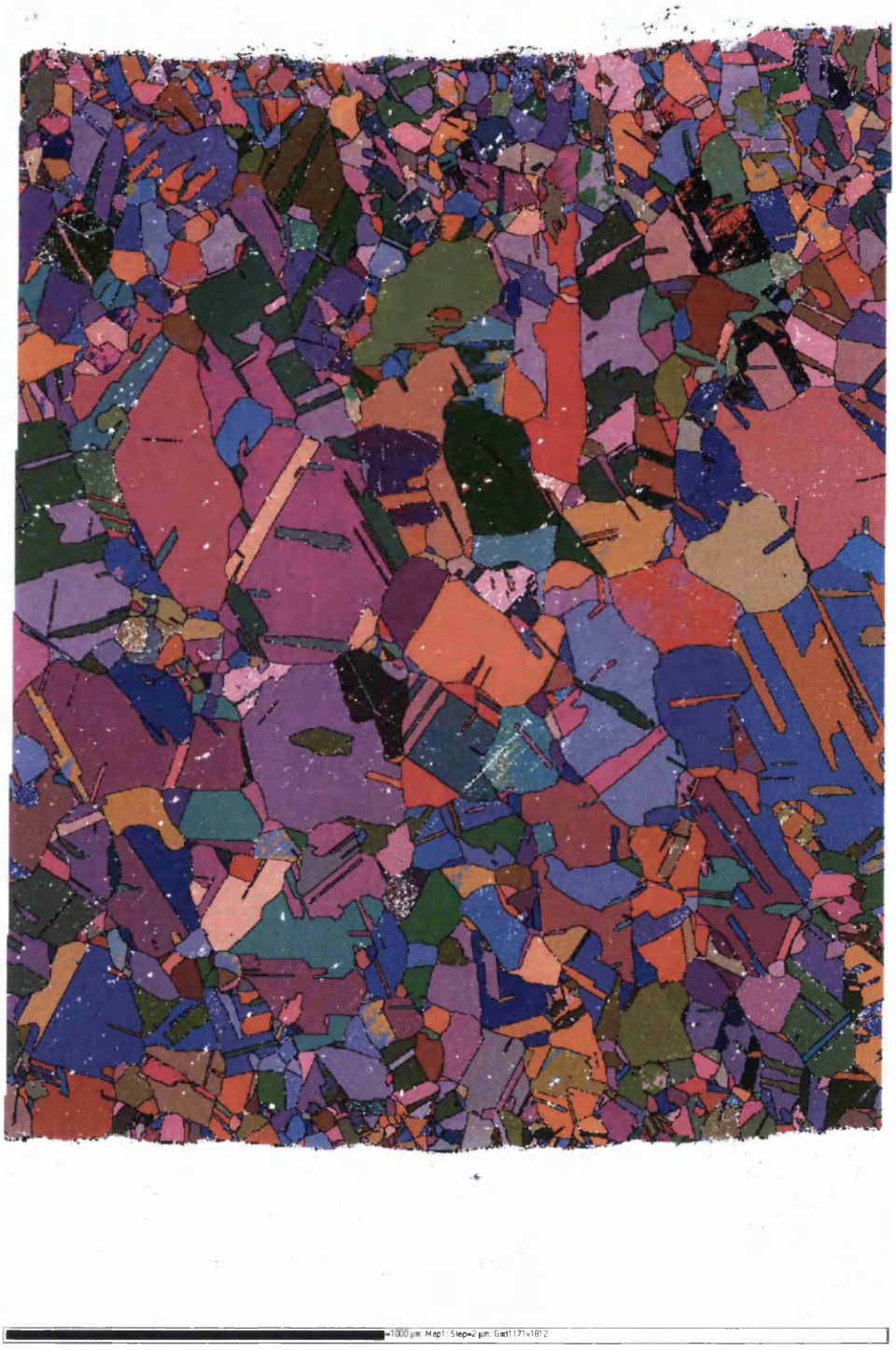

Figure 7.10: Cross section of sample 22. Compressive end is pictured at the top of the page. Average grain size was measured and is provided in Fig. 7.11.

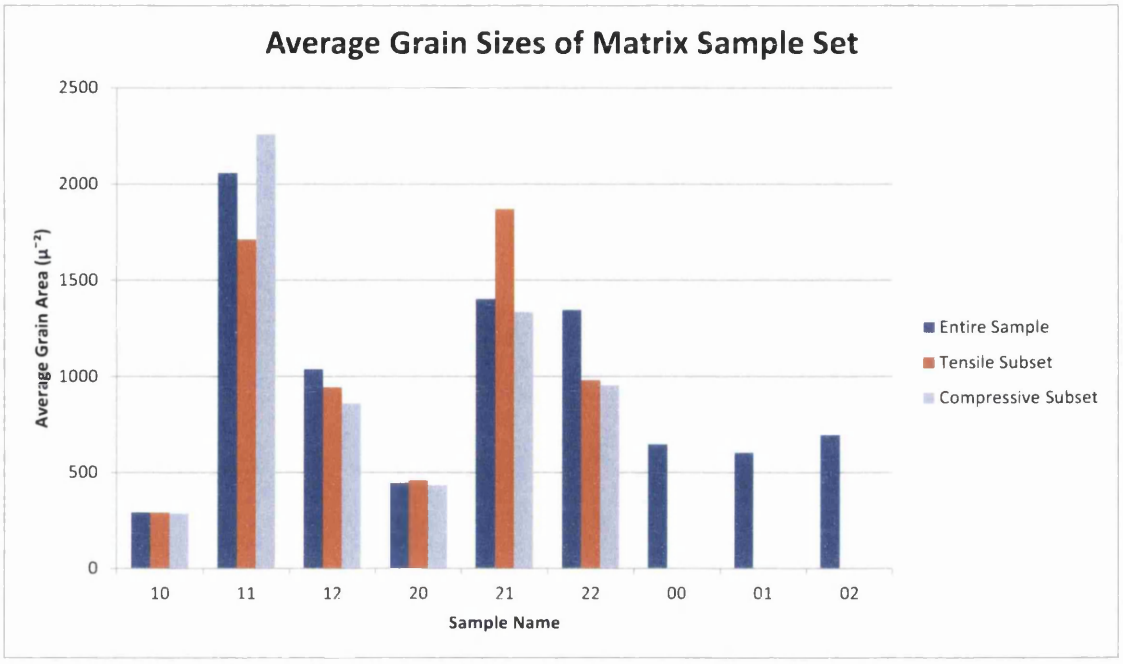

Figure 7.11: Average grain areas in all samples and sample regions of matrix sample set.

7.1 Anomalous Grain Growth

All samples were given an initial anneal at 750°C for 38hrs, which caused anomalous grain growth in the samples. The anomalous grains were not caused by the bending and heat treatment since they are seen in samples which were only bent and did not receive a subsequent heat treatment. An anomalous grain in the centre of sample 10 is shown in Fig. 7.13.

The theoretical grain growth law, Eq. 7.1, is obeyed only for high purity metals at temperatures approaching the melting point.

$$\bar{D} = (KT)^{1/2} \tag{7.1}$$

For a larger range of temperatures, it has been shown that the presence of solute atoms in the parts per million range can affect the activation energy for grain growth, and four stages of grain growth are observed. At certain temperatures and solute atom concentration, a second stage of grain growth is shown to be not normal grain growth, but secondary recrystallization. A few selected large grains

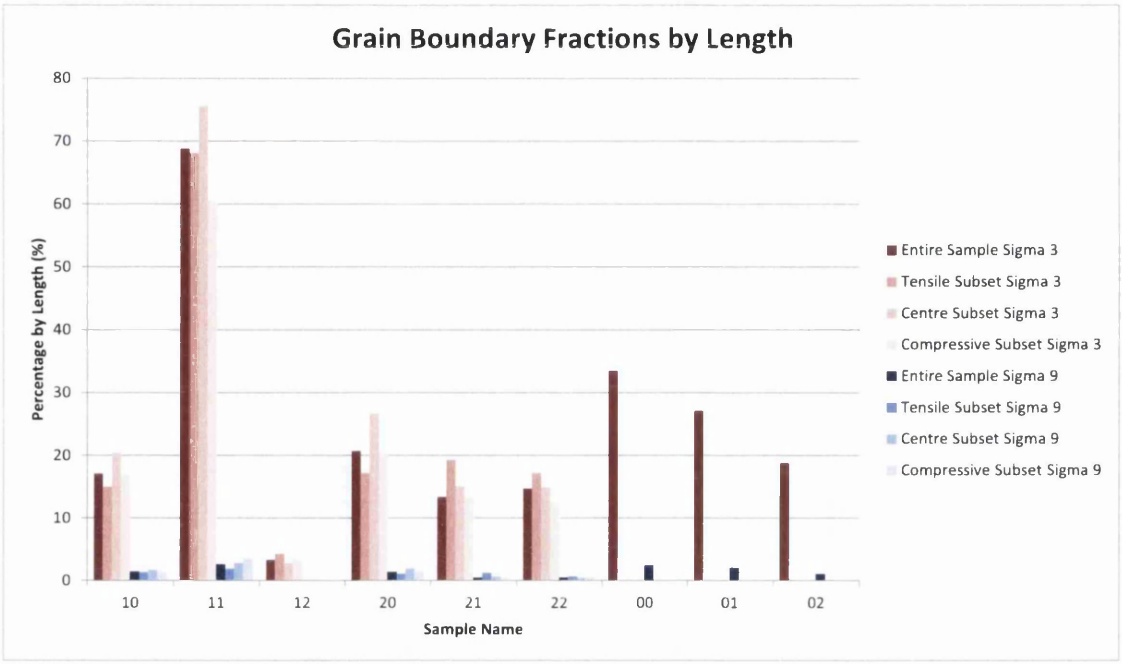

Figure 7.12: $\Sigma 3$ and $\Sigma 9$ boundary fractions in matrix sample set. Fractions are presented as a percentage of total length of boundaries.

grow and consume smaller adjacent neighbours and continue to grow until they impinge on other anomalously large grains. The purity (99.9%) and temperature (750°C) of the heat treatment applied to the samples is in the region of that which could cause the growth of anomalous grains.

The purpose of this sample set is to create a comparison of GND structures formed under differing conditions. Anomalous grains are not within this scope, so care was taken to exclude them from the areas being mapped.

7.2 GND Analysis of Matrix Sample Set

The matrix sample set was created to give an in-depth look at the development of the GND structures seen in sample Pilot 3 of section 5 and sample 20F of section 6. After each deformation or annealing step, a sample was taken for analysis. If a sample involved a deformation step then two GND maps were created, one at the tensile end and one at the compressive end, otherwise one GND map was created in the bulk of the sample away from any edges. Maps were also created in the centre

Figure 7.13: Cross section of sample 10 with anomalous grain in the centre. Care was taken to avoid mapping sample sections with anomalous grains after it was discovered they were present in the samples.

regions of samples 10 and 20 to analyse the deformation at the centre directly after bending.

Each orientation map was created using identical settings, as recommended in Section 4.3. Practical examples of the benefits of both indexing by band centres and band edges were shown in section 6.2 using maps of sample 20F. Due to external microscope time restrictions and so that GND map statistics could be directly compared, one indexing method needed to be chosen to be used when creating the orientation maps for the matrix sample set. Despite the lower noise and more polarized GND maps produced by band centres indexing, indexing by band edges was chosen for the possible smaller misorientations detection and predictable noise distribution. High GND content grains are also more easily distinguished when indexing by band edges, and GND tangles are still visible, while indexing with band centres is useful for highlighting GND tangles but is difficult to discern high GND content grains.

Also, to make any quantitative analysis between GND maps more comparable, each GND map covers the same area. Each map is a 3x3 map stitched together with each piece covering 40300 μm^2. The total area of each map varies slightly due to microscope drift during the map creation and cropping of the finished map to exclude the mounting bakelite. The amount of area covered by each map was selected based on external time constraints on the electron microscope system and not based on the size of any microstructural features. Based on the step size and indexing settings previously chosen, the area of each map is the largest area possible to map within a three day time span. The three day time limit is important as continuous operation of the electron gun degrades the filament, causing decreased accuracy near the end of the map or a worst case scenario of a blown filament.

All maps are oriented according to Fig. 7.14, with the tensile end on the left and compressive end on the right. The red highlighted regions in Fig. 7.14 indicate the regions mapped. Extra maps in the centre regions of samples 10 and 20 were also created with the map oriented in the same manner, tensile end on left and compressive end on right.

Unlike the quantitative GND map comparisons of sample 20F, the maps being compared in this section come from different samples. Using different samples introduces possible discrepancies due to the surface finish of each sample, which

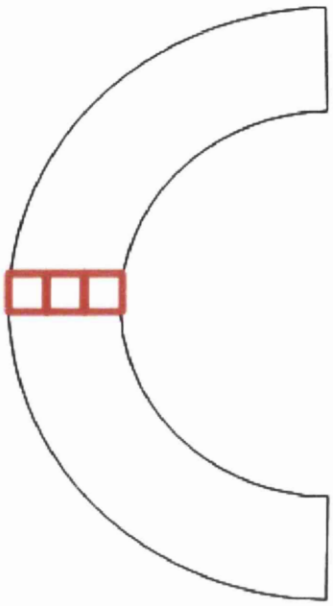

Figure 7.14: Location and orientation of GND maps of matrix samples. Maps were taken in the tensile (left-most red square), centre (corresponding to the geometric centre axis of the bend), and compressive regions (the right-most red square).

was shown to greatly affect results. Care was taken to achieve the best surface finish possible, but since polishing was done manually, not all samples are identical. Fig. 7.15 is given as a guide to the surface finish achieved for each GND map, and therefore the reliability of the results. Each map is given a rating based on the observed 'clean' area, or the total area minus the area occupied by scratches or surface contamination. This rating will be referred to frequently when interpreting the qualitative and quantitative results of the GND maps.

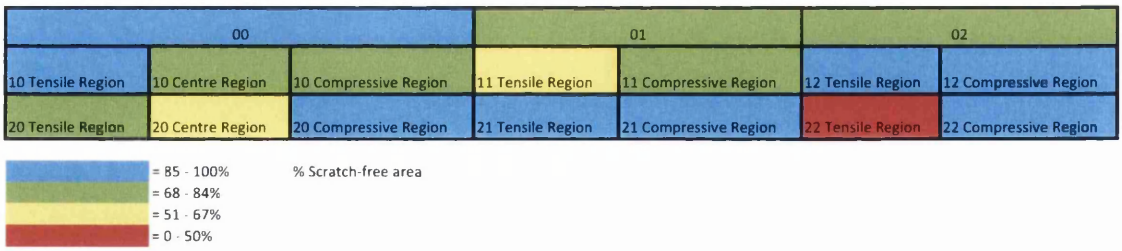

Figure 7.15: Surface condition of matrix samples. Colouring is based on the percent of mapped area that is scratch-free. This is used as a guide for interpreting results in subsequent sections.

7.3 Zero Bend Samples

The orientation and GND maps of samples which did not receive any deformation steps are presented in this section (samples 00, 01, and 02).

A GND map of sample 00 was first created, and is shown in Fig. 7.16a. The GND structure of sample 00 appears to be similar to the non-deformed region of sample 20F. The GND content has grouped together to form tangles, which appear to be emanating from triple junctions, sharp grain boundary corners, and grain boundary steps. There does not appear to be any textural relation to GND content. Twin related domains show grains with GND tangles and non-uniform GND content.

7.4 23mm Bend Samples

The orientation and GND maps of samples receiving a bend around a form of radius 23mm (samples 10, 11, and 12) are presented in this section.

GND maps of sample 10 were first created in the tensile, centre and compressive regions, and are shown in Fig. 7.18. All three maps show high quality surface preparation, with only a low number of fine scratches on each map. Only portions of the compressive region map show cause for concern about the surface finish of the sample. One deep large scratch is easily visible.

The tensile map shows expected high content near the left tensile end, with decreasing content moving towards the centre region. Tangles are still observed in the sample, however less frequently than in sample 00, many of them being broken up by the deformation.

One large grain shows strain concentrations at each of its sharp corners and triple junctions, shown in Fig. 7.17. Plastic strain in this grain is accommodating the rotation of neighbour grains during the bend.

Isolated areas appear possibly to show an orientation relation to GND content through twin related grains alternating high and low content; however, the difference in content between the grains is not particularly significant and it is very infrequent.

The compressive region of the sample also shows the expected high GND con-

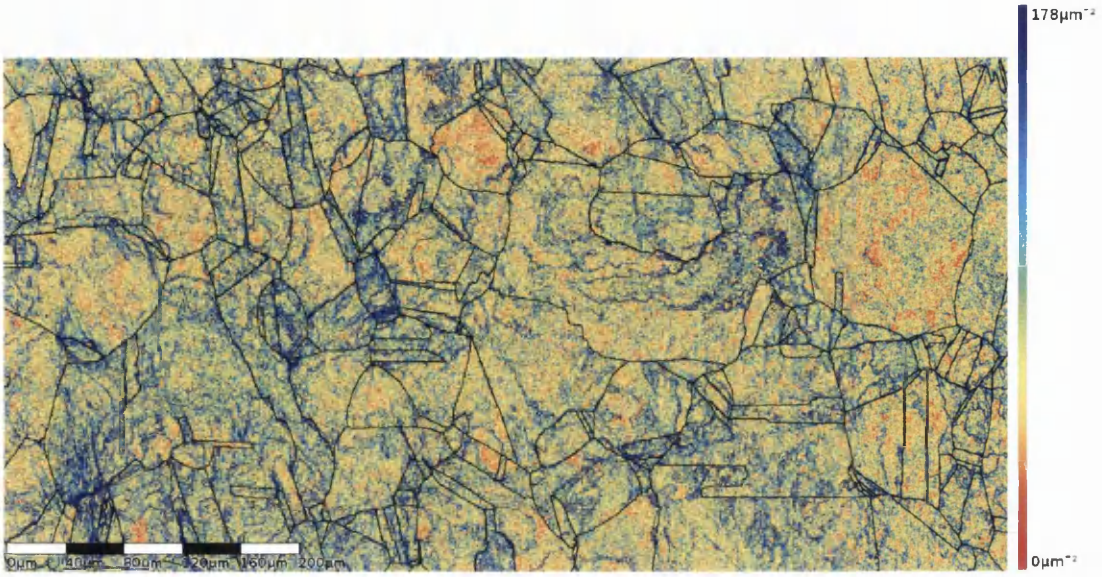

(a) Sample 00

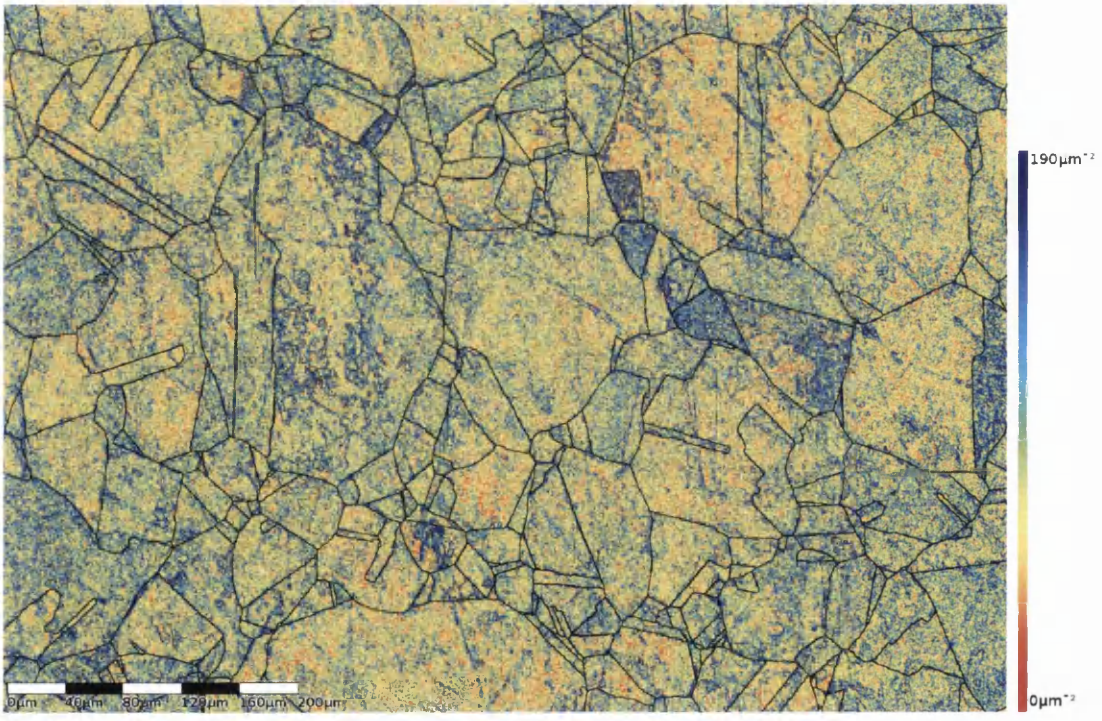

(b) Sample 01

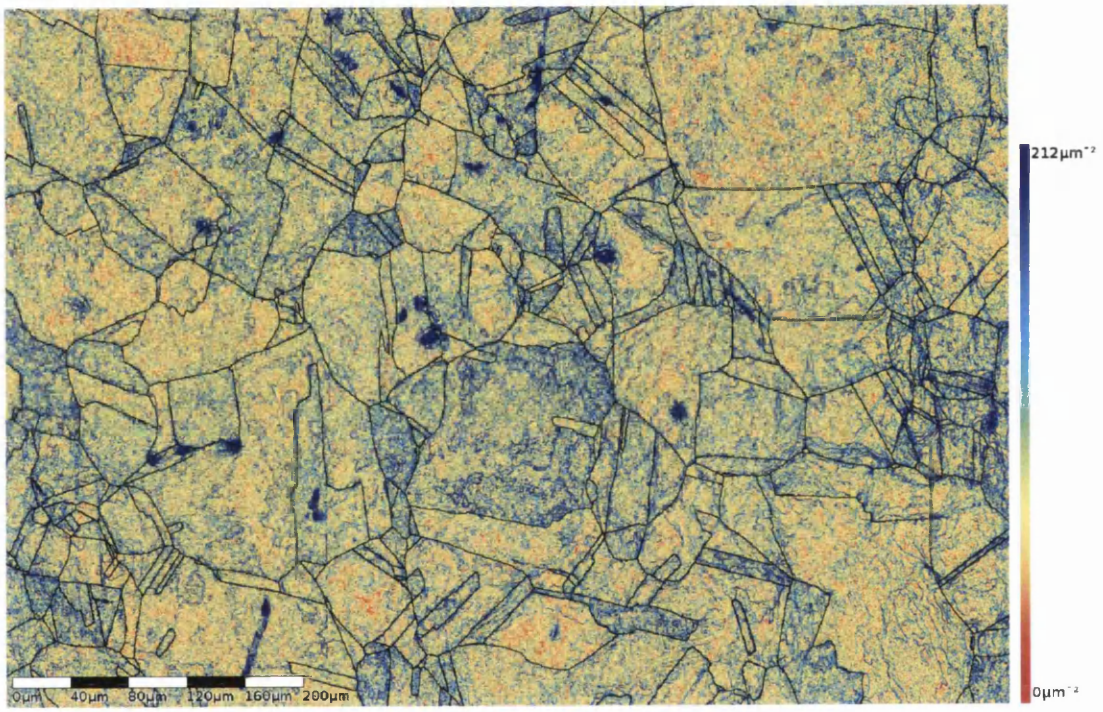

(c) Sample 02

Figure 7.16: Zero bend sample GND maps.

tent at the compressive edge of the sample, decreasing towards the centre region. The compressive region also shows little to no GND tangles. The vast majority of tangles present in the region appear to have been broken up by the bending.

The large twin related domain near the top right of the sample shows significant orientation relation to GND content. One large grain shows high GND content distributed evenly throughout the grain, and twin related grains show lower content. Grains within the twin related domain with a similar orientation to the large deformed grain also show a high GND content.

The centre region of the sample is similar to the deformed region of sample 20F. No GND tangles are observed in this region, with the GND content showing a very diffuse structure. High GND content grains are seen twin related to lower content grains. Some GND content appears at triple junctions and grain corners, but the GND structure does not appear to show a preference for these areas.

The GND map of the centre region of sample 10 Fig. 7.18b is significant because it shows the break up of the GND tangles and division into high and low GND content grains under low stress and before any annealing step is applied. It was speculated after the GND map of sample Pilot 3 showed an orientation relation to GND content that the growth of twins not properly aligned to the applied stress was causing retained strain in certain grains. However, this map shows that high and low content grains are formed during the deformation step without any grain growth.

Despite the lack of grain growth, twinned grains are still the cause of the formation of high GND content grains. The sample is not particularly textured, with twin grains in roughly random orientations. Within a twin related domain, the grains oriented to best accommodate the stress deform preferentially, while the other grains remain relatively unstrained.

Sample 11 was created after applying an annealing step of 30min at 750°C to a sample with an identical history to sample 10. GND maps of the tensile and compressive region of this sample are shown in Fig. 7.19.

Unfortunately, the map of the tensile region is tarnished by scratches and surface contamination in Fig. 7.19a. GND tangles are observed only near the left tensile end, and appear infrequently moving towards the centre region. There also appears to be no high/low GND content twin related grains, however, as with the

GND tangles, the scratches and surface contamination may disguise the presence of these features.

The GND map of the compressive region of sample 11 in Fig. 7.19b shows much more orientation relation to GND content, with readily apparent high/low GND content twin related grain regions. Slight GND tangles are seen near the right compressive end. More GND tangles would likely be observed closer to the compressive end, but the are not seen because the map was cropped to only include the copper sample and no bakelite to allow for the GND calculations, and as such the map does not extend to the absolute compressive end.

Sample 12 was created similarly to sample 11 but with a 30min annealing step at 820°C replacing the 750°C anneal. Because of the higher temperature for the annealing step, a higher driving force for boundary migration and for recovery would be expected. GND maps in the tensile and compressive regions of sample 12 are shown in Fig. 7.20.

The tensile end of the sample shows distinct examples of alternating high/low GND content twin related grains. The grains are also larger than those in the tensile region of sample 10, before any annealing step. GND tangles do not appear in this map, having been broken up by the bending step. New GND tangles are starting to form, as seen by the separation of GND content within grains.

The compressive region of sample 12 shows grains of comparable size to the tensile region, but with considerably less disparity between the GND content of twin related grains. Near the right side compressive end of the sample new GND tangles are shown to have formed. Moving the toward the centre region the GND relation to orientation has disappeared, and the beginnings of tangles are observed.

7.4.1 Summary of 23mm Bend Samples

Three samples with identical thermal histories were bent around a 23mm form and two of the samples were given separate annealing steps; one at 820°C for 30min, and one at 750°C for 30min. The tensile and compressive regions of each sample were mapped for GND content, and the structures analysed.

The three samples show the role of high GND content grains and GND tangles in the deformation and recovery of the material. The differences between the tensile

and compressive regions during deformation and recovery are also highlighted.

Initially, in sample 00, the GND content shows tangled structures extending from triple junctions, grain corners, and other high free volume areas. Upon bending, sample 10 shows that the tangle structures are significantly broken up. At this point, an orientation to GND content develops. Within twin related domains, the orientation best aligned to accommodate the applied stress preferentially deforms, allowing the other grains within the twin related domain to remain relatively unstrained, as shown by the alternating high and low GND content twin related grains in the centre region GND map of sample 10 in Fig. 7.18. At this stage, the compressive region is also showing some texture relation to GND content in the same manner as the centre region.

After a 30min heat treatment at 750°C, sample 11 shows that the tensile region starts to form high/low GND content twin related grains, but much of the sample is obscured by scratches and surface contamination. The compressive region of the sample has more obviously formed the high/low GND content twin related grains.

A 30min anneal at 820°C shows even more advanced stages of recovery. The grains have stopped growing and started recovering as they are comparable in size to the grains in sample 11. The tensile end of sample 12 has more obviously formed high/low GND content twin related grains and is beginning to show the formation of GND tangles. The compressive region shows more advanced GND tangle formation and the high/low GND content twin related grains have disappeared.

These samples show the GND structures present in the material after steps of deformation, grain growth and secondary recovery. They also show that the compressive region of the sample is moving through all stages of restoration faster than the tensile region. These stages will be explored further with the 16.5mm bend samples.

7.5 16.5mm Bend Samples

The orientation and GND maps of samples receiving a bend around a form of radius 16.5mm (samples 20, 21, 22) are presented in this section.

GND maps of sample 20 were first created in the tensile, centre and compressive regions, and are shown in Fig. 7.22. The maps produced in the tensile and centre

regions show significant surface contamination and scratching, and as such are difficult to interpret. The centre region, like sample 10, shows some high GND content grains, while the tensile region does not show any; however, the surface contamination and scratching may be causing or masking any high GND content grains.

The GND map of the compressive region of the sample is of much higher quality than the other two maps. Only one scratch is observed in the map near the compressive edge. The uneven surface preparation is due to the manual preparation method used. Human error can cause uneven pressure to be applied while the sample is in contact with the polishing wheel.

The GND tangles observed in the pre-bent sample 00 have been broken up by the bending in the compressive region of sample 20. Smaller tangle fragments are now seen in the grain bulk. Some GND tangles previously present in the material are still seen emanating from triple junctions and sharp grain boundary corners, however they are much more infrequent. In both the tensile and compressive regions of sample 20, uncharacteristically low GND content grains can be seen at the deformed edge, where the highest deformation would be expected. The strain has moved around and avoided these grains.

Sample 21 was created by applying a heat treatment at 750°C after the bending step to a sample with an identical history to sample 20. Orientation and GND maps of the tensile and compressive region of sample 21 are shown in Fig. 7.23. These maps were the of the highest quality of all maps created.

The GND map of the tensile region of sample 21 shows a diffuse GND structure. An orientation relation to GND content is also observed. High GND content grains are easily visible neighbouring low GND content grains, often within twin related domains. The grains in this region are significantly larger than those seen in pre-heat treatment sample 20 and pre bending sample 00. This is significant because it shows the textural relation to GND content after heat treatment and grain growth.

The centre section of sample 20 received a significantly lower applied stress than the tensile or compressive region of any sample. The centre section GND map showed a textural relation to GND content being formed by the applied stress. The grains within a twin related domain best oriented to accommodate an applied stress deformed preferentially over the other orientations, resulting in

certain grains showing high GND content. The tensile region of samples 10 and 20, not receiving any heat treatment after bending, did not show the orientation relation to GND content. Presumably, the stress was sufficiently high that it could not be accommodated by only the grains oriented preferentially to deform, and so all or most grains deformed under the stress. The tensile region of sample 21 shows the orientation relation to GND content developing during an annealing step. Two separate stages of separation of GND content into grains is shown by these samples.

While the orientation relation to GND content is prevalent in certain grains in the tensile region of sample 21, other grains show a more advanced state of recovery, with the GND content in the bulk of the grain moving outwards towards the boundaries. The GND content has started to migrate towards triple junctions and grain boundaries, however tangles have not yet formed. Fig. 7.21 shows an example of the GND content that has migrated towards a triple junction and grain boundary. At this stage, GND content building up in front of grain boundaries appears related to the energy of the boundary, which is in turn related to the character and CSL number. The example in Fig. 7.21 shows GND content preferentially building up in front of one segment of a grain boundary. The two segments of the boundary have separate plane traces, indicating that the boundary plane, and energy, is probably different for each segment.

The compressive region of sample 21 shows a highly tangled structure in stark contrast to the diffuse structure of the tensile region. Long tangles are seen grouped together and emanating from microstructural features with excess free volume where dislocation may be expected to terminate, such as grain boundary corners and triple junctions. Some GND content is left built-up in front of grain boundaries, but the vast majority has accumulated into the tangles. The compressive region is shown to be at a more advanced stage of restoration than the tensile region of the sample due to the more tangled GND structure seen in the compressive region typical of a restored material.

Sample 22 was created in a similar manner to sample 21 but with a heat treatment step at 820°C after the bend, instead of the 750°C temperature used for sample 21. GND maps of sample 22 in the tensile and compressive regions are shown in Fig. 7.24.

Unfortunately, the surface quality of sample 22 is not of as high a standard as sample 21. Both the tensile and compressive regions are significantly scratched, hindering any observations of the underlying GND structure. The tensile region appears to show high/low GND content neighbouring grains and the compressive region appears to show tight, small, GND tangles; however, the extent to which any GND features are masked by the significant scratching is unknown.

The compressive region shows smaller GND tangles on the interior of grains, unlike previous samples which showed large tangles emanating from high free volume microstructural features. Higher annealing temperatures are known to cause more complete recovery by increasing the rate of dislocation climb and cross slip which are thermally controlled [113]. The higher annealing temperature used for sample 22 increases the rate of dislocation climb, allowing for more rapid and complete recovery than other samples with large dislocation tangles.

7.5.1 Summary of 16.5mm Bend Samples

Three samples with identical histories were bent around a 16.5mm form and two of the samples were given separate annealing steps; one at 820°C for 30min, and one at 750°C for 30min. The tensile and compressive regions of each sample were mapped for GND content, and the structures analysed.

The three samples give more insight into the GND structures during deformation and recovery. After deformation, GND tangles present in the material are broken up. At low stresses, near the centre of the sample, the applied stress is accommodated by grains oriented preferentially to deform, resulting in high GND content focussing within certain grains. Near the tensile and compressive ends, the applied stress is high enough that it cannot be accommodated by only the preferentially oriented grains, and so strain is seen across all grains.

After heat treatment, grain growth occurs in the samples. The tensile region of sample 21 shows an orientation relation to GND content which was not previously seen in the tensile region of sample 20. A different mechanism is responsible for the orientation relation to GND content formation in the tensile region of sample 21 than the orientation relation to GND content caused by deformation seen in the centre regions of sample 10 and 20.

The compressive region of sample 21 shows a significantly tangled GND structure, characteristic of a restored material. It is at a more advanced stage of restoration than the tensile region, which shows a more diffuse GND structure with an orientation relation to GND content, indicating that the compressive region has restored faster than the tensile region. The tensile and compressive regions of sample 22 follow sample 21. The tensile regions appears to show a GND content texture relation and the compressive region appears to show tangles; however, the maps are of significantly lower quality due to surface scratches. Smaller GND tangles are seen in the interior of grains in the compressive region of sample 22, and are attributed to the higher annealing temperature which increases the rate of dislocation climb and cross slip and therefore dislocation annihilation. As a result of the higher temperature anneal, the restoration in sample 22 is also more complete than in other samples. This correlates well to the 23mm bend samples, the cross sectional GND map of sample 20F, and the cross sectional GND map of sample Pilot, which also showed the compressive region at a more advanced stage of restoration than the tensile region. The possible reason for this will be explored in the following section while taking a quantitative analysis to the matrix sample set.

7.6 Analysis of Entire Matrix Sample Set

The matrix sample set reported in this chapter shows the range of GND structures expected at each stage of deformation, grain growth and a second stage of recovery.

The driving force for grain growth and recovery is proportional to the applied strain in the material and the temperature of the heat treatment. As such, a higher driving force would be expected for the samples bent around the smaller 16.5mm radius more than the 23mm radius form, and higher for the samples which received a heat treatment at 820°C than those that were heat treated at 820°C after bending. For example, the driving force for sample 12 would be higher than sample 11, but lower than sample 22.

The GND structures of each sample are consistent with their expected stage of recovery based on the ranking of samples by their driving force. The tensile and compressive regions of each sample show the same stages of deformation and

recovery, however the compressive region is always at a more advanced stage than the tensile region.

The GND structures and stages of deformation and recovery with referenced sample examples are as follows:

1. **Relaxed stage**
   As seen in sample 00. After a sufficiently long anneal, GNDs form tangles which emanate from microstructural defects with a high free volume, such as triple junctions and grain corners.

2. **Deformation Stage**
   The deformation stage differs based on the amount of applied stress. The centre region shows different GND structures than the outer regions since it experiences considerably less stress. The two expected GND structures at the deformation stage are:

   (a) ***Low stress structure***
   The low applied stress first breaks apart the GND tangles present in the material to form a diffuse GND structure. Next, grains oriented preferentially to accommodate the stress deform preferentially. Certain grains show a higher average GND content than other grains oriented less favourably to accommodate the stress. Within twin related domains, the orientation best fitted to accommodate the stress deforms throughout the domain. The low stress structure shows the first stage of GND textural relation development. The low stress structure is seen in the centre region of sample 10, and to a lesser extent sample 20 due to the sharper bend.

   (b) ***High stress structure***
   As the stress is increased, it cannot be accommodated by only the preferentially oriented grains, and so all grains experience roughly equal deformation. The highest GND content is found at the grain edges as grains rotate into each other. The high stress GND structure can be found in the tensile and compressive ends of samples 10 and 20. Interestingly, the grain size appears to affect the low high stress GND

structure transition. The compressive edge of sample 10 shows a large grain with high GND content in relation to its neighbours. The grain is large enough in comparison to its smaller neighbours to wholly accommodate the higher stress at the region where it is located.

3. **Grain Growth**

   The amount of strain is 6% at the ends in the 23mm bend samples and 7.8% in the 16.5mm bend samples. Both samples are on the transition of the amount of strain that would be expected to cause recrystallization. The samples receiving the lower strain likely only experience grain growth upon heat treatment, but the samples receiving the higher strain are likely somewhat recrystallized after heat treatment. The GND structure in the grain growth stage remains diffuse. GND tangles have not yet formed after they were broken up in the previous deformation stage. A second orientation relation to GND content structure is observed in this stage, however the mechanics of formation differ to the GND content orientation relation developed from the deformation stage. In the grain growth stage, grains oriented preferentially to release retained residual stress show lower average GND content than other grains, as explained using the SERM model for recrystallization in section 5.2 for sample Pilot 3. The grain growth GND structure is seen beginning to develop in the tensile regions of sample 11, and fully developed in the compressive region of sample 11. The tensile regions of sample 12 and 21 also show a fully developed grain growth GND structure. The compressive region of sample 12 shows a grain growth structure, however the compressive edge shows tangles beginning to form, indicating it is in transition to the final stage.

4. **Secondary Recovery**

   Recovery and recrystallization are typically competitive mechanisms after deformation, where recovery reduces the driving force for recrystallization and vice versa. However, after recrystallization or grain growth, a second stage of recovery is observed in the samples characterized by the return to a tangled GND structure. The initial stage of recovery, occuring before and to an extent during grain growth, is where any relation to GND content in

front of boundaries and grain boundary character would be expected. GND content builds up in front of boundaries and accumulates at triple junctions. Further recovery after grain growth shows GND tangles forming at triple junctions and sharp grain corners as GND content terminates and continues to interact to form lower energy structures.

Secondary recovery mostly involves the GND content formed behind a mobile boundary. Immediately after grain growth, a diffuse GND structure is observed with an orientation relation to GND content. Grains growing which are not properly orientated to release the maximum amount of retained strain are shown to have a higher GND content than neighbouring grains. In this case, the GND content was not formed by applied strain, but instead left behind by a mobile boundary which are normally expected to leave behind a perfect crystal. Secondary recovery is movement of these GNDs into lower energy structures. The compressive edge of sample 12 shows the transition from the previous grain growth restoration to a secondary recovered GND structure. GND content is seen building up at boundaries and triple junctions and GND tangles are starting to form near the compressive edge. The compressive end of sample 21 also shows a fully recovered GND structure. A recovered GND structure is also shown in the compressive end of sample 22 and likely also in the tensile end, however the lack of adequate surface finish on the sample obscured the GND maps of sample 22. The samples show significant overlap in the GND structures seen in the steps of grain growth and secondary recovery, and so the end of step 3 and beginning of step 4 is not always obvious.

In each sample, the compressive region is shown to be at a more advanced stage of restoration than the tensile region. A higher driving force for restoration must then be present in the compressive region, caused by a difference in magnitude in applied strain in the compressive region than in the tensile region. Pure bending is expected to result in a linear strain gradient from tension to compression with equal bu opposite strain levels on either end of the bend. The true strain, however, is not equal.

Assuming the equal magnitude of elongation in tensile end and contraction

in the compressive end (|Final length − Initial Length|), the engineering strains at each edge will be equal. For equal magnitude, but opposite sign engineering strains, the true strain of the compressive region will always be larger. Observation of a plot of the natural logarithm makes this point more immediately clear, as the slope is larger for tangents to the curve closer to zero.

The larger true strain in the compressive region creates an unequal strain hardening rate between the two ends, displacing the neutral plane away from the compression end. The position of the neutral plane, or the plane at which the stress changes from compressive to tensile in character, is more accurately calculated by considering the axial load. In pure bending, the axial load is zero; that is, the integral of the tensile stresses over the cross sectional tensile area is equal and opposite to the compressive stresses over the cross sectional compressive area.

The position of the neutral plane being closer to the tensile edge of the sample is supported by the cross-sectional GND map of sample 20F, shown in Section 6.2 and Fig. 6.10 and 6.14. The sample underwent a short 20 min anneal at 600°C, and showed significant recovery in the compressive region and the beginnings of grain growth and recovery in the tensile region. A sharp peak in the GND content in the sample was seen near the centre, closer to the tensile end. The peak represents the position of the neutral plane in the sample, where stress and the driving force for restoration is lowest.

A standard linear relationship between the stress and distance to the neutral plane is not, however, seen in the matrix samples. Fig. 7.25 to 7.29 shows the average GND content as a function of position across each sample. The ends of samples 10 and 20 in Fig. 7.26 and 7.27 show the average GND content near the ends of the samples directly after bending. The average content is a plateau around $100\mu m^{-2}$ until approximately $25\mu m$ from each end, where it increases sharply. It is unclear whether the average GND content plots are representative of the absolute deformation. The bending breaks up GND tangles previously present in the material. More dislocation content is resolved as GND content when the dislocations have coalesced into tangles due to the higher point-to-point misorientation of the tangles being much greater than the indexing noise. The cause for the sudden drop in GND content away from the sample edges may be due to the breaking up of the GND tangles, until a point where the dislocation content is suddenly high enough

that the point-to-point misorientations are sufficiently higher than the indexing noise.

With the exception of the sharp peaks near the ends, sample 10 shows the theoretically expected strain relationship to position from the neutral plane. The slope of the curve in the compression end is much shallower than in the tensile end, showing that a minimum will be reached closer to the tensile end. The same relationship is not seen on the plots of sample 20; however the data quality in the tensile and centre regions of sample 20 is significantly lower than sample 10.

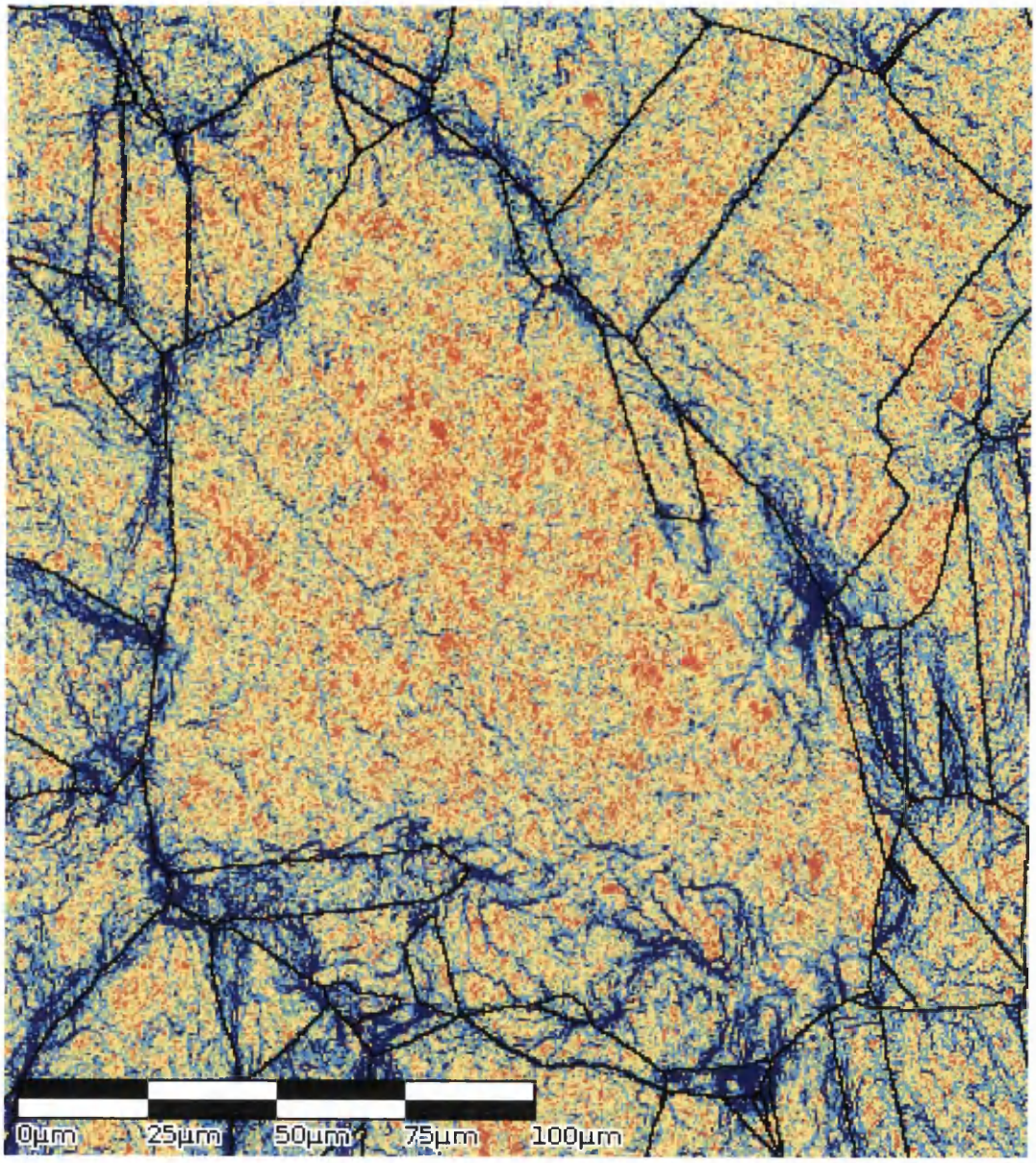

Figure 7.17: Large grain in tensile end of sample 10 accommodating strain of neighbouring grain rotations

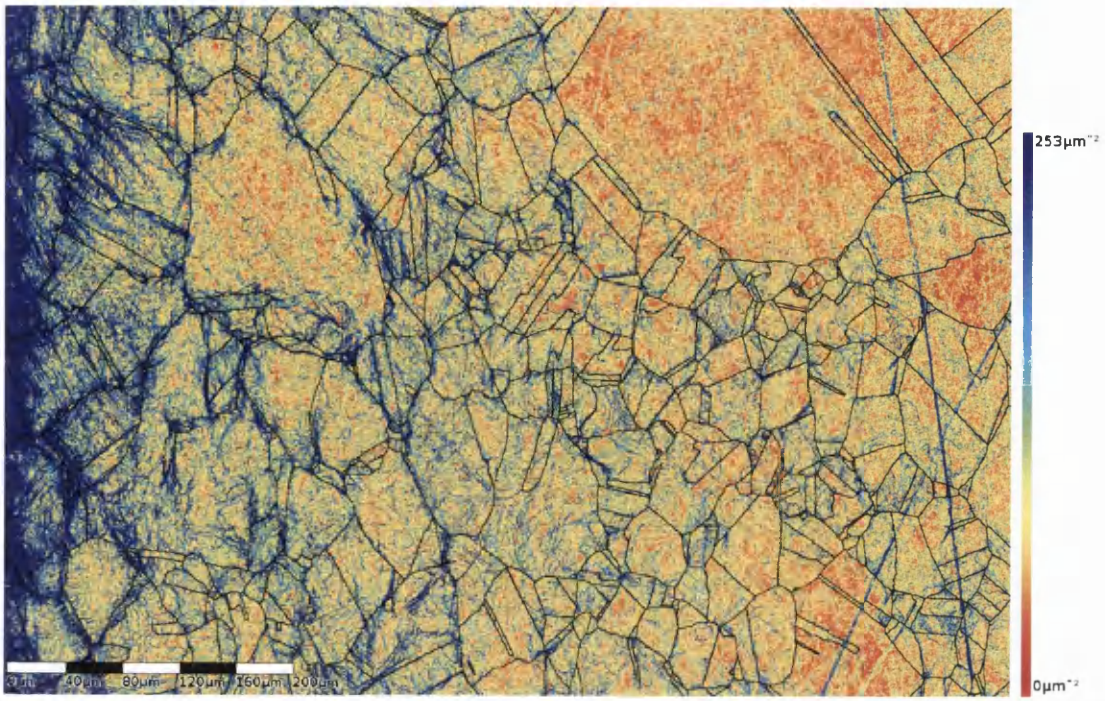

(a) Sample 10 Tensile Region

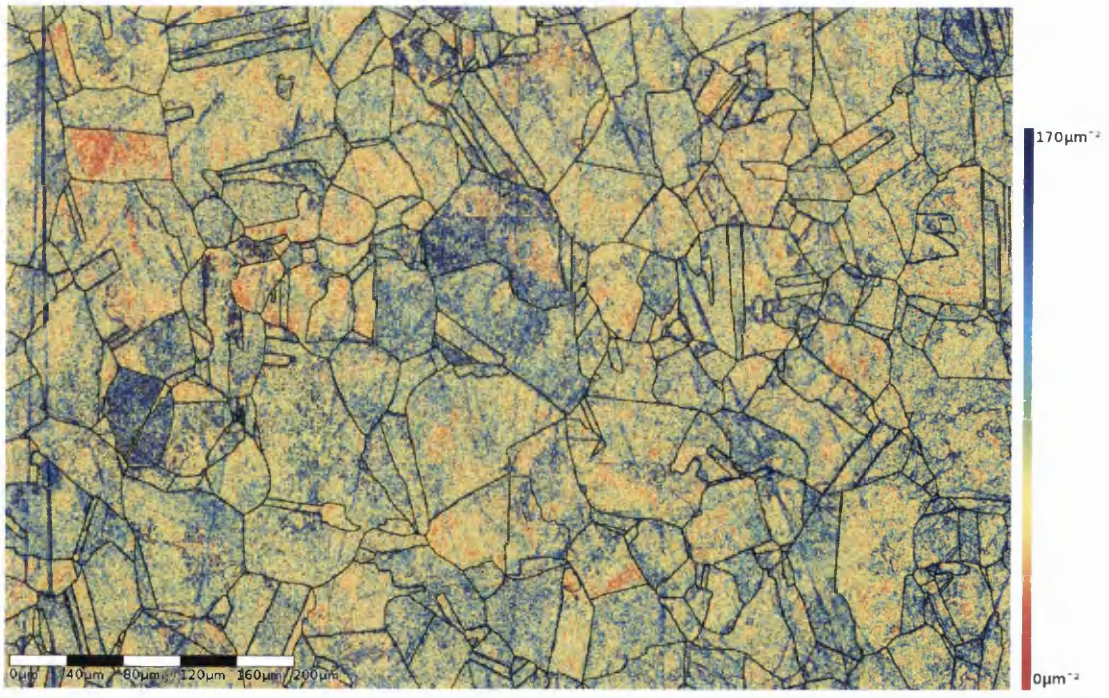

(b) Sample 10 Centre Region

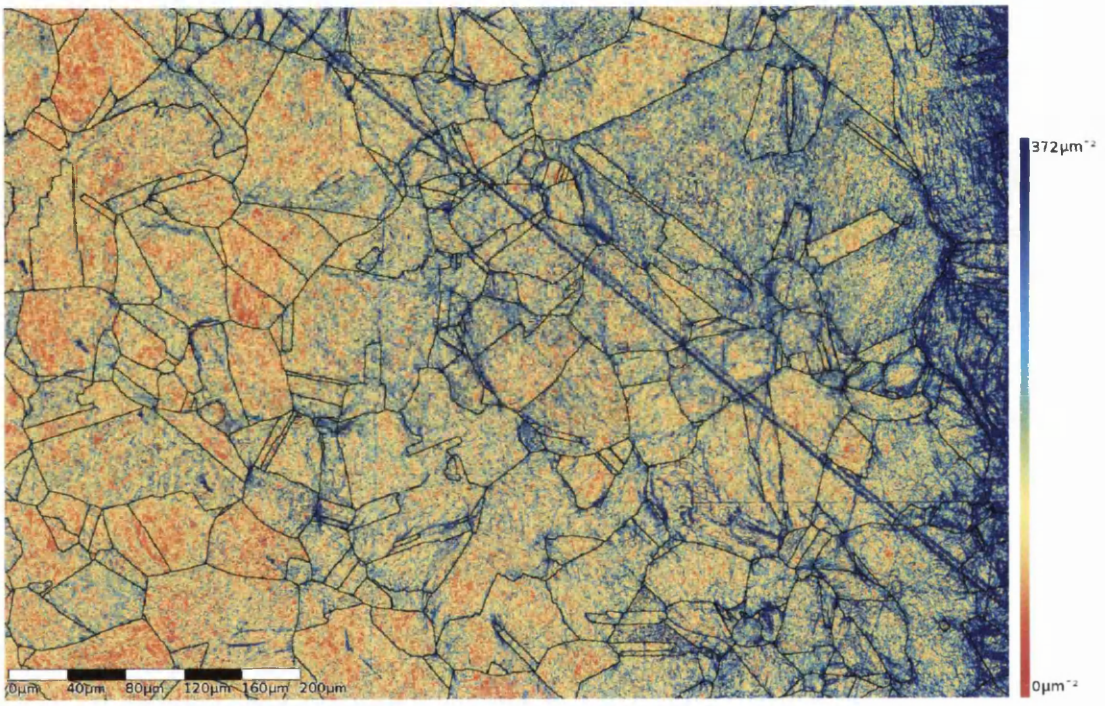

(c) Sample 10 Compressive Region

Figure 7.18: Sample 10 GND maps.

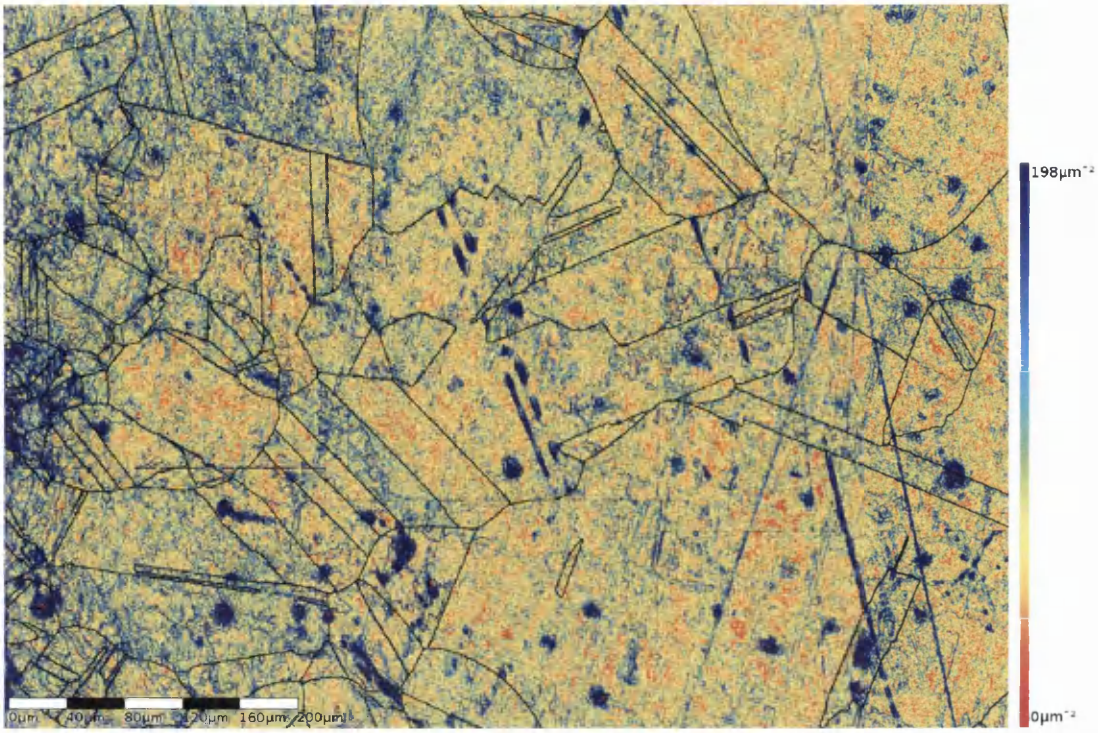

(a) Sample 11 Tensile Region

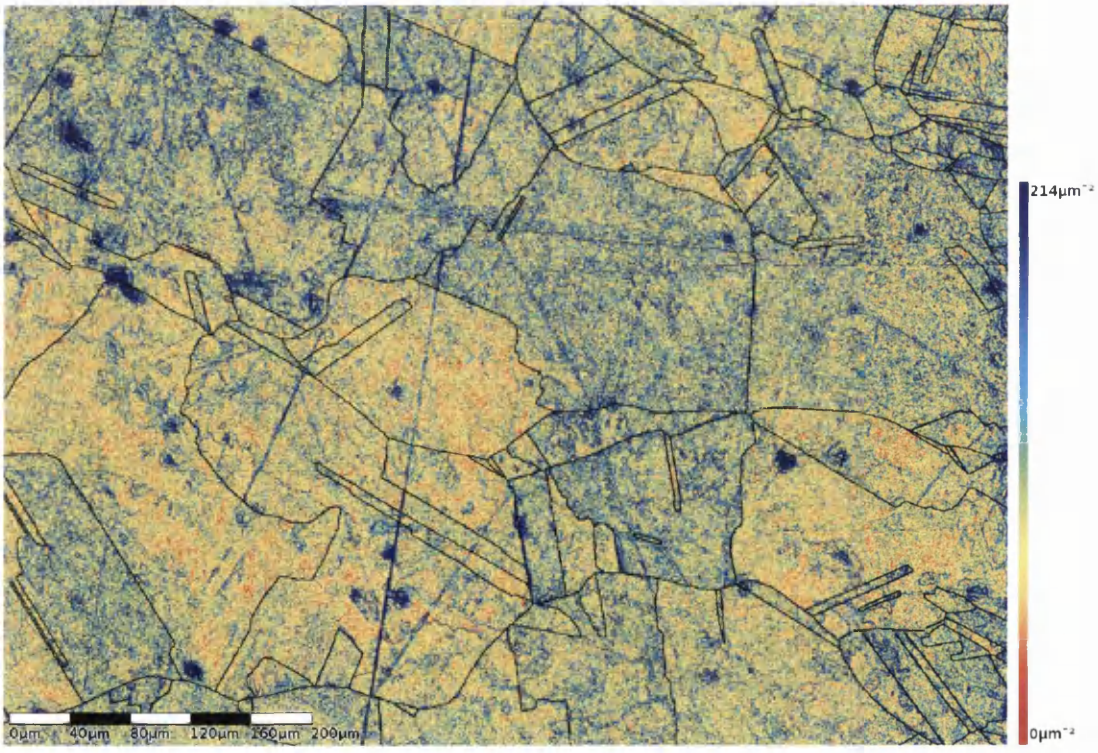

(b) Sample 11 Compressive Region

Figure 7.19: Sample 11 GND maps.

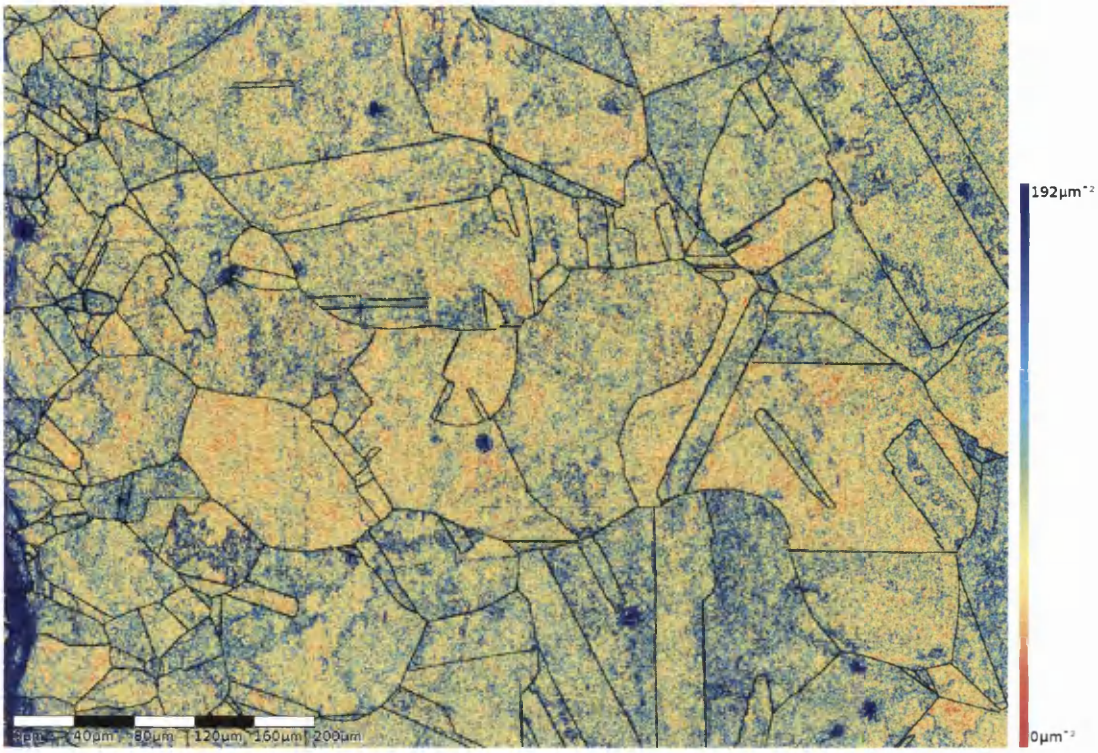

(a) Sample 12 Tensile Region

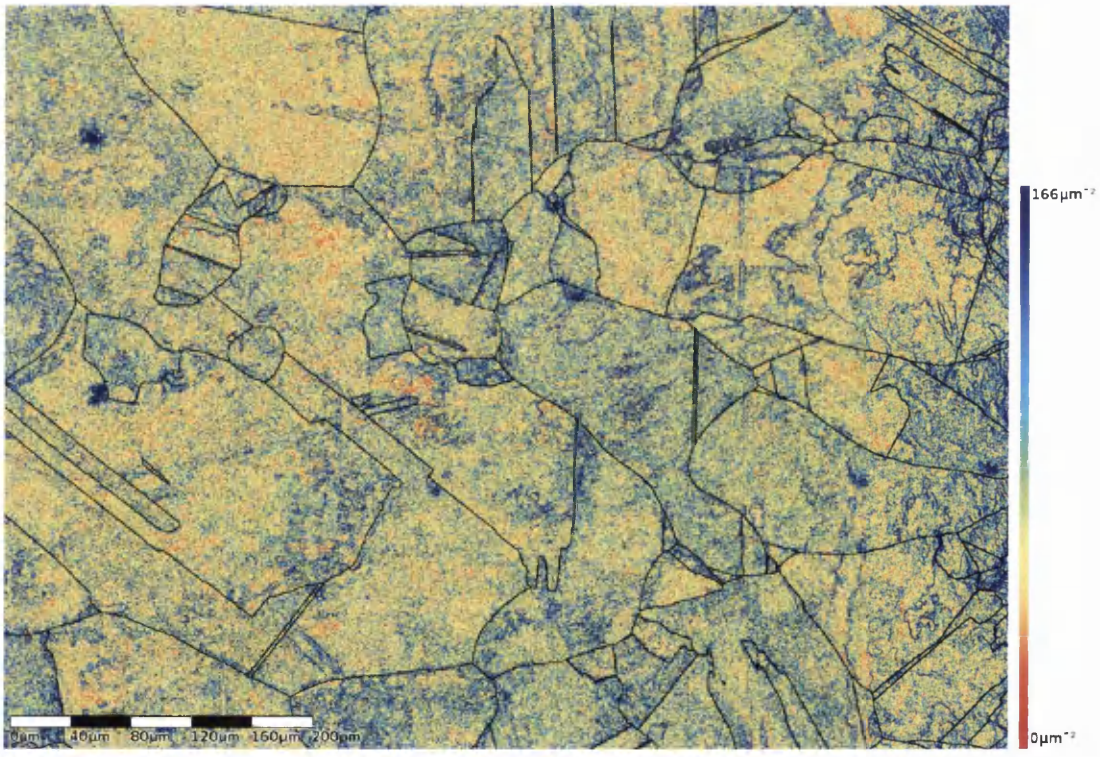

(b) Sample 12 Compressive Region

Figure 7.20: Sample 12 GND maps.

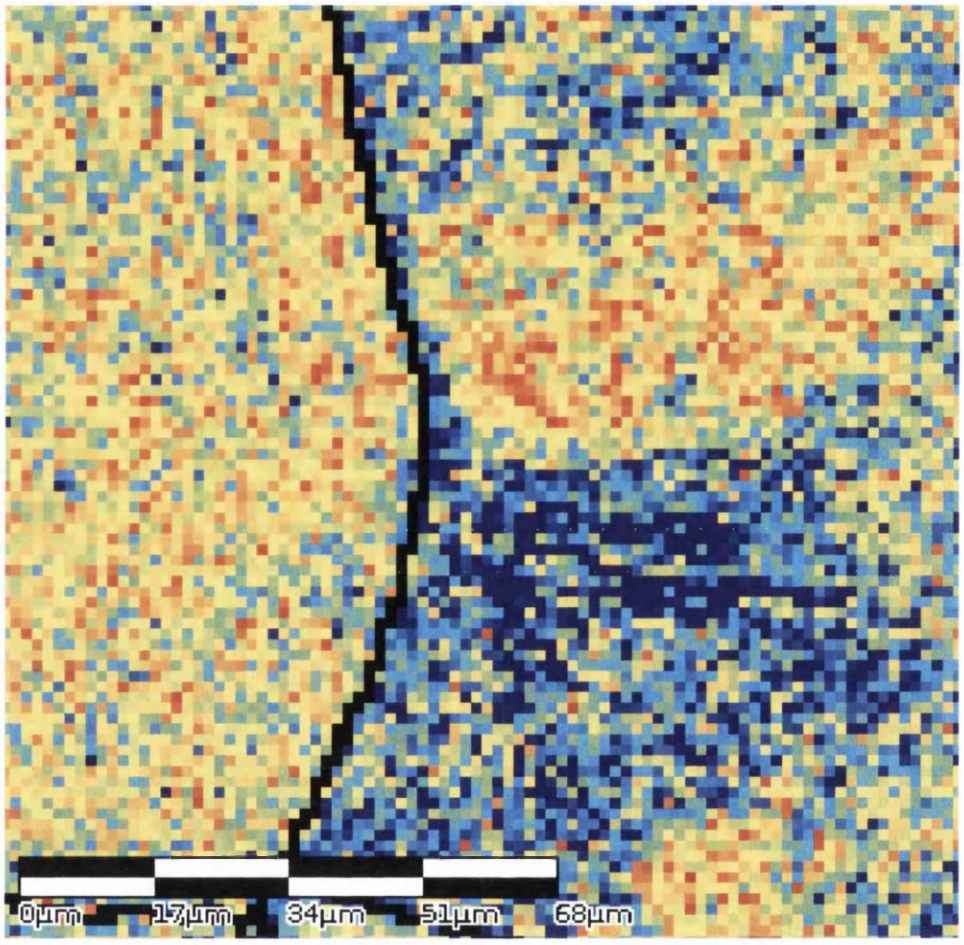

Figure 7.21: Small section of GND map of sample 21 in the tensile region. GND content is shown to build-up preferentially in front of one portion of the boundary.

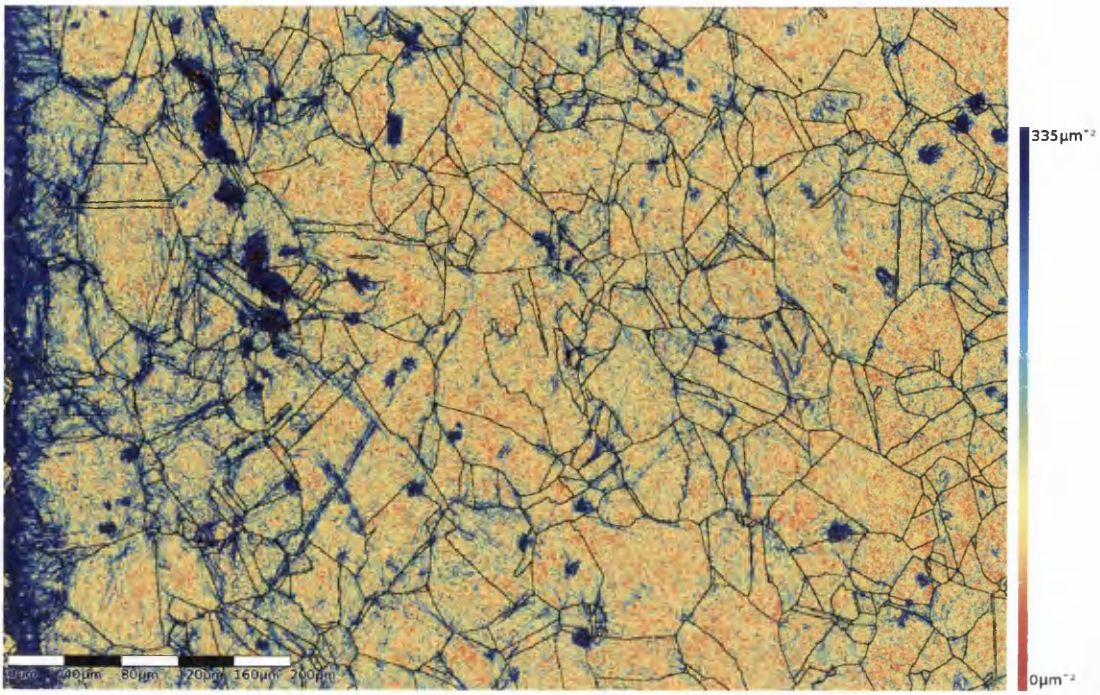

(a) Sample 20 Tensile Region

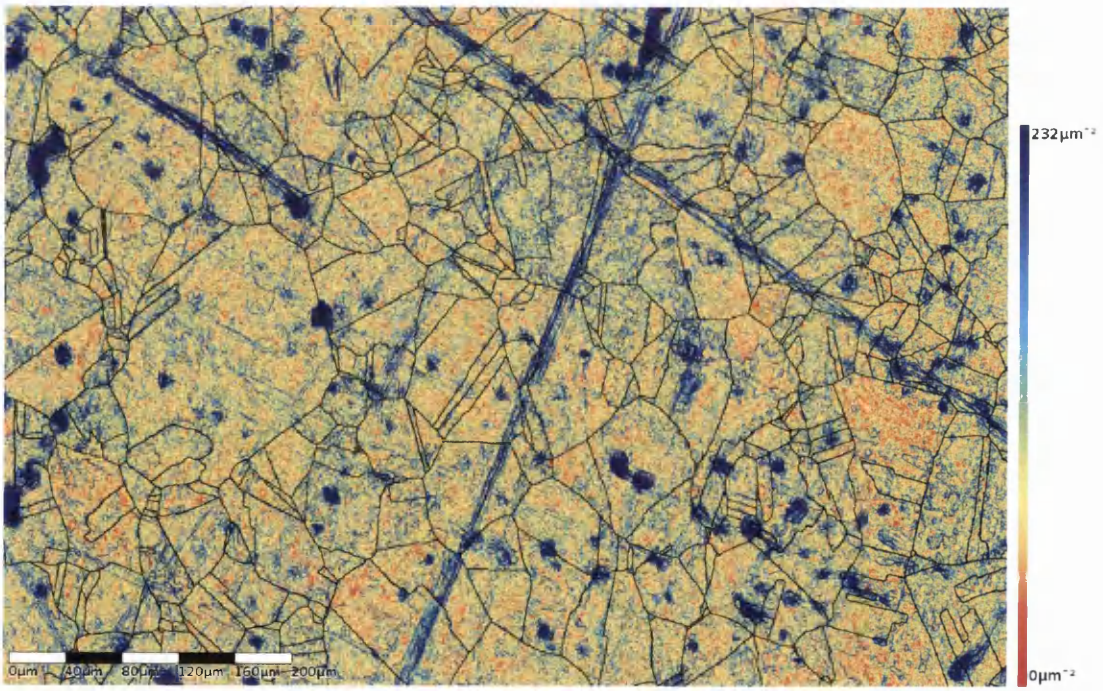

(b) Sample 20 Centre Region

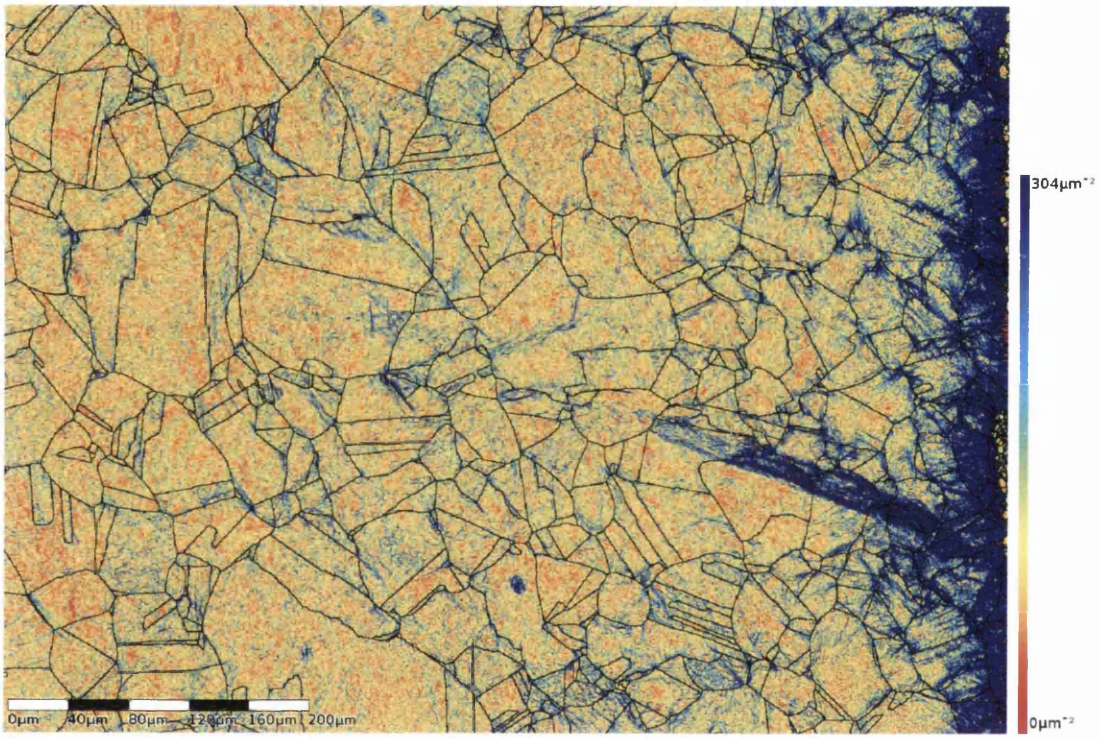

(c) Sample 20 Compressive Region

Figure 7.22: Sample 20 GND maps.

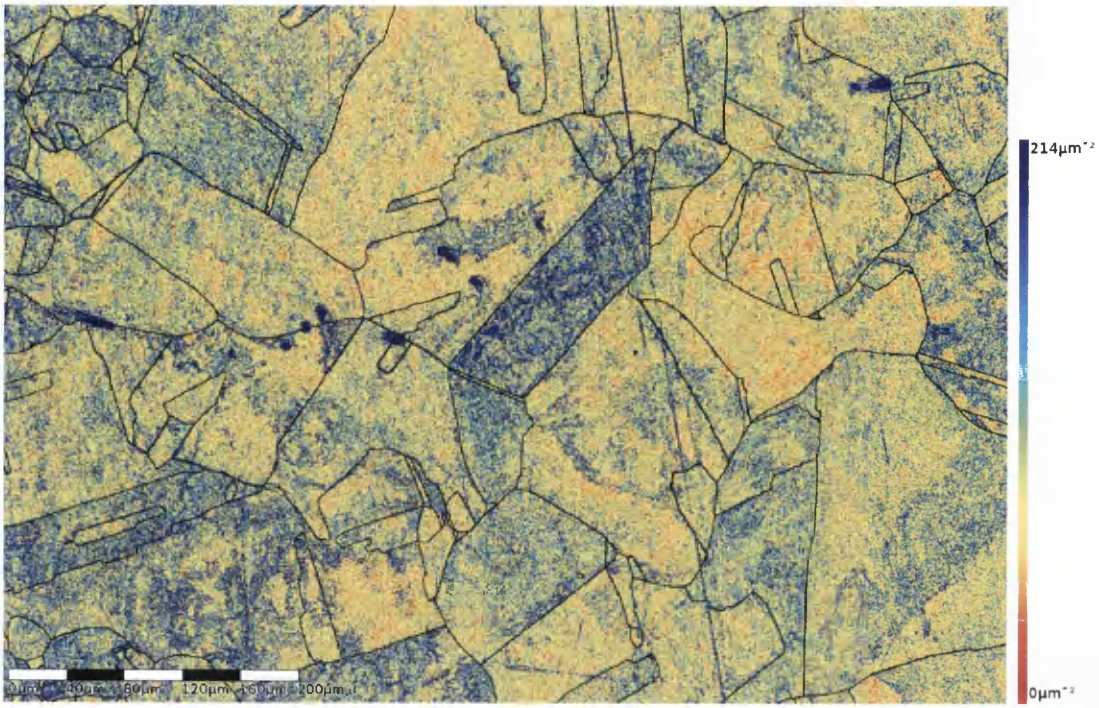

(a) Sample 21 Tensile Region

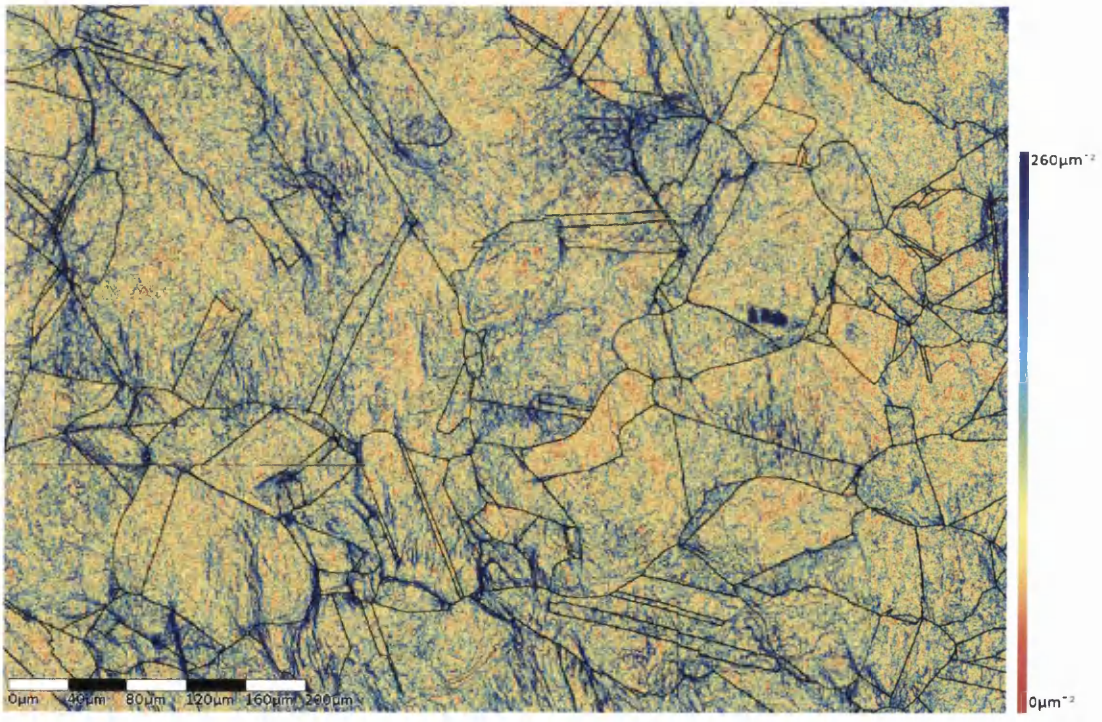

(b) Sample 21 Compressive Region

Figure 7.23: Sample 21 GND maps.

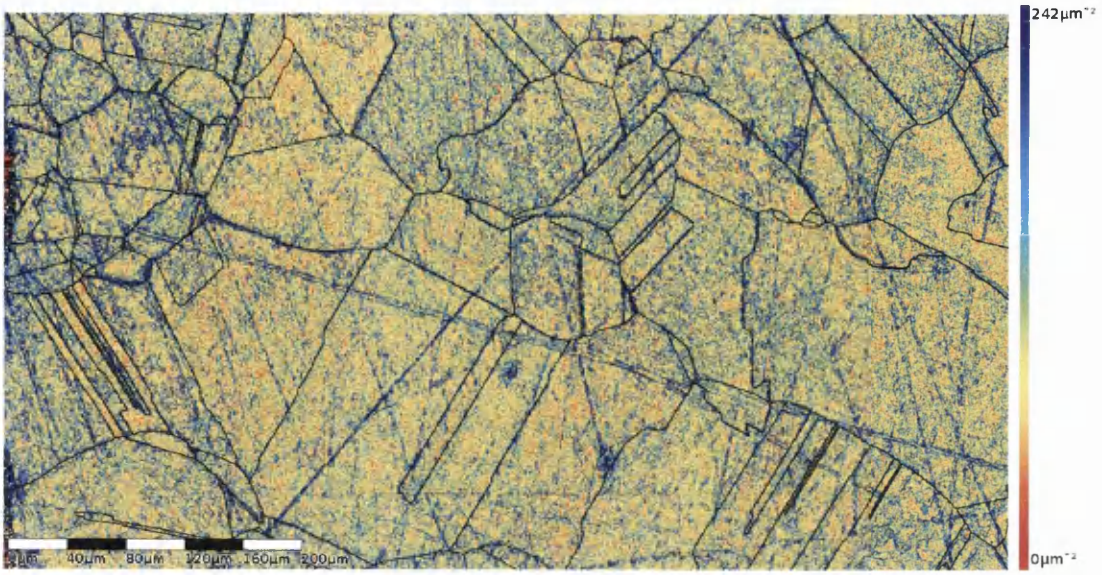

(a) Sample 22 Tensile Region

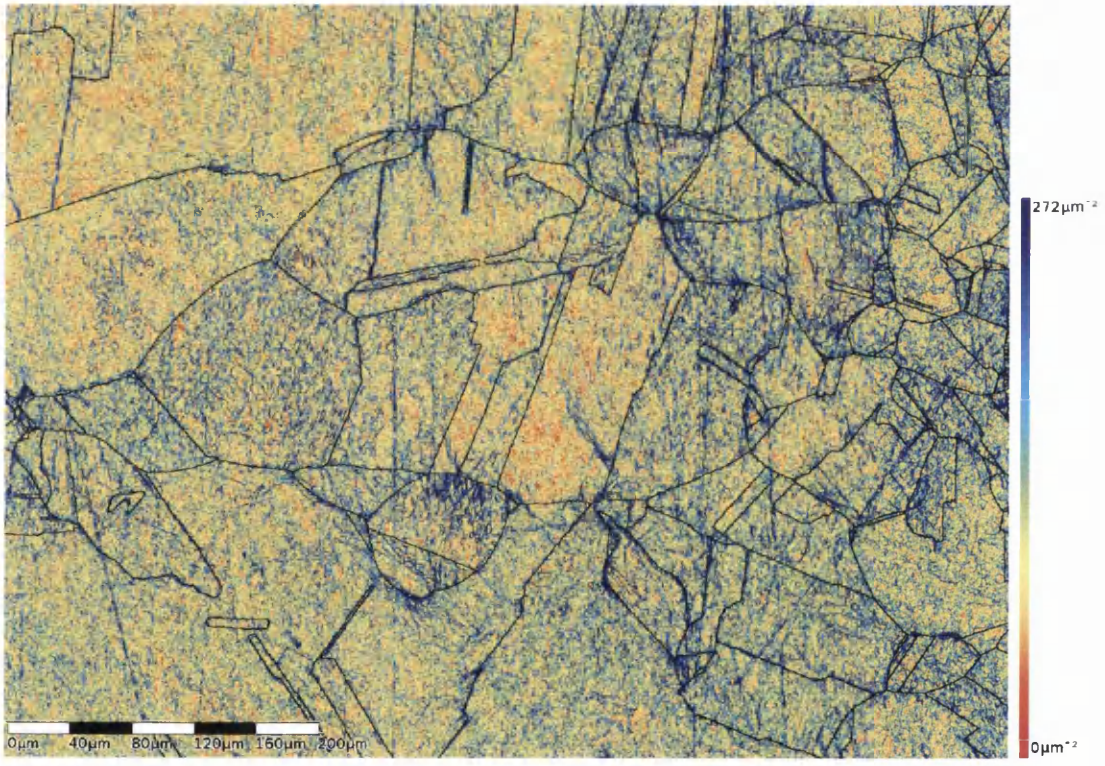

(b) Sample 22 Compressive Region

Figure 7.24: Sample 22 GND maps.

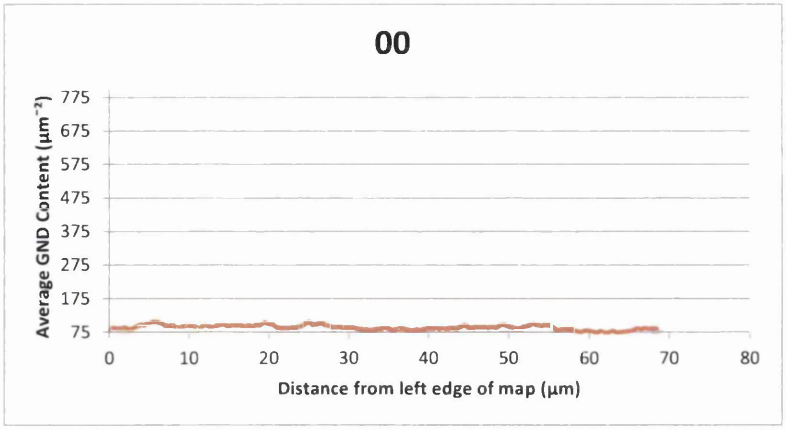

(a) 00

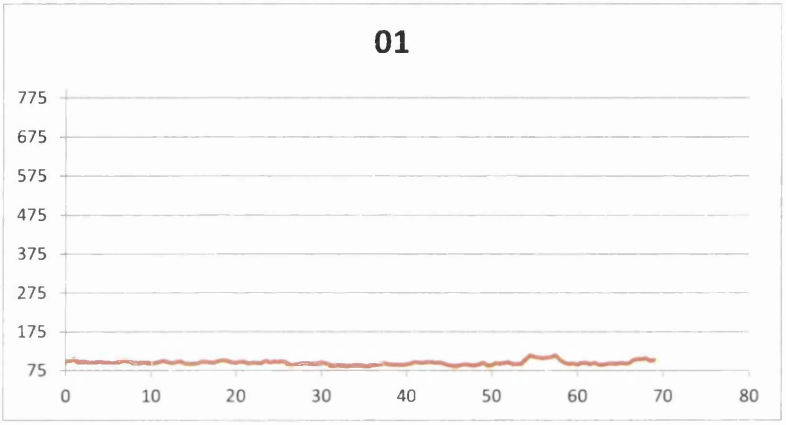

(b) 01

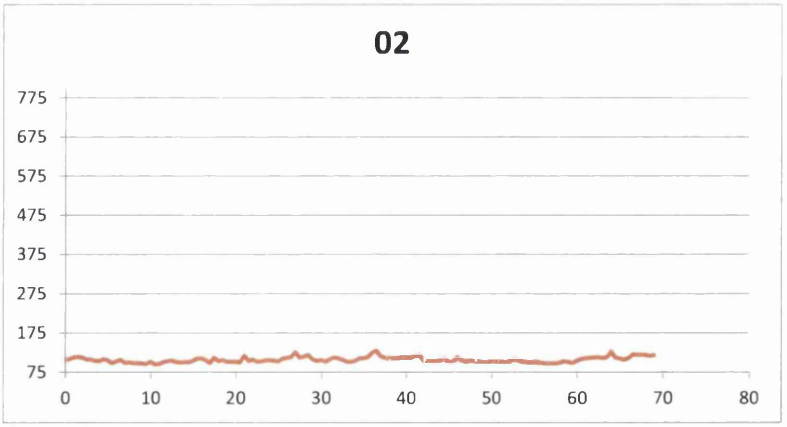

(c) 02

Figure 7.25: GND content profile of zero bend samples. GND content was binned into bins 10 pixels wide, and the average content in each bin calculated. The profile is plotted across the sample as a function of the distance from the left edge of the map.

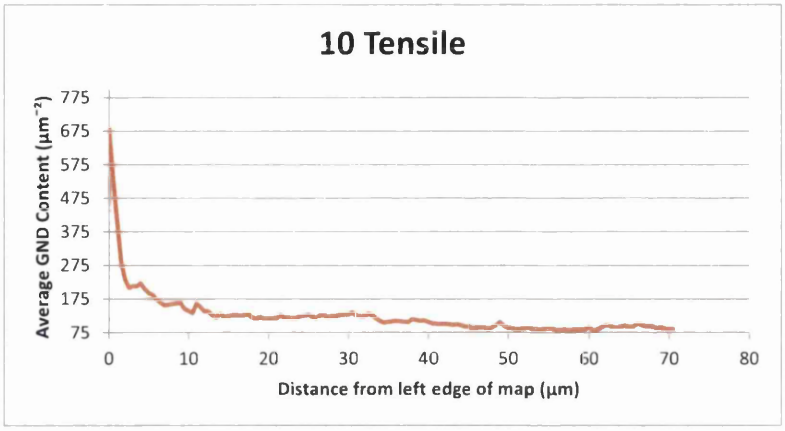

(a) 10 Tensile Region

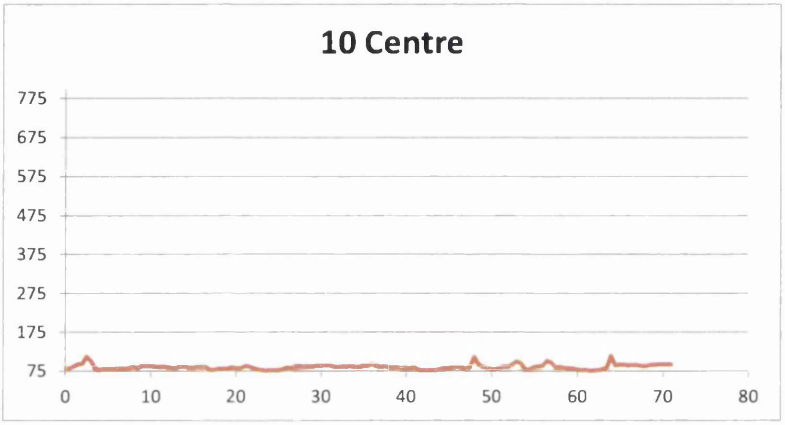

(b) 10 Centre Region

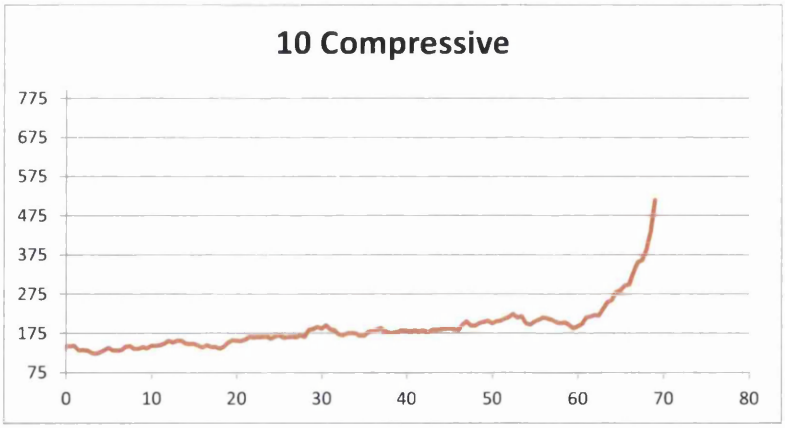

(c) 10 Compressive Region

Figure 7.26: GND content profile of regions in sample 10. GND content was binned into bins 10 pixels wide, and the average content in each bin calculated. The profile is plotted across the sample as a function of the distance from the left edge of the map.

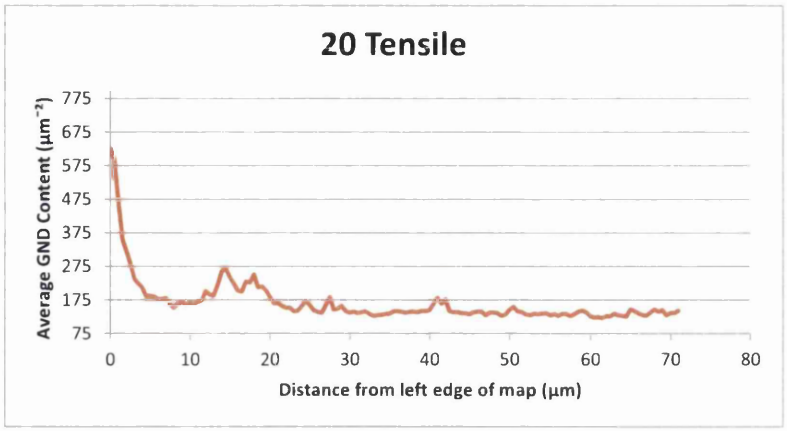

(a) 20 Tensile Region

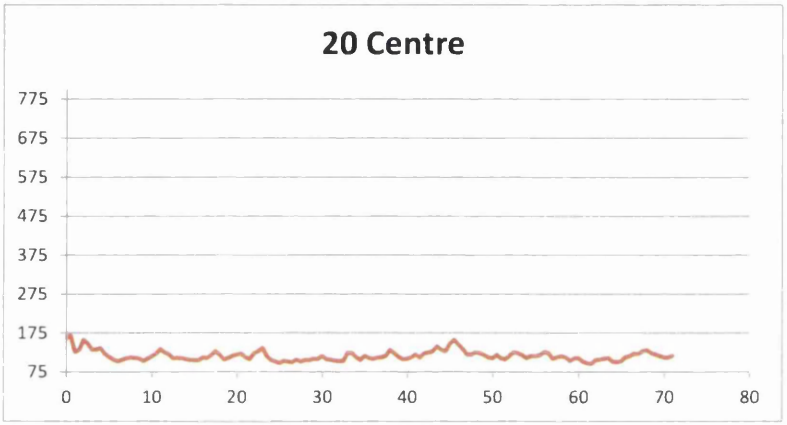

(b) 20 Centre Region

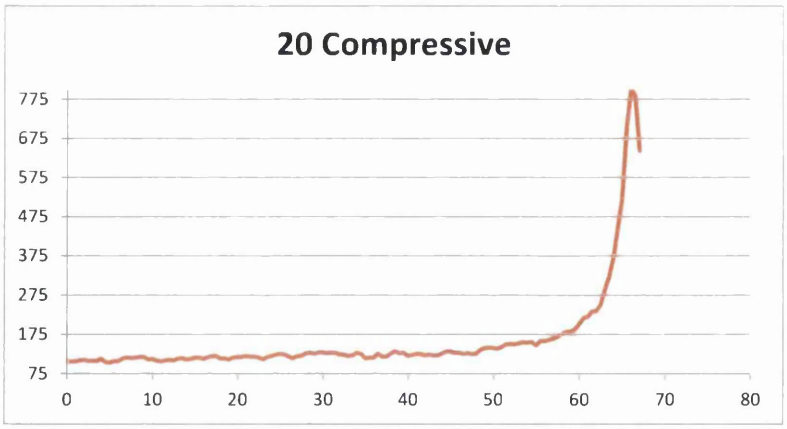

(c) 20 Compressive Region

Figure 7.27: GND content profile of regions in sample 20. GND content was binned into bins 10 pixels wide, and the average content in each bin calculated. The profile is plotted across the sample as a function of the distance from the left edge of the map.

An orientation relationship to GND content is often referred to when describing the GND structure present in many samples in the matrix sample set. This structure is observed by high GND content wholly contained within a grain with low GND content wholly contained within neighbouring grains which are often twin related and contained within twin related domains. In section 5.2, an orientation relation to GND content was observed in the tensile region of sample Pilot 3 and low GND content grains were found to have a preference for {111} plane normals parallel to the sample surface normal. A similar investigation was attempted for the matrix sample set; however any preferential direction for low or high GND content could not be found, as shown in Fig. 7.30 to 7.46. An average GND content was determined for each map and points with higher and lower than average GND content were plotted on separate pole figures. Similarly, both sets of points were plotted on an inverse pole figure of the three sample directions. Neither methods reveal any preferential directions for high or low GND content. The number of grains measured in the GND maps of samples in the matrix sample set was significantly less than sample Pilot 3 due to the smaller step size used for mapping, and so a larger sampling of grains may be required to determine a preferential direction for low or high GND content.

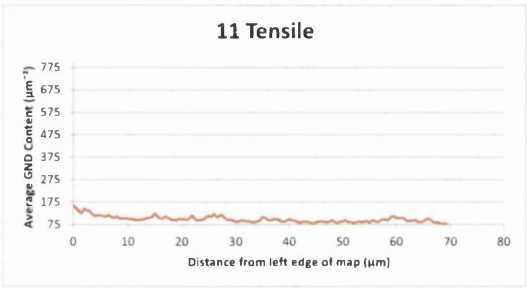

(a) 11 Tensile Region

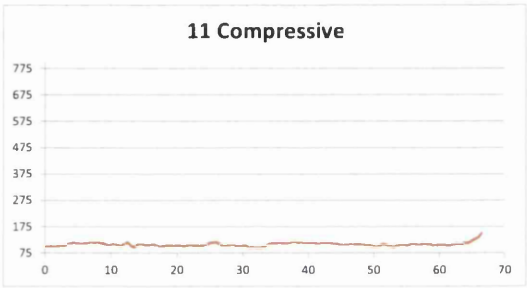

(b) 11 Compressive Region

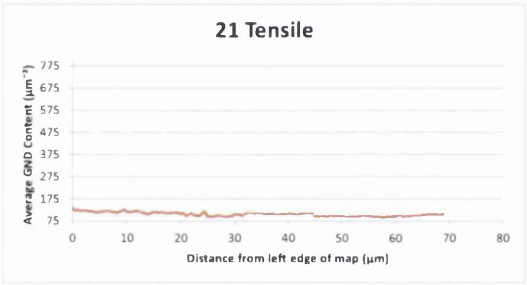

(c) 21 Tensile Region

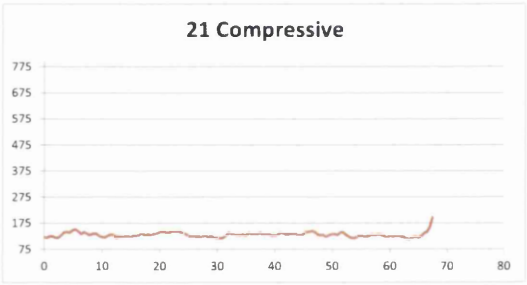

(d) 21 Compressive Region

Figure 7.28: GND content profile of regions in sample 11 and 21. GND content was binned into bins 10 pixels wide, and the average content in each bin calculated. The profile is plotted across the sample as a function of the distance from the left edge of the map.

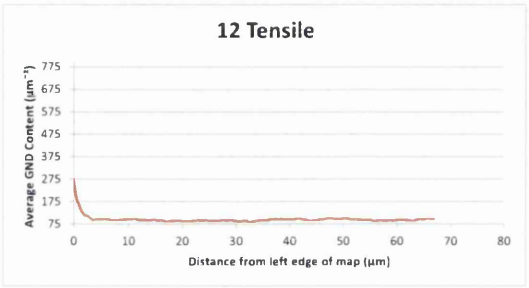

(a) 12 Tensile Region

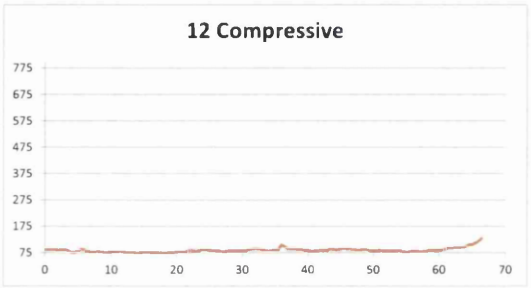

(b) 12 Compressive Region

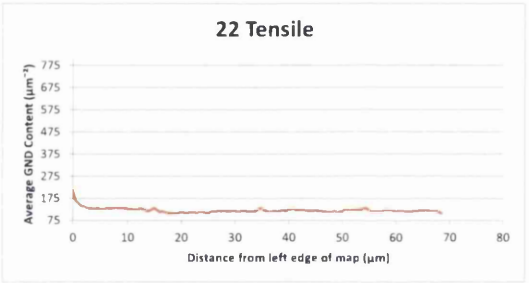

(c) 22 Tensile Region

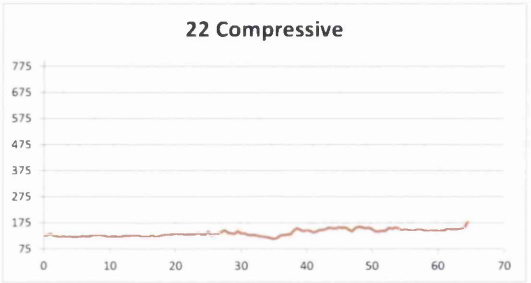

(d) 22 Compressive Region

Figure 7.29: GND content profile of regions in sample 12 and 22. GND content was binned into bins 10 pixels wide, and the average content in each bin calculated. The profile is plotted across the sample as a function of the distance from the left edge of the map.

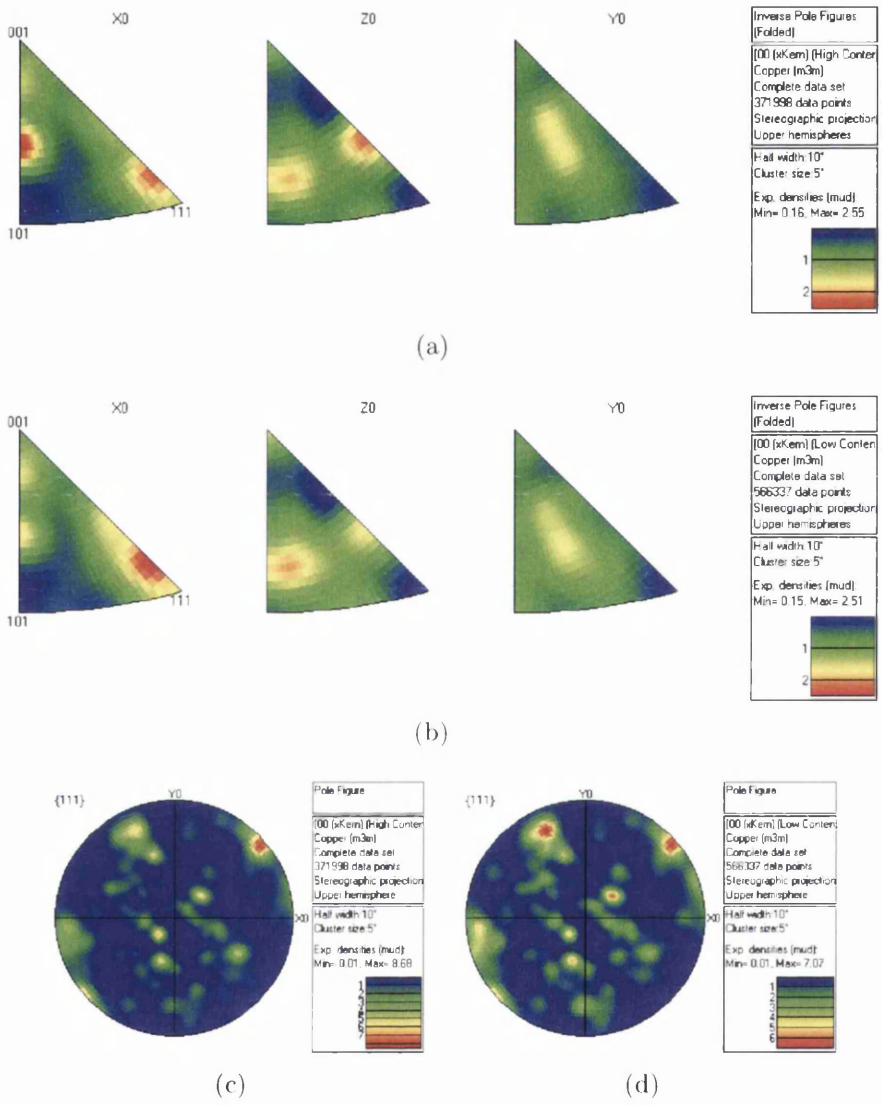

Figure 7.30: Inspection of orientation relationship to GND content for sample 00. (a) Inverse pole figure of points with higher than average GND content, (b) Inverse pole figure of points with lower than average GND content, (c) Pole figure of points with higher than average GND content, (d) Pole figure of points with lower than average GND content.

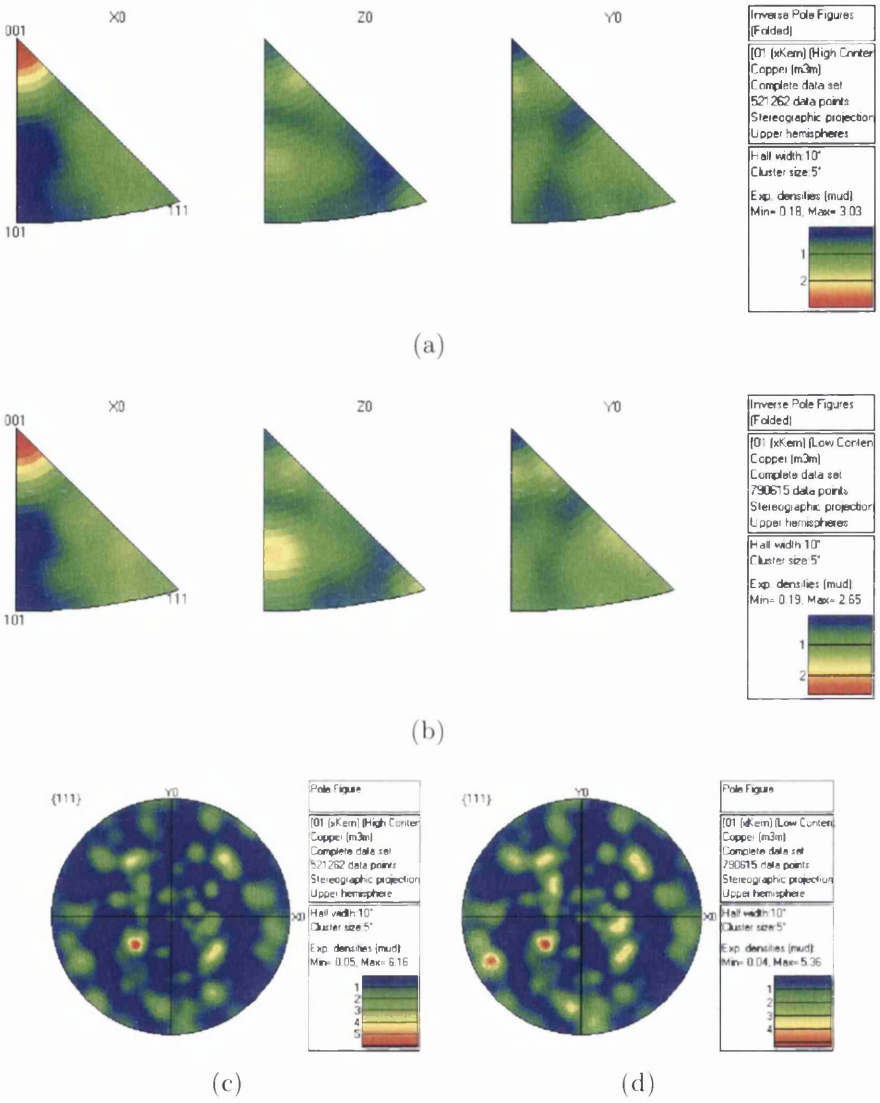

Figure 7.31: Inspection of orientation relationship to GND content for sample 01. (a) Inverse pole figure of points with higher than average GND content, (b) Inverse pole figure of points with lower than average GND content, (c) Pole figure of points with higher than average GND content, (d) Pole figure of points with lower than average GND content.

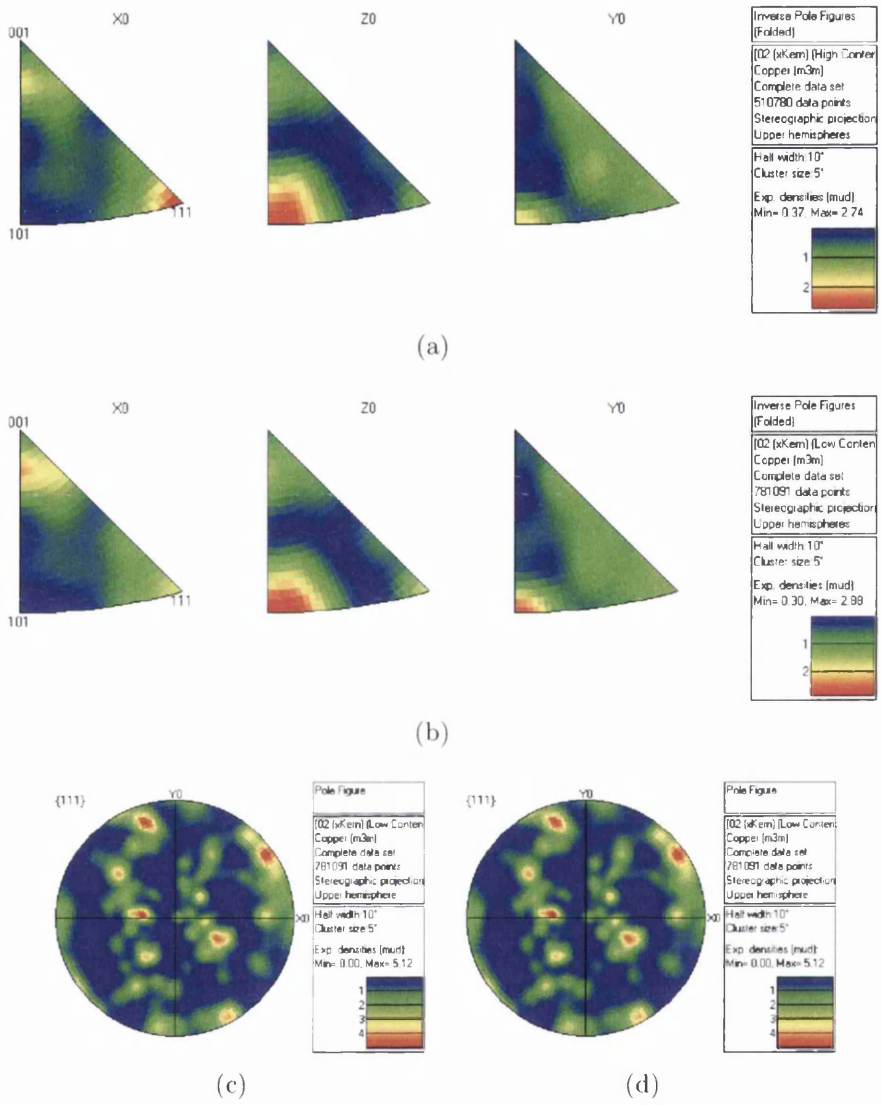

Figure 7.32: Inspection of orientation relationship to GND content for sample 02. (a) Inverse pole figure of points with higher than average GND content, (b) Inverse pole figure of points with lower than average GND content, (c) Pole figure of points with higher than average GND content, (d) Pole figure of points with lower than average GND content.

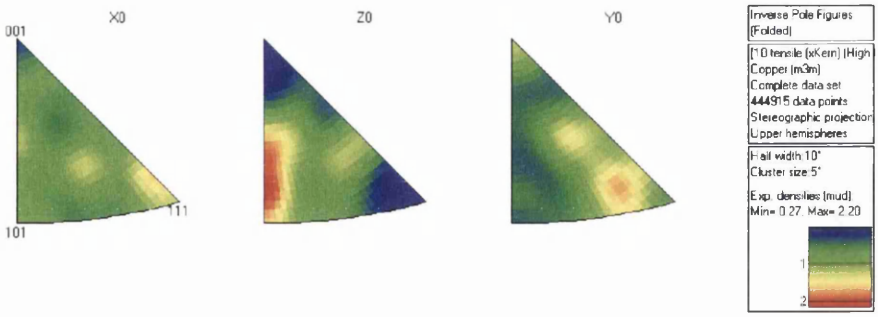

(a)

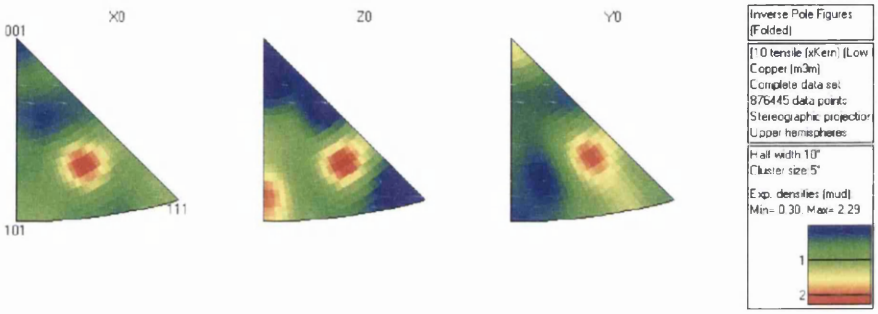

(b)

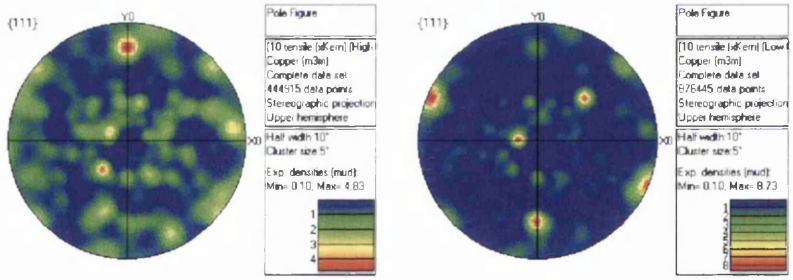

(c) (d)

Figure 7.33: Inspection of orientation relationship to GND content for sample 10 tensile region. (a) Inverse pole figure of points with higher than average GND content, (b) Inverse pole figure of points with lower than average GND content, (c) Pole figure of points with higher than average GND content, (d) Pole figure of points with lower than average GND content.

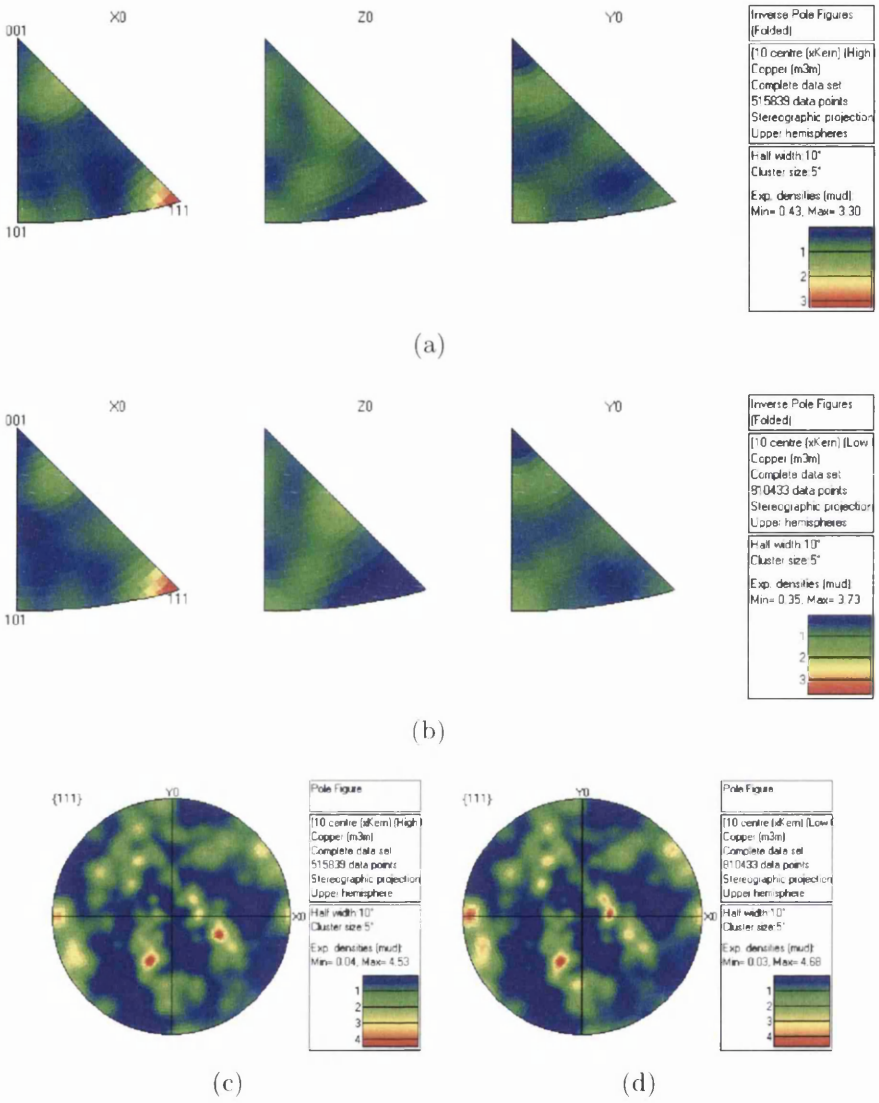

Figure 7.34: Inspection of orientation relationship to GND content for sample 10 centre region. (a) Inverse pole figure of points with higher than average GND content, (b) Inverse pole figure of points with lower than average GND content, (c) Pole figure of points with higher than average GND content, (d) Pole figure of points with lower than average GND content.

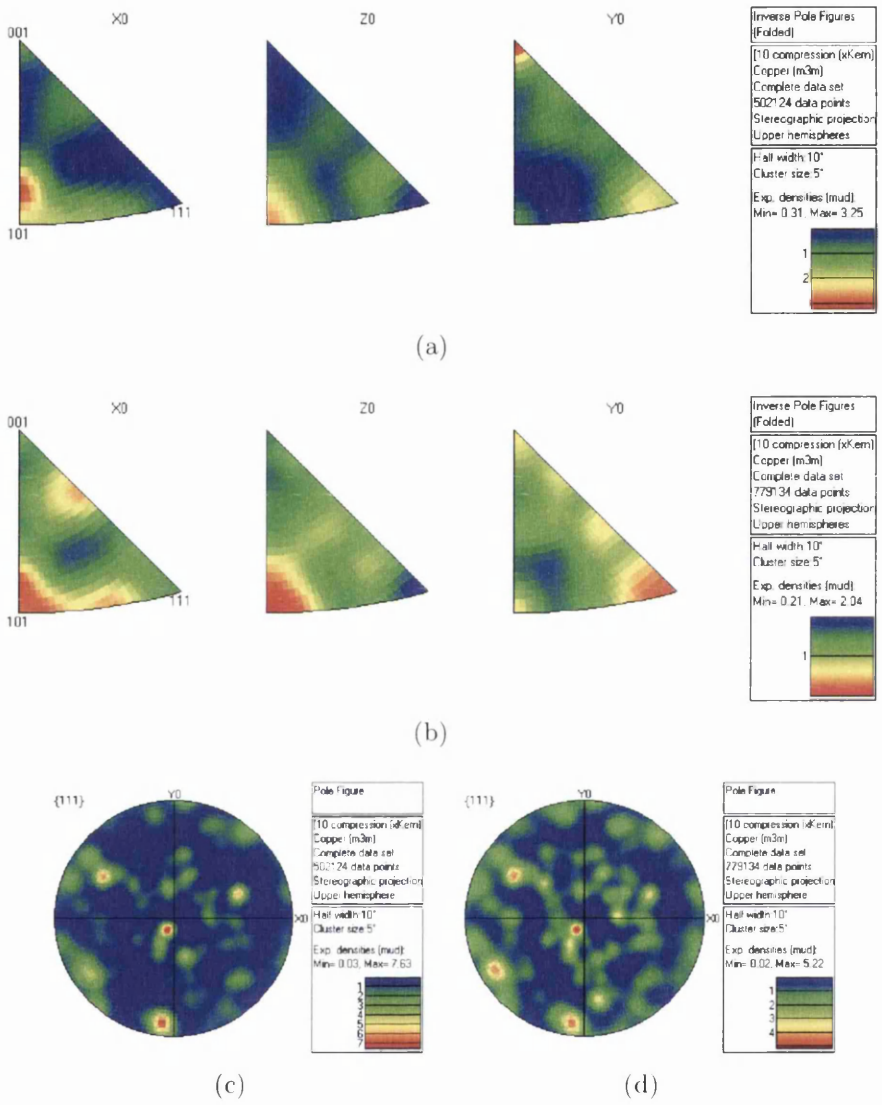

Figure 7.35: Inspection of orientation relationship to GND content for sample 10 copmression region. (a) Inverse pole figure of points with higher than average GND content, (b) Inverse pole figure of points with lower than average GND content, (c) Pole figure of points with higher than average GND content, (d) Pole figure of points with lower than average GND content.

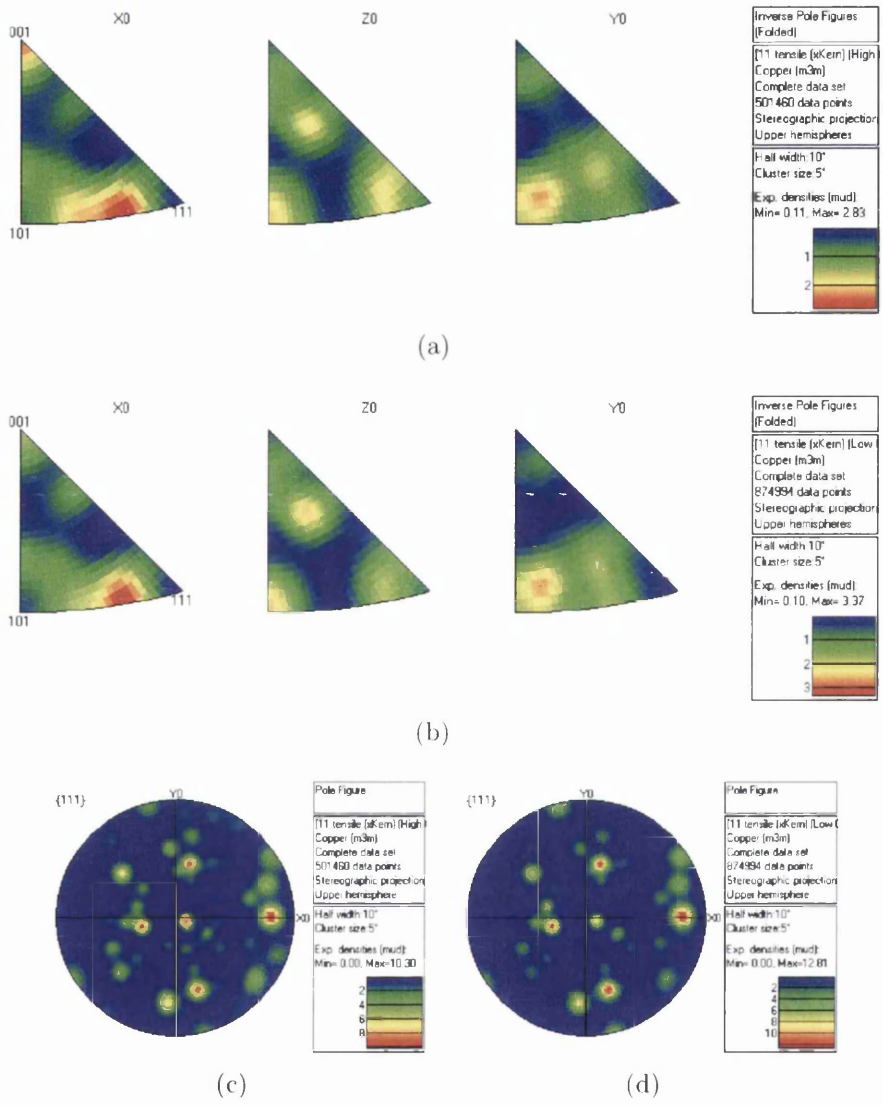

Figure 7.36: Inspection of orientation relationship to GND content for sample 11 tensile region. (a) Inverse pole figure of points with higher than average GND content, (b) Inverse pole figure of points with lower than average GND content, (c) Pole figure of points with higher than average GND content, (d) Pole figure of points with lower than average GND content.

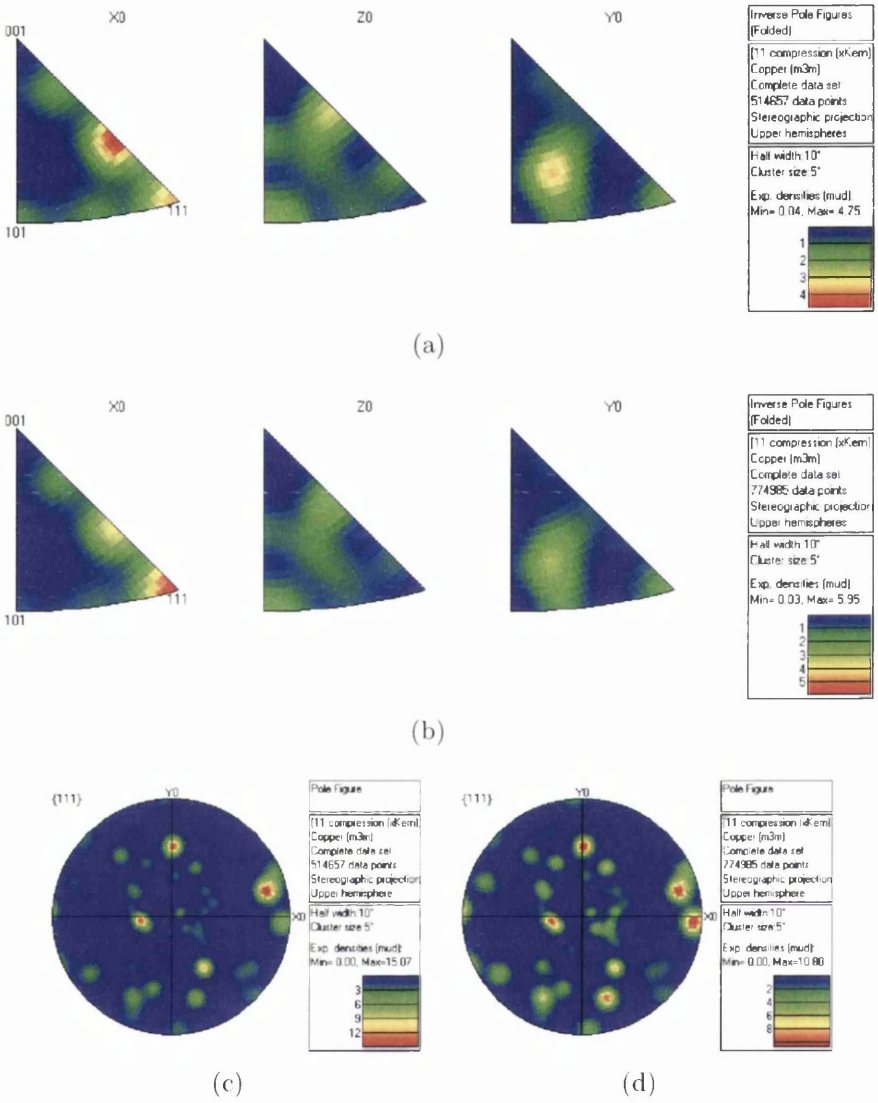

Figure 7.37: Inspection of orientation relationship to GND content for sample 11 compression region. (a) Inverse pole figure of points with higher than average GND content, (b) Inverse pole figure of points with lower than average GND content, (c) Pole figure of points with higher than average GND content, (d) Pole figure of points with lower than average GND content.

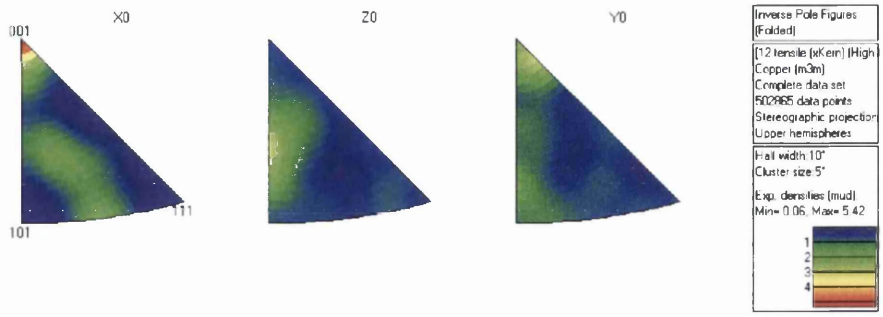

(a)

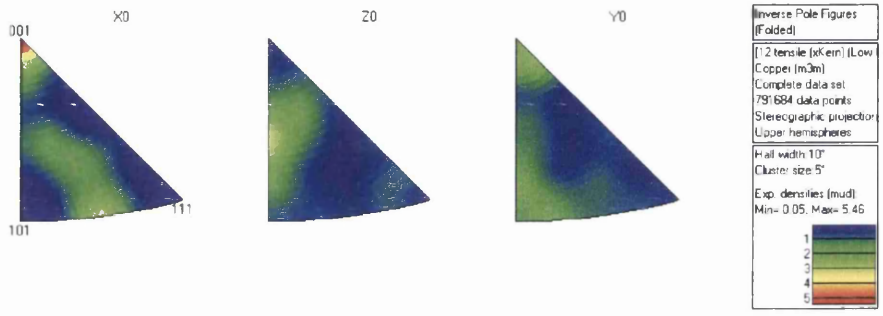

(b)

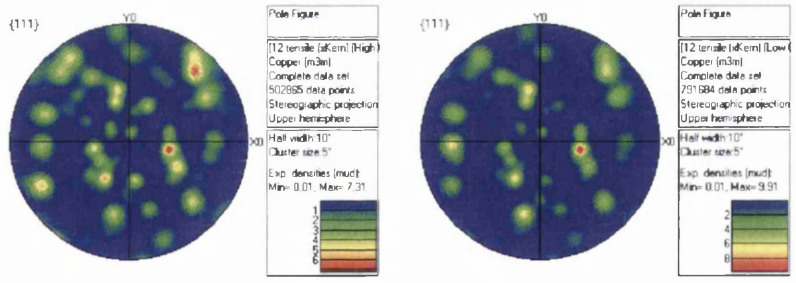

(c) (d)

Figure 7.38: Inspection of orientation relationship to GND content for sample 12 tensile region. (a) Inverse pole figure of points with higher than average GND content, (b) Inverse pole figure of points with lower than average GND content, (c) Pole figure of points with higher than average GND content, (d) Pole figure of points with lower than average GND content.

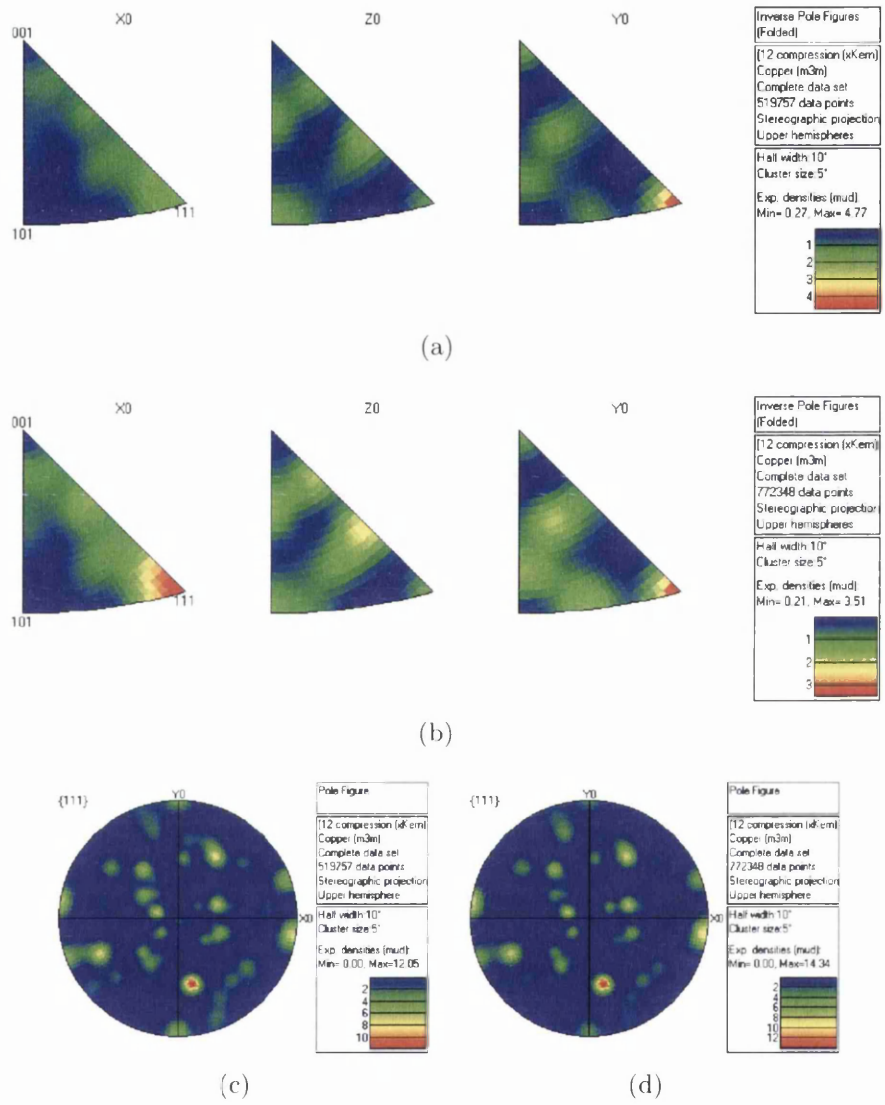

Figure 7.39: Inspection of orientation relationship to GND content for sample 12 compression region. (a) Inverse pole figure of points with higher than average GND content, (b) Inverse pole figure of points with lower than average GND content, (c) Pole figure of points with higher than average GND content, (d) Pole figure of points with lower than average GND content.

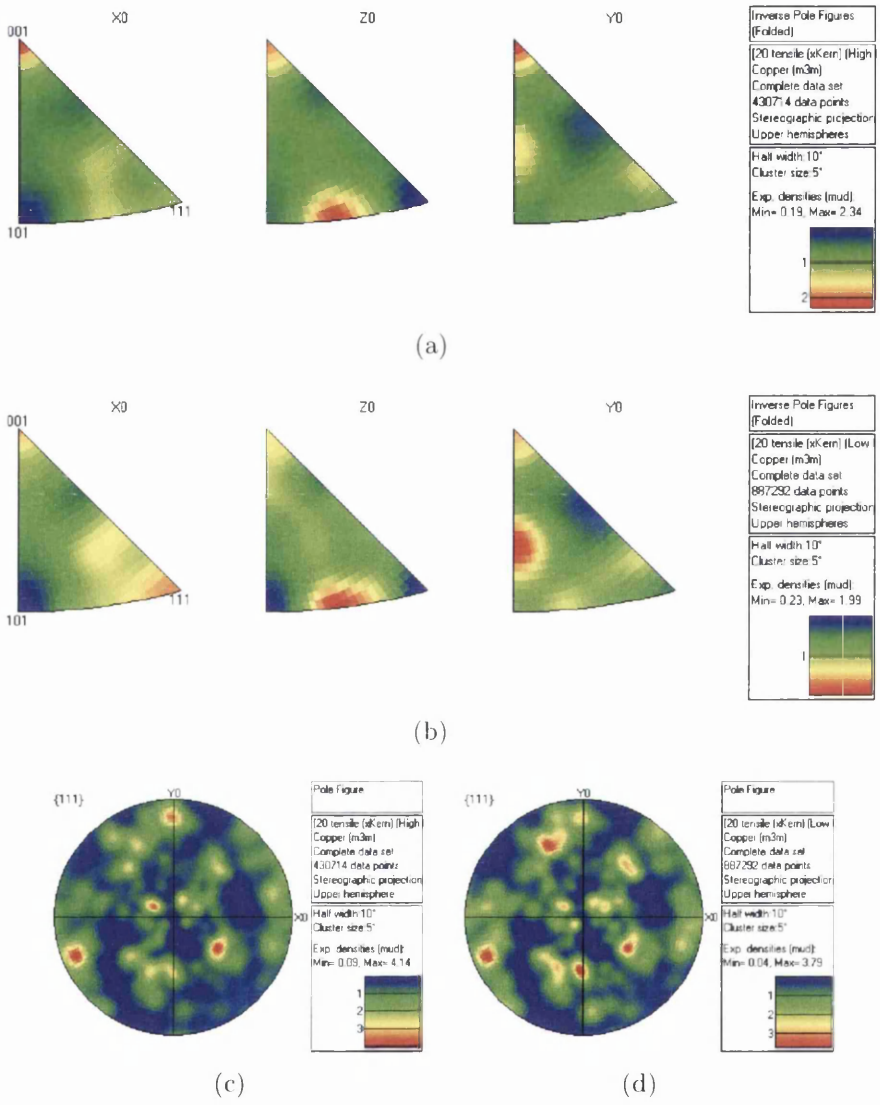

Figure 7.40: Inspection of orientation relationship to GND content for sample 20 tensile region. (a) Inverse pole figure of points with higher than average GND content, (b) Inverse pole figure of points with lower than average GND content, (c) Pole figure of points with higher than average GND content, (d) Pole figure of points with lower than average GND content.

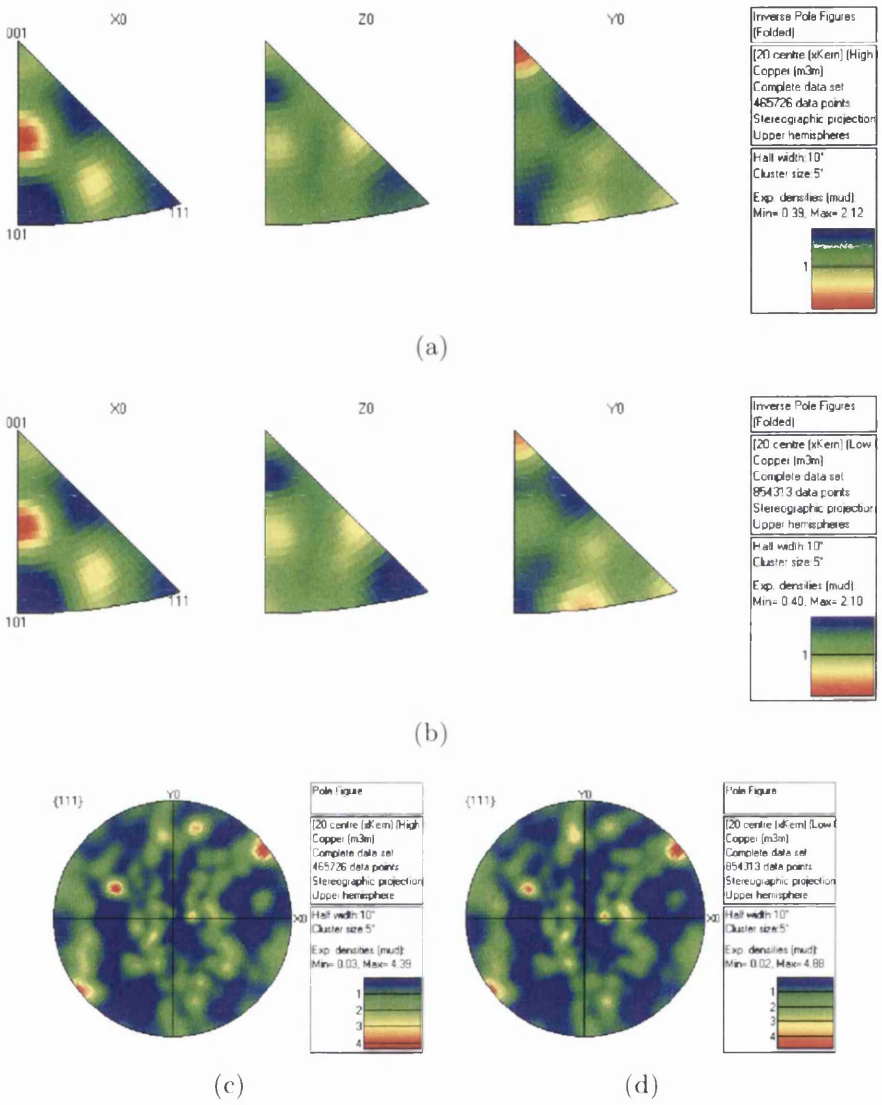

Figure 7.41: Inspection of orientation relationship to GND content for sample 20 centre region. (a) Inverse pole figure of points with higher than average GND content, (b) Inverse pole figure of points with lower than average GND content, (c) Pole figure of points with higher than average GND content, (d) Pole figure of points with lower than average GND content.

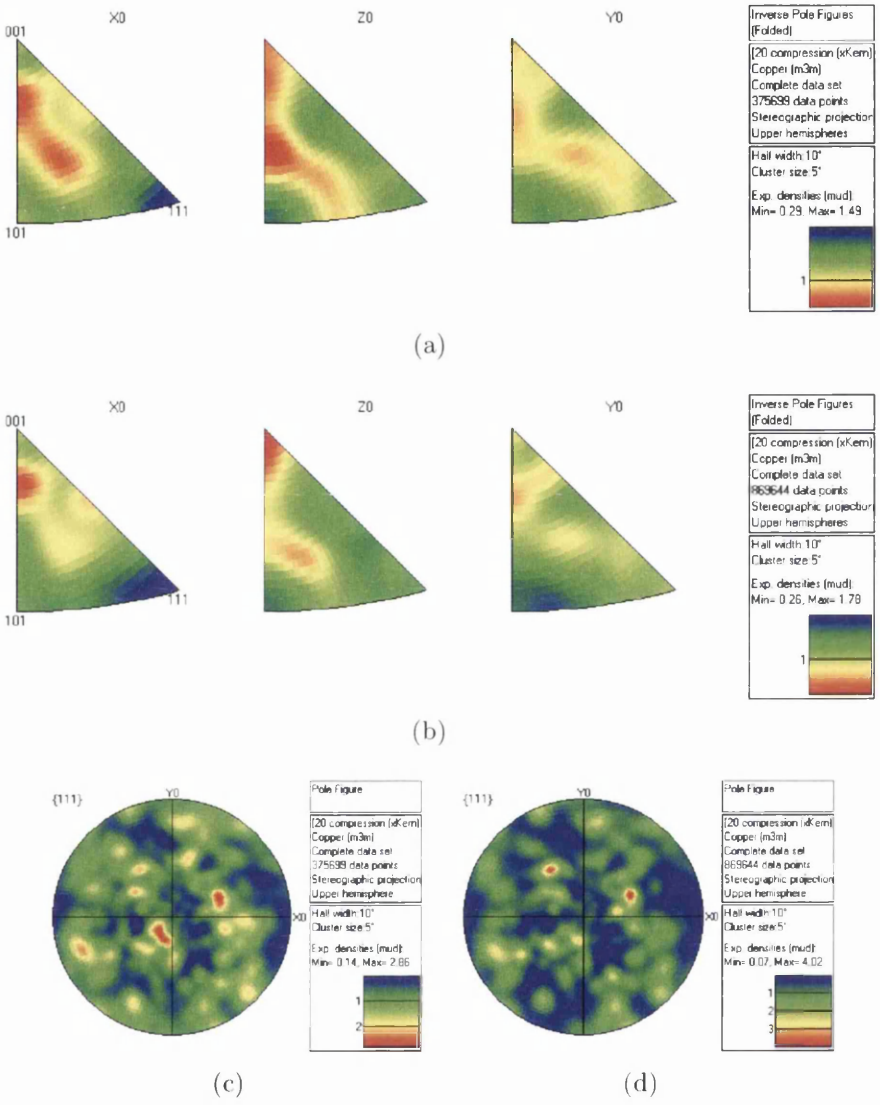

Figure 7.42: Inspection of orientation relationship to GND content for sample 20 compression region. (a) Inverse pole figure of points with higher than average GND content, (b) Inverse pole figure of points with lower than average GND content, (c) Pole figure of points with higher than average GND content, (d) Pole figure of points with lower than average GND content.

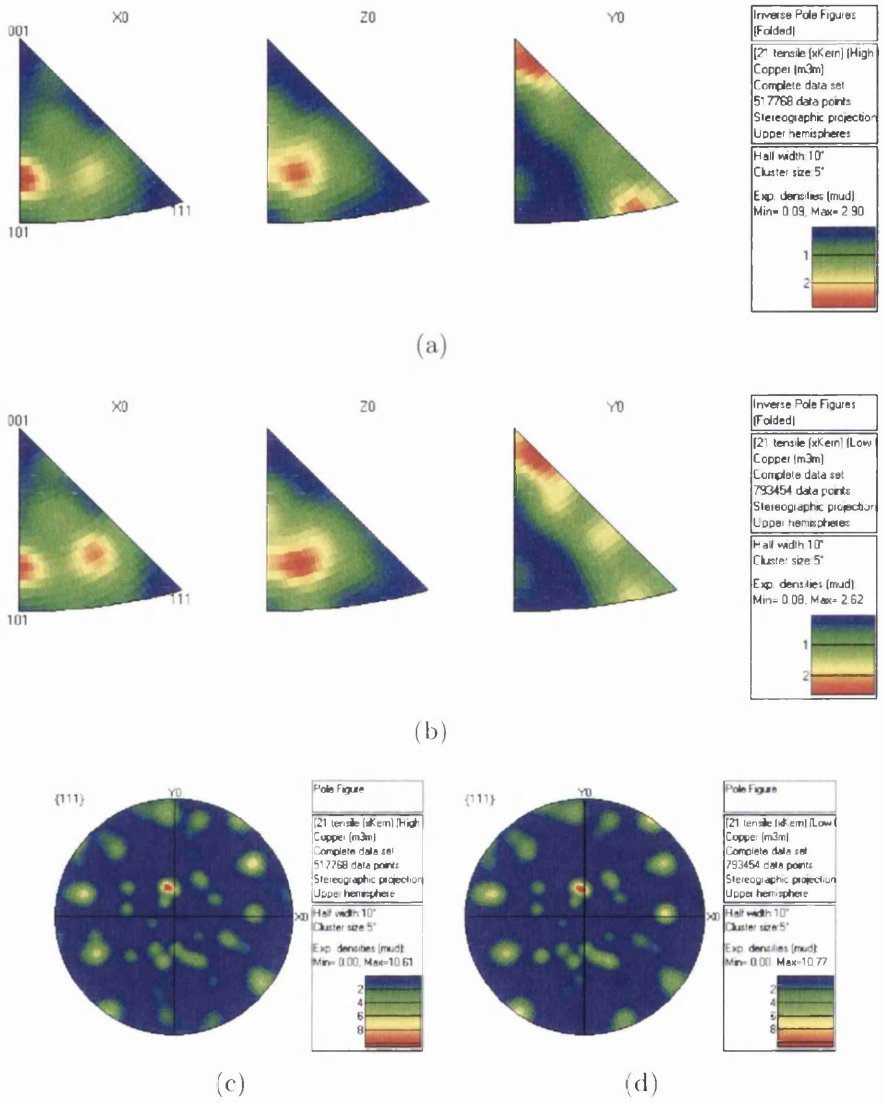

Figure 7.43: Inspection of orientation relationship to GND content for sample 21 tensile region. (a) Inverse pole figure of points with higher than average GND content, (b) Inverse pole figure of points with lower than average GND content, (c) Pole figure of points with higher than average GND content, (d) Pole figure of points with lower than average GND content.

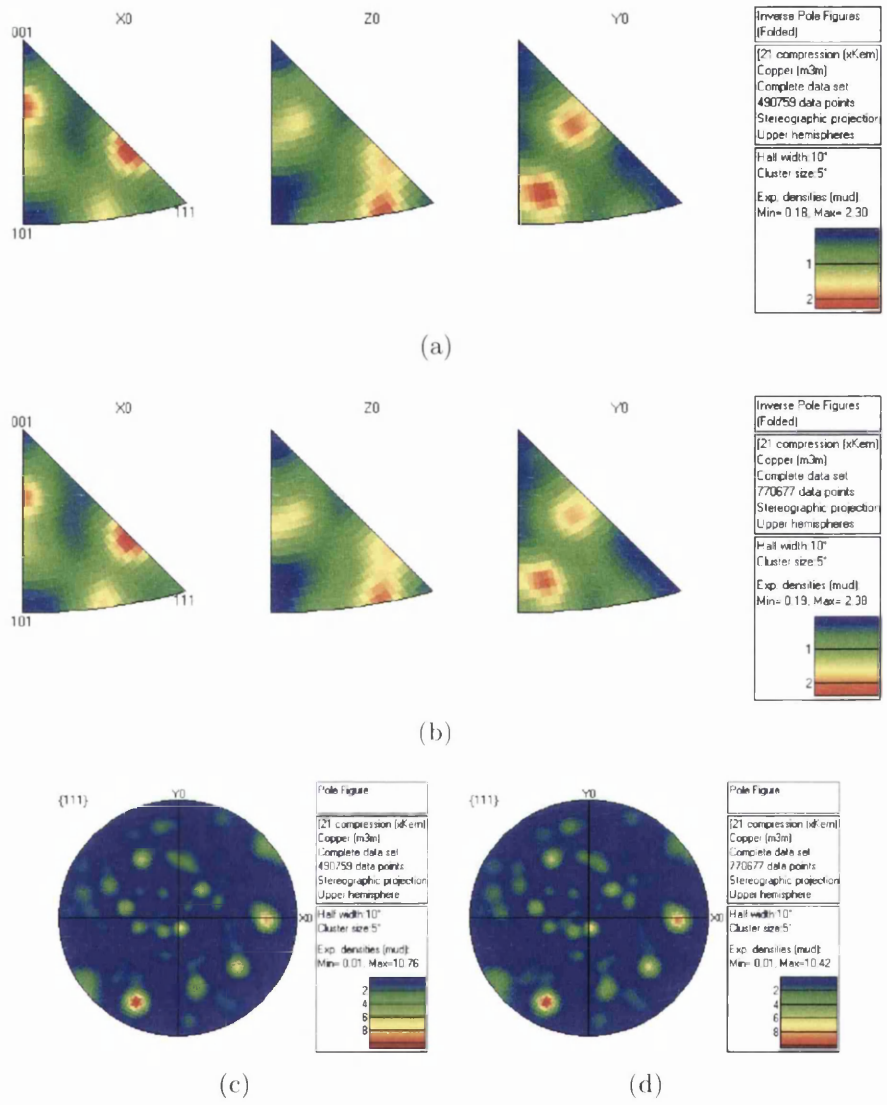

Figure 7.44: Inspection of orientation relationship to GND content for sample 21 compression region. (a) Inverse pole figure of points with higher than average GND content, (b) Inverse pole figure of points with lower than average GND content, (c) Pole figure of points with higher than average GND content, (d) Pole figure of points with lower than average GND content.

7.6.1 GND Content in Front of Grain Boundaries

The relation to GND content in front of boundaries and boundary character is now explored. Fig. 7.47 to 7.50 shows the average GND content based position across the boundary interface for $\Sigma 3^n$ type boundaries and non-CSL boundaries in each sample. The data is also replotted for one-sided boundary content in Fig. 7.51 to 7.54.

It is apparent in Fig. 7.51 of samples 00, 01, and 02, that without any deformation, higher GND content is seen directly in front of boundaries which are $\Sigma 3$ in character. This is shown by a higher peak in the $\Sigma 3$ plots than in the non-CSL plots. Lower content is then shown away from the interface for $\Sigma 3$ boundaries compared to the non-CSL. GNDs are shown piling up in front of $\Sigma 3$ boundaries creating a higher peak than non-CSL, but twinned grains have lower GND content near the bulk.

When a small deformation step is applied, the separation of the $\Sigma 3$ and non-CSL peaks closes, shown in the non-CSL and $\Sigma 3$ plots in Fig. 7.52a and 7.52c of sample 10 in the tensile and compression regions. Even further deformation, shown in Fig. 7.52d and 7.52f of sample 20 in the tensile and compression regions, then causes the non-CSL peak to raise significantly higher than the $\Sigma 3$ peak. The centre sections of samples 10 and 20 reinforce this trend as they show little change from the original 00 plots and experience little to no deformation.

The shape of the non-CSL plots is affected by deformation while the $\Sigma 3$ plots are not. Before deformation, both plots show a positive parabolic shape in the one-sided boundary content graphs, with the slope of the tangent to the curve increasing towards the boundary interface. After deformation, the trend for the non-CSL plots is reversed, instead showing a negative parabolic shape with the slope of the tangent to the curve decreasing towards the boundary interface. GND content is lower in the grain bulk and increases towards grain boundaries for $\Sigma 3$s. Grains with non-CSL boundaries show deformation further back from the boundary. The bulk of grains with $\Sigma 3$ boundaries are shielded from the more significant deformation shown by grains with random boundaries.

Upon heating, the trends seen in samples 00, 01, and 02 are restored. A slightly higher peak is seen for $\Sigma 3$ boundaries directly in front of the interface and lower

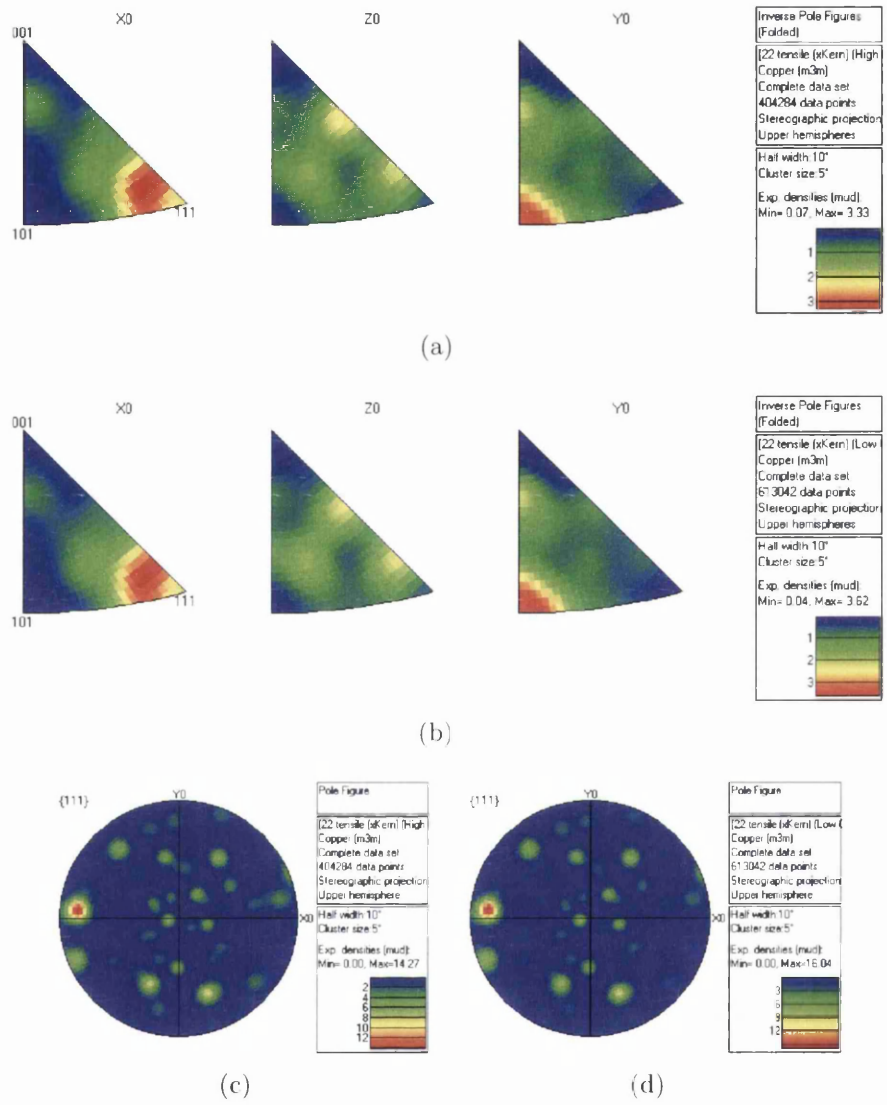

Figure 7.45: Inspection of orientation relationship to GND content for sample 22 tensile region. (a) Inverse pole figure of points with higher than average GND content, (b) Inverse pole figure of points with lower than average GND content, (c) Pole figure of points with higher than average GND content, (d) Pole figure of points with lower than average GND content.

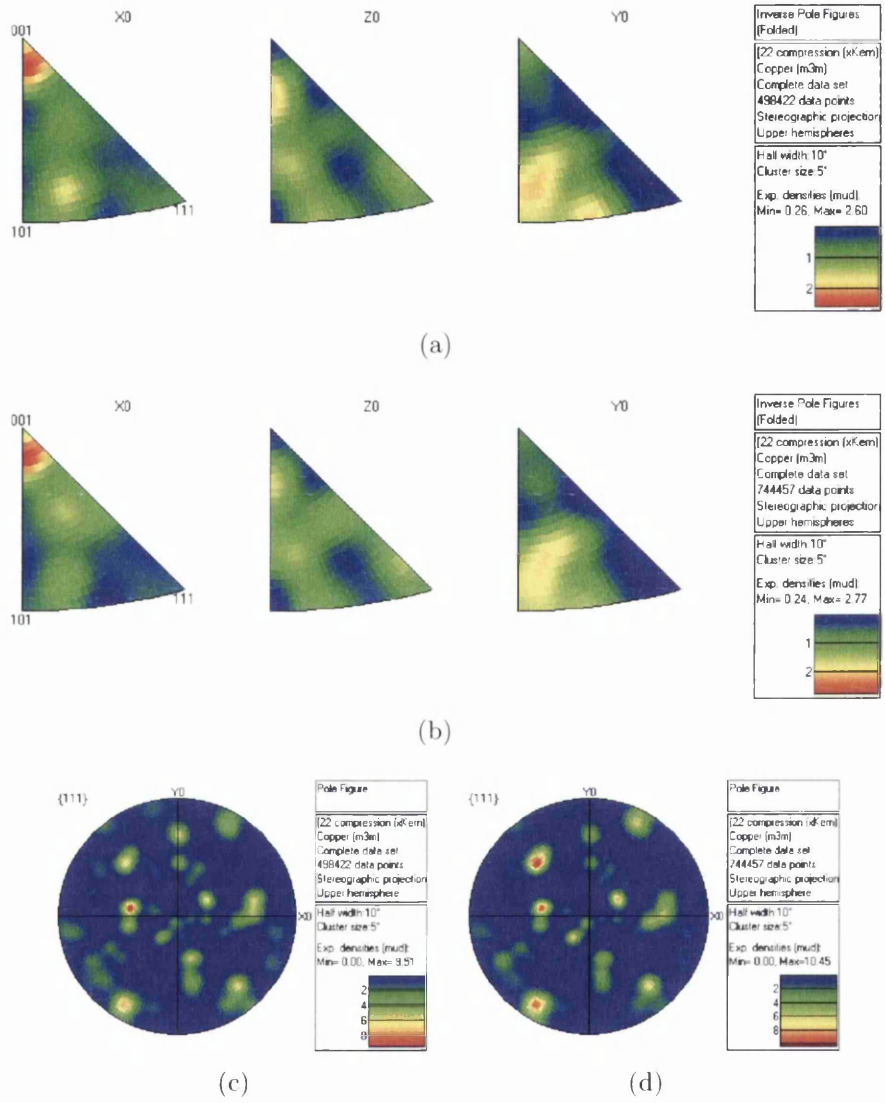

Figure 7.46: Inspection of orientation relationship to GND content for sample 22 compression region. (a) Inverse pole figure of points with higher than average GND content, (b) Inverse pole figure of points with lower than average GND content, (c) Pole figure of points with higher than average GND content, (d) Pole figure of points with lower than average GND content.

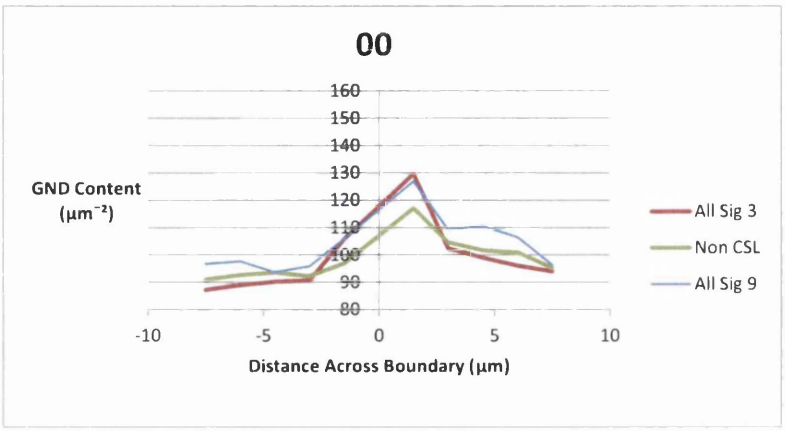

(a) 00

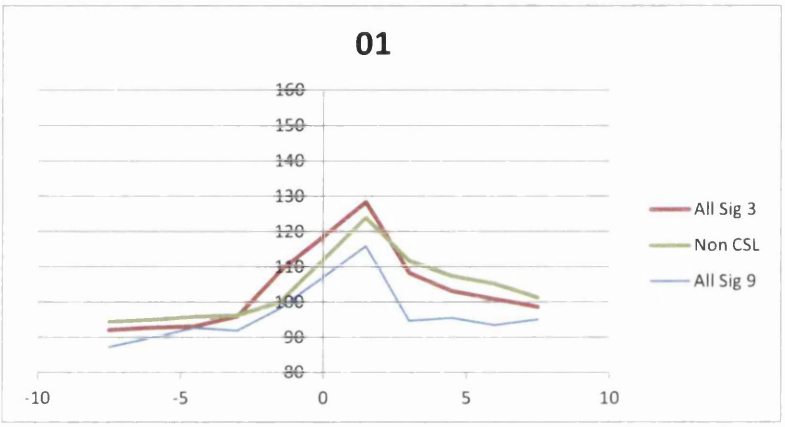

(b) 01

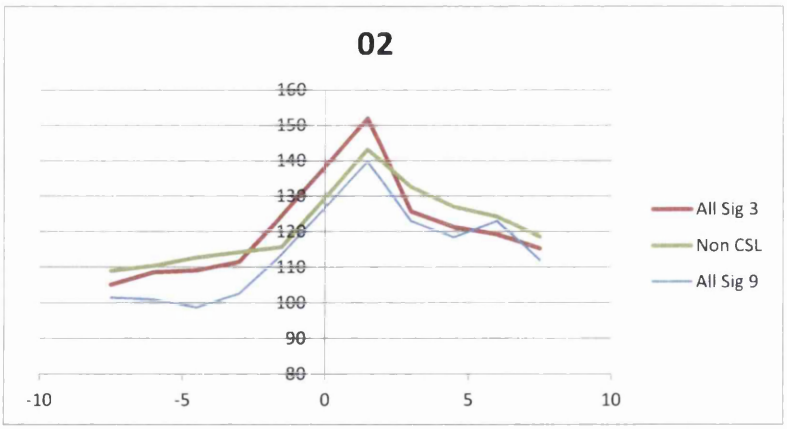

(c) 02

Figure 7.47: Average GND content across boundaries by boundary character for zero bend samples.

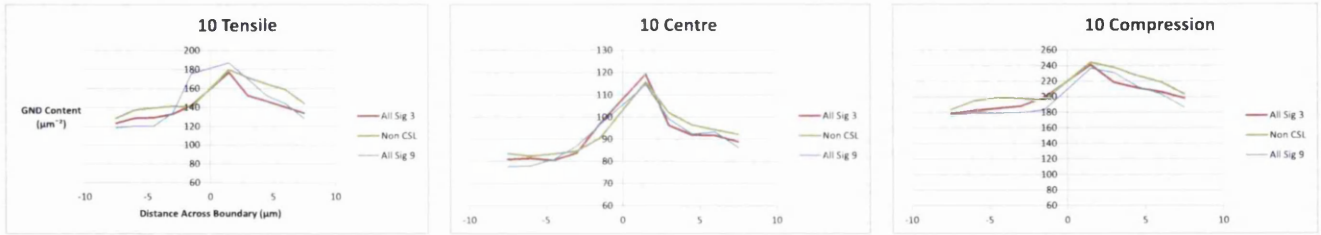

(a) 10 Tensile Region (b) 10 Centre Region (c) 10 Compressive Region

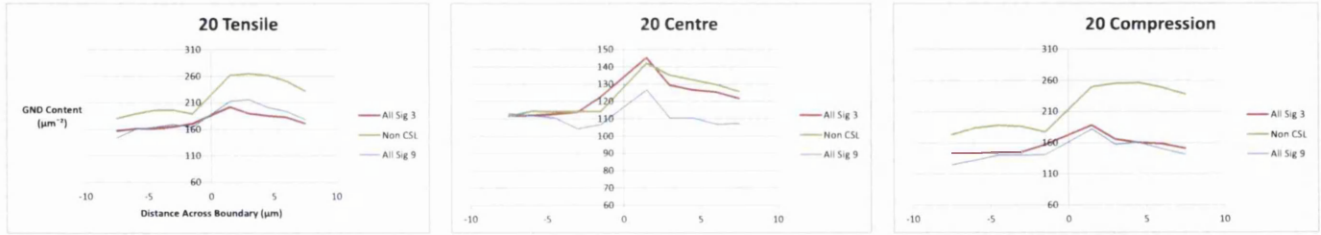

(d) 20 Tensile Region (e) 20 Centre Region (f) 20 Compressive Region

Figure 7.48: Average GND content across boundaries by boundary character for bent samples not receiving additional anneal step

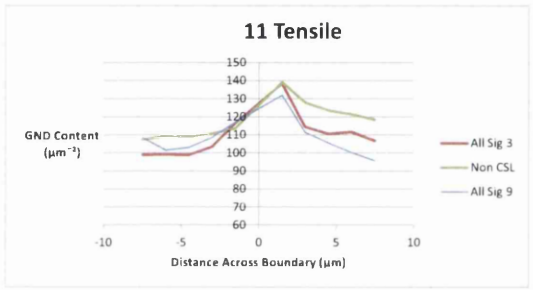

(a) 11 Tensile Region

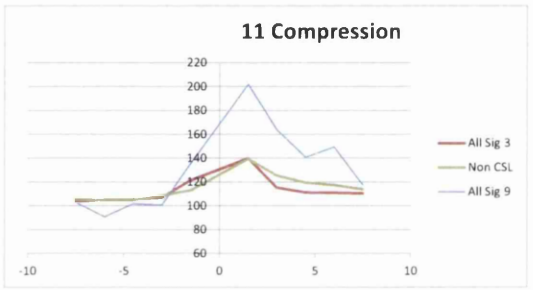

(b) 11 Compressive Region

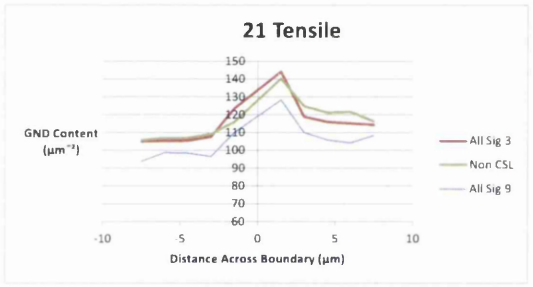

(c) 21 Tensile Region

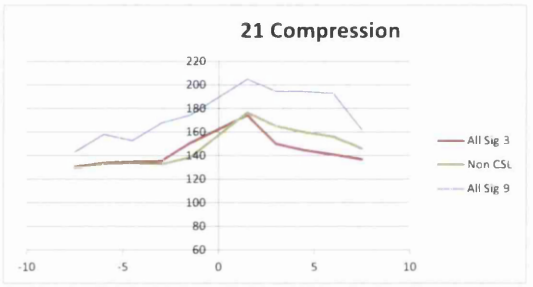

(d) 21 Compressive Region

Figure 7.49: Average GND content across boundaries by boundary character for bent samples receiving an annealing step at 750°C after bending

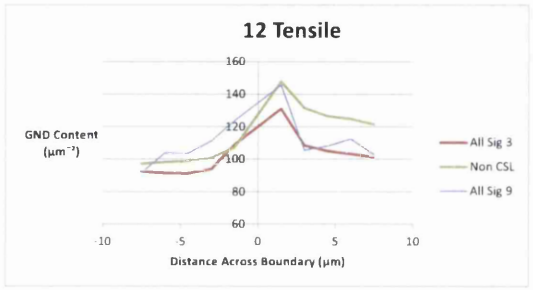

(a) 12 Tensile Region

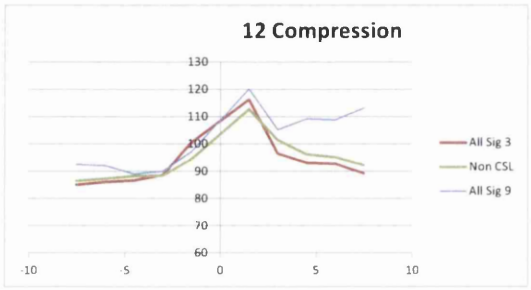

(b) 12 Compressive Region

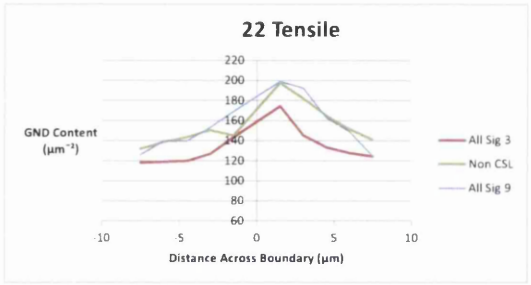

(c) 22 Tensile Region

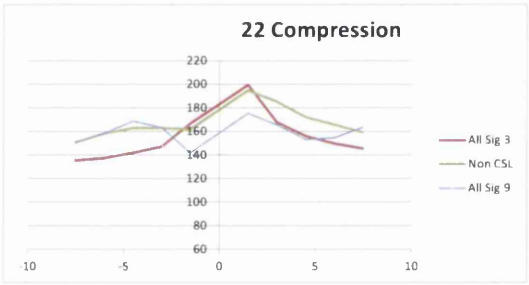

(d) 22 Compressive Region

Figure 7.50: Average GND content across boundaries by boundary character for bent samples receiving an annealing step at 820°C after bending

GND content towards the bulk of the grain, with both Σ3 and non-CSL plots returning to a positive parabolic shape. Interestingly, the non-CSL plots in the tensile region for samples receiving deformation and a high temperature anneal (12 and 22) show a significantly higher non-CSL peak in front of the interface not seen in other plots. The reason for this is not apparent, however inspection of the two-sided GND content plots of Fig. 7.50a and 7.50c show similar values for non-CSL and Σ3 boundaries directly in front of the interface on the lower GND content side. It may be that the higher temperature causing faster dislocation movement creates dislocation pile-ups in front of the random boundaries where they may otherwise terminate at the free volume of the boundary or move across the boundary.

After Σ3 boundaries, the next most common CSL boundary is Σ9. Plots of Σ9 boundaries are included in each figure, however there are significantly fewer Σ9 boundaries than Σ3 or non-CSL boundaries. The plots of Σ9 boundaries may be affected by the smaller sample size, but plots of Σ9 boundaries from samples with similar histories still show similar patterns. The shape of the plots of Σ9 boundaries and their relation to Σ3 and non-CSL plots are similar between maps which only differ in the amount of applied strain. The similar patterns may be representative of trends were larger sample sizes to be taken. Before deformation, Σ9 boundaries show similar plot shape to Σ3 boundaries with lower GND content in front of the interface. After bending around a 23mm radius, the plots of GND content in front of Σ9 boundaries remains similar to Σ3 boundaries, with one larger outlying peak in Fig. 7.52a. The GND content in front of Σ9 boundaries after bending around a 16.5mm radius tends to be lower than non-CSL boundaries and Σ3 boundaries in the grain bulk, as seen in Fig. 7.52d to 7.52f.

Upon heat treatment, further patterns are observed. Heating at 750°C causes GND content in front of Σ9 boundaries in the tensile region to remain lower than Σ3 boundaries (Fig. 7.53a and 7.53c), but increase to significantly larger than non-CSL and Σ3 boundaries in the compression region (Fig. 7.53b and 7.53d). These patterns change when heating at 820°C, where the tensile region show GND content in between the non-CSL and Σ3 plots in the bulk of the grain and increasing to higher than the non-CSL peak in front of the interface (Fig. 7.54a and 7.54c). The compression region shows that GND content in front of Σ9 boundaries is larger in

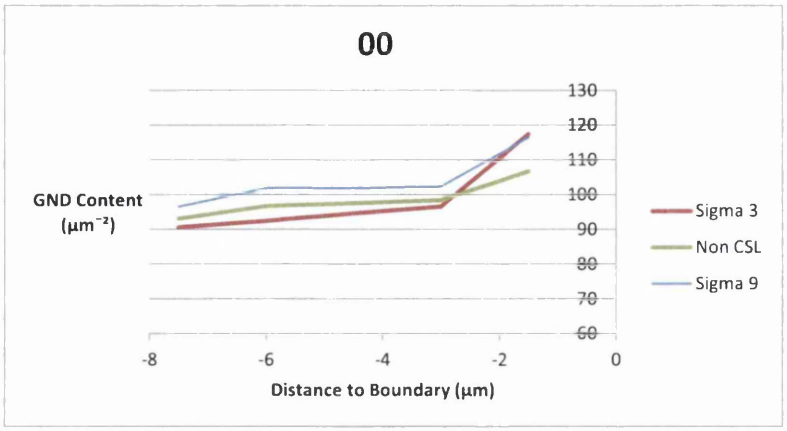

(a) 00

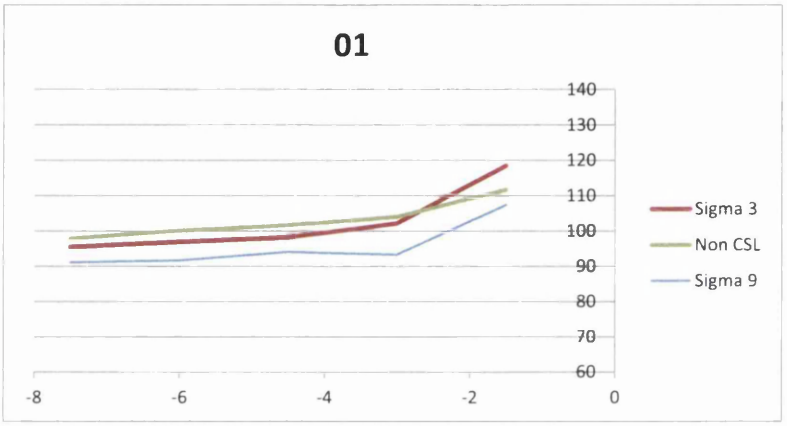

(b) 01

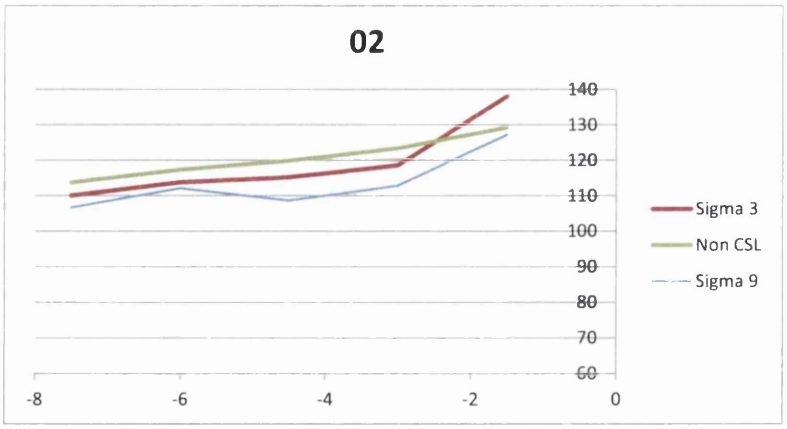

(c) 02

Figure 7.51: Average GND content in front boundaries by boundary character for zero bend samples

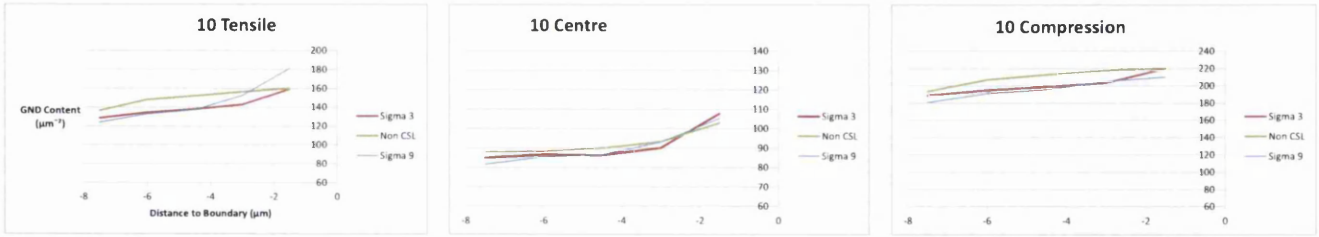

(a) 10 Tensile Region

(b) 10 Centre Region

(c) 10 Compressive Region

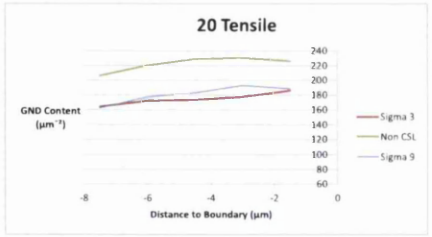

(d) 20 Tensile Region

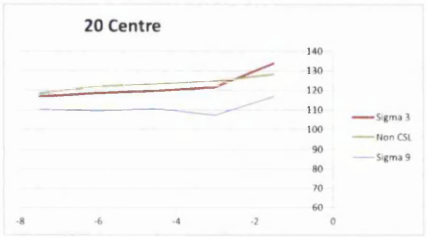

(e) 20 Centre Region

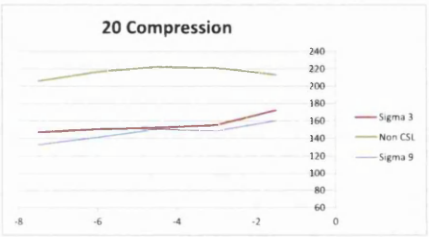

(f) 20 Compressive Region

Figure 7.52: Average GND content in front boundaries by boundary character for bent samples not receiving additional anneal step

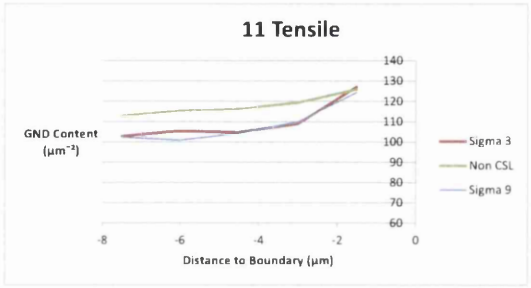

(a) 11 Tensile Region

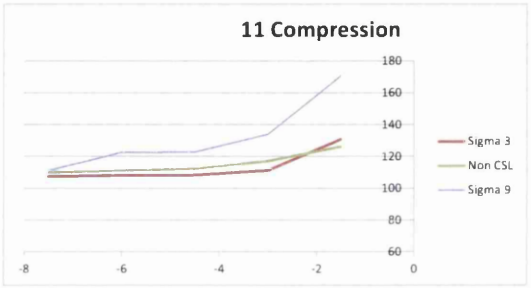

(b) 11 Compressive Region

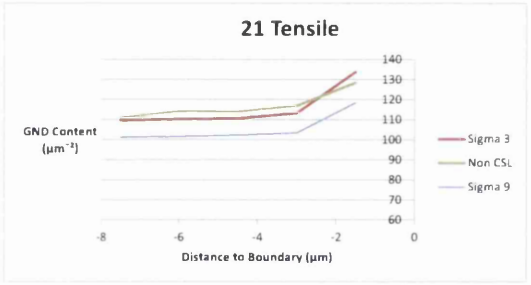

(c) 21 Tensile Region

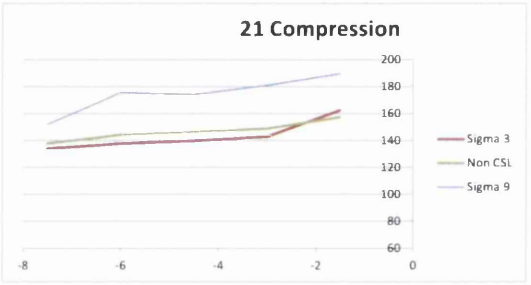

(d) 21 Compressive Region

Figure 7.53: Average GND content in front boundaries by boundary character for bent samples receiving an annealing step at 750°C after bending

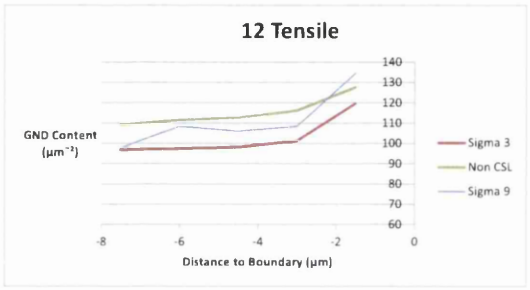

(a) 12 Tensile Region

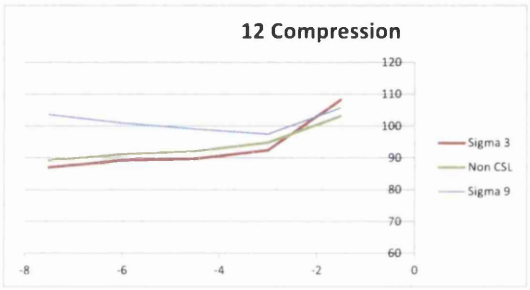

(b) 12 Compressive Region

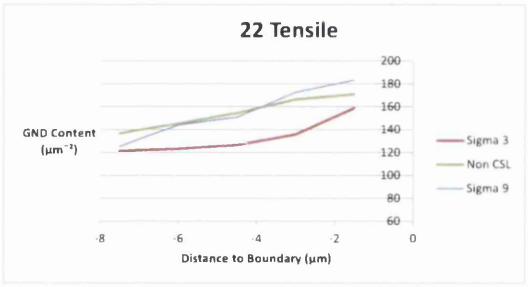

(c) 22 Tensile Region

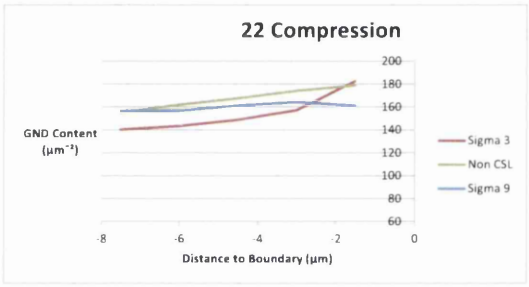

(d) 22 Compressive Region

Figure 7.54: Average GND content in front boundaries by boundary character for bent samples receiving an annealing step at 820°C after bending

the bulk of the grains than in comparable regions in grains with $\Sigma 3$ boundaries, and also decreases to a smaller peak than $\Sigma 3$ boundaries in front of the interface (Fig. 7.54b and 7.54d).

The cause of these patterns is not apparent based on the GND content plots alone, and further work would need to be done to collect a sufficiently large sample size to confirm the shape of the trends. However, differences in the strain in front of $\Sigma 9$ boundaries (and $\Sigma 27$) would be expected based on the temperature, as is shown in these plots. $\Sigma 9$ boundaries lying on irrational boundary planes form as crystallographically constrained linkages between $\Sigma 3$ boundaries, the rate of formation and growth of which is affected by the annealing temperature, during iterative treatment of grain boundary engineering [112]. The GND content in front of $\Sigma 9$ boundaries may then be indicative of the fraction of $\Sigma 9$ boundaries lying on irrational planes and also the stage of recovery and grain growth in the material. Further work would be required to investigate this.

Chapter 8

Discussion of GND Methods and Suggestions for Future Use

In chapters 5, 6, and 7, maps of GND content were used to identify the neutral plane of a fold, the strain experienced by grains after bending, and the strain in front of boundaries based on boundary character. In each case, results were presented within the context of the map they were created and as a difference of the feature in question from the rest of the map. That is to say that the actual GND values calculated were given little to no consideration away from the context of the map it came from. This is due to the difference in surface preparation of each sample causing error, but also the difference in underlying dislocation structure changing the fraction of dislocations recoverable as GNDs. The GND structure is the most valuable information obtainable from a GND map rather than the scalar GND values, that is the relation of the value at a point to the values at neighbouring points rather than the individual values.

The ability to detect the dislocation structure would be a desirable outcome as it would allow for the prediction of materials properties that depend on the recovered or relaxed state of dislocations in a material. For this reason, attempts were made to detect the degree of connectivity of GNDs in a GND map. What was first a materials science problem then became an image analysis problem within the context of materials science.

The highest quality maps are required for reliable dislocation structure detec-

tion. The highest quality maps with significantly differing dislocation structures was found to be in sample 21. The tensile region of sample 21 show a very diffuse dislocation structure, while the compressive region shows high GND connectivity into dislocation tangles.

First, each map was run through a de-noising algorithm. The results, plotted on a grey scale, are shown in Fig. 8.1. A structure tensor was then applied. The structure tensor gives information on the degree and direction of anisotropy of the GND content at each point based on its neighbours. By careful selection of structure tensor window size and thresholding of connectivity properties which constitute a dislocation tangle, the path and size of dislocation tangles can be effectively detected. The full code and algorithms are given in Appendix E. The code was written in collaboration with Dr. Ben Spencer.

An example of detected tangles in the GND maps of sample 21 is shown in Fig. 8.4. Dislocation tangles are coloured according to their respective size based on the number of pixels constituting that tangle. Colours range from green for small tangles, to yellow, orange, and red for large tangles. One obvious error is shown by the large scratch in the tensile region being detected as a large tangle, however it does show that connected groups of high GND content is being detected. It is visually apparent from the tangle maps in Fig. 8.4 that there is a greater connectedness of GND content in the compressive region, and since the number of tangles and size of each is known, quantifying the difference between the two regions is possible.

The tangles are then plotted according to their size and frequency in Fig. 8.5. Tangles of each size are plotted against the number of pixels in each image belonging to a tangle of that size. The connectivity of GNDs is shown to be effectively detected by the difference in signal from the plots of each GND map. The peak of the compressive region map is lower and pushed to the right towards the larger tangle sizes compared to the tensile region map, showing the higher GND connectivity in that map. Both GND maps also show higher connectivity than a control map filled by random noise, also plotted in Fig. 8.5.

Tangles end more frequently at triple junctions and sharp grain corners, however some are seen to begin and end within a grain bulk as in Fig. 7.23b (which is a two dimensional map and so may only be showing short portions of tangles which

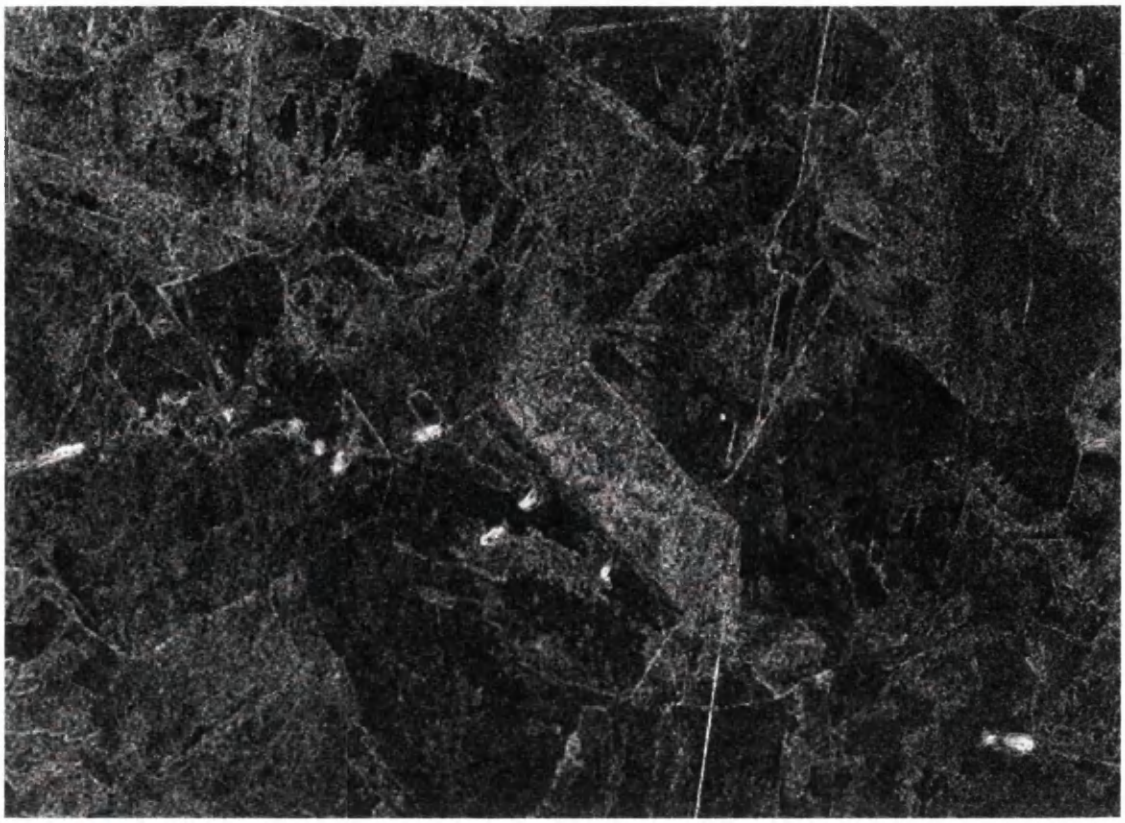

(a) Tensile Region

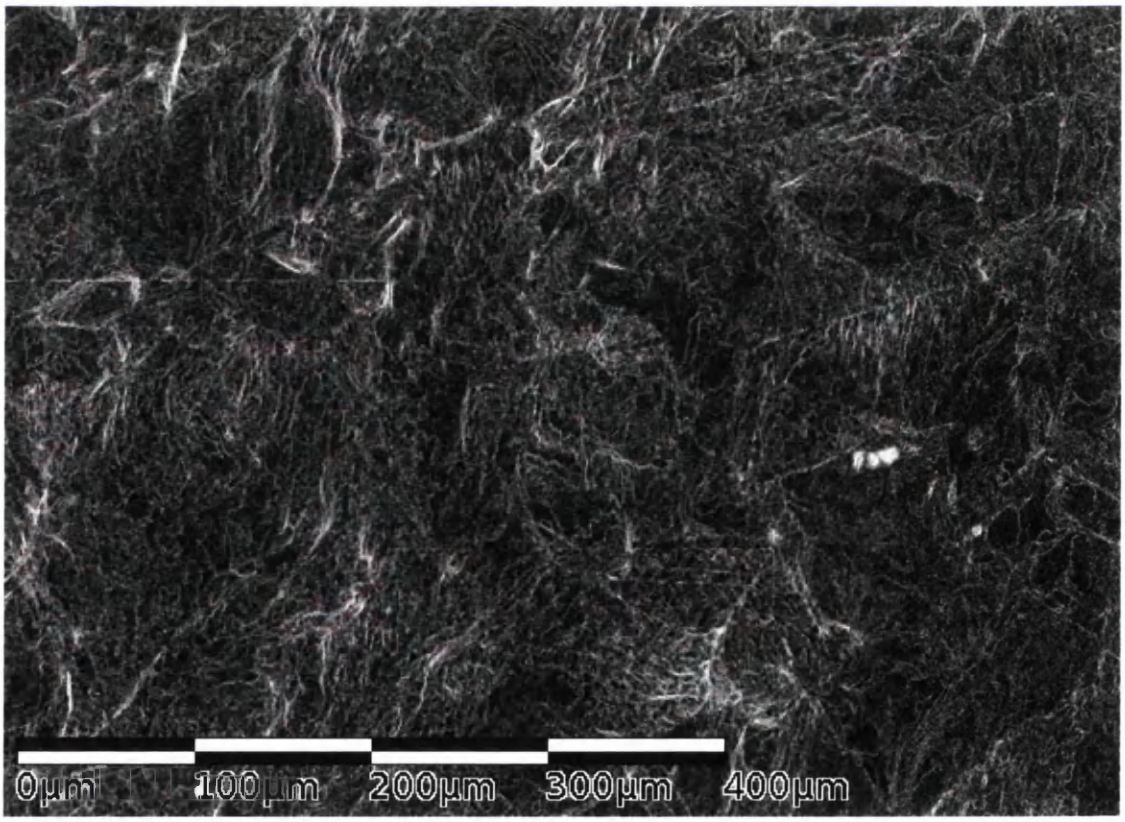

(b) Compressive Region

Figure 8.1: Grey scale image of de-noised sample 21 GND maps.

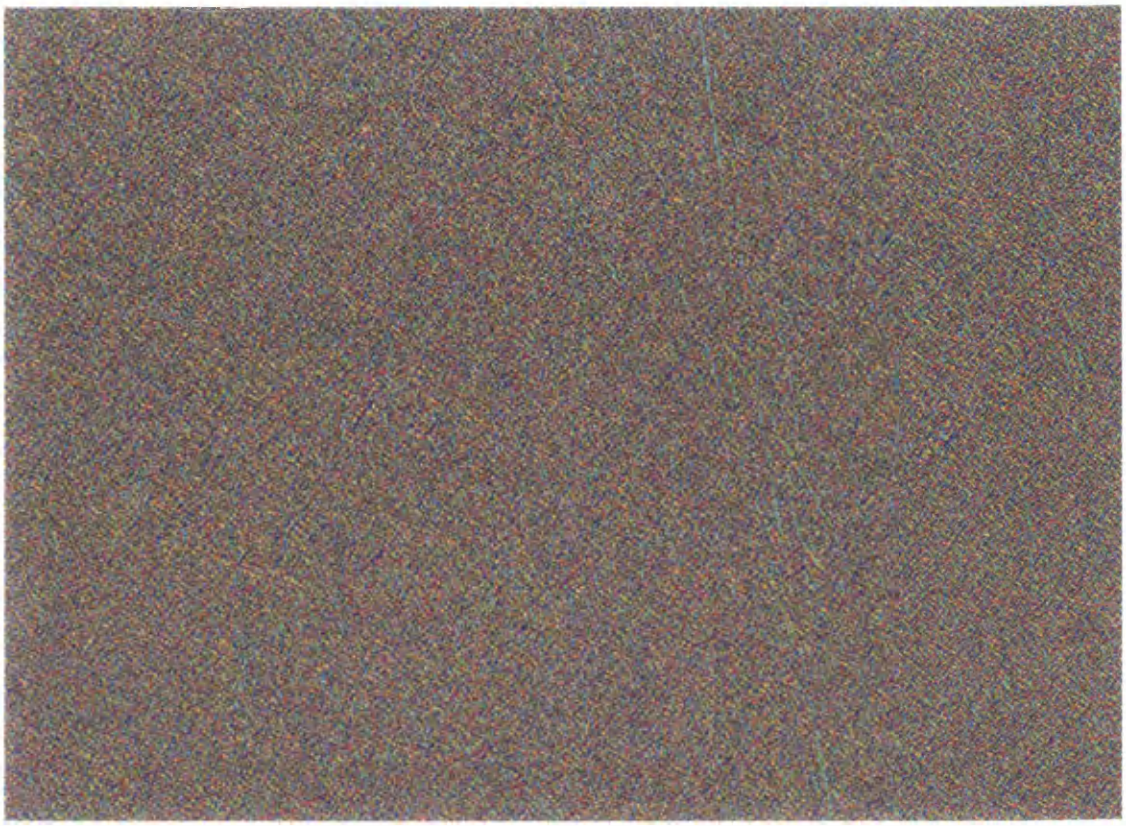

(a) Tensile Region

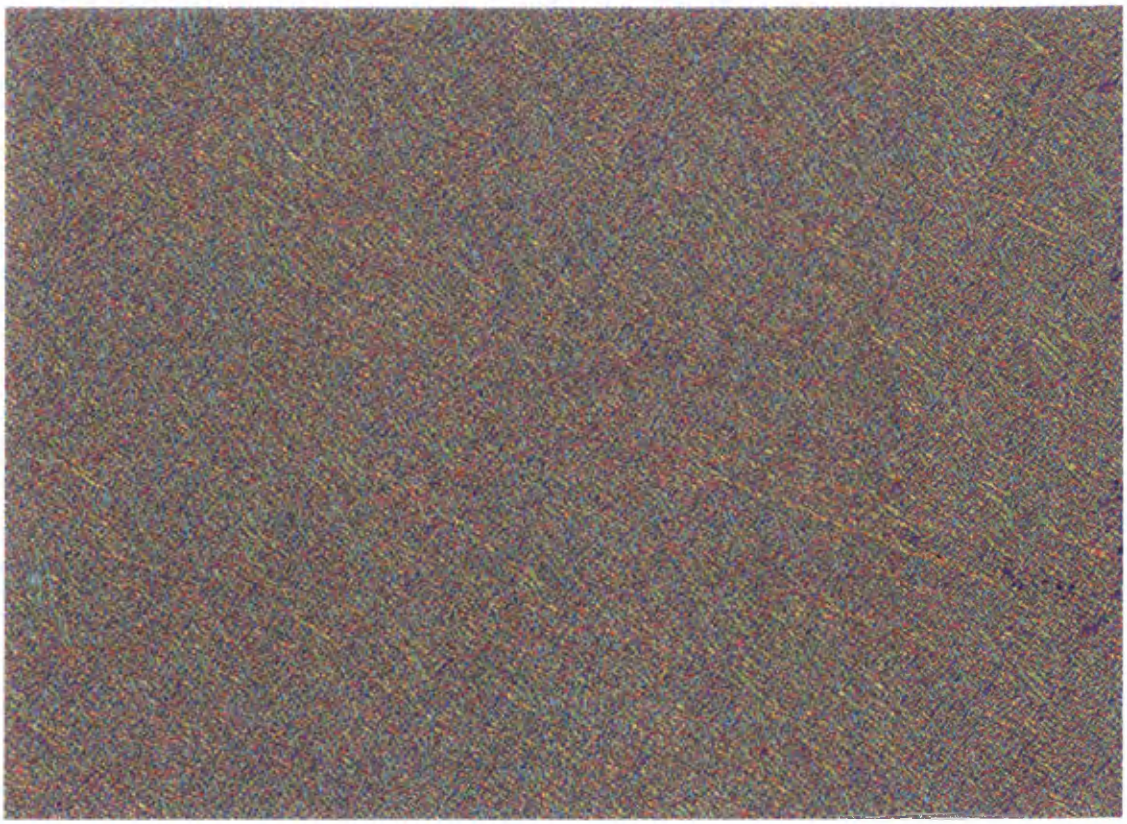

(b) Compressive Region

Figure 8.2: The direction of anisotropy of the GND content is plotted at each point in the maps of the tensile and compressive regions. The colour key is shown in Fig.8.1

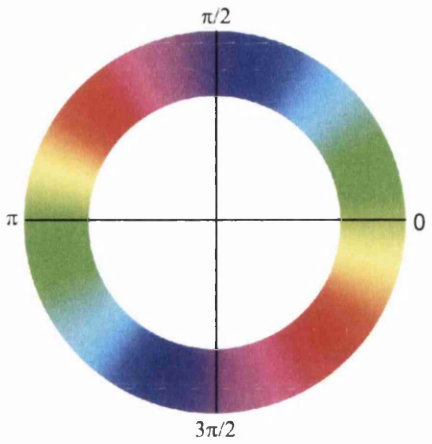

Figure 8.3: The colour wheel used for plotting the direction of anisotropy of Fig.8.2

are primarily normal to the map plane). In future, the plots may be modified for grain size as it appears to affect the size and frequency of tangles by changing the number of possible end points.

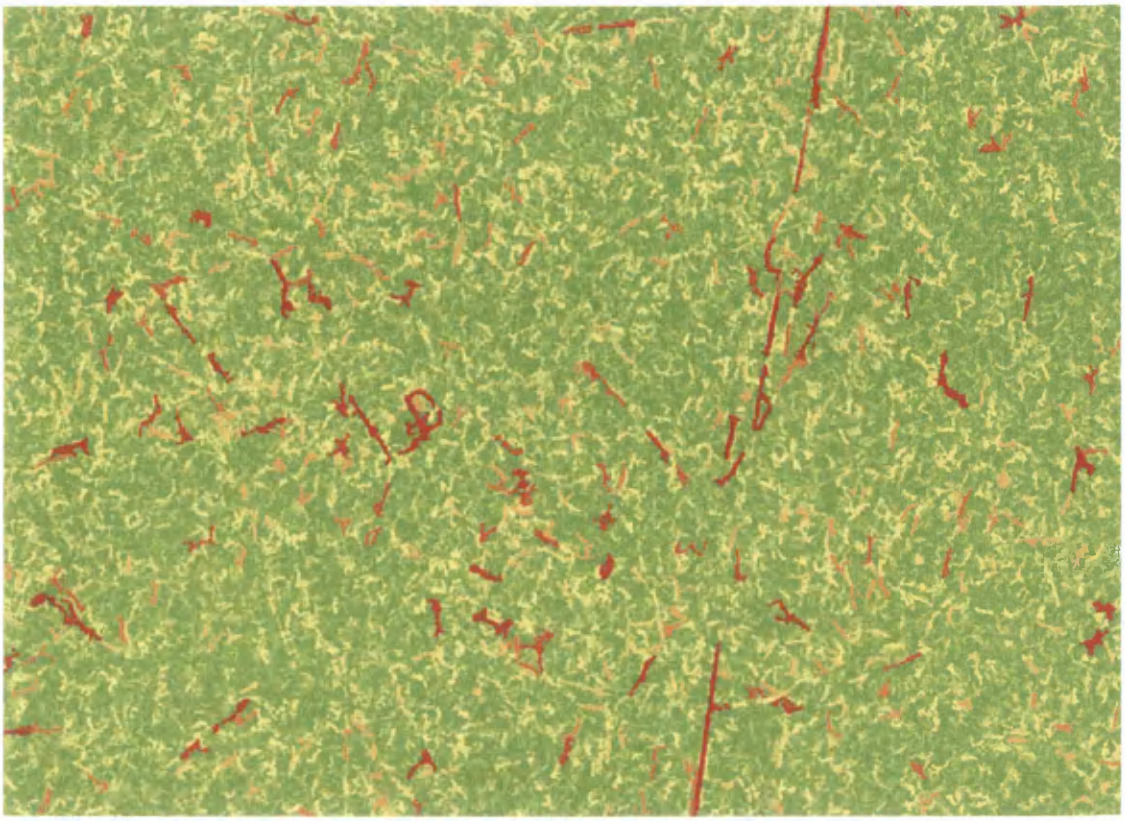

(a) Tensile Region

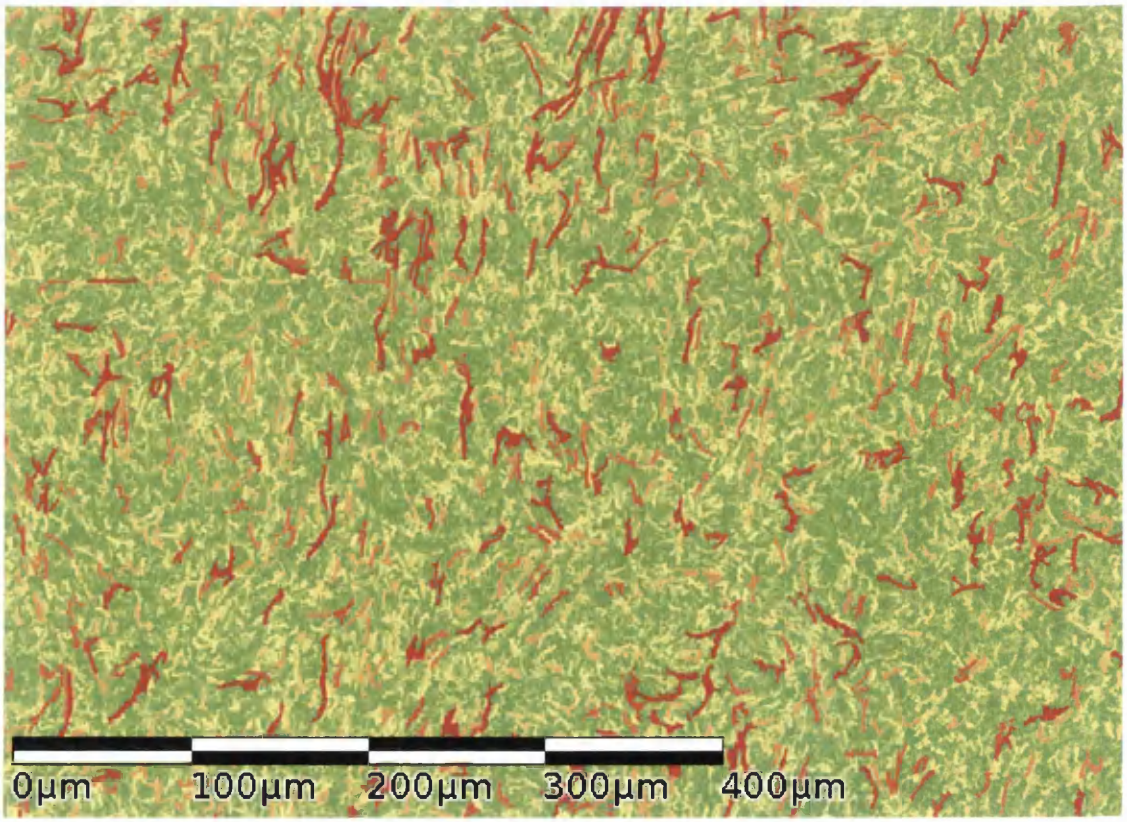

(b) Compressive Region

Figure 8.4: Detected tangles in de-noised GND maps of sample 21.

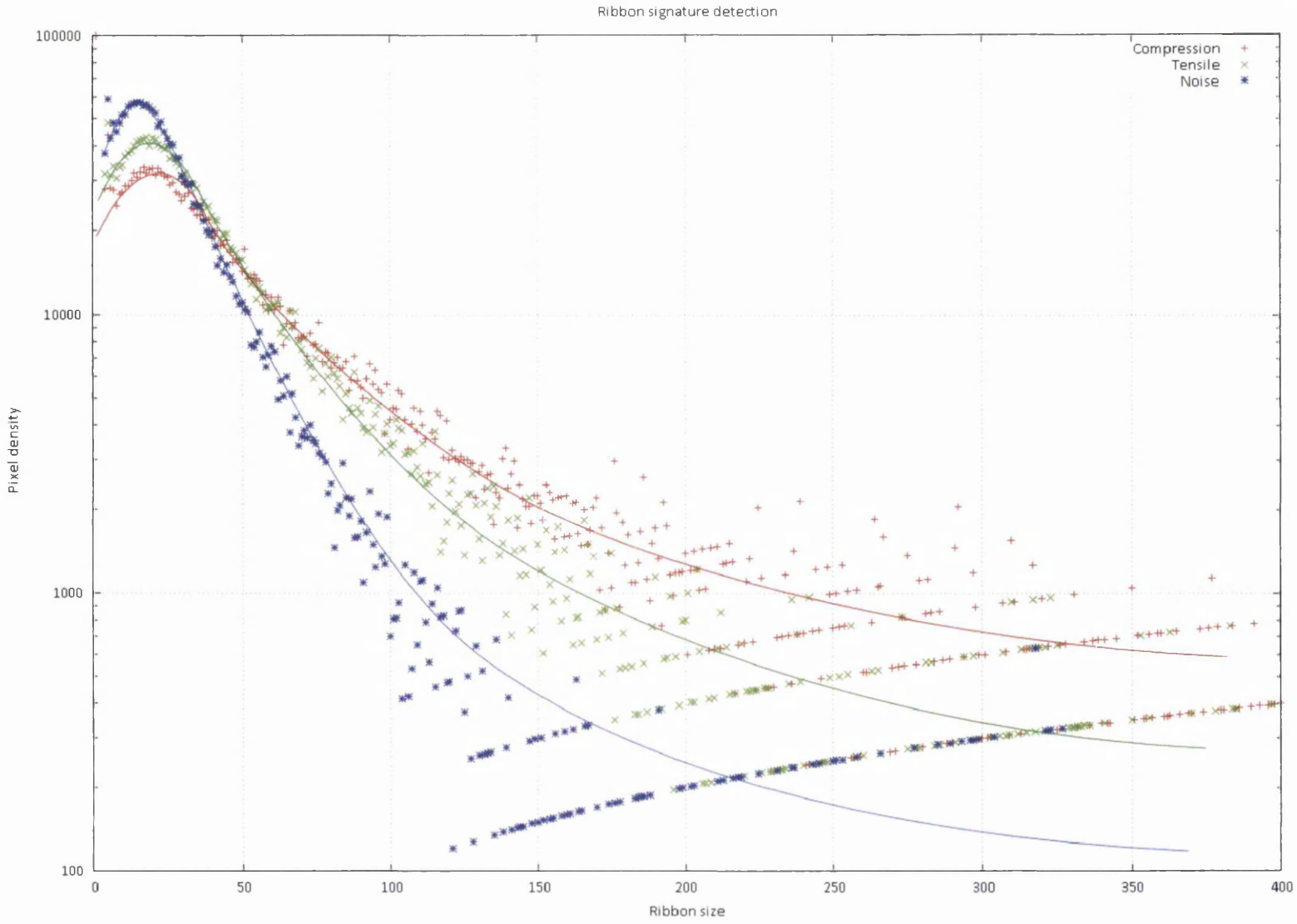

Figure 8.5: The tangle size plotted against the number of pixels in each image constituting tangles of each according size for the maps of the tensile and compressive regions of sample 21. Detected tangles in a map containing entirely noise is also plotted as a control. An approximate line of best fit is supplied as a visual aid.

Chapter 9

Conclusions

Three sets of bent copper samples were prepared with varying amounts of deformation and heat treatments. Software was then written to resolve small orientation changes into GND content. The code written is included in Appendix D. The position of the GND content within the sample and around key features was then used to characterize the development of the microstructure after deformation and subsequent heat treatments. The following conclusions can be drawn concerning the technique of measuring GNDs using the commonly used hough transformation;

1. Optimal settings for resolving GNDs were determined as follows. Settings were optimized for indexing accuracy while also allowing for reasonably large maps to be created within a feasible time scale. The highest Hough space resolution available, in this case using Flamenco software, is 125. This was used as it was found to increase accuracy with negligible time cost. Final settings also included a $0.5\mu m$ step size, a 2x2 binned Kikuchi pattern image, 2 frames averaging, indexing using 3-6 bands, high gain, and indexing by band edges. Indexing by band edges and band centres was found to have similar accuracy, with band centres giving slightly more reproducible results. The two methods differed in the profile of indexing noise, with band edges showing a normally distributed noise profile. Indexing by band edges was then selected with the suggested use of a noise reduction algorithm for normally distributed noise.

2. In addition to the indexing noise, the accuracy of GND maps was affected

by the surface preparation of samples and the underlying structure of dislocations. Micro-scratches were observed on sample surfaces which affected the indexing in those areas and, as samples were prepared by hand, the size a frequency of scratches was inconsistent between samples. It is therefore recommended that any future work use automatic preparation methods to obtain a more repeatable surface finish. The GND maps were also affected by the underlying structure of dislocations. Dislocations arranged into tangles were more easily resolved into GNDs due to the larger point-to-point misorientation angle associated with the higher concentration of dislocations, which was then more easily discernible from indexing noise. In contrast, a lower percentage of total dislocations in a diffuse dislocation structure is resolved as GNDs. As a result, comparison of GND content between maps is of no value. A region of high GND content is taken as only being high in contrast to other regions within the map from where it was taken. For this reason, maps taken from the tensile deformed edge of sample 20F showed a diffuse GND structure, with a lower average GND content than a map taken in the non-deformed region away from the fold with a tangled GND structure.

3. GND maps are most effective when used to determine the structure of dislocations in a material rather than the magnitude. To this effect, it is proposed that the connectedness of GNDs be quantified. A method of detecting GND tangles is proposed which allows the quantification of the size and frequency of dislocation tangles which could then be used to predict mechanical properties of the material which are affected by the relaxed structure of dislocations in the material.

The following conclusions can be drawn concerning the development of the microstructure of copper samples after deformation and annealing;

1. The neutral plane, at which the strain changes from tensile to compression in character, is located closer to the tensile end of the sample. This is evidenced by the large peaks in the GND content profile across sample 20F which were located closer to the tensile end. Also, the more advanced stages

of restoration seen in the compression end of all samples is indicative of a larger driving force for restoration due to higher strain.

2. The structure of GNDs changes during deformation and restoration and separate stages can be identified. A relaxed structure after sufficiently long heat treatment initially shows GNDs agglomerating into low energy structures resembling tangles. Upon deformation, additional dislocations start to produce a diffuse dislocation structure. Increasing deformation causes certain grains to accommodate more strain than neighbours, showing certain grains with higher GND content. Annealing causes recovery to occur, and an evening out of the GND content across the grains. Continued annealing and grain growth again shows certain grains with higher GND content than neighbours, which is likely caused by a grain twinning and the resulting twin orientation not being aligned for maximum reduction of retained strain. Further annealing shows a second recovery stage where the dislocations formed behind a mobile boundary interact to form tangles.

3. After the GND content in front of a sufficiently large sampling of $\Sigma 3$ and non-CSL boundaries is taken, a typical profile is obtained. $\Sigma 3$ boundaries show higher GND content close to the boundary interface than non-CSL boundaries but lower GND content moving into the grain bulk. $\Sigma 3$ boundaries also act to shield the grain bulk from deformation under an applied strain, while GND content in grains with non-CSL boundaries increases in the grain bulk and in front of the boundary interface with increasing strain.

Appdx A

Appendix A is included in the pdf version.

Appdx B

Appendix B is included in the pdf version.

Appdx C

Appdx D

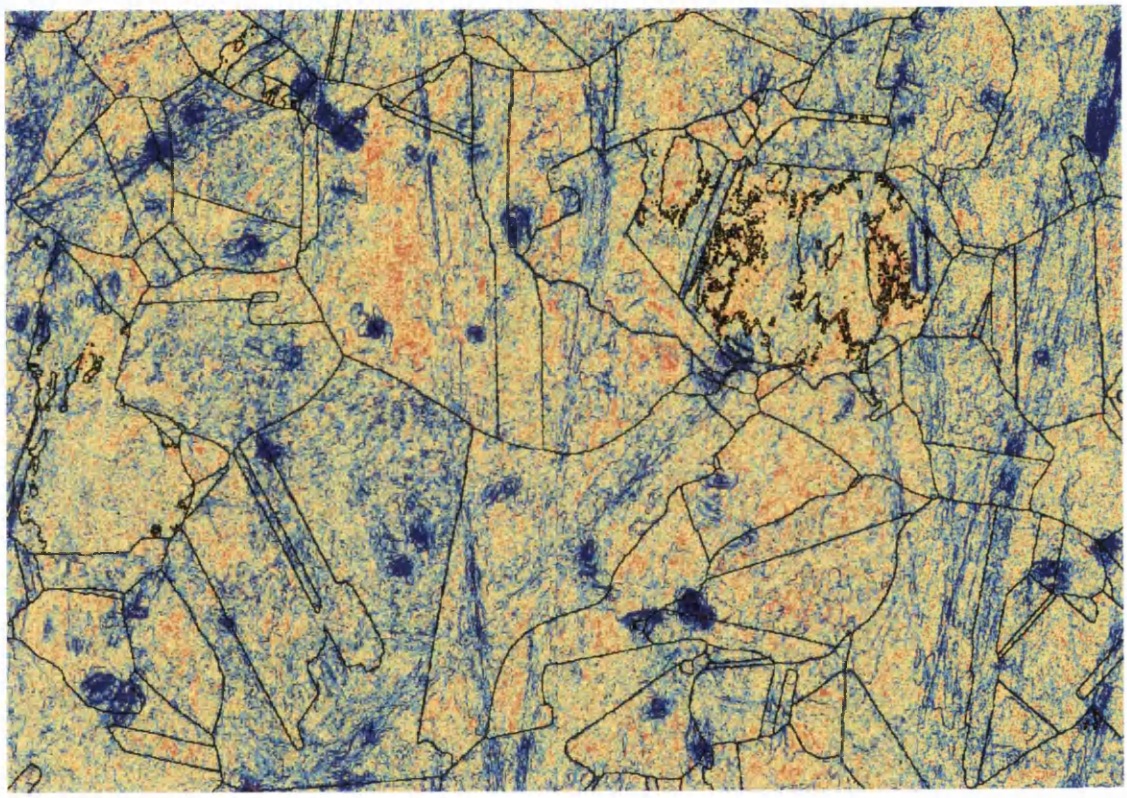

Appdx E

Appendix E is included in the pdf version.

References

[1] A. Wilkinson *Ultramicroscopy*, vol. 62, pp. 237–247, 1996. 1, 46, 69, 77

[2] W. Pantleon *Scripta Mater.*, vol. 58, pp. 994–997, 2008. 1, 40, 41, 45, 74

[3] J. Nye *Acta Metall.*, vol. 1, p. 153, 1953. 1, 35, 36, 45, 119

[4] A. Wilkinson *Scripta Mater.*, vol. 44, pp. 2379–2385, 2001. 2, 46, 69, 119

[5] B. Britton, S. Birosca, M. Preuss, and A. Wilkinson *Scripta Materialia*, vol. 62, pp. 639–642, 2010. 2

[6] M. Calcagnotto, D. Ponge, E. Demir, and D. Raabe *Materials Science and Engineering A.*, vol. 527, pp. 2738–2746, 2010. 2, 45, 46

[7] V. Randle *Materials Science and Technology*, vol. 26, pp. 253–261, 2010. 2, 6, 31

[8] D. Hull and D. Bacon, *Introduction to Dislocations.* Butterworth-Heinemann, 1984. 8, 9, 13, 15, 24, 26

[9] D. Wolf and S. Yip. Springer, 1992. 11, 12, 13, 15, 23

[10] G. Palumbo, K. Aust, P. King, A. Brennenstuhl, and P. Lichtenberger *Phys Stat Sol.*, vol. 131, pp. 425–428, 1992. 11

[11] V. Randle, *The Role of the Coincidence Site Lattice in Grain Boundary Engineering.* Institute of Materials, 1996. 13, 14, 26

[12] D. Warrington and M. Boon *Scripta Metall.*, vol. 23, pp. 599–607, 1975. 13

[13] P. Pumphrey and K. Bowkett *Scripta Metall.*, vol. 5, pp. 365–369, 1971. 14, 17

[14] P. Pumphrey and K. Bowkett *Scripta Metall.*, vol. 6, pp. 31–34, 1972. 14, 17

[15] V. Randle *Materials Characterization*, vol. 47, pp. 411–416, 2001. 14, 18, 21, 30

[16] M. Kronberg and M. Wilson *Met Trans.*, pp. 501–514, 1949. 16

[17] D. Brandon, B. Ralph, S. Ranganathan, and M. Wald *Acta Metall.*, vol. 12. 17

[18] D. Brandon *Acta Metall.*, pp. 1479–1484, 1966. 17, 90

[19] G. Palumbo and K. Aust *Acta Metall.*, vol. 38, p. 2343, 1990. 17

[20] G. Palumbo, K. Aust, E. Lehockey, U. Erb, and P. Lin *Scripta Mater.*, vol. 38, pp. 1685–1690, 1998. 17

[21] J. Rutter and K. Aust *Acta Metall.*, vol. 13, pp. 181–186, 1965. 18

[22] X. Fang, W. Wang, H. Guo, X. Zhang, and B. Zhou *Journal of Iron and Steel Research International*, vol. 14, pp. 339–343, 2007. 18

[23] G. Hasson and C. Goux *Scripta Metall.*, vol. 5, pp. 965–968, 1971. 18

[24] D. Olmsted, S. Foiles, and E. Holm *Acta Mater.*, vol. 57, pp. 3694–3703, 2009. 19, 20

[25] T. Skidmore, R. Buchheit, and M. Juhas *Scripta Mater*, vol. 50, pp. 873–877, 2004. 20

[26] G. Rohrer, E. Holm, A. Rollett, S. Foiles, J. Li, and D. Olmsted *Acta Mater.*, vol. 58, pp. 5063–5069, 2010. 20

[27] J. Li, S. Dillon, and G. Rohrer *Acta Mater.*, vol. 57, pp. 4304–4311, 2009. 20

[28] E. Holm, D. Olmsted, and S. Foiles *Scripta Mater.*, vol. 63, pp. 905–908, 2010. 20

[29] K. Barmak, J. Kim, C. Kim, W. Archibald, G. Rohrer, A. Rollet, D. Kinderlehrer, S. Ta'asan, H. Zhang, and D. Srolovitz *Scripta Mater.*, vol. 54, pp. 1059–1063, 2006. 20

[30] Y. Amouyal and E. Rabkin *Acta Mater.*, vol. 55, pp. 6681–6689, 2007. 20

[31] G. Bleris and T. Karakostas *Acta Crystall. A*, vol. 45, pp. 297–303, 1989. 21

[32] V. Gertsman *Acta Crystall. A*, vol. 57, pp. 369–277, 2001. 21

[33] V. Gertsman and C. Henager *Interfacial Science*, vol. 11, pp. 403–415, 2003. 21, 27

[34] V. Randle *Acta Mater.*, vol. 52, pp. 4067–4081, 2004. 22, 30, 31, 32, 33, 34

[35] V. Randle *Acta Metall.*, vol. 46, pp. 1459–1480, 1997. 22, 23

[36] W. Xu, M. Ferry, N. Mateescu, J. Cairney, and F. Humphreys *Materials Characterization*, vol. 58, pp. 961–967, 2007. 24

[37] D. Saylor, B. El Dasher, and G. Rollet, A Rohrer *Acta Mater.*, vol. 52, pp. 3649–3655, 2004. 24

[38] C.-S. Kim, Y. Hu, G. Rohrer, and V. Randle *Scripta Mater.*, vol. 52, pp. 633–637, 2005. 24

[39] G. Rohrer, V. Randle, C.-S. Kim, and Y. Hu *Acta Mater.*, vol. 54, pp. 4489–4502, 2006. 24

[40] V. Randle, G. Rohrer, H. Miller, M. Coleman, and G. Owen *Acta Mater.*, vol. 56, pp. 2363–2373, 2008. 24

[41] S. Mahajan, C. Pande, M. Imam, and B. Rath *Acta Mater.*, vol. 45, pp. 2633–2638, 1997. 26, 27, 28, 29

[42] R. Fullman and J. Fischer *J Appl Phys.*, vol. 22, p. 1350, 1951. 27

[43] S. Dash and N. Brown *Acta Metall.*, p. 1067, 1963. 27

[44] M. Myers and L. Murr *Acta Metall.*, vol. 26, p. 951, 1978. 27

[45] G. Gindraux and W. Form *J Inst Met.*, vol. 101, p. 85, 1973. 27

[46] H. Gleiter *Acta Metall.*, vol. 17, p. 1421, 1969. 28

[47] B. Rath, M. Imam, and C. Pande *Mater Phys Mech I.*, pp. 61–66, 2000. 28, 29

[48] C. Pande, M. Imam, and B. Rath *Met Trans A*, vol. 21A, p. 2891, 1990. 28

[49] D. Field, L. Bradford, M. Nowell, and T. Lillo *Acta Mater.*, vol. 55, pp. 4233–4241, 2007. 29, 93

[50] D. Field, R. Eames, and L. TM *Scripta Mater.*, vol. 54, pp. 983–986, 2006. 29

[51] H. Miura, T. Sakai, and J. Jonas *Scripta Mater.*, vol. 55, pp. 167–170, 2006. 29, 94

[52] T. Watanabe *Res Mech.*, vol. 11, pp. 47–84, 1984. 30

[53] P. Lin, G. Palumbo, U. Erb, and K. Aust *Scripta Metall Mater.*, vol. 33, p. 1387, 1995. 30

[54] V. Randle *Acta Mater.*, vol. 47, pp. 4187–4196, 1999. 31

[55] S.-L. Lee and N. Richards *Materials Science and Engineering A.*, vol. 390, pp. 81–87, 2005. 32

[56] S.-L. Lee and N. Richards *Materials Science and Engineering A.*, vol. 405, pp. 74–85, 2005. 32

[57] C. Thomson and V. Randle *Acta Mater.*, vol. 45, pp. 4909–4916, 1997. 32

[58] C. Thomson and V. Randle *Scripta Mater.*, vol. 35, pp. 385–390, 1996. 32

[59] W. King and A. Schwartz *Scripta Mater.*, vol. 38, pp. 449–455, 1998. 32

[60] V. Randle and H. Davies *Metallurgical and Materials Transactions A*, vol. 33, pp. 1853–1857, 2002. 33, 47, 50

[61] V. Randle and C. M *Acta Mater.*, vol. 57, pp. 3410–3421, 2009. 33

[62] T. Watanabe *Materials Science and Engineering A*, vol. 176, pp. 39–49, 1994. 34

[63] V. Randle and O. G *Acta Mater.*, vol. 54, pp. 1777–1783, 2006. 34

[64] P. Fortier, W. Miller, and K. Aust *Acta Mater.*, vol. 45, pp. 3459–3467, 1997. 34

[65] M. Kumar, W. King, and A. Schwartz *Acta Mater.*, vol. 48, pp. 2081–2091, 2000. 34

[66] S. Tsurekawa, S. Nakamichi, and T. Watanabe *Acta Mater.*, vol. 54, pp. 3617–3626, 2006. 34

[67] C. Schuh, M. Kumar, and W. King *Acta Mater.*, vol. 51, pp. 687–700, 2003. 34

[68] M. Frary and C. Schuh *Acta Mater.*, vol. 53, pp. 4323–4335, 2005. 34

[69] C. Schuh and M. Frary *Scripta Mater.*, vol. 54, pp. 1023–1028, 2006. 34

[70] D. Fullwood, J. Basinger, and B. Adams *Acta Mater.*, vol. 54, pp. 1381–1388, 2006. 34

[71] J. Basinger, E. Homer, and B. Adams *Scripta Mater.*, vol. 53, pp. 959–963, 2005. 34

[72] A. Schwartz, W. King, and M. Kumar *Scripta Mater.*, vol. 54, pp. 963–968, 2006. 34

[73] B. Reed and M. Kumar *Scripta Mater.*, vol. 54, pp. 1029–1033, 2006. 34

[74] M. Ashby *Phil Mag*, vol. 21, p. 399, 1970. 35, 36, 38

[75] A. Evans and J. Hutchinson *Acta Mater.*, vol. 57, pp. 1675–1688, 2009. 35, 36

[76] G. Taylor *J Inst Metals*, vol. 62, p. 307, 1938. 36

[77] N. Fleck, G. Muller, M. Ashby, and J. Hutchinson *Acta Metall et Mater.*, vol. 42, pp. 475–487, 1994. 36

[78] W. Nix and H. Gao *Phys Solids*, vol. 46, p. 411, 1998. 36

[79] H. Gao, Y. Huang, W. Nix, and J. Hutchinson *J Mech Phys Solids*, vol. 47, p. 1239, 1999. 36, 45

[80] N. Fleck and J. Hutchinson *Journal of the Mechanics and Physics of Solids*, vol. 49, pp. 2245–2271, 2001. 36

[81] A. Arsenlis and D. Parks *Acta Mater.*, vol. 47, pp. 1597–1611, 1999. 37, 39, 40, 42, 43, 44

[82] E. Kroner *Appl Mech Rev.*, vol. 15, p. 599, 1962. 38

[83] E. Kroner *Int J Engng Sci.*, pp. 219–251, 1981. 38

[84] S. Sun, B. Adams, C. Shet, S. Saigal, and W. King *Scripta Mater.*, vol. 39, pp. 501–508, 1998. 40

[85] S. Sun, B. Adams, and W. King *Philosophical Magazine A*, vol. 80, pp. 9–25, 2000. 40

[86] B. El Dasher, B. Adams, and A. Rollett *Scripta Mater.*, vol. 48, pp. 141–145, 2003. 40, 41, 46

[87] V. Randle, N. Hansen, and D. Jensen *Philosophical Magazine A*, vol. 73, p. 265, 1996. 40

[88] D. Field, P. Trivedi, S. Wright, and M. Kumar *Ultramicroscopy*, vol. 103, pp. 33–39, 2005. 40

[89] A. Wilkinson and D. Randman *Philosophical Magazine*, vol. 90, pp. 1159–1177, 2010. 41, 45, 46

[90] L. Kubin and A. Mortensen *Scripta Mater.*, vol. 48, pp. 119–125, 2003. 45

[91] T. Baudin and R. Penelle *Metall Trans A*, vol. 24, pp. 2299–2311, 1993. 47

[92] "Experimental set up of ebsd system," 2012. 48

[93] J. Hjelen. PhD thesis, The Institute of Physics, The University of Trondheim, 1990. 50

[94] A. Wilkinson and P. Hirsch *Micron*, vol. 28, pp. 279–308, 1997. 50

[95] H. Bunge, *In Preferred Orientation in Deformed Metals and Rocks: an Introduction to Modern Texture Analysis.* Academic Press Inc., 1985. 52

[96] D. Field, K. Magid, I. Mastorakos, J. Florando, D. Lassila, and J. Morris Jr *Phil Mag*, vol. 90, pp. 1451–1464, 2010. 60

[97] R. Duda and P. Hart *Communications of the ACM*, vol. 15, pp. 11–15, 1972. 62

[98] X. Tao and A. Eades *Microsc Microanal*, vol. 11, pp. 79–87, 2005. 63

[99] N. Krieger Lassen, D. Juul Jensen, and K. Conradsen *Scanning Microscopy*, vol. 6, pp. 115–121, 1992. 63

[100] N. Krieger Lassen *Micron and Microscopica Acta*, vol. 23, pp. 191–192, 1992. 63

[101] V. Vijaykumar, P. Vanathi, and P. Kanagasabapathy *International Journal of Computer Science*, vol. 37, 2010. 70

[102] R. Garnett, T. Huergerich, and C. Chui *IEEE Trans on Image Processin*, vol. 14, pp. 1747–1754, 2005. 71

[103] M. Kamaya *Ultramicroscopy*, vol. 111, pp. 1189–1199, 2011. 73

[104] M. Kamaya *Materials Characterization*, vol. 66, pp. 56–67, 2012. 73

[105] A. Wilkinson, G. Meaden, and D. Dingley *Ultramicroscopy*, vol. 106, pp. 307–313, 2006. 77

[106] U. Singh and H. Jiang *Materials Science Forum*, vol. 702-703, pp. 667–670, 2011. 88

[107] J. Zelinski, "An evaluation of grain boundary engineering technology and processing scale-up," Master's thesis, University of Michigan, 2005. 90

[108] A. Wilkinson *Acta Metal Mater*, vol. 39, pp. 3047–3055, 1991. 90

[109] S.-H. Kim, S. Han, C. Kim, I.-Y. Hwang, and F. Yin *Materials Transactions*, vol. 50, pp. 537–543, 2009. 91

[110] D. Lee *International Journal of Mechanical Sciences*, vol. 42, pp. 1645–1678, 2000. 92, 100

[111] D. Armstrong, A. Wilkinson, and S. Roberts *Journal of Materials Research*, vol. 24, pp. 3268–3276, 2009. 92

[112] V. Randle, M. Coleman, and M. Waterton *Metallurgical and Materials Transactions A*, vol. 42A, pp. 582–586, 2011. 125, 217

[113] F. Humphreys, *Recrystallization and Related Annealing Phenomena*. Pergamon, 1995. 167

Acronyms

BCC Body-Centred Cubic.

BSE Back-Scattered Electron.

CSL Coincidence-Site Lattice.

EBSD Electron Back-Scatter Diffraction.

EBSP Electron Back-Scatter Diffraction Pattern.

FCC Face-Centred Cubic.

FIB Focussed Ion Beam.

GBE Grain Boundary Engineering.

GND Geometrically-Necessary Dislocations.

SEM Scanning Electron Microscope.

SSD Statistically Stored Dislocations.

TEM Transmission Electron Microscope.

XCF Cross-Correlation Function.